Dissertation Advisor: Brendan J. Meade Meredith Avery Langstaff

Mechanical Models of Continental Plate Boundaries: Fault Slip Rates and Interseismic Stress Rotation Rates

Abstract

We first describe the methodology for a two-dimensional, elastic deformable microplate modeling approach for continental plate boundaries. Deformable microplate models combine discrete slip on microplate boundaries (faults) with continuous deformation in block interiors. Two idealized models simulating continental collision are presented, one with two microplates and one with four microplates.

We then apply the deformable microplate modeling approach to two continental boundaries: the India-Asia collision zone and the southern California fault system. For the India-Asia boundary, we show a suite of six models, varying only in boundary conditions. The model with a convergence displacement boundary condition on the eastern three-quarters of the Himalayan Range front combined with a force boundary condition on the southeastern margin best predicts slip rates on the major Tibetan faults and the southeastern extrusion of Tibetan crustal material.

For the southern California fault system, we test models ranging from fully distributed deformation (all Pacific-North America plate motion located on the western boundary of the model) to fully localized deformation (all Pacific-North America plate motion localized on the San Andreas fault). Models with $\sim 75\%$ of plate motion on the San Andreas fault and

$\sim 25\%$ on the western boundary best predict the along-strike slip rate of the San Andreas fault.

Finally, we derive an equation for the rotation rate of the principal stress axes as a function of a regionally constant background stress, a tectonic stressing rate, and time. We show the results of a parameter sensitivity analysis and give the expected magnitude of the stress rotation rate for a range of idealized background stresses and stressing rates. The stress rotation rates across an infinitely long strike-slip fault are shown for a range of background stresses. We then combine block model-derived southern California tectonic stressing rates with candidate background stresses to predict the expected interseismic principal stress axes rotation rates as a function of the magnitude of a regionally constant background stress.

Contents

List of Figures

List of Tables

Acknowledgements

My adviser, Brendan Meade, has been an invaluable support over the course of my graduate student career. He has provided immeasurable patience, insight, and guidance over the course of my six years at Harvard. Without him this thesis would not have been possible.

I would also like to thank my committee members, Rick O'Connell, John Shaw, Dave Johnston, and Francis Macdonald, for the questions, comments, and conversations that have helped guide and shape this research into a stronger project.

Within the broader Earth and Planetary Sciences community, I would like to thank the entire EPS graduate student and post-doc community for their friendship and camaraderie. I would also like to thank the EPS administrative and custodial staff for their unwavering help and support. Special thanks go to Sarah Colgan, who has been an immeasurable resource over my entire graduate school career.

I am particularly grateful to the other members of the Meade Group: Jack Loveless, Eileen Evans, Phoebe Robinson, and Ben Thompson, who have spent countless hours brainstorming scientific concepts with me and who have provided valuable scientific insight. Over the course of my six years in the EPS department, I have shared an office with a number of remarkable individuals, and I would like to thank them for their support and encouragement over the years: Laurel Senft, Veronika Soukhovitskaya, Kristian Bergen, Natalya Gomez,

Ben Thompson, Harriet Lau, Jackie Austermann, Blake Hodgin, Phoebe Robinson, and Erik Chan. I owe a special debit of gratitude to Eric Morrow, who has become a dear friend and who has helped me brainstorm ideas, debug code, and edit manuscripts, and to Carling Hay, who has helped me edit this thesis.

Beyond the EPS community, I would like to give special acknowledgment to George Baker, for broadening my horizons with a wealth of teaching and learning opportunities and innumerable stimulating and inspiring conversations.

I owe my success as a graduate student to the love and support of my friends. They have lent an ear when I needed to talk and have helped me find the motivation and inspiration to keep going when I was lost.

Finally, I would not be here without my family. They have been the source of bottomless encouragement, humor, and love and have given me the confidence to strike out on my own. Thank you to my parents, David H. Langstaff and Cynthia Shauer Langstaff, my brothers, Chris, Todd, and Will, my aunt, Lee M. Langstaff, and my grandparents, Ken and Sally Shauer and Ken and Percy Langstaff. Lastly, thank you to my husband, Owen Morrison. He has been my confidante, my rock, and my partner, and I look forward to many adventures to come.

Chapter 1

Introduction

The goal of this work is to provide testable predictions of interseismic fault slip rates and principal stress rotation rates. Over the past several decades, significant progress has been made in geologically and geodetically characterizing the nature of slip on faults at continental boundaries (e.g., Bilham et al., 1997; Fialko, 2006; Loveless and Meade, 2011b; Meade and Hager, 2005; Savage and Burford, 1973; Wright et al., 2004; Yue et al., 2001). Over the same time period, extensive work has been done in an effort to constrain the crustal stress field, both directly with borehole breakout measurements, and indirectly with inversions of earthquake focal mechanisms and p-axes (e.g., Gephart and Forsyth, 1984; Hardebeck and Michael, 2006; Michael, 1984; Wilde and Stock, 1997; Yang and Hauksson, 2013; Zhao et al., 1997; Zoback and Healy, 1992). By developing models that are independent of these fault slip rate and principal stress axes estimates we can make quantitative predictions that can be compared back to these data.

The research presented here focuses on two major continental boundaries: the India-Asia boundary and the Pacific-North America boundary. As the largest region of continental deformation in the world, the tectonics of the India-Asia collision zone have been the focus

of intense study since the 1970s. While the Tibetan plateau is the hallmark feature of this boundary, the India-Asia collision zone is also characterized by several major, geographically extensive strike-slip faults that extend more than a thousand kilometers and that have accommodated hundreds of kilometers of slip (Fu and Awata, 2007; Leloup et al., 2001, 1995; Molnar and Tapponnier, 1975; Murphy et al., 2000; Yue et al., 2001). Geodetic and geologic slip rate estimates on these faults provide independent data against which model predictions may be compared. The India-Asia boundary and the Tibetan plateau have also served as the locus of debate for two prevailing hypotheses regarding the nature of continental tectonics and deformation: the first as the relative motion of multiple rigid blocks (Avouac and Tapponnier, 1993; Meade, 2007; Tapponnier et al., 1982; Thatcher, 2007), and the second as a thin viscous sheet undergoing continuous deformation (England and McKenzie, 1982; England and Molnar, 1997, 2005; Flesch et al., 2001).

The second continental boundary considered is the Pacific-North America plate boundary and the southern California fault system. The San Andreas fault is the dominant feature of this system: stretching from the Gulf of California in the south to the Mendocino Triple Junction in the north, it poses a considerable seismic threat to Los Angeles and San Francisco (Weldon et al., 2005; Working Group on California Earthquake Probabilities, 1995). Slip rates on the southern San Andreas fault, here defined as the Parkfield segment in the north to the Imperial fault in the south, are constrained from a dense sampling of both geologic and geodetic measurements (e.g., Chuang and Johnson, 2011; Fialko, 2006; Loveless and Meade, 2011b; McGill et al., 2013; Meade and Hager, 2005; Murray et al., 2001; Savage and Burford, 1973; Schmalzle et al., 2006; Segall, 2002; Sieh and Jahns, 1984). Researchers

have also attempted to constrain the state of stress in southern California through regional borehole breakouts (Wilde and Stock, 1997), scientific drilling sites into the San Andreas (Boness and Zoback, 2004; Hickman and Zoback, 2004; Shamir and Zoback, 1992; Townend and Zoback, 2004; Zoback et al., 2011; Zoback and Healy, 1992; Zoback et al., 1987), and focal mechanism and p-axis inversions (i.e., Gephart and Forsyth, 1984; Hardebeck and Hauksson, 2001; Hardebeck and Michael, 2006; Hauksson, 1990, 1994; Michael, 1987; Yang and Hauksson, 2013; Zhao et al., 1997). The wealth of southern California slip rate and stress field measurements allows us to compare predictions of fault slip rates and principal stress rotation rates against real data and may help to constrain future measurement studies.

This thesis is organized into four chapters. Chapter 2 introduces a new modeling approach, Deformable Microplate (DM) modeling, which is a hybrid approach between traditional rigid block models (e.g., Meade and Hager, 2005; Tapponnier et al., 1982) and thin viscous sheet models (e.g., England and McKenzie, 1982; England and Molnar, 2005). The DM models developed here incorporate both localized slip on frictionless faults and continuous deformation within microplate interiors. The second chapter describes the methodology for this two-dimensional, linear elastic, two-stage modeling approach and solves for two idealized problems simulating a continental collision.

Chapter 3 presents a suite of six DM models for Tibet. We construct a 10-microplate DM model discretized according to the major mapped structures of the Tibetan plateau (Taylor and Yin, 2009). Using the DM approach we analyze a variety of Dirichlet and force boundary conditions to determine which are required to explain the geologically and geodetically constrained slip rates on major Tibetan faults. All models make slip rate predictions for

the Altyn Tagh, Karakorum, Kunlun, Jiali, and Xianshuihe stike-slip faults. We find that a model that combines a 37 mm/yr (Wang et al., 2001) convergence condition on the eastern three-quartes of the Himalayan Range Front with a 1500 N/m force boundary condition in southeast Asia is most consistent with slip rates on Tibetan faults and with the geodetically observed southeastern extrusion of Tibetan crustal material.

In Chapter 4, we apply the DM modeling approach to southern California to develop a model that best explains slip rates on the southern San Andreas fault. We construct a 19-microplate model from the major mapped faults in the Southern California Earthquake Center Community Fault Model (Plesch et al., 2007). We then use the model to test a range of boundary conditions spanning from 100% distributed deformation (with all Pacific-North America plate motion applied to the western edge of the model domain) to 100% localized deformation (with all Pacific-North America plate motion localized as slip beneath the San Andreas fault). By minimizing the weighted sum of squared residuals between the model-predicted slip rate on the San Andreas and a compendium of geologically and geodetically sampled slip rates, we find that models with 75% of plate motion localized on the San Andreas and 25% applied to the edges of the deforming plate boundary best predict slip rates on the San Andreas.

Chapter 5 explores the evolution of the southern California stress field over the earthquake cycle. Previous focal mechanism inversion studies have posited that large earthquakes both do (e.g., Abers and Gephart, 2001; Gephart and Forsyth, 1984; Hardebeck and Michael, 2006) and do not (e.g., Hardebeck and Hauksson, 2001; Hauksson, 1994; Jones, 1988) rotate the regional stress field. If earthquakes do modulate the regional stress field, we may expect

the orientation of the maximum principal stress axes to evolve interseismically as tectonic stress accumulates. In Chapter 5 we develop an analytical equation for the rotation rate of the principal stress axes as a function of time, stressing rate, and regional background stress. We perform a sensitivity analysis to determine the range of background stresses and stressing rates for which principal stress axes rotations may be expected, and we calculate the principal stress axes rotation rates across an idealized fault (e.g., Savage and Burford, 1973). We then combine a southern California tectonic stressing rate model (Loveless and Meade, 2011b) with a suite of background stresses to constrain the range of hypothetical background stresses for which principal stress axes rotations would be observed in southern California.

Chapter 2

An Introduction to Deformable Microplate Models: Mathematics, Methodology, and Sample Calculations

We present an elastic, two-dimensional, dual-cover deformable microplate modeling technique for continental boundary deformation. Deformable microplate models combine localized slip on faults (microplate boundaries) with distributed deformation within microplate interiors in a two-stage finite element analysis driven by Dirichlet (displacement) and force boundary conditions. Because these models are independent of geologic and geodetic measurements, we can make testable predictions of fault slip rates as a function of different boundary conditions. In this chapter, we first review other techniques for modeling contact behavior between multiple deforming bodies, and then we provide a detailed description of the mathematical formulation for deformable microplate modeling. A sample pseudocode, based on our Matlab model, is included. We also explore two simple idealized continental collision models, one with two blocks and one with four blocks, and show the model-predicted fault slip rates and velocity field.

2.1 Introduction

Since the early 1980s, two end-member hypotheses have emerged to explain behavior at continental boundary zones. In the first, continental boundaries are approximated as a thin viscous sheet undergoing continuous deformation (England and McKenzie, 1982; England and Molnar, 1997, 2005; Flesch et al., 2001). Although these approaches allow for mathematically simplistic linear formulations of the equilibrium equations, they cannot explicitly incorporate localized deformation on faults. A second approach, pioneered by the Tapponnier et al. (1982) plasticene model, treats boundary zone deformation as the relative rigid-body motion between discrete microplates. This class of models forms the foundation for block models, which integrate earthquake cycle processes with tectonics rotations to explain interseismic geodetic observations (Chen et al., 2004; Chuang and Johnson, 2011; Hilley et al., 2009; Loveless and Meade, 2011a,b; Meade, 2007; Meade and Hager, 2005; Thatcher, 2007). Block models have been widely used to estimate slip rates on faults at continental boundaries, but because they invert geodetic and geologic observations, they cannot independently predict fault slip rates and internal block deformation as a result of applied boundary conditions.

Here we present a simple dual-cover elastic finite element technique that unites both the continuum and discrete block end-member approaches, resulting in testable predictions of fault slip rates at continental boundary zones. These models incorporate both localized slip on major faults and distributed deformation within microplates, thus allowing us to analyze the force and displacement boundary conditions necessary to drive geologically and geodetically observed fault slip rates.

2.2 A survey of numerical techniques for modeling contact behavior between deforming bodies

Contact problems, and in particular methods for integrating contact problems with finite element analyses, have been the subject of active discussion, research, and debate since the advent of finite element methods (e.g., Laursen, 2002; Wriggers, 2006). Traditional formulations for contact problems in finite element methods typically rely on iterative techniques for identifying contacting interfaces: in the first step, a global search occurs to identify boundaries that may be in contact; in the second step, a local search is implemented to identify node-node or node-surface pairs that are in contact (Wriggers, 2006). Numerous techniques exist for introducing the weak formulation of the contact problem into the finite element calculation, but the most common methods employ Lagrangian multipliers (e.g. Taylor, 2013; Zienkiewicz and Taylor, 2005) or penalty functions (Maerten and Maerten, 2002; Munjiza, 2004) and are described below. These calculations are performed in a two-step process: first, nodal displacements from the finite element solution are calculated, resulting in the penetration of one body by another; second, the Lagrangian, or penalty function, approach is implemented, forcing penetrating nodes out of other bodies, which in turn modifies the system displacement calculations (Laursen, 2002; Wriggers, 2006).

Significant effort has gone towards developing these and other finite element techniques for integrating the localized faulting and the distributed deformation observed at continental boundary zones. Table 2.1 provides an overview on the similarities and differences between many of these codes. Melosh and Raefsky (1981) modified the split node finite element technique introduced by Jungles (1973) and Jungels and Frazier (1973) such that it can be

implemented on the local, or individual node, level. In this formulation a single continuously deforming body is partially cut by faults. Nodes on fault planes are simultaneously part of elements on either side of the fault plane, and displacements for this node are split such that the node may have two displacements, u^+ and u^-, corresponding to the elements on either side of the fault. Slip node finite element formulations require that the displacement along the fault be prescribed, and thus these techniques cannot be used to make fault slip rate predictions.

Dunbar and Cook (2003) proposed a finite element approach for geologic and geophysical restorations. Using a hyperelastic membrane and triangular finite elements, they construct a geometric model of the geologic region with internal openings (cracks) at faults. The topology and geology of the model domain are particularly important for Dunbar and Cook (2003) restorations. The restoration flattens folds, closes fault gaps, and removes fault overlaps while imposing the least possible residual strain on the restored geometry. The Dunbar and Cook (2003) approach requires fault slip rates and offsets as model inputs. Because this data is required for model restorations, we cannot use the Dunbar and Cook (2003) approach to make fault slip rate predictions or test the boundary conditions necessary for driving fault behavior at continental boundaries.

Dynel, introduced by Maerten and Maerten (2002), is a geomechanical restoration tool designed for reservoir modeling, but it can also be used to run forward models of continental deformation. Like Dunbar and Cook (2003), Dynel relies on two-dimensional triangular meshes cut by faults, fractures, or bedding planes (though it can be extended to three dimensions with tetrahedral meshes), but, unlike the Dunbar and Cook (2003) method,

	Zienkiewicz and Taylor (2005)	*Dunbar and Cook* (2003)	*Muron* (2005)	*Maerten and Maerten* (2006)	*Munjiza* (2004)	*Langstaff and Meade* (2013)
strain formulation	small and large	small	small	small	small	small
rheology	various	linear elastic	linear elastic	linear elastic	various	linear elastic
element type	various	linear triangle	linear triangle	linear triangle	various	linear triangle
contact constraints	hard	soft	hard	unknown	hard	hard
kinematic contact	no	partial	yes	yes	no	yes
three-dimensional	partial	no	yes	no	partial	no
optimization criteria	force balance	energy + contact	energy	unknown	energy	force balance
energy conservative	yes	no	unknown	unknown	no	yes
code name	FEAP	unknown	gOcad	Dynel	CDFEM	DM
source code	FORTRAN	unknown	C++	unknown	C	Matlab

Table 2.1: Comparison of finite element codes that have been used to investigate continental deformation.

Dynel uses a linear elastic rheology. In contrast to most finite element approaches, which rely on the weak formulation of the equilibrium equations and construct a global stiffness matrix, Maerten and Maerten (2002) invoke an iterative solver based on the Gauss-Seidel method. In this formulation, the system is initially at equilibrium, but locally applied displacements, forces, and/or stresses will perturb the system and induce nodal forces. Forces, and thus displacements, are transmitted from node to node until the system returns to equilibrium and the final displacement field is calculated. Interface contacts between opposite sides of a fault, fracture, or bedding plane are modeled using a slave node and master segment relationship. If a slave node penetrates a master segment, a contact force is applied to the node to push it outside of the element containing the master segment. Contact forces, however, may not fully prevent penetration of one body by another. These forces, in turn, perturb the equilibrium and result in displacements within the system.

The Finite Element Analysis Program (FEAP, Taylor, 2013; Zienkiewicz and Taylor, 2005) provides flexibility in element type and model rheology and can include one- and three-dimensional geometries, as well as small or large strain modeling options. Users may choose between two contact constraints: a slave node-master node (or surface) approach, or a tied interface (Taylor, 2013). The slave node-master node approach prevents penetration between bodies by implementing penalty functions, Lagrangian multipliers, or augmented Lagrangian multipliers, as specified by the user. Penalty function approaches may not fully prevent penetration between bodies, and they introduce contact forces at nodes to push the penetrating node outside of the master segment. Lagrangian techniques add energy to the finite element system by implementing constraints to the weak form of the virtual work

equation (Wriggers, 2006). Like the penalty function method, Lagrangian multipliers often do not fully prevent the penetration of one body by another, and augmented Lagrangians are designed to further reduce the impingement of the slave node.

Another modeling software, gOcad, is widely used in both industry and academic geologic and geophysical modeling (Durand-Riard et al., 2010; Muron, 2005). This three-dimensional modeling software uses a discrete topological model, and allows for partitioning of the geological space considered. Each individual region is then meshed using tetrahedra with regularly spaced vertices. gOcad software has been used extensively to generate three-dimensional balanced restorations of complex geological volumes and faults (e.g. Durand-Riard et al., 2010; Muron, 2005). Like Dynel, gOcad may also be used for forward modeling of continental deformation. gOcad employs a master-slave node treatment to maintain fault compliance and minimizes the global strain energy using an iterative dynamic relaxation algorithm (e.g., Oakley and Knight, 1995). As with FEAP, the master-slave relationship introduces displacements to boundary nodes.

Alternatively, tied interfaces in FEAP are implemented only for two-dimensional problems and can be used to connect elements from subregions with different meshing sizes. This type of modeling introduces an interface between the two mesh regions, and is implemented using a dual mortar (or domain decomposition for partial differential equations) Lagrangian multiplier method. These techniques, which are based on the Lagrangian techniques discussed above, allow for numerical convergence at boundaries (Laursen, 2002).

Munjiza (2004) wrote a book and code for modeling phenomena that contain simultaneous continuous and discontinuous processes. The combined finite-discrete element method

draws on both finite element modeling for continuous deformation, and on discrete element modeling for discontinuous interactions between distinct particles. Bodies may also fracture as strain accumulates within the model. Contact interactions are governed by a penalty function approach: when one body (the contactor) penetrates another body (the target) a contact force is generated at the boundary of each body. Munjiza (2004) adopts a distributed contact force that is dependent on the total area of contact. The penalty function approach is designed to enforce the specific contact constraints of the problem, however, in practice, this approach may not eliminate gaps and overlaps between contacting bodies because penalty forces are distributed across contacting nodes. This result suggests that these models may not be capable of accurately capturing the physics at continental plate boundaries, where gaps and overlaps are an unrealistic representation of plate behavior. Further, the Munjiza (2004) methodology is designed to solve purely inertial problems. The combined finite-discrete element method solves for displacements by integrating the Newtonian force formulation twice, and as a result, the inertial terms must be damped out. This formulation is unrealistic for non-inertial plate boundary zone simulations, and therefore not appropriate for our purposes.

2.3 Deformable microplate models

The deformable microplate models presented here combine the continuum and block modeling approaches described in the Introduction (above). Microplates may slide relative to each other at their boundaries (faults) and deform internally in response to applied boundary conditions. Unlike many of the previously described modeling techniques, the

DM models described here feature multiple continuously deforming bodies. A deformable microplate pseudocode, containing the primary functions used to calculate deformation at plate boundaries, is included at the end of this chapter.

All finite element solutions are two-dimensional and elastic, with the weak form of the quasi-static equilibrium equations discretized on a triangular mesh of linear plane stress finite elements. Meshes are constructed using the Matlab MESH2D toolbox.[1] This algorithm uses an iterative approach to optimize vertex positions. Meshes are generated quickly and automatically from a prescribed geometry. Mesh densities are easily adaptable, and thus microplates may be discretized more finely in regions of geometric complexity.

All models use a Young's modulus of 30 GPa and a Poisson's ratio of 0.3. In the first step, microplate geometries are defined (Figure 2.1a) and microplates are individually meshed (Figure 2.1b). We next construct a global mesh (Figure 2.1c) using the boundaries from the entire model domain. To accurately ensure that model boundary nodes are incorporated into the global geometry, and that the entire model domain is fully represented in the global mesh, we generate a $200 - 3000$ m buffer around the perimeter of each microplate (Figure 2.2). The buffer is constructed using the Matlab function bufferm2, which generates a specified number of buffer points at a chosen distance from the polygon to be buffered.[2] For each polygon node we then select the buffer point to be used by minimizing the distance between the buffer point and the node. This buffer maintains the geometry of the microplate it

[1]MESH2D can be downloaded (with documentation) from: http://www.mathworks.com/matlabcentral/fileexchange/25555-mesh2d-automatic-mesh-generation.

[2]Downloadable from: http://www.mathworks.com/matlabcentral/fileexchange/11095-bufferm2.

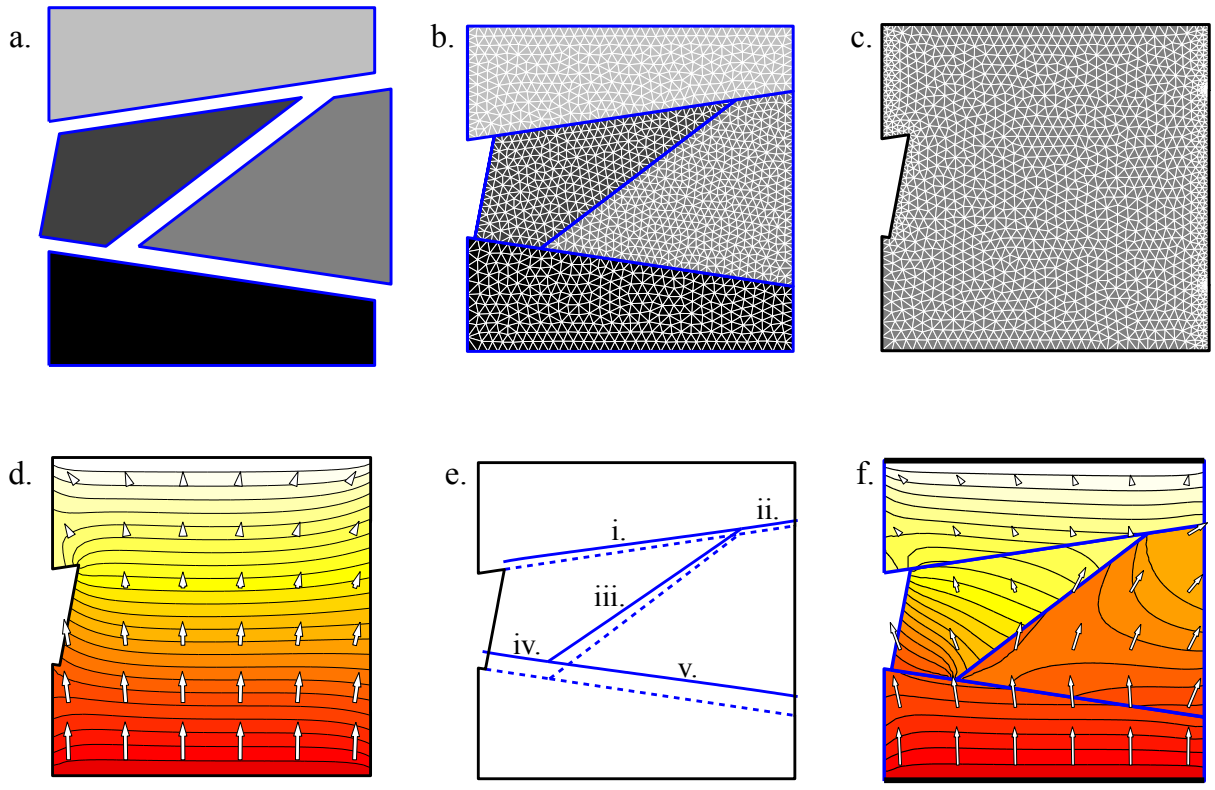

Figure 2.1: Schematic illustration of the stages in the deformable microplate model for a synthetic four-block case. a) microplate geometries, b) individual microplate meshes, c) global geometry and mesh, d) velocity arrows and shaded velocity magnitudes resulting from the deformation of the global mesh in response to applied boundary conditions, e) exaggerated fault advection interpolated from the global displacement field, and f) velocity arrows and shaded velocity magnitudes resulting from the deformation of individual meshes to recover fault compliance. This simple model is driven by displacement boundary conditions applied in the $+y$-direction at the base of the model. The northern (upper) boundary of the model is subject to a no-slip boundary condition. In panels d. and f. redder colors indicate larger velocity magnitudes.

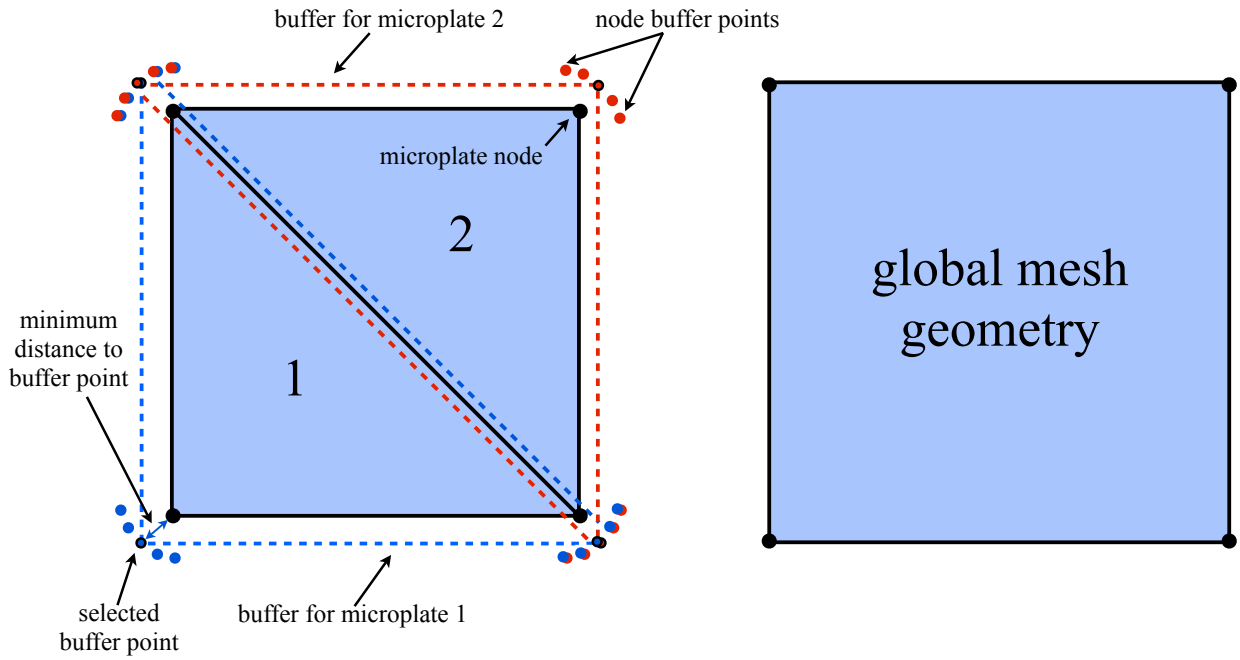

Figure 2.2: Exaggerated microplate buffer for the construction of the global geometry and mesh. Buffer points are generated at a specified radius from the nodes in each microplate (blue points around microplate 1 and red points around microplate 2). The buffer point closest to the microplate node is selected (red and blue points with black borders) to create a buffer region around the perimeter of each microplate (blue dotted line for microplate 1, red dotted line for microplate two). By finding the union of regions defined by microplate buffers, we construct the global mesh (right) which is slightly larger than the original model domain. In addition, by identifying points that fall within the buffers of other microplates, we can identify the boundary nodes subject to local rotations in the finite element calculation.

encompasses, but, when plotted together, microplate buffer boundaries overlap such that on interior edges the constructed buffer falls within the adjacent microplate. We then use the Matlab function inpolygon, which identifies points inside of a specified polygonal region.[3] When running inpolygon, the only buffer points that do not lie within the coordinates of other microplate buffers will necessarily be those that define the edges of the entire model domain. This process allows us to quickly identify model boundaries without defining them by hand, and becomes important when running multiple models. It should be noted that, although buffer generation is an automated process, in most cases the complex geometries of microplates at continental boundaries might require that at least one buffer point be hand selected. In particular, highly acute angles may require manual selection, as the distance minimization process may fail to select the buffer point that most accurately reflects the microplate geometry (Figure 2.3). The selected buffer point coordinates are saved and used to construct the buffer around the perimeter of the microplate. The microplate buffers are combined using polybool, a Matlab function that allows us to find the union of polygonal regions.[4] The resulting polygon, which encompasses the entire model domain, defines the geometry and the coordinates for the global mesh.

Using these global coordinates, we construct a global mesh and stiffness matrix, $\mathbf{K_G}$, for the entire model region. It should be noted that because the global mesh is constructed from the microplate buffers, the model region is larger than the area defined by the microplates

[3]Documentation for inpolygon is available at http://www.mathworks.com/help/matlab/ref/inpolygon.html.

[4]Documentation for polybool is available at: http://www.mathworks.com/help/map/ref/polybool.html.

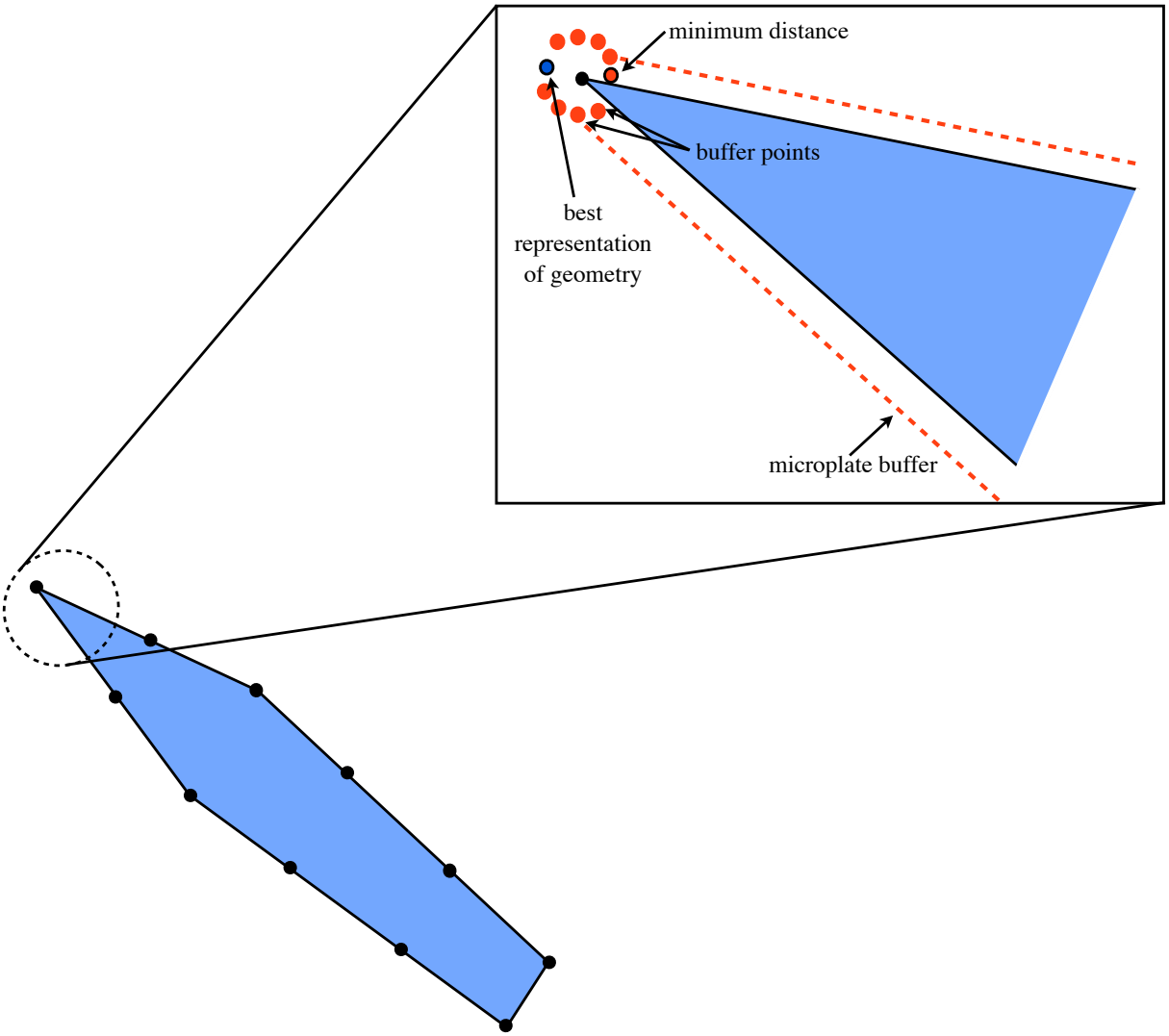

Figure 2.3: In some cases, manual selection of buffer points is necessary. The block is shown in blue above, and the block boundary is outlined in black. Black circles indicate boundary nodes, and the figure inside of the rectangle is a blown-up version of the region shown in the dotted black circle. For blocks with acute geometries, like the one shown above, the buffer points (red circles) form a nearly complete circle around the node at the block tip. In these cases, the closest buffer point (shown here as red outlined in black) may not accurately capture the block geometry. For these cases, it is sometimes necessary to manually select the preferred buffer point for this node (shown above as blue outlined in black) so that the buffer accurately reflects the block geometry.

alone. However, this increase is insignificant, as in all cases it represents a total increase of <0.1% in area for the models considered here.

Global displacement, $\mathbf{u_G^*}$, and force, $\mathbf{f_G}$, boundary conditions are applied to the global mesh, and global displacements, $\mathbf{u_G}$, are calculated using the Galerkin formulation of the finite element method, $\mathbf{u_G} = \mathbf{K_G^{-1}f_G}$ (e.g., Kwon and Bang, 2000). We then use the microplate buffers and the inpolygon function to automatically identify the individual micoplate boundaries. Although this process is not strictly necessary for the single timestep models discussed here, it allows for the straightforward application of this modeling technique to models with multiple timesteps. The deflection of faults (i.e., microplate boundaries) is calculated from the cubic interpolation of this global displacement field (Figure 2.1d,e). These calculations are done in Matlab using the function TriScatteredInterp, which uses Delaunay triangulation and allows for interpolation at any point within the defined region.[5] Microplates are therefore advected according to the new boundary (fault) locations determined by the global displacement field. Microplate boundaries that are subject to displacement boundary conditions (e.g. the bottom boundary of the bottom block in Figure 2.1a,e) are advected upwards by the prescribed displacement.

In the second finite element calculation the advected microplate boundaries serve as displacement boundary conditions for individual finite element solutions for each microplate. In this way models maintain geometric compliance at faults, and physically unrealistic gaps and

[5]Documentation for TriScatteredInterp is available at: http://www.mathworks.com/help/matlab/ref/triscatteredinterp.html.

overlaps between crustal microplates are prevented. By assuming that microplate boundaries are locally straight near individual boundary nodes, we can apply this compliance condition linearly. We define a local matrix, $\mathbf{R_l}$, for each boundary node, and construct a local coordinate system, x' and y', with axes parallel and perpendicular to the fault, respectively (Figure 2.4). The local rotation matrix is defined as:

$$\mathbf{R_l} = \begin{bmatrix} \cos\theta & -\sin\theta \\ \sin\theta & \cos\theta \end{bmatrix}, \tag{2.1}$$

where θ is the angle between the global coordinate system and the locally defined coordinate system (shown in Figure 2.4). For nodes that do not lie along microplate boundaries (boundary nodes), $\theta = 0$. We then construct $\mathbf{R}$, the sparse matrix containing the local rotation matrices, $\mathbf{R_l}$. Because each node has two degrees of freedom (in the x and y directions), $\mathbf{R}$ is a square matrix of dimension $2n \times 2n$, where n is the number of nodes in the microplate.

This rotation at microplate boundaries serves to locally rotate the global stiffness matrix, $\mathbf{K_M}$, at the boundary node. The global stiffness matrix, then, becomes:

$$\mathbf{K_M} = \mathbf{R'K_MR}. \tag{2.2}$$

So if, for example, node 8 is on the microplate boundary and the angle between the local coordinate axes, x' and y', and the global coordinate axes, x and y, is $-71°$, then the local rotation matrix becomes:

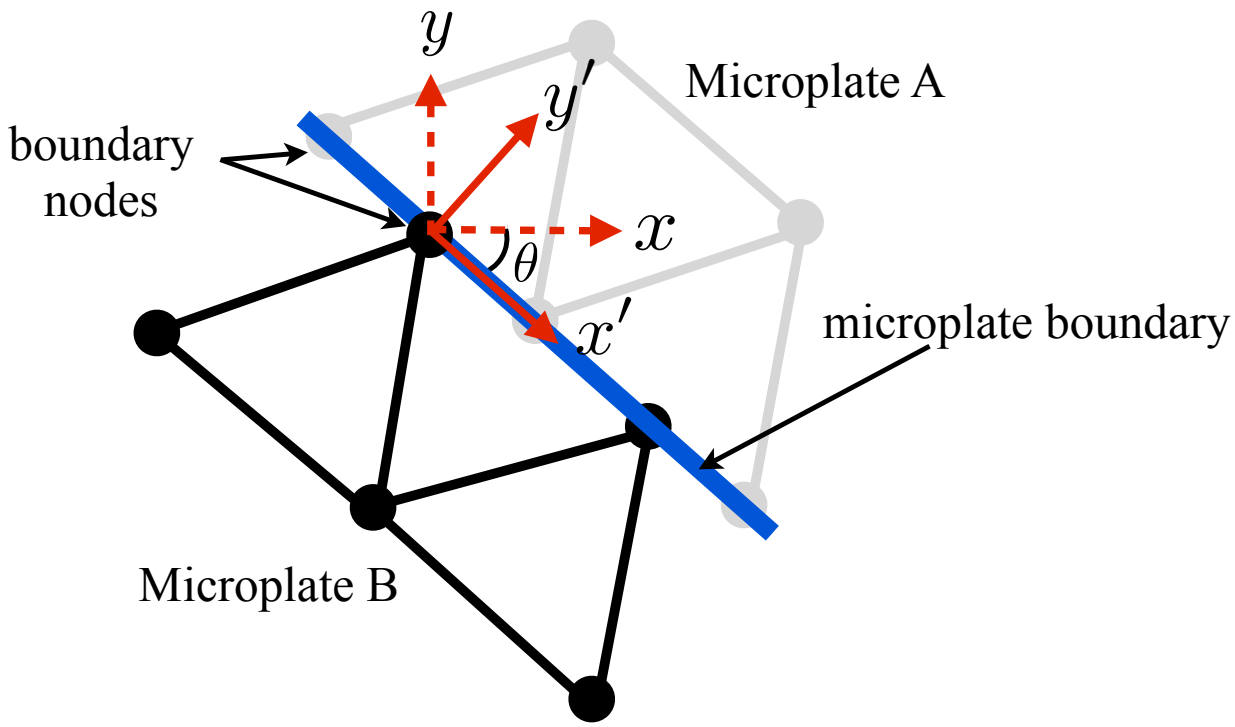

Figure 2.4: Local boundary node rotations for the second phase of the DM models. An individual rotation matrix, $\mathbf{R_l}$, acts on each boundary node such that x' and y' are locally tangent and perpendicular to the microplate boundary (fault), respectively. The microplate compliance condition requires that nodes may only be advected along the microplate boundary (the x' direction), and displacements in the y' direction must necessarily be zero.

$$\mathbf{R_l} = \begin{bmatrix} 0.33 & 0.95 \\ -0.95 & 0.33 \end{bmatrix}. \tag{2.3}$$

The values in equation (2.3) are therefore also the values in the sparse microplate rotation matrix, $\mathbf{R}$, at rows 15 to 16 and columns 15 to 16 (corresponding to the values for the 8th node in the problem):

$$\mathbf{R}(15:16, 15:16) = \begin{bmatrix} 0.33 & 0.95 \\ -0.95 & 0.33 \end{bmatrix}. \tag{2.4}$$

If the stiffness matrix values for this node (also in the 15th and 16th rows and columns of the stiffness matrix) correspond to:

$$\mathbf{K_M}(15:16, 15:16) = \begin{bmatrix} 1.04 \times 10^{11} & 0.19 \times 10^{11} \\ 0.19 \times 10^{11} & 0.54 \times 10^{11} \end{bmatrix}, \tag{2.5}$$

then after the rotation matrix is applied these values become:

$$\mathbf{K_M}(15:16, 15:16) = \begin{bmatrix} 0.48 \times 10^{11} & 0.01 \times 10^{11} \\ 0.01 \times 10^{11} & 1.10 \times 10^{11} \end{bmatrix}. \tag{2.6}$$

Within the context of the local coordinate system, fault compliance is maintained by allowing the boundary node in question to be advected only along the microplate boundary, in the x'-direction. Because faults are frictionless, the boundary node is allowed to vary freely in this fault-parallel direction. To prevent gaps and overlaps, displacements in the y'-direction must necessarily be zero, and thus the displacement degrees of freedom reduce

to one. This process is repeated for every boundary node in the individual microplate calculations. Displacement fields for each microplate (Figure 2.1f) must be calculated in a two-step process because of the locally rotated boundary nodes. First, displacements at nodes that are not subject to local boundary rotations are calculated:

$$\mathbf{u_M}(M_{idx}) = \mathbf{K_M^{-1}}(M_{idx}, M_{idx})\mathbf{f_M}(M_{idx}), \tag{2.7}$$

where $\mathbf{u_M}$ are the calculated microplate displacements, M_{idx} is the index of node degrees of freedom which are not subject to local boundary rotations, and $\mathbf{f_M}$ are the initial force conditions (uniformly set to zero because individual microplate finite element calculations are formulated as purely Dirichlet problems). Here the microplate stiffness matrix, $\mathbf{K_M}$, has already been multiplied by the microplate rotation matrix, as described above. At microplate boundary nodes subject to local rotations only local y'-direction Dirichlet conditions are applied to satisfy fault compliance. The distance, L_d, between the boundary node and the boundary segment is calculated (Figure 2.5) and the microplate displacement at these nodes becomes:

$$\mathbf{u_M}(B_{idx}) = L_d(B_{idx}), \tag{2.8}$$

where B_{idx} is the index of y-direction degrees of freedom for the boundary nodes. To return all displacements to the Cartesian coordinate system, we must rotate the boundary nodes back to Cartesian space by multiplying again by the rotation matrix:

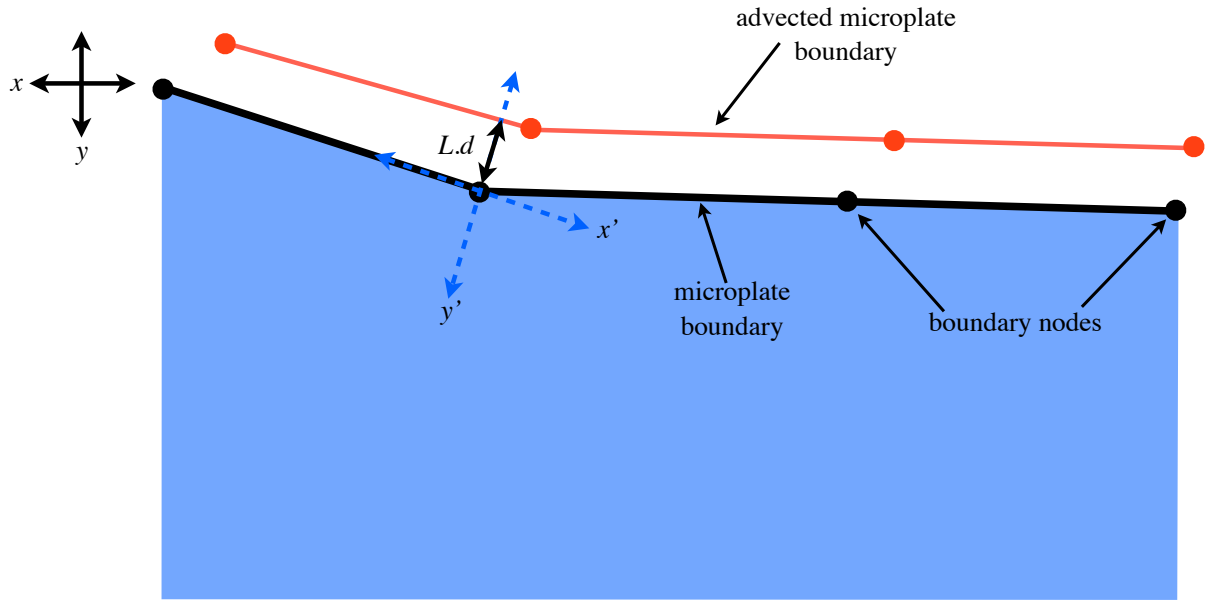

Figure 2.5: For locally rotated boundary nodes, y'-direction Dirichlet boundary conditions are equal to the distance between the boundary node and the advected microplate boundary segment. In the blue microplate above, boundary nodes are indicated by black circles and the advected boundary is shown in red. The black arrows on the left indicate the Cartesian coordinate space, and the dotted blue arrows at the boundary node show the locally rotated $x' - y'$ coordinate system. The distance, L_d, between the boundary node and the advected microplate boundary is calculated. To maintain fault compliance the boundary node is subject to the Dirichlet (displacement) boundary condition in the y-direction such that $\mathbf{u_M} = L_d$, where $\mathbf{u_M}$ is the microplate displacement field. Microplates are unconstrained in the x'-direction to allow for sliding on the boundary (fault).

$$\mathbf{u_M} = \mathbf{R}\mathbf{u_M}. \tag{2.9}$$

Thus, boundary zone deformation is accommodated in a set of nested finite element solutions: in the first, microplate boundaries are advected using the global displacement field; in the second, microplates deform and slide relative to each other.

The elastic microplate problem described above is connected to deformation rates by the assumption that the applied Dirichlet boundary conditions are equal to the boundary displacements over one year. In this way, we can annualize fault slip as a slip rate and make direct comparisons to geodetic and geologic observations. Slip rates at microplate boundaries are calculated as the difference in position between boundary node pairs nearest to one another and yet on opposite sides of a fault (Figure 2.6). In two dimensions with nodes A and B on adjacent microplates, the differential strike-slip motion is:

$$s = ||\mathbf{x_A} - \mathbf{x_B}|| - ||\mathbf{x_A} + \mathbf{u_A} - (\mathbf{x_B} + \mathbf{u_B})||, \tag{2.10}$$

where $\mathbf{x_A}$ and $\mathbf{x_B}$ are the initial nodal positions and $\mathbf{u_A}$ and $\mathbf{u_B}$ are the displacements from the individual microplate finite element solutions. Because of the two-dimensional nature of these models, only strike-slip rates are calculated and fault normal rates are necessarily zero.

2.4 Idealized two-block collision

To test the deformable microplate models described above we construct an idealized two-block collision (Figure 2.7). Within this idealized framework, the model domain is a

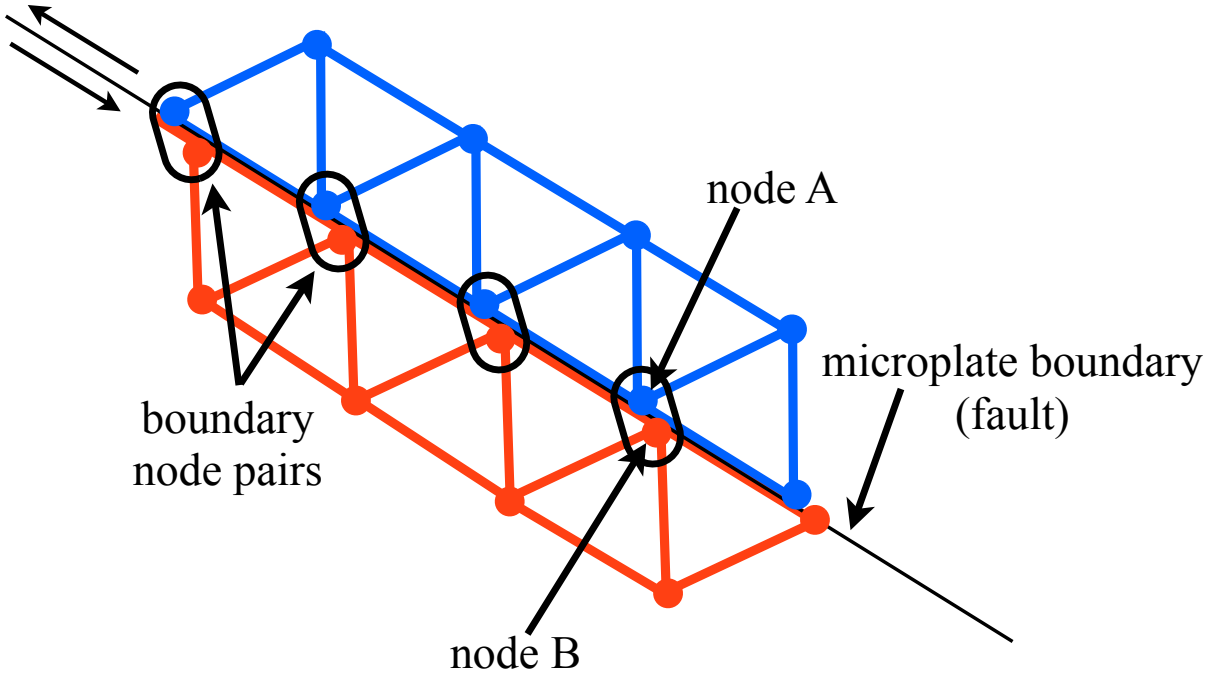

Figure 2.6: Boundary node pairs for fault slip rate calculations. Nodes from opposite sides of the microplate boundary (fault) are paired (e.g., node A and node B) and the differential strike-slip motion is calculated. Because of the two-dimensional nature of the DM models, only strike-slip rates can be calculated.

500 by 500 km square. The model domain is divided into two equal-sized blocks cut by a single 707 km-long fault that runs southeast to northwest along the diagonal of the square. As described above, all meshes are constructed with linear elastic triangular elements, and the Youngs modulus is 30 GPa and the Poissons ratio 0.3. The southernmost boundary of the model is subject to an initial displacement boundary condition of 50 mm/yr in the positive y-direction (north) and zero displacement in the x-direction (east-west). A zero-slip displacement condition is placed on the northernmost boundary of the model.

Figure 2.7 shows the model-predicted slip rate at three locations for the fault in this idealized model. In this model, the fault is entirely left-lateral, with a maximum slip rate

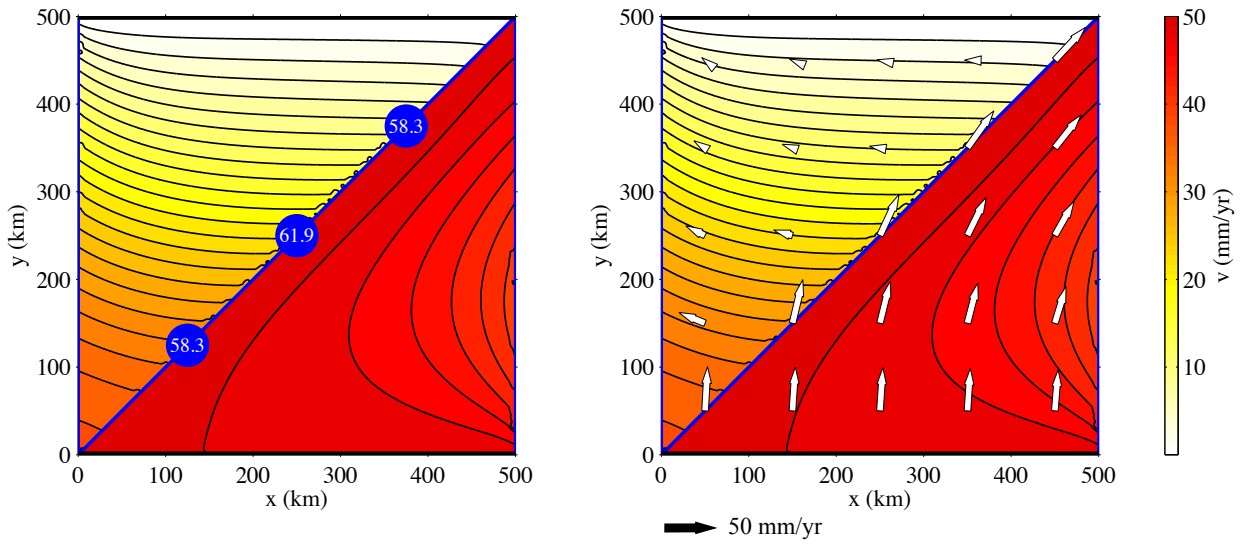

Figure 2.7: Slip rates (left) and velocities (right) from an idealized two-block collision. Microplate boundaries are shown as blue lines, and the locations of applied boundary conditions are shown as thick black lines. A 50 mm/yr displacement boundary condition is applied in the $+y$-direction along the base of the model. The top of the model is subject to a no-slip boundary condition. A single fault, running diagonally from the top right to the bottom left, forms the boundary between the two microplates in this model. The slip rate is shown at three locations along strike (left) and is highest on the central portion of the fault. Slip rates taper off symmetrically towards the fault termination. All calculated slip rates are left-lateral. The velocity field (white arrows) indicates that the lower microplate is sliding past the top microplate, consistent with sinisteral motion. Color shading shows velocity magnitudes, where redder colors indicate faster velocities. The maximum velocities equal the 50 mm/yr displacement condition applied at the base of the model.

of 61.9 mm/yr on the central portion of the fault and minimum slip rates of 51.2 mm/yr on the far eastern and western extremes. Velocity magnitudes in the south are consistent with boundary conditions of 50 mm/yr of vertical motion, but velocity magnitudes in the northern half of the bottom block have fault-parallel orientations. In the top block, maximum deformation is concentrated in the southern tip of the block, consistent with its proximity to the driving boundary condition. Further north, velocity magnitudes are smaller and display a western orientation, consistent with left-lateral sliding on the fault.

2.5 Idealized four-block collision

To further explore the deformable microplate models described above, we design an idealized four-block collision (Figure 2.8). Like the two-block collision described above, the model domain is approximately square. In an effort to simulate a collision more similar to the India-Asia boundary, the model domain is approximately 2000 by 2000 km and is cross cut by two east-west trending faults and one northeast-southwest structure. Meshes are again composed of linear triangular elements, and the Youngs modulus is 30 GPa and the Poissons ratio 0.3. As with the two-block case, boundary conditions are prescribed along the northern and southern model boundaries. The model is subject to 50 mm/yr of due north displacement on the southernmost boundary, and a zero-slip displacement condition is imposed on the northernmost edge of the model.

Model slip rates are shown in Figure 2.8. In all cases, slip rates vary along strike. Significantly, faults bounding the central eastern block slip the fastest. The southernmost fault bounding this block is the only right-lateral feature, with slip rates ranging from 7-18

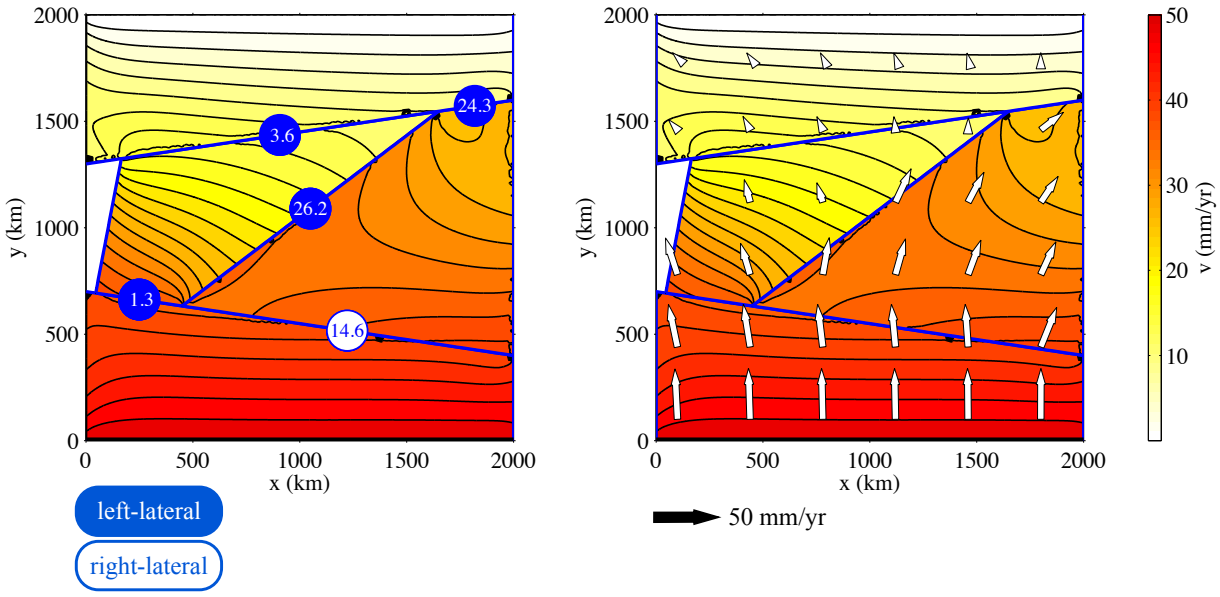

Figure 2.8: Slip rates (left) and velocity field (right) from an idealized four-block collision. All microplate boundaries are shown as blue lines. As with the two-block collision described above, the base of the model is subject to a 50 mm/yr displacement boundary condition in the $+y$-direction and the top of the model is constrained by a zero-slip condition. Slip rates are plotted on the left, where left-lateral slip is shown by white text in blue circles and right-lateral motion is indicated by blue text in white circles. For clarity, only representative slip rates are shown. The sub-vertical fault that forms the boundary between the two center microplates is the fastest moving fault in this model, with > 26 mm/yr of left-lateral motion. Only the bottom sub-horizontal fault shows any right-lateral motion, and the sense of slip on this structure switches direction. On the right, white arrows show the velocity vectors. The center-left microplate is being extruded to the left, consistent with the observed left-lateral faults above and to the left of the microplate and the right-lateral fault below this block. Color shading shows velocity magnitudes, where redder colors indicate faster velocities and maximum velocities equal the 50 mm/yr displacement boundary condition at the base.

mm/yr. The southwest-northeast fault on the western side of this block is left lateral, with slip rates ranging form 11-27 mm/yr. Slip rates are lowest in the southwest, with offsets of 11 mm/yr, and reach a maximum of 27 mm/yr on the central portion of the fault before tapering off to 22 mm/yr in the northeast. Faults to the north and south of the western central block have comparatively small slip rates, with slip rates of 3-4 mm/yr and 2-3 mm/yr of dexteral slip, respectively. These slip rates are best understood in the context of Figure 2.8, where white arrows indicate the velocity magnitude. As the southern block moves upward and the northern block is held fixed, the central eastern block is extruded to the east, resulting in high slip rates on its bounding faults. However, the model geometry constrains the central western block, minimizing east-west extrusion and forcing it to deform internally.

2.6 Summary

The deformable microplate models introduced here represent a hybrid approach that combines both block and continuum modeling. By combining these two approaches, we eliminate the unrealistic gapping and overlapping observed in block models, and are able to explicitly incorporate the faults that thin viscous sheet models neglect. Deformable microplate models require no a priori assumptions of geologically or geodetically derived fault slip rates. Instead, only displacement and force boundary conditions are considered. Thus, these models may be used to make predictions for fault slip rates on major faults at continental boundary zones that may be tested against geologic and geodetic observations. Future chapters will apply the deformable microplate approach to major faults in Tibet and southern California.

function Deformable Microplate Calculation

N: structure containing microplate node coordinates, connectivity, boundary indexing, and angle for local rotations
D: structure containing microplate Dirichlet boundary conditions
F: structure containing microplate force boundary conditions
B: structure containing microplate boundary indexing and coordinates
P: structure containing microplate boundary node coordinates
MD: structure containing master driving Dirichlet boundary conditions
MF: structure containing master fixed Dirichlet boundary conditions
NNN: structure containing global mesh coordinates, connectivity, and indexing
d: structure containing global mesh Dirichlet boundary conditions
f: structure containing global mesh force boundary conditions
$[s_x, s_y]$: Dirichlet boundary condition, typically equal to boundary displacement in one year

read in block geometries
for all blocks i **do**
transform block coordinates to Cartesian coordinate space
h_0 = maximum allowable mesh size for each block
$[p, t]$ = mesh2d on all block coordinates to generate individual block meshes
check meshes for consistency
$N(i).x$ = x-coordinates of mesh nodes for block i
$N(i).y$ = y-coordinates of mesh nodes for block i
$N(i).con$ = nodes comprising triangular elements for block i
end for

$D(i).x$ = zeros(size($N(i).x$)), storage for x-displacements at nodes for each mesh
$D(i).y$ = zeros(size($N(i).y$)), storage for y-displacements at nodes for each mesh
$D(i).tog$ = zeros(size($N(i).x$)), storage for index indicating if node is on mesh boundary
$[s_x, s_y]$ = Dirichlet boundary conditions to be applied (typically annualized to displacement in 1 year)

identify all nodes $[N(i).x, N(i).y]$ subject to driving Dirichlet boundary condition:
$[MD_x, MD_y]$ = coordinates for the master driving boundary condition
for all blocks i **do**
for all points $[MD_x, MD_y]$ **do**
identify all nodes $[N(i).x, N(i).y]$ subject to the driving Dirichlet boundary conditions
$D(i).tog = 1$, index nodes subject to Dirichlet condition
end for

end for

identify all nodes $[N(i).x, N(i).y]$ subject to zero-displacement boundary condition:
$[MF_x, MF_y]$ = coordinates for the master fixed boundary condition
for all blocks i **do**
  for all points $[MF_x, MF_y]$ **do**
    identify all nodes $[N(i).x, N(i).y]$ subject to the fixed boundary conditions
    $D(i).tog = 1$, index nodes subject to Dirichlet condition
  end for
end for

Construct buffers around microplates:
for all blocks i **do**
  $[P(i).x, P(i).y]$ = boundary nodes of each mesh
  $[P(i).xb, P(i).yb]$ = suite of buffer points for each point $[P(i).x, P(i).y]$
  select the buffer point closest to each point $[P(i).x, P(i).y]$
  $[PP(i).x, PP(i).y]$ = matrix of same size as $[P(i).x, P(i).y]$ containing selected mesh buffer points
end for

Identify mesh interfaces (locations where block meshes are in contact):
$B = [\,]$
$bcount = 1$
for all blocks i **do**
  for all blocks j **do**
    if $i \neq j$ **then**

      find buffer points that are inside other buffers:
      $idx1 = \text{inpolygon}(PP(i).x, PP(i).y, PP(j).x, PP(j).y)$
      $idx2 = \text{inpolygon}(PP(j).x, PP(j).y, PP(i).x, PP(i).y)$

      save the corresponding boundary point:
      $x1 = P(i).x(idx1)$
      $y1 = P(i).y(idx1)$
      $x2 = P(j).x(idx2)$
      $y2 = P(j).y(idx2)$
      $x = [x1; x2]$
      $y = [y1; y2]$
      ensure all saved points are unique:
      $localkey = \text{sort}([i, j])$
      ensure that this boundary (with the same $localkey$) has not already been stored

      save boundary points in boundary structure, B

$B(bcount).key = localkey$
$B(bcount).x = x$
$B(bcount).y = y$
$bcount = count + 1$, to identify the next boundaries
end if
end for
end for

remove boundaries with a single node:
for the number of boundaries, b **do**
if numel$(B(b).x) < 2$ **then**
$B(b).x = [\,]$
$B(b).y = [\,]$
end if
end for

Construct the global mesh:

Initialize the first perimeter with the buffer of the first block:
$x = PP(1).x$
$y = PP(1).y$

find the union of the block buffers using the polybool function:
for all blocks i **do**
$[x, y] =$ polybool$('+', x, y, PP(i).x, PP(i).y)$, the global mesh boundaries
end for

$[p, t]$ =mesh2d on global boundary coordinates
check meshes for consistency
$NNN.x = x$-coordinates of global mesh nodes
$NNN.y = y$-coordinates of global mesh nodes
$NNN.con =$ nodes comprising triangular elements for the global mesh
identify global boundary nodes
$d(i).x =$ zeros(size$(NNN.x)$), storage for global x-displacements
$d(i).y =$z eros(size$(NNN.y)$) storage for global y-displacements
$d(i).tog =$ zeros(size$(NNN.x)$), storage for index indicating if node is on global mesh boundary
$f(i).x =$ zeros(size$(NNN.x)$), x-direction forces on global nodes
$f(i).y =$ zeros(size$(NNN.y)$), y-direction forces on global nodes
$[GB_xGB_y] =$ boundary nodes for global mesh

Identify global mesh nodes subject to Dirichlet boundary conditions:

The driving boundary conditions:

for all global mesh boundary points, $[GB_x, GB_y]$ **do**
  for all points in master driving boundary condition, $[MD_x, MD_y]$ **do**
    calculate distance between driving boundary & each global boundary node, $[GB_x, GB_y]$

    if distance between $[GB_x, GB_y]$ & driving boundary is $\sim$ size of buffer **then**
      $d([GB_x, GB_y]).tog = 1$
      $d([GB_x, GB_y]).x = s_x$
      $d([GB_x, GB_y]).y = s_y$
    end if
  end for
end for

The fixed boundary conditions:
for all global mesh boundary points $[GB_x, GB_y]$ **do**
  for all points in the master fixed boundary condition $[MF_x, MF_y]$ **do**
    calculate distance between fixed boundary & each global boundary node, $[GB_x, GB_y]$

    if distance between $[GB_x, GB_y]$ & fixed boundary is $\sim$ size of buffer, **then**
      $d([GB_x, GB_y]).tog = 1$
    end if
  end for
end for

Calculate the global displacement $\mathbf{u_G}$, the global forces, $\mathbf{f_G}$, the global stresses, $\boldsymbol{\sigma}_{\mathrm{G}}$, and the global strains, $\boldsymbol{\epsilon}_{\mathrm{G}}$, using the Young's modulus, E, and the Poisson ratio, ν

$[\mathbf{u_G}, \mathbf{f_G}, \boldsymbol{\sigma}_{\mathrm{G}}, \boldsymbol{\epsilon}_{\mathrm{G}}] = \mathrm{TriLin}([NNN.x, NNN.y], NNN.con, f, d, E, \nu)$

Advect microplate boundaries:
for all boundaries, $B(b)$, **do**
  interpolate global displacements to the points on the boundary
  $B(b).x = B(b).x + x$-displacement interpolated from global mesh
  $B(b).y = B(b).y + y$-displacement interpolated from global mesh
end for

Also advect the locations of the master boundary conditions:
for all master driving boundary points, $[MD_x, MD_y]$ **do**
  interpolate global displacements to points in the master driving boundary
  $MD_x = MD_x + x$-displacement interpolated from global mesh
  $MD_y = MD_y + y$-displacement interpolated from global mesh
end for

for all master fixed boundary points, $[MF_x, MF_y]$ **do**

interpolate global displacements to points in the master fixed boundary
$MF_x = MF_x + x$-displacement interpolated from global mesh
$MF_y = MF_y + y$-displacement interpolated from global mesh
end for

Identify individual mesh nodes that are inside the buffer of the other blocks and store their boundary code:
$N(i).blist$ = zeros(size($N(i).x$)), storage for the boundary code for each node
for all blocks i **do**
for all blocks j **do**
if $i \neq j$ **then**

find points in block i that fall within the buffer of block j:
$invals$ = inpolygon($N(i).x, N(i).y, PP(j).x, PP(j).y$)
if the number of elements in $invals > 0$ **then**
$blocklabels$ = sort(i, j)

index the block that the node from block i is interacting with:
$inidx$ = find when $invals = j$

find the boundary that corresponds to the *blocklabels*:
for all boundaries $B(b)$ **do**
if $blocklabels = B(b).key$ **then**

blist is the boundary code for the node:
$N(i).blist(inidx) = j$
end if
end for
end if
end if
end for
end for

Advect the blocks subject to the driven boundary condition:
for all blocks subject to a driven boundary condition, k **do**
$N(k).x = N(k).x + s_x$
$N(k).y = N(k).y + s_y$
end for

Calculate individual finite element solutions:

for all blocks i **do**

For individual meshes the forces are always set to zero:

$F(i).x = \text{zeros}(\text{size}(N(i).x))$, forces in the x-direction
$F(i).y = \text{zeros}(\text{size}(N(i).y))$, forces in the y-direction

Identify the number of boundaries each block is subject to:
$nbound = \text{numel}(\text{unique}(N(i).blist)) - 1$ (minus one because we are only interested in the non-zero boundaries)

Identify the boundaries:
$blistvals = \text{unique}(N(i).blist)$ and set $blistvals(1) = [\,]$ to remove the 0.
$d.x = D(i).x$, the x-direction Dirichlet conditions
$d.y = D(i).y$, the y-direction Dirichlet conditions
$d.tog = D(i).tog$, node indexing for Dirichlet boundary conditions
$D(i).\theta = \text{zeros}(\text{size}((D(i).x)))$, storage for angle between Cartesian axis & local $x' - y'$ axis for boundary nodes (for non-boundary nodes $D(i).\theta = 0$)
for all of the boundaries, k, that block i is subject to **do**
$idx =$ index locations where $N(i).blist = blistvals(k)$

for all values, j, in the vector idx **do**

for all points, m, in the boundary $B(blistvals(k)), -1$ **do**

Identify line segments on the boundary:
$[L_{1_x}(m), L_{1_y}(m)] = [B(blistvals(k)).x(m), B(blistvals(k)).y(m)]$

$L_{2_x}(m), L_{2_y}(m) = [B(blistvals(k).x(m+1), B(blistvals(k)).y(m+1)]$

$[L_{M_x}(m), L_{M_y}(m)] =$ midpoint of line segment $\overline{L_1(m)L_2(m)}$

find distance between each boundary node and each boundary segment

$[N_{N_x}(j), L_{N_y}(j)] = [N(i).x(idx(j)), N(i).y(idx(j))]$, node coordinates

$L_{dist} = j \times m$, matrix containing the distance between each boundary point and the midpoint of each line segment, $\overline{L_1(m)L_2(m)}$

end for
end for

for all values, j, in the vector idx **do**

$L_{idx}(j) =$ index minimum value in row j of L_{dist} (i.e., closest boundary segment)

$L_d(j) =$ distance between closest boundary segment & boundary node

$L_{int}(j)$ = intersection pt. b/w closest boundary segment & boundary node

$L_{dx}(j) = L_{2_x}\left(L_{idx}(j)\right) - L_{1_x}\left(L_{idx}(j)\right)$,
x-component of boundary segment slope

$L_{dy}(j) = L_{2_y}(L_{idx}(j)) - L_{1_y}(L_{idx}(j))$,
y-component of boundary segment slope

$D(i).\theta(j) = \tan^{-1}\left(\frac{L_{dy}(j)}{L_{dx}(j)}\right)$

end for

$d.tog(idx) = 6$, index boundary nodes to indicate Dirichlet boundary condition
$d.y(idx) = L_d$, the y-boundary condition for boundary nodes: nodes must snap to the closest boundary segment

end for

Perform finite element calculation for each microplate to find microplate displacements at each node, $\mathbf{u_M}$, microplate forces on each node, $\mathbf{f_M}$, microplate stresses, $\boldsymbol{\sigma}_{\mathrm{M}}$, and microplate strains, $\boldsymbol{\epsilon}_{\mathrm{M}}$, using microplate nodes, connectivity, Young's modulus, E, and Poisson ratio, ν.

$[\mathbf{u_M}(i), \mathbf{f_M}(i), \boldsymbol{\sigma}_{\mathrm{M}}(i), \boldsymbol{\epsilon}_{\mathrm{M}}(i)] = \mathrm{TriLinRot}([N(i).x, N(i).y], N(i).con, F, d, E, \nu, \theta)$

end for

end function

function TriLinRot(coord, nodes, f, d, E, ν)
modified from Kwon and Bang (2000)

coord: node coordinates
nodes: node connectivity to form elements
f: force initial conditions
d: Dirichlet boundary conditions
E: Young's modulus
ν: Poisson ratio

n_{el} = number of elements (i.e., length(nodes((:, 1))))
$n_{bel} = 3$, number of nodes per element
$n_{dof} = 2$, degrees of freedom per node

n_{node} = number of nodes
$s_{dof} = n_{dof} * n_{node}$, number of degrees of freedom in the system
$e_{dof} = n_{bel} * n_{dof}$, number of degrees of freedom per element

Create large rotation matrix, $\mathbf{R}$:
$\mathbf{R}$ = diag(ones(s_{dof}, 1)), storage for sparse matrix, $\mathbf{R}$, which has a size $s_{dof} \times s_{dof}$

for all nodes, i, **do**

$$\mathbf{R_l} = \begin{bmatrix} \cos\theta & -\sin\theta \\ \sin\theta & \cos\theta \end{bmatrix}$$

$idx1 = 2 * (i - 1) + 1$, first degree of freedom for node i
$idx2 = 2 * (i - 1) + 2$, second degree of freedom for node i

fit $\mathbf{R_l}$ into large rotation matrix:
$\mathbf{R}(idx1 : idx2, idx1 : idx2) = \mathbf{R_l}$

end for

Apply boundary conditions:
$bcval = [\,]$, matrix for storing boundary condition values
$bcdof = [\,]$, matrix for indexing boundary condition node degrees of freedom

Locate and apply boundaries where there is a master boundary condition applied:
idx = index of values for which $D.tog = 1$

for all values, j, in vector idx **do**
$bcdof = [bcdof, 2 * idx(j) - 1, 2 * idx(j)]$, boundary condition node d.o.f.
$bcval = [bcval, D.x(idx(j)), D.y(idx(j))]$, Dirichlet boundary conditions
end for

Locate and apply boundaries where the mesh interacts with a boundary:
idx = index of values for which $D.tog = 6$

for all values, j, in vector idx **do**
$bcdof = [bcdof, 2 * idx(j)]$, boundary condition node d.o.f. - node only constrained in y-direction
$bcval = [bcval, D.y(idx(j))]$, Dirichlet boundary conditions
end for

Load force vector:
f = zeros(s_{dof}, 1), storage for force vector
$f(1 : 2 : \text{end}) = F.x$, force conditions in the x-direction
$f(2 : 2 : \text{end}) = F.y$, force conditions in the y-direction

$\mathbf{K} = \text{zeros}(s_{dof}, s_{dof})$, initialize stiffness matrix
$matmtx = \text{fematiso}(1, E, \nu)$, matrix of material properties indicating plane stress, Young's modulus, E, and Poisson ratio, ν

Construct the stiffness matrix:
for all elements j **do**
$n_1 = \text{nodes}(j, 1)$, first connected node of element j
$n_2 = \text{nodes}(j, 2)$, second connected node of element j
$n_3 = \text{nodes}(j, 3)$, third connected node of element j
$x_1 = \text{coord}(n_1, 1)$, x-coordinate of first node
$y_1 = \text{coord}(n_1, 2)$, y-coordinate of first node
$x_2 = \text{coord}(n_2, 1)$, x-coordinate of second node
$y_2 = \text{coord}(n_2, 2)$, y-coordinate of second node
$x_3 = \text{coord}(n_3, 1)$, x-coordinate of third node
$y_3 = \text{coord}(n_3, 2)$, y-coordinate of third node
$index = \text{feeldof}([n_1, n_2, n_3], n_{bel}, n_{dof})$, extract system d.o.f. from element j

Find derivatives of the shape functions:
$A = 0.5 * (x_1 * y_2 + x_2 * y_3 + x_3 * y_1 - x_1 * y_3 - x_2 * y_1 - x_3 * y_2)$

$\frac{\partial h}{\partial x} = \left[\frac{y_2 - y_3}{2A}, \frac{y_3 - y_1}{2A}, \frac{y_1 - y_2}{2A}\right]$, derivatives of shape functions, h, with respect to x

$\frac{\partial h}{\partial y} = \left[\frac{x_3 - x_2}{2A}, \frac{x_1 - x_3}{2A}, \frac{x_2 - x_1}{2A}\right]$, derivatives of shape function, h, with respect to y

$kinmtx = \text{fekine2d}\left(n_{el}, \frac{\partial h}{\partial x}, \frac{\partial h}{\partial y}\right)$, the kinematic matrix

$k = kinmtx' * matmtx * kinmtx * A$, the element stiffness matrix
$\mathbf{K} = \text{feasmbl1}(\mathbf{K}, k, index)$, assemble the microplate stiffness matrix

end for

Multiply the stiffness matrix by the rotation matrix:

$\mathbf{K} = \mathbf{R}'\mathbf{K}\mathbf{R}$, locally rotate the microplate stiffness matrix for nodes on boundaries

Calculate microplate displacements $\mathbf{u_M}$, and microplate forces, $\mathbf{f_M}$:

$\mathbf{u_M} = \text{zeros}(s_{dof}, 1)$, storage for displacement vector
$\mathbf{u_M}(bcdof) = bcval$, insert Dirichlet boundary conditions. Because these are displacement boundary conditions, these nodes must move to the new locations provided in $bcval$

$M = \text{ones}(s_{dof}, 1)$ storage for nodes without Dirichlet boundary conditions

$M(bcdof) = 0$, set nodes with Dirichlet boundary conditions such that $M = 0$
M_{idx} = index of nodes without Dirichlet boundary conditions (i.e., $M = 1$)

$\mathbf{u_{temp}} = \mathbf{K^{-1}}(M_{idx}, M_{idx} * f(M_{idx}) - \mathbf{K}(M_{idx}, bcdof) * \mathbf{u_M}(bcdof)$,
calculated displacements fror nodes not subject to local rotations

$\mathbf{u_M}(M_{idx}) = \mathbf{u_{temp}}$, insert calculated displacements into $\mathbf{u_M}$
$\mathbf{u_M} = \mathbf{R} * \mathbf{u_M}$, rotate the displacements back to the Cartesian axis
$\mathbf{f_M} = \mathbf{R} * \mathbf{K} * \mathbf{R'} * \mathbf{u_M}$, the microplate forces at each node

Calculate microplate stresses, $\boldsymbol{\sigma}_{\mathrm{M}}$, and microplate strains, $\boldsymbol{\epsilon}_{\mathrm{M}}$:
for all elements j **do**
$n_1 = \text{nodes}(j, 1)$, first connected node of element j
$n_2 = \text{nodes}(j, 2)$, second connected node of element j
$n_3 = \text{nodes}(j, 3)$, third connected node of element j
$x_1 = \text{coord}(n_1, 1)$, x-coordinate of first node
$y_1 = \text{coord}(n_1, 2)$, y-coordinate of first node
$x_2 = \text{coord}(n_2, 1)$, x-coordinate of second node
$y_2 = \text{coord}(n_2, 2)$, y-coordinate of second node
$x_3 = \text{coord}(n_3, 1)$, x-coordinate of third node
$y_3 = \text{coord}(n_3, 2)$, y-coordinate of third node
$index = \text{feeldof}([n_1, n_2, n_3], n_{bel}, n_{dof})$, extract system d.o.f. from element j

for all degrees of freedom, m, in element j **do**
$e_{disp}(m) = \mathbf{u_M}(index(m))$
end for

Find derivatives of the shape functions:
$A = 0.5 * (x_1 * y_2 + x_2 * y_3 + x_3 * y_1 - x_1 * y_3 - x_2 * y_1 - x_3 * y_2)$

$\frac{\partial h}{\partial x} = \left[\frac{y_2 - y_3}{2A}, \frac{y_3 - y_1}{2A}, \frac{y_1 - y_2}{2A}\right]$, derivatives of shape functions, h, with respect to x

$\frac{\partial h}{\partial y} = \left[\frac{x_3 - x_2}{2A}, \frac{x_1 - x_3}{2A}, \frac{x_2 - x_1}{2A}\right]$, derivatives of shape function, h, with respect to y

$kinmtx = \text{fekine2d}\left(n_{el}, \frac{\partial h}{\partial x}, \frac{\partial h}{\partial y}\right)$, the kinematic matrix
$e_\epsilon = kinmtx * e_{disp}$
$e_\sigma = matmtx * e_\epsilon$

Put stress and strain into $[xx, yy, xy]$ form:
for the three independent stress coordinates, s **do**
$\boldsymbol{\epsilon}_{\mathbf{M}}(j, s) = e_\epsilon$, the strain on node j in $[xx, yy, xy]$ form
$\boldsymbol{\sigma}_{\mathbf{M}}(j, s) = e_\sigma$, the stress on node j in $[xx, yy, xy]$ form
end for

end for

end function

function $\mathbf{K} =$ FEASMBL1$(\mathbf{K}, k, index)$
modified from Kwon and Bang (2000)

$\mathbf{K}$: microplate stiffness matrix
k: element stiffness matrix
$index$: the degree of freedom vector associated with a specific element

$e_{dof} = \text{length}(index)$, element degrees of freedom (6)

for each element degree of freedom, i **do**
$ii = index(i)$

for each element degree of freedom, j **do**
$jj = index(j)$
$\mathbf{K}(ii, jj) = \mathbf{K}(kk, jj) + k(i, j)$
end for

end for

end function

function $kinmtx2 =$ FEKINE2D$(n_{el}, \frac{\partial h}{\partial x}, \frac{\partial h}{\partial y})$
modified from Kwon and Bang (2000)

n_{nel}: the number of nodes per element

$\frac{\partial h}{\partial x}$: derivative of the shape function, h, with respect to x

$\frac{\partial h}{\partial y}$: derivative of the shape function, h, with respect to y

for all nodes in an element, i **do**
$a = 2 * (i - 1) + 1$
$b = a + 1$

$kinmtx2(1, a) = \frac{\partial h}{\partial x}$

$kinmtx2(2,b) = \frac{\partial h}{\partial y}$

$kinmtx2(3,a) = \frac{\partial h}{\partial y}$

$kinmtx2(3,b) = \frac{\partial h}{\partial x}$

end for

end function

function $matmtx =$ FEMATISO(p, E, ν)

modified from Kwon and Bang (2000)

E: Young's Modulus
ν: Poisson Ratio
p: index indicating material properties for the finite element analysis. All DM models are run with plane stress but can be extended for other types of analysis

if $p = 1$ **then**

$$matmtx = \frac{E}{1-\nu^2}\begin{bmatrix} 1 & \nu & 0 \\ \nu & 1 & 0 \\ 0 & 0 & \frac{1-2\nu}{2} \end{bmatrix}, \text{ plane stress analysis}$$

else if $p = 2$ **then**

$$matmtx = \frac{E}{(1+\nu)(1-2\nu)}\begin{bmatrix} 1-\nu & \nu & 0 \\ \nu & 1-\nu & 0 \\ 0 & 0 & \frac{1-2\nu}{2} \end{bmatrix}, \text{ plane strain analysis}$$

else if $p = 3$ **then**

$$matmtx = \frac{E}{(1+\nu)(1-2\nu)}\begin{bmatrix} 1-\nu & \nu & \nu & 0 \\ \nu & 1-\nu & \nu & 0 \\ \nu & \nu & 1-\nu & 0 \\ 0 & 0 & 0 & \frac{1-2\nu}{2} \end{bmatrix}, \text{ axisymmetric analysis}$$

else if $p = 4$ **then**

$$matmtx = \frac{E}{(1+\nu)(1-2\nu)}\begin{bmatrix} 1-\nu & \nu & \nu & 0 & 0 & 0 \\ \nu & 1-\nu & \nu & 0 & 0 & 0 \\ \nu & \nu & 1-\nu & 0 & 0 & 0 \\ 0 & 0 & 0 & \frac{1-2\nu}{2} & 0 & 0 \\ 0 & 0 & 0 & 0 & \frac{1-2\nu}{2} & 0 \\ 0 & 0 & 0 & 0 & 0 & \frac{1-2\nu}{2} \end{bmatrix}, \text{ 3D analysis}$$

end if

end function

Chapter 3

Edge-Driven Mechanical Microplate Models of Strike-Slip Faulting in the Tibetan Plateau

The India-Asia collision zone accommodates the relative motion between India and Eurasia through both shortening and pervasive strike-slip faulting. To gain a mechanical understanding of how fault slip rates are driven across the Tibetan plateau, we develop a two-dimensional, linear elastic, two-stage, deformable microplate model for the upper crust based on the behavior of an idealized earthquake cycle. We use this approach to develop a suite of simple India-Asia collision zone models, differing only in boundary conditions, to determine which combination of edge forces and displacements are consistent with both the slip rate measurements along major Tibetan faults as well as the geodetically observed extrusion of crustal material toward southeast Asia. Model predictions for the Altyn Tagh (1–14 mm/yr), Kunlun (3–10 mm/yr), Karakorum (5–12 mm/yr), and Haiyuan (3–5 mm/yr) faults are in agreement with geologically and geodetically inferred slip rates. Further, models that accurately reproduce observed slip rate gradients along the Altyn Tagh and Kunlun faults feature two critical boundary conditions: 1) oblique compressive displacement along the Himalayan

range front west of the Shillong plateau, and 2) forcing in southeast Asia. Additionally, the ratio of internal-block potency rate to the total potency rate for each microplate ranges from 28% to 79%, suggesting a hybrid view of deformation in Tibet as simultaneously localized on major faults and distributed at length scales <500 km.

3.1 Introduction

The India-Asia collision zone spans at least 7 million km^2 and encompasses the Tibetan plateau, which stands at a mean elevation of 4 km and is dissected by large-scale strike-slip faults exceeding 1500 km in length. Modern-day convergence between the Indian and Eurasian plates is accommodated on the southern edge of the plateau by ∼20 mm/yr of shortening at the Main Himalayan Thrust (Bilham et al., 1997; Jouanne et al., 2004; Lavé and Avouac, 2000), in the northwest at the northern boundary of the Tarim Basin by at least 14 mm/yr of convergence across the Tien Shan (Abdrakhmatov et al., 1996; Thompson et al., 2002), and in the northeast by distributed shortening and rotation (Hetzel et al., 2004; Loveless and Meade, 2011a; Tapponnier et al., 1990; Wang et al., 2001). The time-integrated effect of this shortening has been suggested as a mechanism contributing to the thickening of the Tibetan crust to 60–80 km (Chen and Molnar, 1981; Kind et al., 2002; Owens and Zandt, 1997; Zhang and Klemperer, 2005).

Despite crustal thickening leading to isostatically compensated surface uplift on the order of 4 km, the largest documented post-collisional deformation signals in Tibet are those associated with large-scale strike-slip faults that have accrued hundreds of kilometers of displacement. The largest, the left-lateral Altyn Tagh fault (Figure 3.1), extends more than

1300 km along the northern boundary of the Tibetan Plateau (Molnar and Tapponnier, 1975). Post Oligocene-early Miocene cumulative offsets have been estimated between 350–400 km (Yue et al., 2001), geologically inferred slip rates range from 9–18 mm/yr (Cowgill et al., 2009; Mériaux et al., 2005; Yue et al., 2001), and geodetically inferred slip rate estimates fall between 5–9 mm/yr (Bendick et al., 2000; Loveless and Meade, 2011a; Meade, 2007; Wallace et al., 2004). South of the Altyn Tagh fault, estimated offsets for the east-west trending Kunlun fault (Figure 3.1), may be as high as 100 ± 20 km (Fu and Awata, 2007), consistent with the extrapolation of late Pleistocene-Holocene slip rates (11.7 ± 1.5 mm/yr, Van der Woerd et al., 2002b) back to a possible initiation in the mid-Miocene, ∼15 Ma (Jolivet et al., 2003). The Red River fault (Figure 3.1), which trends southeast from the high plateau into south China, has accommodated between 500–900 km of left-lateral slip in the Oligo-Miocene; however, since then several tens of kilometers of right-lateral slip have been documented (Leloup et al., 2001, 1995). Strike-slip faulting is also present along the western edge of the Tibetan plateau, most notably along the 1200 km right-lateral Karakorum fault, which has accommodated ∼250 km of displacement since ∼17 Ma (Murphy et al., 2000). Karakorum slip rate estimates vary by an order of magnitude, with geologic estimates ranging from as low as 4 mm/yr (Brown et al., 2002) to as high as 11 mm/yr (Chevalier et al., 2005), inferences from InSAR measurements of ∼1 mm/yr (Wright et al., 2004), and block models constrained by GPS observations suggesting 2–4 mm/yr of right-lateral motion (Loveless and Meade, 2011a; Meade, 2007).

We present a two-dimensional deformable microplate (DM) model for the India-Asia boundary that makes testable predictions of fault slip rates. Predicting fault slip rates as a

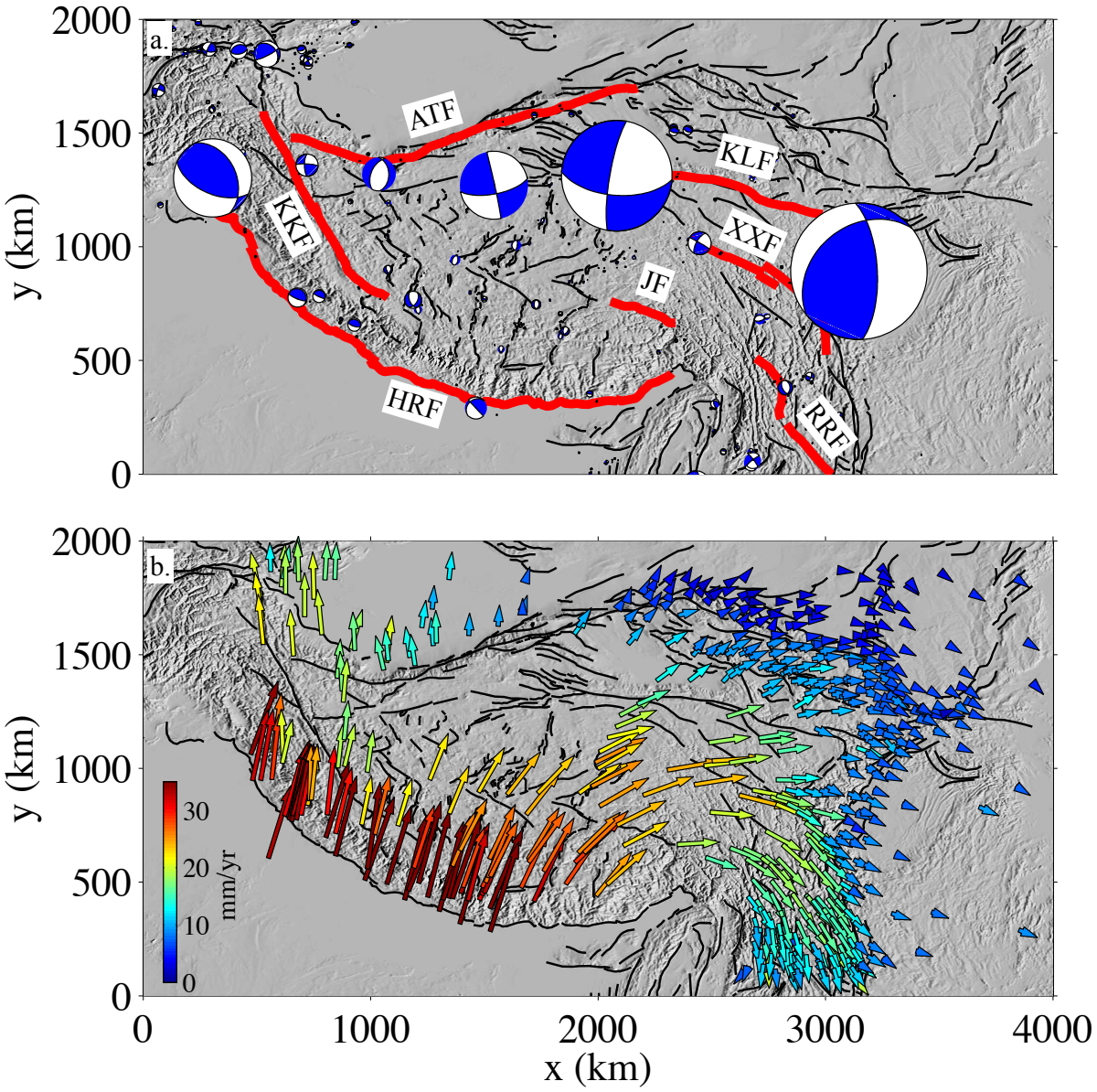

Figure 3.1: Traces of major faults, earthquake focal mechanisms ≤40 km deep (Global CMT database), compressional quadrants shaded blue, panel a), and GPS velocities Loveless and Meade (2011a) compilation, panel b) in the greater Tibetan plateau region. Black fault traces are from Taylor and Yin (2009) and red traces indicate the major branches of the Altyn Tagh (ATF), Kunlun (KLF), Karakoram (KKF), Jaili (JF), Xianshuehui (XXF), and Red River (RRF) faults and the trace of the Main Frontal Thrust along the Himalayan range front (HRF). GPS velocities in a nominally Eurasian reference frame are color coded by velocity magnitude with warmer colors indicating faster velocities.

function of applied boundary conditions is distinct from the approach taken by Pelzer and Saucier (1996), who assumed fault slip rates and solved for a regional velocity field. This class of model incorporates both localized slip along major faults and distributed deformation within microplates with a two-dimensional, two-step finite element model. Using this approach, we analyze six Tibetan plateau models to interrogate the force and displacement boundary conditions required to produce geologically and geodetically constrained slip rates along the Altyn Tagh, Kunlun, Karakoram, and Haiyuan faults.

3.2 Dynamic microplate models of the Tibetan plateau

3.2.1 Microplate geometry and boundary conditions

Model discretization of the Tibetan plateau is based on the locations of major mapped structures and locations previously hypothesized to serve as important mechanical boundaries (Figure 3.1a, Figure 3.2). Major strike-slip faults represented include the Karakoram, Karakash, Altyn Tagh, Kunlun, Jaili, and Xianshuihe faults. Other structures such as the Ganzi, Red River, and Longmu-Gohza faults are not represented in the simplified model considered here. This fault network forms ten microplates constituting the Tibetan plateau, Tarim Basin, and Asia (Figure 3.2). The Asia microplate is limited in latitudinal extent by the northern edge of the Tien Shan, which approximately marks the termination of collision-related deformation in the western half of the model domain (Abdrakhmatov et al., 1996). In contrast, east of 90°E, collision-related deformation may propagate far into northeast Asia (e.g., Calais et al., 2003), and we consider this boundary to either be stress-free or constrained by local boundary conditions described below.

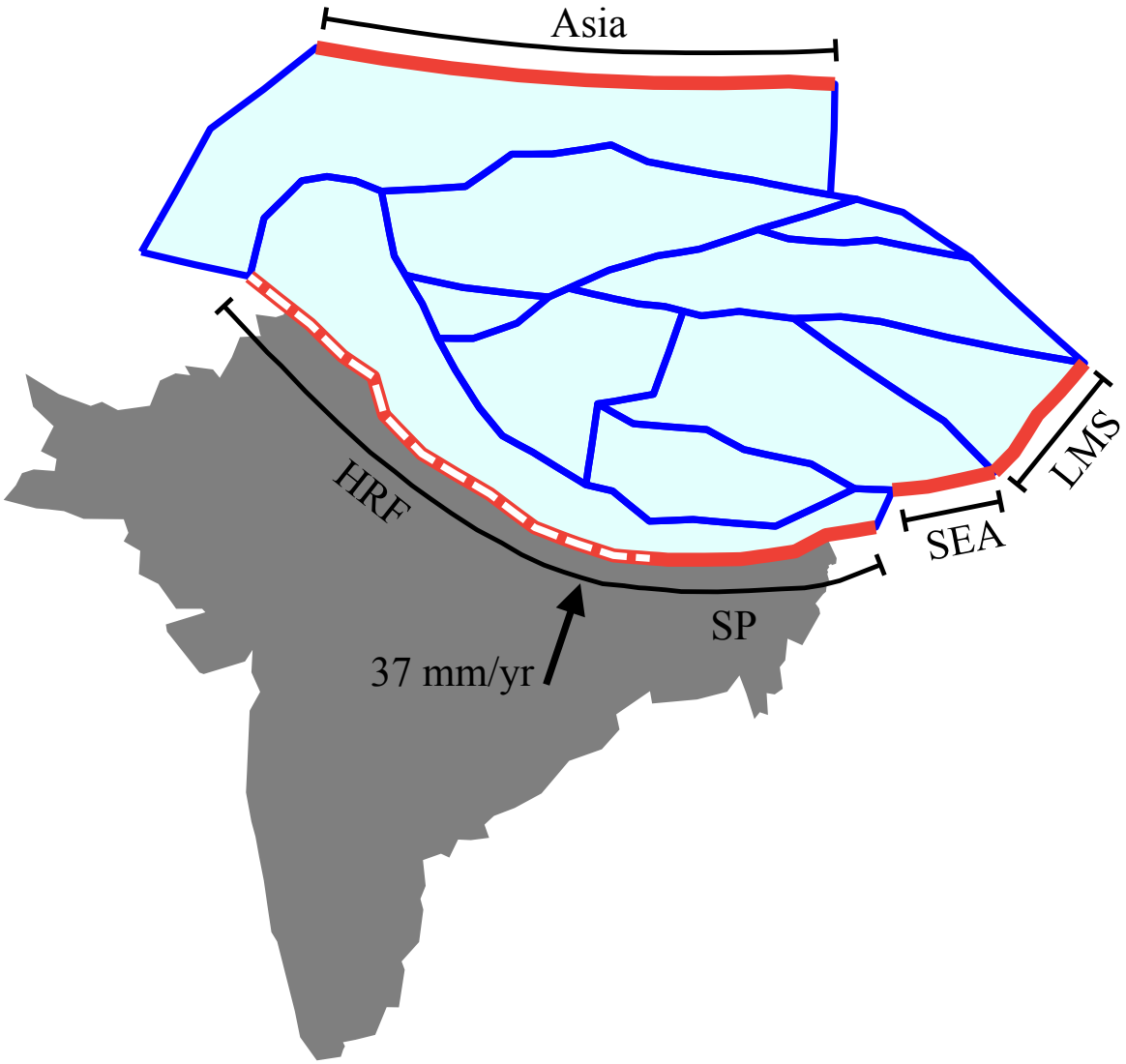

Figure 3.2: Microplate geometry and boundary conditions for DM models. Microplate boundaries are shown in blue and locations of non-stress free boundaries are shown in red. The Asia boundary is subject to a zero displacement boundary condition in all models. Convergence between India and Asia at the Himalayan range front (HRF) is assumed to be 37 mm/yr throughout (Wang et al., 2001) though two different spatial extents are considered. In the first, convergence is assumed to extend over the entire HRF, while in the second, convergence is isolated to the HRF west (dashed line) of the Shillong plateau (SP). Models with zero displacement Dirichlet conditions west of the Sichuan basin at the Longmen Shan range (LMS) are also considered, as are models with force boundary conditions in southeast Asia (SEA).

The northern edge of the Eurasian block represents a kinematic boundary and is modeled with zero-displacement boundary conditions (Figure 3.2). Three additional boundary conditions are considered in models discussed here: 1) extent of convergence along the Himalayan range front (Dirichlet), 2) resistance at the western margin of the Sichuan basin (Dirichlet), and 3) forces acting at the southeast margin of the plateau (von Neumann). All of these are applied only at model domain edges. Each of these idealized representations of forces and displacements acting on the Tibetan plateau is motivated by a specific observation or hypothesis. Oblique (northeast-southwest) convergence between India and Asia at $\sim$37 mm/yr is imposed as a displacement boundary condition at the Himalayan range front, consistent with geodetically observed shortening (Wang et al., 2001). The spatial extent of this convergence is limited not only by the eastern and western syntaxes, but also by active shortening across the Shillong plateau $\sim$200 km south of the Himalayan range front (Ambraseys and Bilham, 2003). Thus we consider models where the convergence along the HRF is uniform along its entire extent and those where it is limited to the $\sim$75% of the range front west of 90°E. At the eastern margin of the plateau, the Sichuan basin has been proposed as a mechanically strong structural element preventing the eastward propagation of deformation (e.g., Chen et al., 2004; Li et al., 2006; Wang et al., 2003). Southwest of the Sichuan basin, geodetic observations suggest the extrusion of upper crustal material from eastern Tibet into southeast Asia (e.g., Wang et al., 2003). Finally, the geodetically observed movement of crustal material into southeast Asia (e.g., Chen et al., 2012; Zhen-Kang et al., 2005) south of the Sichuan basin has been attributed to active local forces, such as laterally constrained lower crustal flow or mantle tractions associated with rollback of the

Model	Altyn Tagh	Karakorum	Kunlun	Xianshuihe	Jiali	Haiyuan	Extrusion
T1. HRF	1 – 11	(3 – 11)	(6) – 3	(1 – 4)	(1 – 7)	(1) – 2	N
T2. HRF, Fixed LMS	1 – 11	(3 – 11)	(6) – 2	(3) – 6	(1 – 4)	0 – 6	N
T3. ¾ HRF	2 – 13	(4 – 12)	(1) – 4	1	(1) - 2	2	N
T4. ¾ HRF, Fixed LMS	1 – 12	(3 – 12)	(8) – 3	2 – 8	(1) – 3	2 – 5	N
T5. HRF, SEA Force BC	1 – 12	(4 – 12)	(2) – 3	(4 – 13)	(2 – 9)	1 – 2	N
T6. ¾ HRF, SEA Force BC	1 – 14	(5 – 12)	3 – 10	(11) – 3	(2) – 5	3 – 5	Y

Table 3.1: Predicted slip rates (mm/yr) and extent of southeastern extrusion from six DM models. Right-lateral slip rates are denoted with parentheses while left-lateral slip rates are not. For each fault the total variation in slip rates is given. For the case of southeast extrusion, models are deemed inconsistent with the geodetic observations only if there is no motion to the south and east along the southeastern-most boundary of the plateau. In all cases the Altyn Tagh fault is left-lateral and the Karakoram is right-lateral; however, the sense of slip varies for all other major faults. Extrusion of material toward southeast Asia is only present in models that include a local applied force along the southeastern edge of the model and convergent forcing isolated along the western ¾ of the Himalayan range front. DM Model T6 (bottom) is the only one to predict an entirely left-lateral Kunlun fault.

Indo-Burman slab (Royden et al., 2008).

3.2.2 Sufficient mechanisms for strike-slip faulting

To understand the role of edge forces in driving strike-slip faulting within the Tibetan plateau, we consider six DM models differing only in the combinations of boundary conditions described above (Table 3.1). Models T1 to T6 are described below. It must be noted that like continuously deforming dynamic models (e.g., England and Molnar, 1997, 2005; Flesch et al., 2001), direct comparison to geodetic observations is not yet possible for DM models due to their neglect of earthquake cycle processes which may significantly modulate GPS observations obtained during the nominally interseismic part of the seismic cycle in Tibet (e.g., Bilham et al., 1997; Chen et al., 2004; Feldl and Bilham, 2006; Hilley et al., 2005,

2009; Meade, 2007). To avoid this problem, we instead make comparisons with slip rate estimates inferred from geologic interpretations or geodetic observations interpreted with steady state or time-dependent earthquake cycle models along specific faults. Our criteria for evaluating models is based on model prediction of three well-resolved features of the India-Asia boundary: the left-lateral slip rates on the well sampled Altyn Tagh and Kunlun faults and the southeastern extrusion of Tibetan crustal material. A summary of all six models described here is provided in Table 3.1.

Model T1: Full Himalayan range front convergence

Model T1 (Table 3.1) is the simplest in our suite of Tibetan models and features oblique convergence across the entire Himalayan range front. Deformation rates (Figure 3.3) are highest in the south and east of our model, but the southeastern extrusion of Tibetan crustal material is not observed. Instead, internal block deformation is approximately parallel to the convergence boundary condition across the Himalayan Range Front, with maximum deformation rates equal to the convergence rate.

Model T1 slip rate predictions for the Karakorum fault (Figure 3.4) are right-lateral and range from 3–11 mm/yr. Slip is fastest in the northwest near the junction with the Altyn Tagh fault and holds steady at ∼8 mm/yr for ∼600 km south of the junction. Minimum slip rates occur on the southern portion of the fault. These results are higher than geologic estimates of 10.7 ± 0.7 mm/yr (Chevalier et al., 2005) from the central and southern portion of the Karakorum, but are broadly consistent with geologic estimates of 4 ±1 mm/yr (Brown et al., 2002) and InSAR estimates of 1 ± 3 mm/y (Wright et al., 2004) from similar regions.

Model T1 predicts a change in the sense of slip on the Haiyuan fault from left-lateral

Figure 3.3 *(following page)*: Slip rates, velocities, and principal stresses from DM model T1, with full Himalayan range front convergence. In all figures microplate boundaries are shown as blue lines and the Indian sub-continent is shaded in gray. Panel a) shows fault slip rates with left-lateral rates shown as white text in blue circles and right-lateral text shown as blue text in white circles. For clarity, only representative slip rates are shown here. Color shading shows velocity magnitudes, where redder colors indicate faster velocities. Maximum velocities equal the differential motion between India and Eurasia. Here the Altyn Tagh is the fastest left-lateral fault and the Karakorum and Jiali are the fastest right-lateral faults. The Kunlun switches from right-lateral to left-lateral from west to east along strike and the Xianshuihe is right-lateral. Panel b) shows velocity vectors (white arrows) superimposed over the velocity magnitude field. Velocity azimuths are dominantly north-northeast, consistent with the imposed convergence boundary condition on the HRF. Panel c) shows the principal stresses. Principal stresses are dominantly convergent (compression) and are broadly consistent with the direction of convergence.

Figure 3.3: (continued)

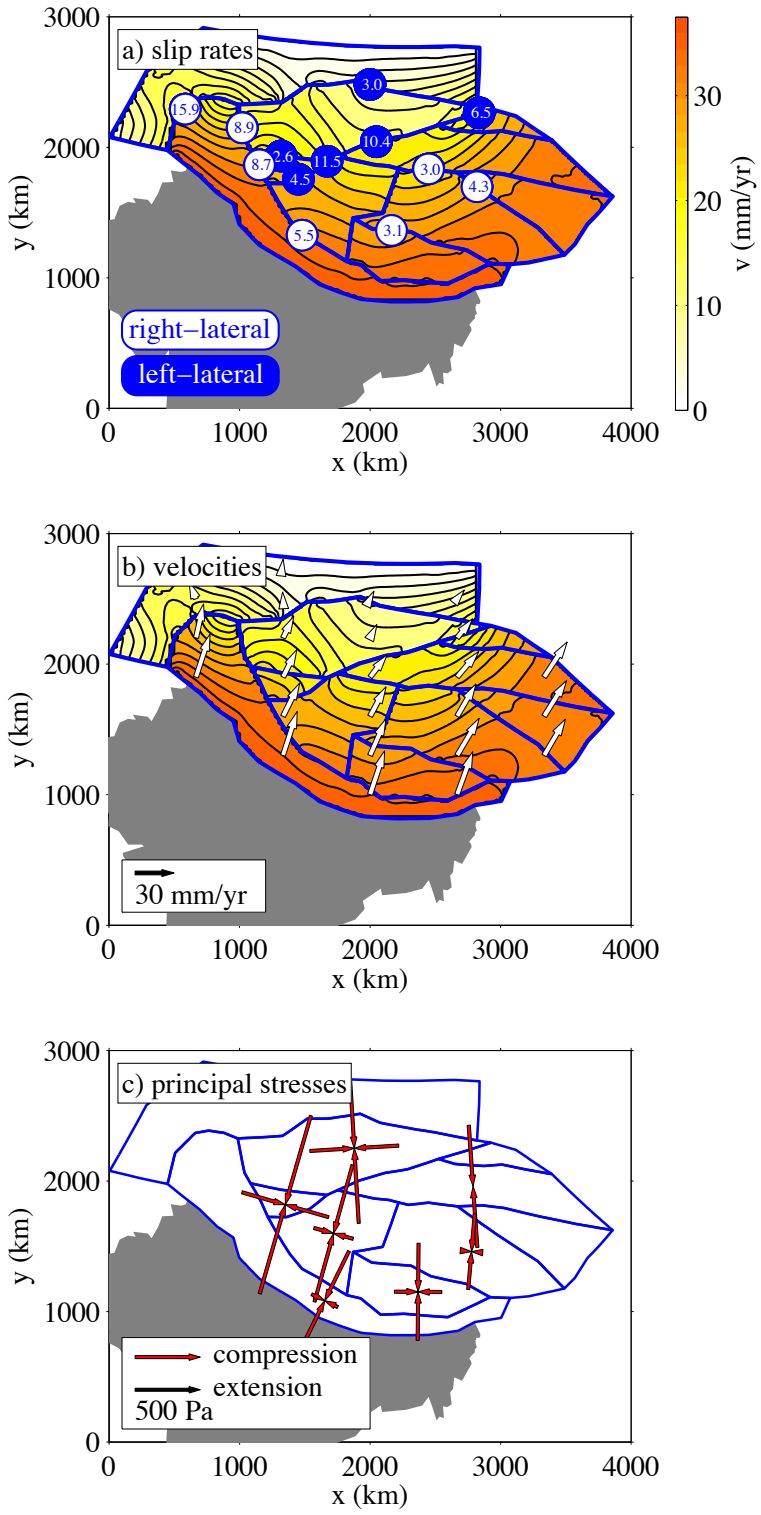

to right-lateral (slip rate values range from 1 mm/yr of right-lateral slip to 2 mm/yr of left-lateral slip). These observations are inconsistent with well-documented left-lateral displacement on the fault of 3.4–9 mm/yr (Cavalié et al., 2008; Li et al., 2009; Meade, 2007).

Slip rates on the Altyn Tagh fault (Figure 3.5) are left-lateral and vary by an order of magnitude along strike. Peak slip rates of ∼11 mm/yr occur in the central western portion of the fault south of the Tarim Basin and fall off to a minimum (∼1 mm/yr) at the western fault tip. Fault slip rates are ∼6 mm/yr on the eastern ∼300 km of the fault. These slip rates agree well with InSAR observations of 5 ± 5 mm/yr in the west (Wright et al., 2004) and geologic (11.5 ± 2.5 mm/yr; Cowgill et al., 2009) and geodetic (9 ± 4 mm/yr; Wallace et al., 2004) observations in the central portion of the fault. However, these predictions are higher than geodetic observations on the eastern portion of the fault (3 ± 2 mm/yr; Meade, 2007) and lower than geologic observations of 14 ± 2 mm/yr (Yue et al., 2001) and 17.8 ± 3.6 mm/yr (Mériaux et al., 2005).

The primary reason that model T1 is not considered an accurate model for describing strike-slip faulting in Tibet is because of its failure to predict slip rates on the densely sampled Kunlun fault (Figure 3.6). Numerous geologic and geodetic studies have shown that Kunlun slip is left-lateral and range from 3 ± 2 mm/yr on the western Manyi splay (Bell et al., 2011) to 9–17.8 mm/yr (Meade, 2007; Van der Woerd et al., 2002b) in the center portion of the fault and 1.6–6 mm/yr (Kirby et al., 2007) on the eastern section. Model T1 predicts left-lateral slip rates of ∼3 mm/yr on the westernmost portion of the Manyi splay, but slip quickly becomes right-lateral (up to 6 mm/yr in the center of the fault) and remains dexteral for more than 1500 km along strike.

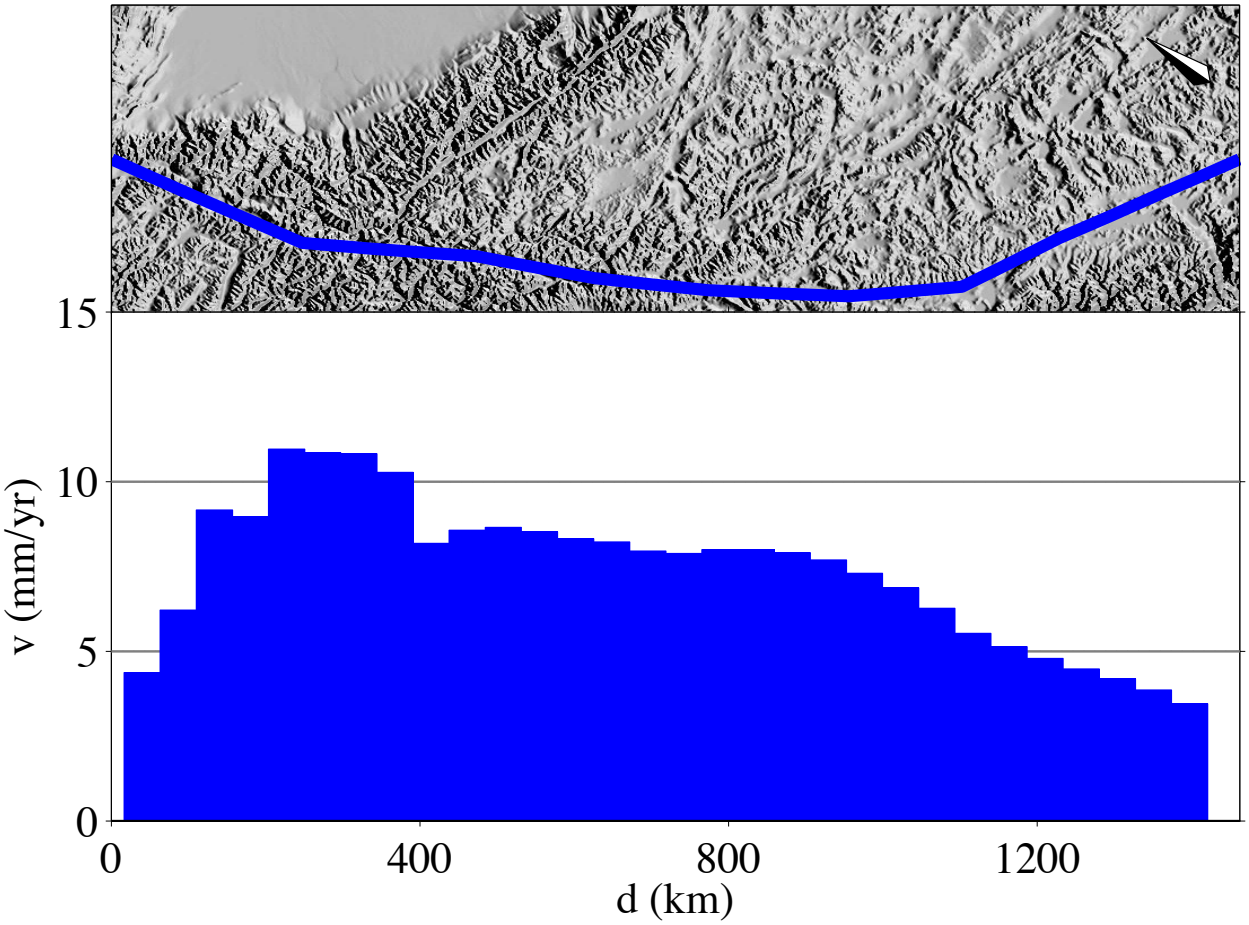

Figure 3.4: Along-strike slip variation for the Karakorum fault at the western boundary of the Tibetan Plateau predicted by DM model T1. The upper panel shows the rotated fault trace and topography within 200 km of the fault endpoints. The compass rose points north. Right-lateral slip rates predicted by model T1 are shown as blue fill. Slip is lowest (∼3 mm/yr) in the south and highest (∼11 mm/yr) just south of the intersection with the Altyn Tagh. Slip is relatively constant at ∼8 mm/yr on the central portion of the fault. The peak slip rate predicted is consistent with geologic observations of 10.7 ± 0.7 mm/yr (Chevalier et al., 2005) while the northern and southern extremes of the fault are consistant with other geologic (4 ± 1 mm/yr, Brown et al., 2002) and InSAR (1 ± 3 mm/yr, Wright et al., 2004) estimates.

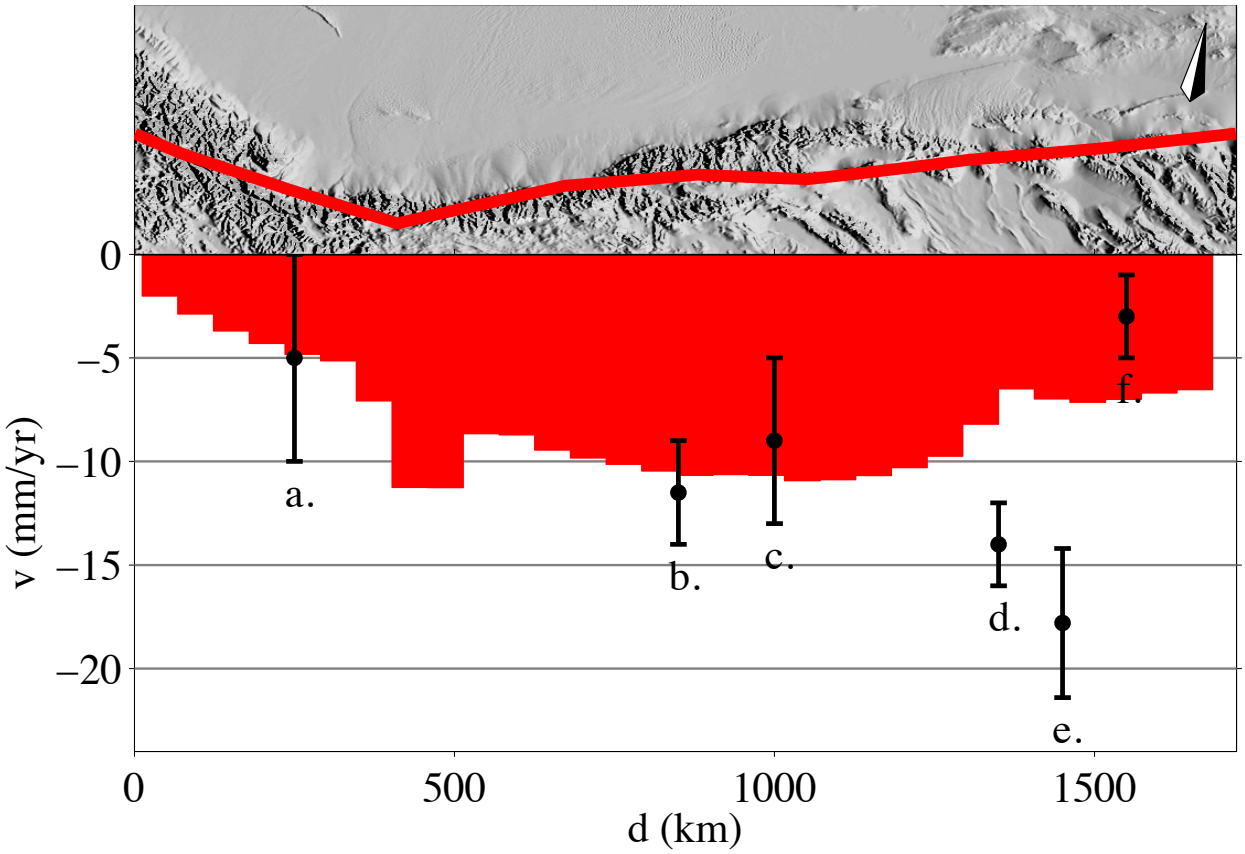

Figure 3.5: Slip rate variation predicted by DM model T1 along the Altyn Tagh-Karakash fault system at the northern boundary of the Tibetan plateau. The upper panel shows the rotated fault trace and topography within 200 km of the fault endpoints with the compass rose pointing north. Slip rates predicted by T1 are shown as the red fill in the lower panel with geologic and geodetic fault slip rate estimates shown as black circles with reported 1-sigma error bars. Negative numbers and red colors indicate left-lateral motion. Model T1 predicts peak slip rates on the central portion of the fault (up to ∼11 mm/yr). The slip rate reaches a minimum on the western extent of the fault (∼1 mm/yr) and is ∼6 mm/yr on the eastern tip. Slip rates inferred from geologic and geodetic data are from west to east: a. 5 ± 5 mm/yr, Wright et al. (2004), b. 11.5 ± 2.5 mm/yr, Cowgill et al. (2009), c. 9 ± 4 mm/yr, Wallace et al. (2004), d. 14 ± 2 mm/yr, Yue et al. (2001), e. 17.8 ± 3.6 mm/yr, Mériaux et al. (2005), and f. 3 ± 2 mm/yr, Meade (2007).

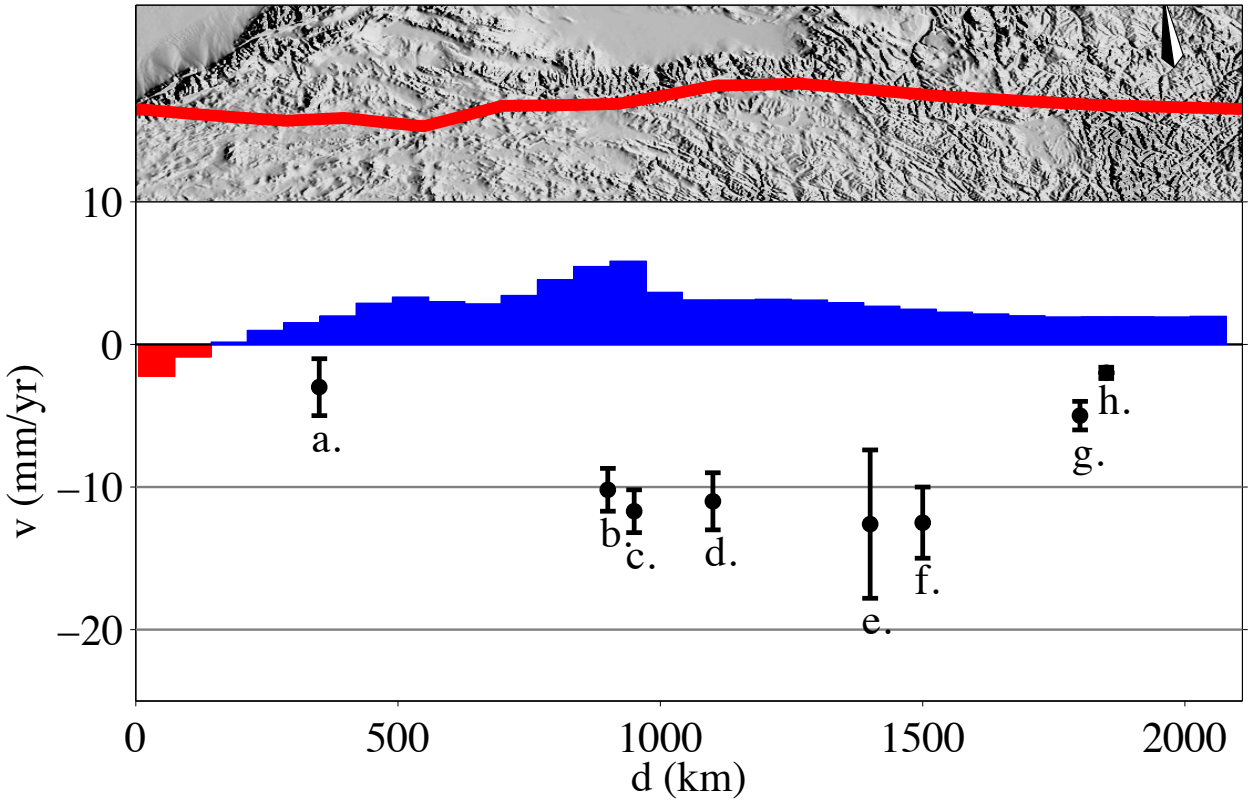

Figure 3.6: Slip rate variation predicted by DM model T1 along the east-west trending Kunlun fault system. The upper panel shows the rotated fault trace and topography within 200 km of the fault endpoints with the compass rose pointing north. Slip rates predicted by T1 are shown as the red and blue fill in the lower panel with geologic and geodetic fault slip rate estimates shown as black circles with reported 1–sigma error bars. Red colors and negative numbers indicate left-lateral motion, blue colors and positive numbers indicate right-lateral motion. The fault is very briefly left-lateral on the western Manyi splay (with a slip rate of ∼3 mm/yr) and then is right-lateral for the eastern ∼2250 km of fault (with maximum right-lateral slip rates of ∼6 mm/yr). These predictions are in poor agreement with well documented left-lateral slip on the fault (shown in black above). Slip rates inferred from geologic and geodetic data are from west to east: a. 3 ± 2 mm/yr, Bell et al. (2011), b. 10.2 ± 1.5 mm/yr, Hilley et al. (2005), c. 11.7 ± 1.5 mm/yr (at ∼94°E), van Van der Woerd et al. (2002b), d. 11 ± 2 mm/yr, Meade (2007), e. 12.6 ± 5.2 mm/yr (at ∼99°E), Van der Woerd et al. (2002b), f. 12.5 ± 2.5 mm/yr (at ∼100.5°E), Van der Woerd et al. (2002b), g. 5 ± 1 mm/yr, at (∼101.5°E), Kirby et al. (2007), and h. 2.0 ± 0.4 mm/yr (at ∼101.75°E), Kirby et al. (2007).

Model T1 predictions on the Xianshuihe fault are completely right-lateral (Figure 3.7), in contrast to geologic and geodetic estimates of 9–20 mm/yr of sinisteral slip (Allen et al., 1991; He et al., 2006; Meade, 2007; Wang et al., 2009). Model T1 also predicts entirely right-lateral slip on the Jiali fault (Figure 3.8) on the order of 1–7 mm/yr. These results are consistent with the observed sense of slip on the Jiali and with block model estimates of 3–4 mm/yr (Meade, 2007) but lower than geologic estimates of 10–20 mm/yr (Armijo et al., 1989).

Internal microplate principal stresses from model T1 are largely compressive and broadly consistent with the displacement condition at the Himalayan range front (Figure 3.3). However, microplates at the eastern extent of the model have compressional stresses < 50 Pa and, in the case of the Longmen Shan and the two blocks north of it, there is a small tensional stress.

Model T2: Full Himalayan range front convergence and fixed Longmen Shan

We next attempt to capture Tibetan extrusion into southeast Asia and left-lateral slip on the Kunlun fault by testing a model with convergence across the full Himalayan range front and a fixed Sichuan basin. This model is achieved by applying a fixed Dirichlet boundary condition to the eastern edge of the Longmen Shan block. Model T2 results (Figure 3.9) show the strongest deformation close to the Himalayan range front and are largely consistent with the convergent boundary condition. Deformation in the northeastern part of the model (e.g., the eastern Kunlun block and Haiyuan block) is east northeast in direction but does not exhibit the previously documented southeastern extrusion of Tibet (Meade, 2007).

Model T2 predicted slip rates on the Karakorum (Figure 3.10) and Altyn Tagh (Figure

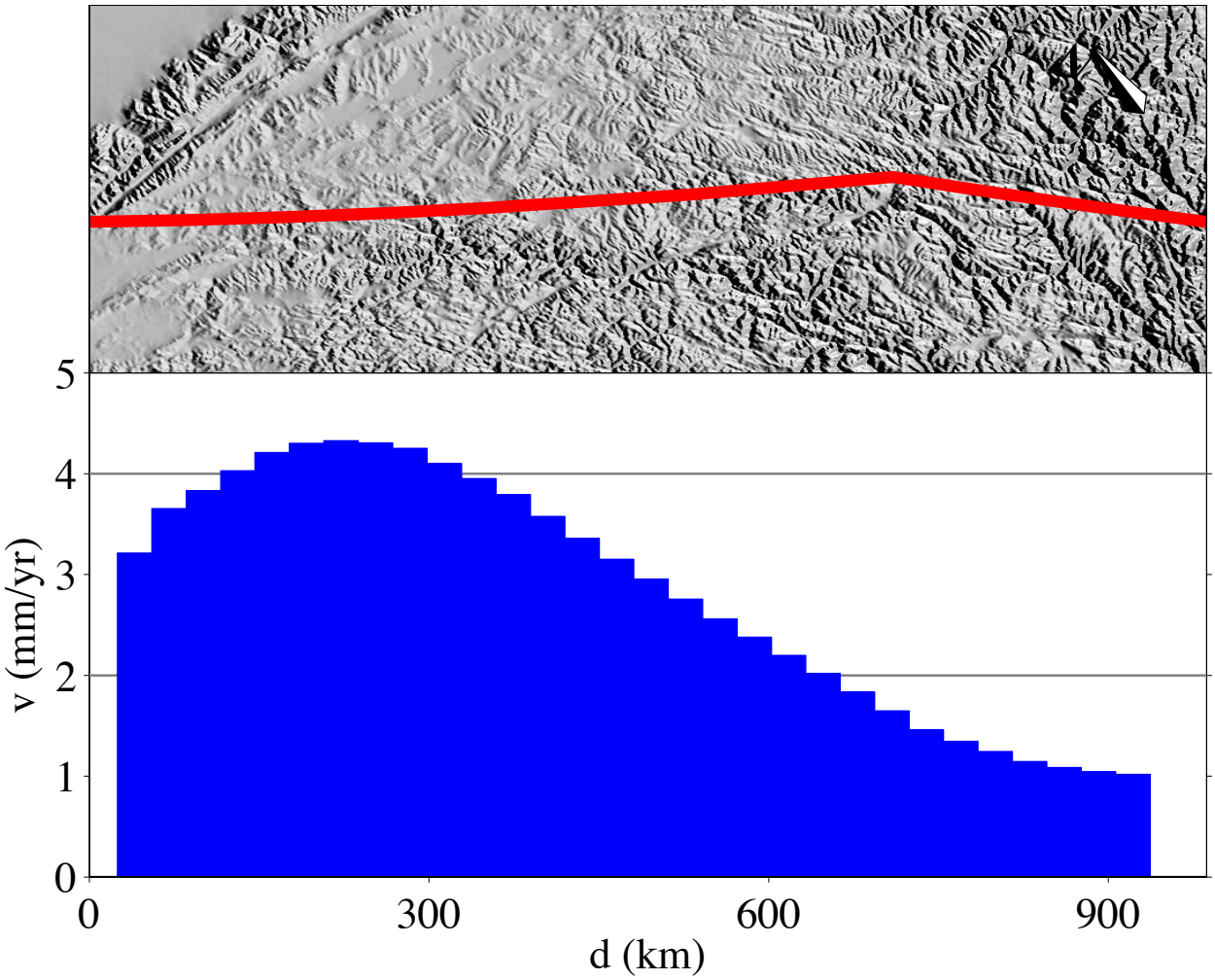

Figure 3.7: Slip rate variation predicted by DM model T1 along the Xianshuihe fault in eastern Tibet. The upper panel shows the rotated fault trace and topography within 200 km of the fault endpoints. The compass rose points north. Model T1 predicts entirely right-lateral slip on the fault, with maximum slip rates of ∼4 mm/yr in the west and minimum rates of ∼1 mm/yr in the east. These predictions are are in contradiction with sinisteral slip estimates of ∼15 mm/yr from geologic estimates (Allen et al., 1991; He et al., 2006), 9–12 mm/yr inferred from InSAR observations (Wang et al., 2009), and 3–20 mm/yr from geodetically constrained block models (Meade, 2007).

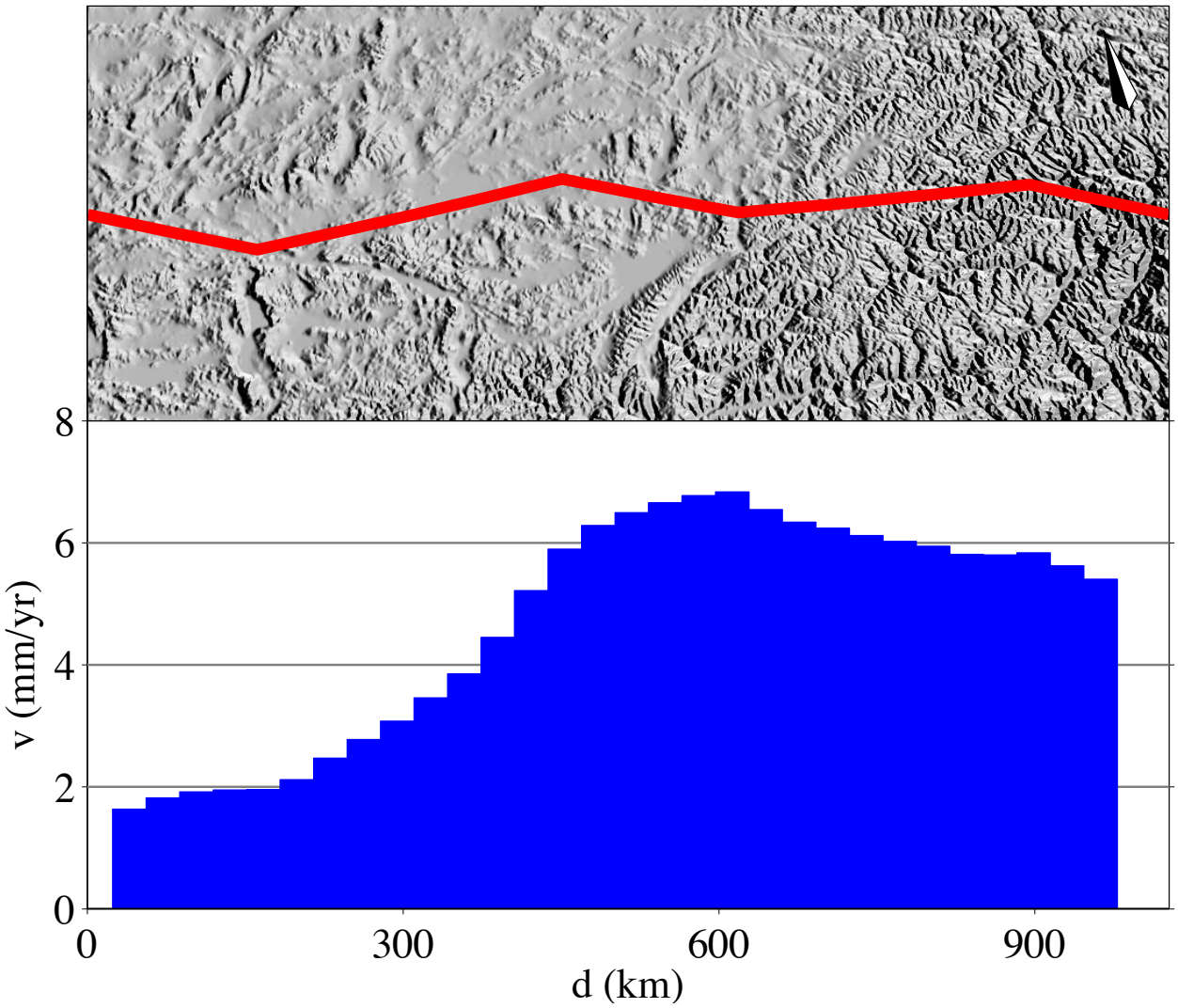

Figure 3.8: Along-strike slip rate variations predicted by DM model T1 for the Jiali fault in southeastern Tibet. The upper panel shows the rotated fault trace and topography within 200 km of the fault endpoints. The compass rose points north. Right-lateral slip rates are plotted as blue fill. Model T2 predicts that the Jiali is entirely right-lateral, with minimum slip rates of ∼1 mm/yr in the west and maximum slip rates of ∼7 mm/yr on the central portion of the fault. Although geologic and geodetic data are sparse for this structure, these results are lower than geologic observations of 10-20 mm/yr of right-lateral slip (Armijo et al., 1989), but western slip rate predictions agree with block model estimates of 3-4 mm/yr of dexteral motion (Meade, 2007).

Figure 3.9 *(following page)*: Slip rates, velocities, and principal stresses from DM model T2, with a full Himalayan convergence condition and a zero-slip boundary on the eastern margin of the Longmen Shan block. In all figures microplate boundaries are shown as blue lines and the Indian sub-continent is shaded in gray. Panel a) shows fault slip rates with left-lateral rates shown as white text in blue circles and right-lateral text shown as blue text in white circles. For clarity, only representative slip rates are shown here. Color shading shows velocity magnitudes, where redder colors indicate faster velocities. Maximum velocities equal the differential motion between India and Eurasia. Here the Altyn Tagh is the fastest left-lateral fault and the Karakorum is the fastest right-lateral fault. The Kunlun switches from right-lateral to left-lateral from west to east along strike, and the sense of slip on the Xianshuihe also changes. Panel b) shows velocity vectors (white arrows) superimposed over the velocity magnitude field. Velocity azimuths are dominantly north-northeast, consistent with the imposed convergence boundary condition on the HRF, but in the eastern portion of the model they become very small and go to zero (a result of the Longmen Shan boundary condition). Panel c) shows the principal stresses. Principal stresses are dominantly convergent (compression) and are broadly consistent with the direction of convergence. In the Longmen Shan block they are slightly rotated because of the zero-slip condition applied there.

Figure 3.9: (continued)

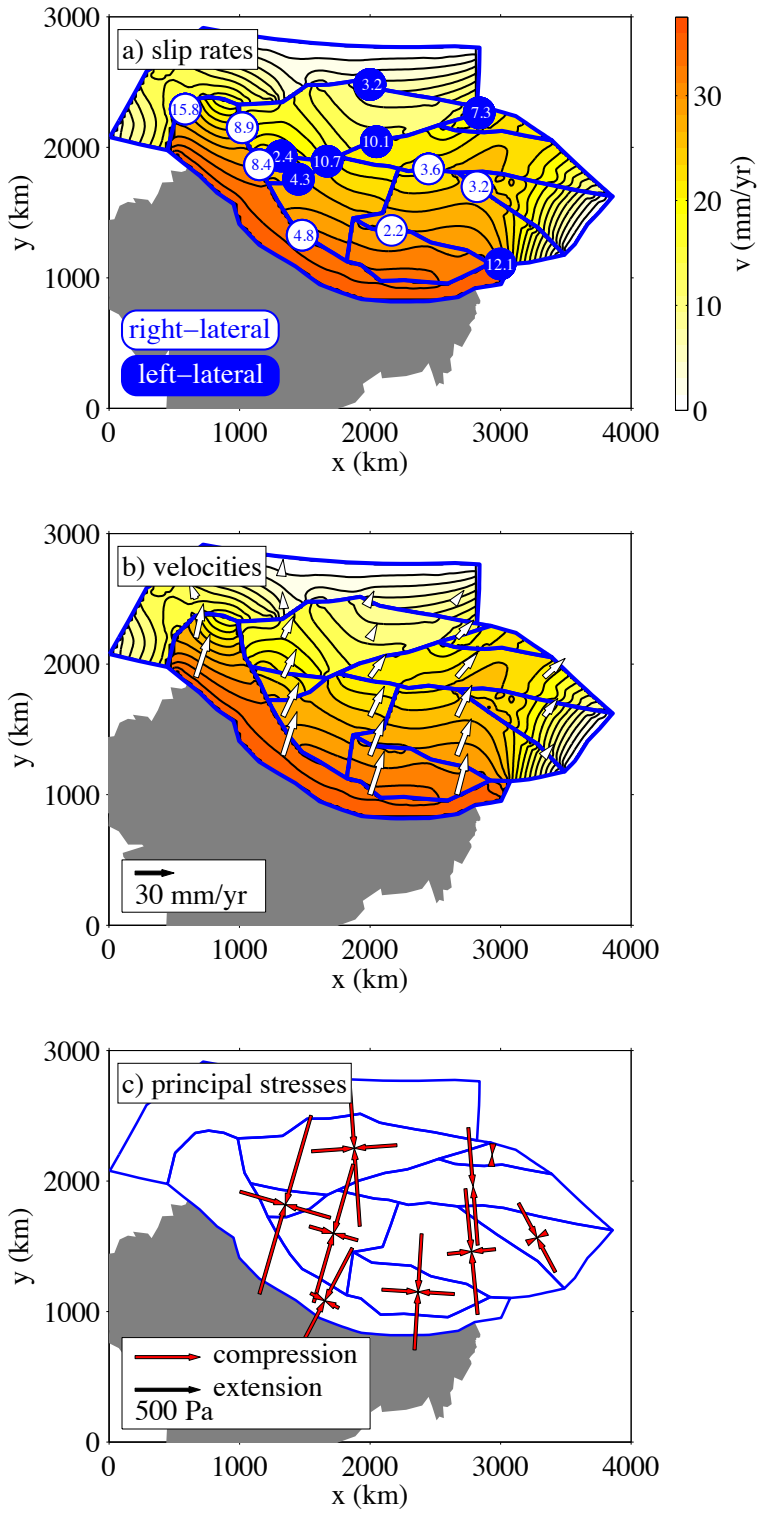

3.11) faults are nearly identical to that predicted in model T1. As with model T1, Karakorum slip rates range from ∼3–11 mm/yr of right-lateral slip and Altyn Tagh slip rates range from ∼1–11 mm/yr of left-lateral slip. Unlike model T1, Haiyuan fault slip rate predictions are left-lateral and range from 0–6 mm/yr.

Model T2 slip rates on the Kunlun fault (Figure 3.12) are nearly identical to those from model T1 for the first ∼1200 km of the fault: slip rates are left-lateral on the far western portion of the Manyi splay (∼2 mm/yr) but quickly become right-lateral, reaching ∼6 mm/yr of dexteral motion at ∼1000 km along strike. However, the predicted slip rate differs from model T1 on the eastern half of the fault: at ∼1500 km slip becomes left-lateral again (reaching ∼2 mm/yr of sinisteral motion) before becoming right-lateral (∼6 mm/yr) again on the far eastern extent of the fault. Left-lateral slip rates are consistently below geologic observations for the eastern portion of the fault (Kirby et al., 2007), and model T2 does not accurately predict Kunlun slip rates.

The model T2-predicted sense of slip on the Xianshuihe fault (Figure 3.13) is right-lateral on the western ∼400 km of the fault (with maximum right-lateral slip rates of ∼3 mm/yr on the central eastern portion of the fault) before becoming left-lateral for the eastern portion of the fault (with maximum left-lateral slip rates of 6 mm/yr in the east). These predictions are inconsistent with the geologic and geodetic estimates of entirely left-lateral slip of 9–20 mm/yr (Allen et al., 1991; He et al., 2006; Meade, 2007; Wang et al., 2009).

Jiali fault slip rate predictions (Figure 3.14) are right-lateral and range from 1–4 mm/yr, with slip rates peaking on the central portion of the fault. These predictions are consistent with block model estimates of 3–4 mm/yr (Meade, 2007) but are much lower than geologic

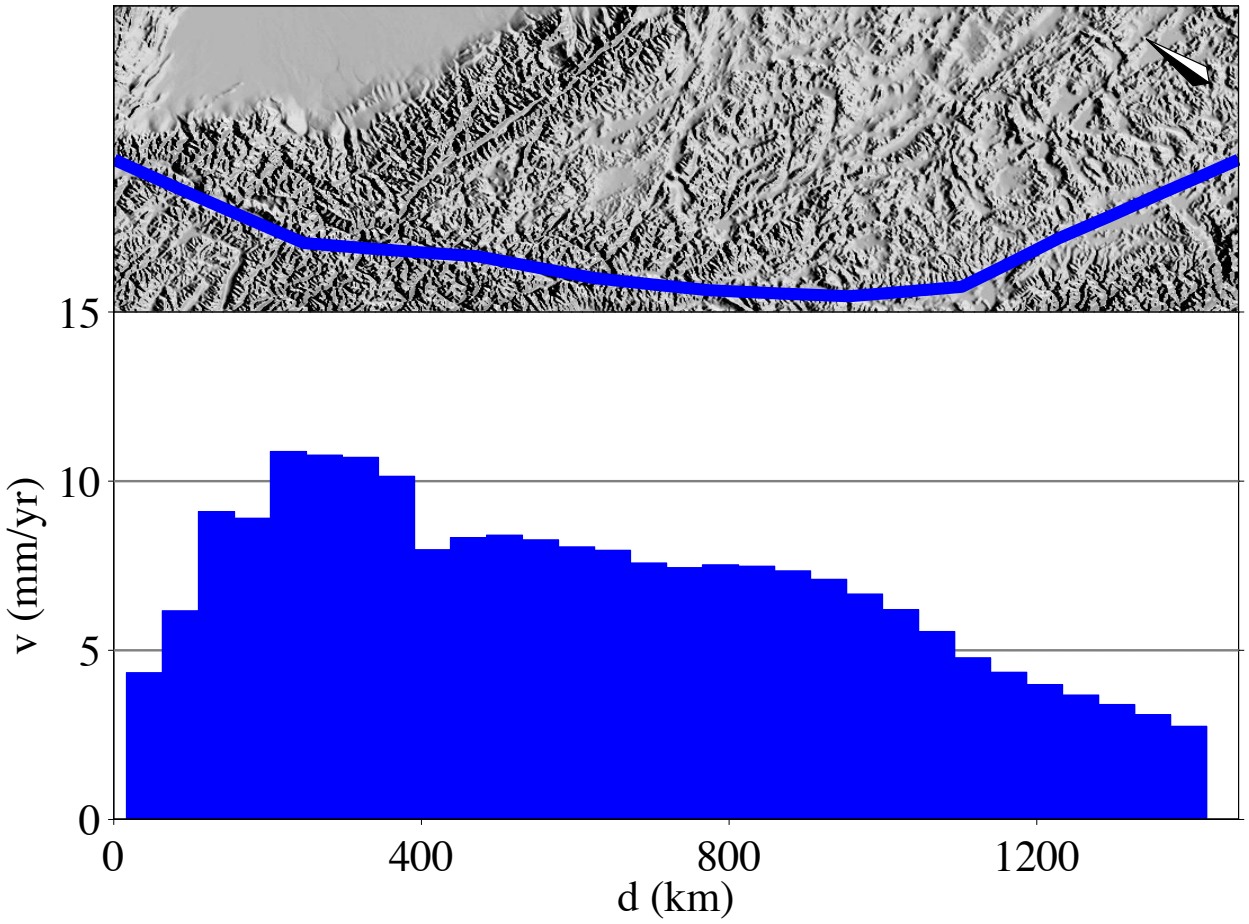

Figure 3.10: Along-strike slip variation for the Karakorum fault at the western boundary of the Tibetan Plateau predicted by DM model T2. The upper panel shows the rotated fault trace and topography within 200 km of the fault endpoints. The compass rose points north. Right-lateral slip rates predicted by model T2 are shown as blue fill. Slip is lowest ($\sim$3 mm/yr) in the south and highest ($\sim$11 mm/yr) just south of the intersection with the Altyn Tagh. After the intersection with the Altyn Tagh the slip rate decreases to the minimum value. The peak slip rate predicted is consistent with geologic observations of 10.7 $\pm$ 0.7 mm/yr (Chevalier et al., 2005) while the northern and southern extremes of the fault are consistant with other geologic (4 $\pm$ 1 mm/yr, Brown et al., 2002) and InSAR (1 $\pm$ 3 mm/yr, Wright et al., 2004) estimates.

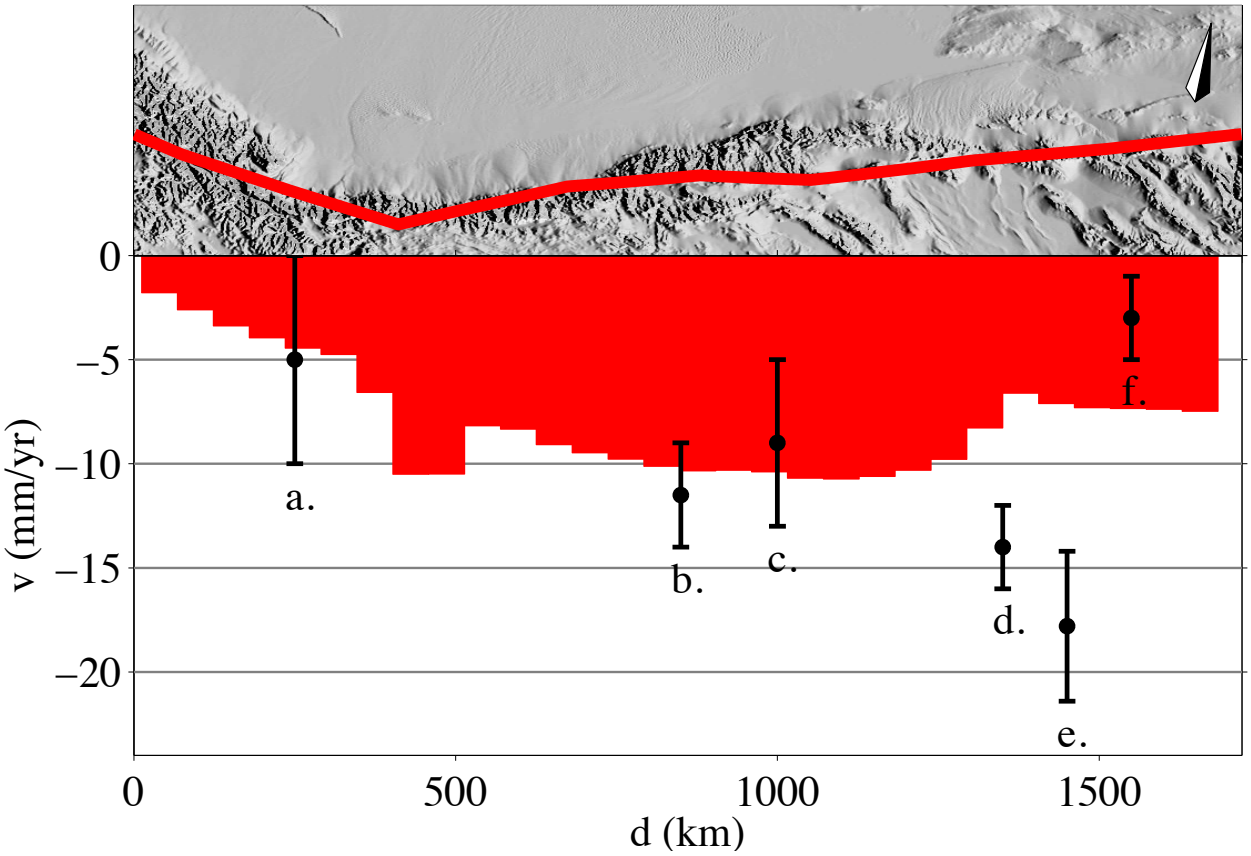

Figure 3.11: Slip rate variation predicted by DM model T2 along the Altyn Tagh-Karakash fault system at the northern boundary of the Tibetan plateau. The upper panel shows the rotated fault trace and topography within 200 km of the fault endpoints with the compass rose pointing north. Slip rates predicted by T2 are shown as the red fill in the lower panel with geologic and geodetic fault slip rate estimates shown as black circles with reported 1-sigma error bars. Negative numbers and red colors indicate left-lateral motion. Model T2 predicts peak slip rates on the central portion of the fault (up to ∼11 mm/yr). The slip rate reaches a minimum on the western extent of the fault (∼1 mm/yr) and is ∼7 mm/yr on the eastern tip. Slip rates inferred from geologic and geodetic data are from west to east: a. 5 ± 5 mm/yr, Wright et al. (2004), b. 11.5 ± 2.5 mm/yr, Cowgill et al. (2009), c. 9 ± 4 mm/yr, Wallace et al. (2004), d. 14 ± 2 mm/yr, Yue et al. (2001), e. 17.8 ± 3.6 mm/yr, Mériaux et al. (2005), and f. 3 ± 2 mm/yr, Meade (2007).

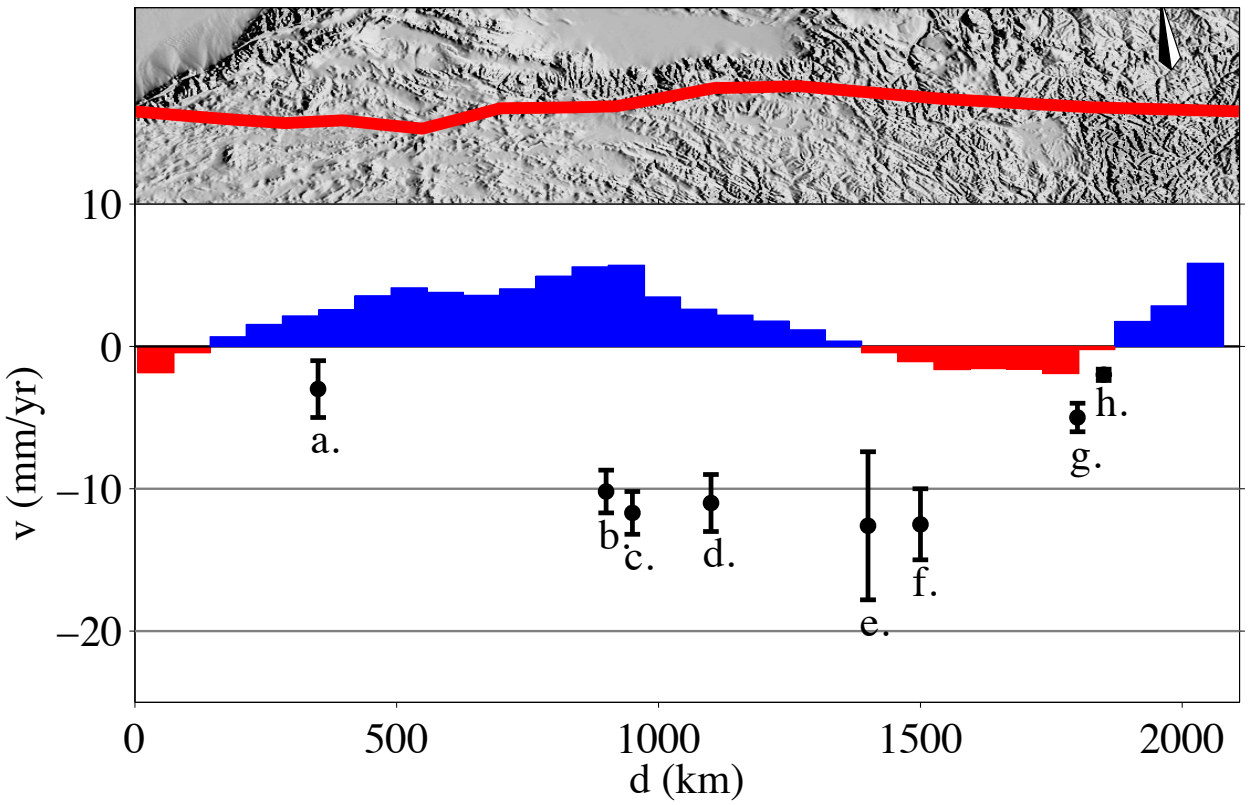

Figure 3.12: Slip rate variation predicted by DM model T2 along the east-west trending Kunlun fault system. The upper panel shows the rotated fault trace and topography within 200 km of the fault endpoints with the compass rose pointing north. Slip rates predicted by T2 are shown as the red and blue fill in the lower panel with geologic and geodetic fault slip rate estimates shown as black circles with reported 1-sigma error bars. Red colors and negative numbers indicate left-lateral motion, blue colors and positive numbers indicate right-lateral motion. The fault is very briefly left-lateral on the western Manyi splay (with a slip rate of ∼2 mm/yr) and then is right-lateral for ∼1250 km of fault (with maximum right-lateral slip rates of ∼6 mm/yr). For the next ∼400 km, the fault is again left-lateral (∼2 mm/yr) and then the sense of slip again becomes right-lateral for the last ∼200 km along strike. These predictions are in poor agreement with well documented left-lateral slip on the fault (shown in black above). Slip rates inferred from geologic and geodetic data are from west to east: a. 3 ± 2 mm/yr, Bell et al. (2011), b. 10.2 ± 1.5 mm/yr, Hilley et al. (2005), c. 11.7 ± 1.5 mm/yr (at ∼94°E), Van der Woerd et al. (2002b), d. 11 ± 2 mm/yr, Meade (2007), e. 12.6 ± 5.2 mm/yr (at ∼99°E), Van der Woerd et al. (2002b), f. 12.5 ± 2.5 mm/yr (at ∼100.5°E), Van der Woerd et al. (2002b), g. 5 ± 1 mm/yr at (∼101.5°E), Kirby et al. (2007), and h. 2.0 ± 0.4 mm/yr (at ∼101.75°E), Kirby et al. (2007).

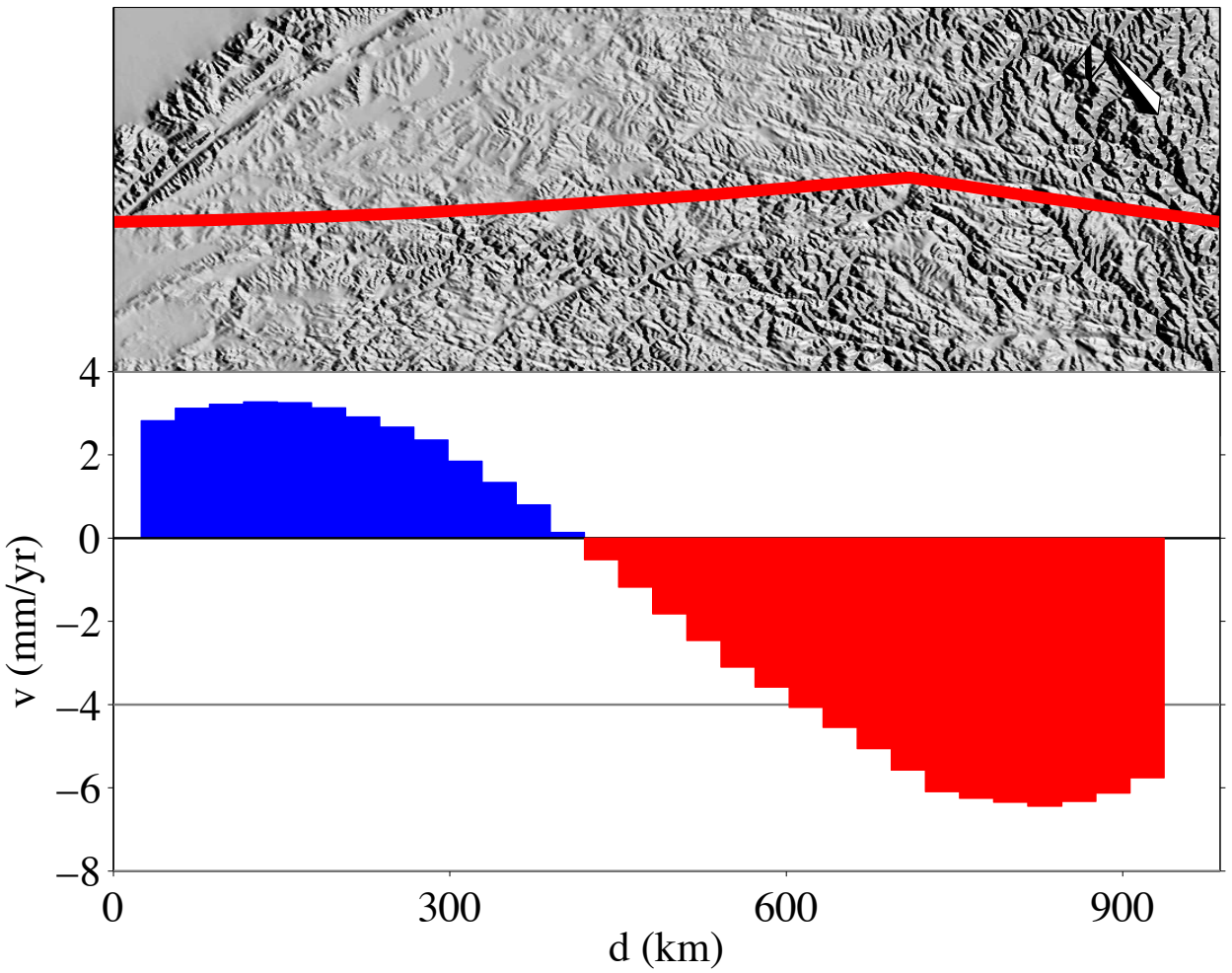

Figure 3.13: Slip rate variation predicted by DM model T2 along the Xianshuihe fault in eastern Tibet. The upper panel shows the rotated fault trace and topography within 200 km of the fault endpoints. The compass rose points north. T2 model predictions of low magnitude (∼3 mm/yr) right-lateral slip rates are plotted as blue fill and as positive values. The predicted sense of slip changes to left-lateral in the center of the fault, with maximum sinisteral slip rate values of ∼ 6 mm/yr (red fill; negative numbers). These predictions do not match geologic and geodetic estimates: block models predict left-lateral slip of of 3 ± 2 mm/yr on the eastern portion of the fault (Meade, 2007), and geologic and geodetic observations suggest a fully left-lateral Xianshuihe. The left-lateral predictions are lower than sinisteral slip estimates of ∼15 mm/yr from geologic estimates (Allen et al., 1991; He et al., 2006), 9–12 mm/yr inferred from InSAR observations (Wang et al., 2009), and ∼20 mm/yr from geodetically constrained block models (Meade, 2007).

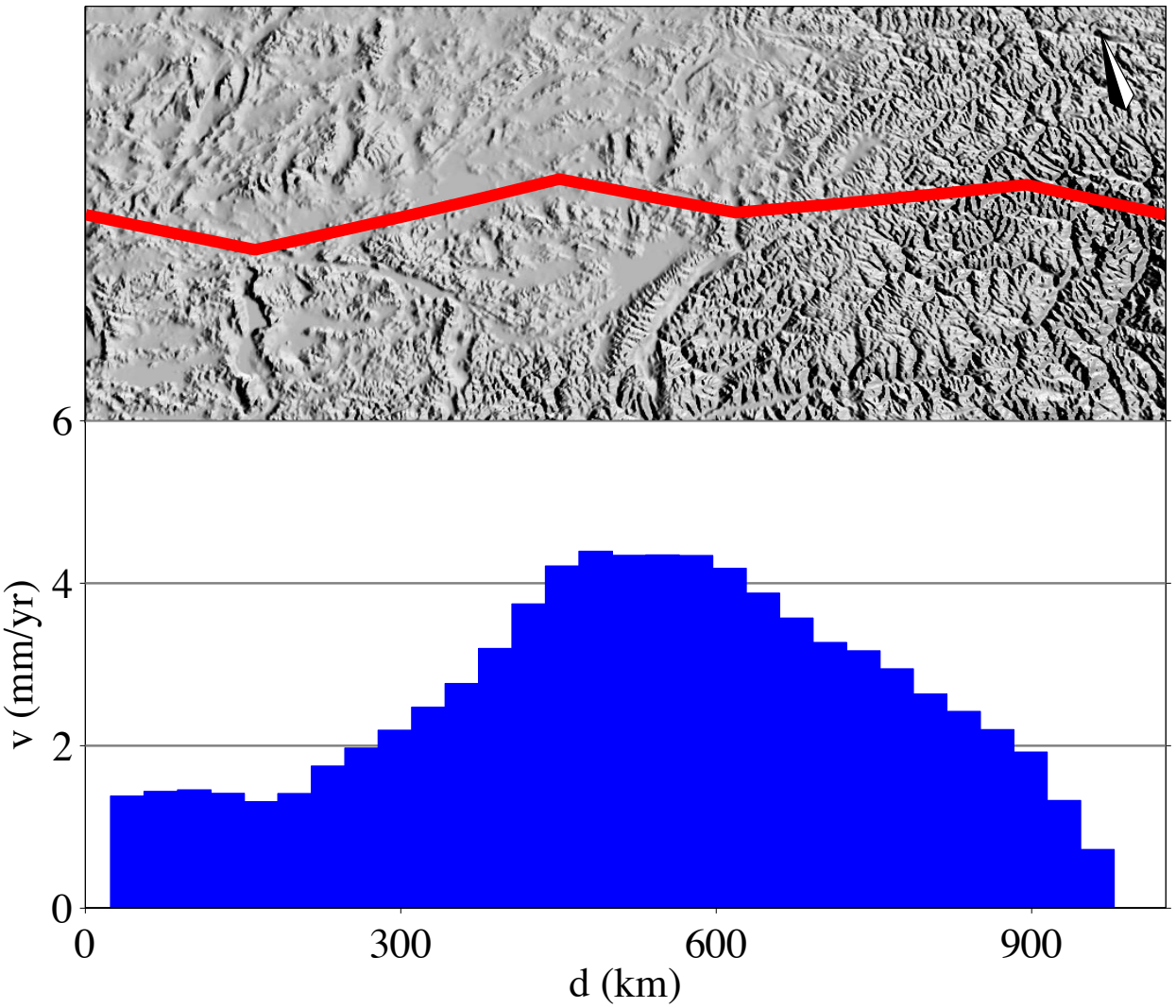

Figure 3.14: Along-strike slip rate variations predicted by DM model T2 for the Jiali fault in southeastern Tibet. The upper panel shows the rotated fault trace and topography within 200 km of the fault endpoints. The compass rose points north. Right-lateral slip rates are plotted as blue fill. Model T2 predicts that the Jiali is entirely right-lateral, with minimum slip rates of ∼1 mm/yr in the east and maximum slip rates of ∼4 mm/yr on the central portion of the fault. Although geologic and geodetic data are sparse for this structure, these results are lower than geologic observations of 10-20 mm/yr of right-lateral slip (Armijo et al., 1989), but eastern and western slip rate predictions agree with block model estimates of 3-4 mm/yr of dexteral motion (Meade, 2007).

sampling of the fault (10–20 mm/yr, Armijo et al., 1989).

The principal stresses predicted by model T2 (Figure 3.9) are nearly identical to those predicted by model T1 for the western blocks in the model. In the east, blocks show higher compressional stresses than in model T1, particularly in the Longmen Shan block and the block bounded by the Xianshuihe and Jiali faults. The predicted principal stress in the interior of the Longmen Shan block is oriented at ∼45 degrees from the x-axis and is likely a result of the zero-slip displacement boundary condition applied on the block boundary.

Model T3: ¾ Himalayan range front convergence

In an effort to prevent right-lateral motion on the Kunlun fault we explore models where the convergence boundary condition is only applied on the western ¾ of the Himalayan range front. Model setup for T3 is similar to model T1 but the convergence condition is limited to points west of the Shilong Plateau. Internal microplate deformation (Figure 3.15) is highest where the convergence condition is applied. Model T3 velocities (Figure 3.15), while still primarily northward in direction, show more eastward extrusion than models T1 or T2 (where full Himalayan range front convergence is applied).

The slip rates predicted by model T3 on the Karakorum fault (Figure 3.16) are nearly identical to those predicted by models T1 and T2 and range from 4–12 mm/yr of right-lateral motion. Slip on the Haiyuan fault is ∼2 mm/yr of left-lateral motion everywhere on the structure.

Model T3 predicted slip rates on the Altyn Tagh fault (Figure 3.17) range from 2–13 mm/yr and are extremely similar to the slip rate profiles predicted by models T1 and T2.

Figure 3.15 *(following page)*: Slip rates, velocities, and principal stresses from DM model T3, with ¾ Himalayan range front convergence. In all figures microplate boundaries are shown as blue lines and the Indian sub-continent is shaded in gray. Panel a) shows fault slip rates with left-lateral rates shown as white text in blue circles and right-lateral text shown as blue text in white circles. For clarity, only representative slip rates are shown here. Color shading shows velocity magnitudes, where redder colors indicate faster velocities. Maximum velocities equal the differential motion between India and Eurasia. Here, the Altyn Tagh is the fastest left-lateral fault and the Karakorum is the fastest right-lateral fault. The Kunlun and Jiali faults switch from right-lateral to left-lateral along strike. Panel b) shows velocity vectors (white arrows) superimposed over the velocity magnitude field. Velocity azimuths are dominantly north-northeast, consistent with the imposed convergence boundary condition on the HRF. Panel c) shows the principal stresses. Principal stresses are largely convergent (compression) and are broadly consistent with the oblique direction of convergence.

Figure 3.15: (continued)

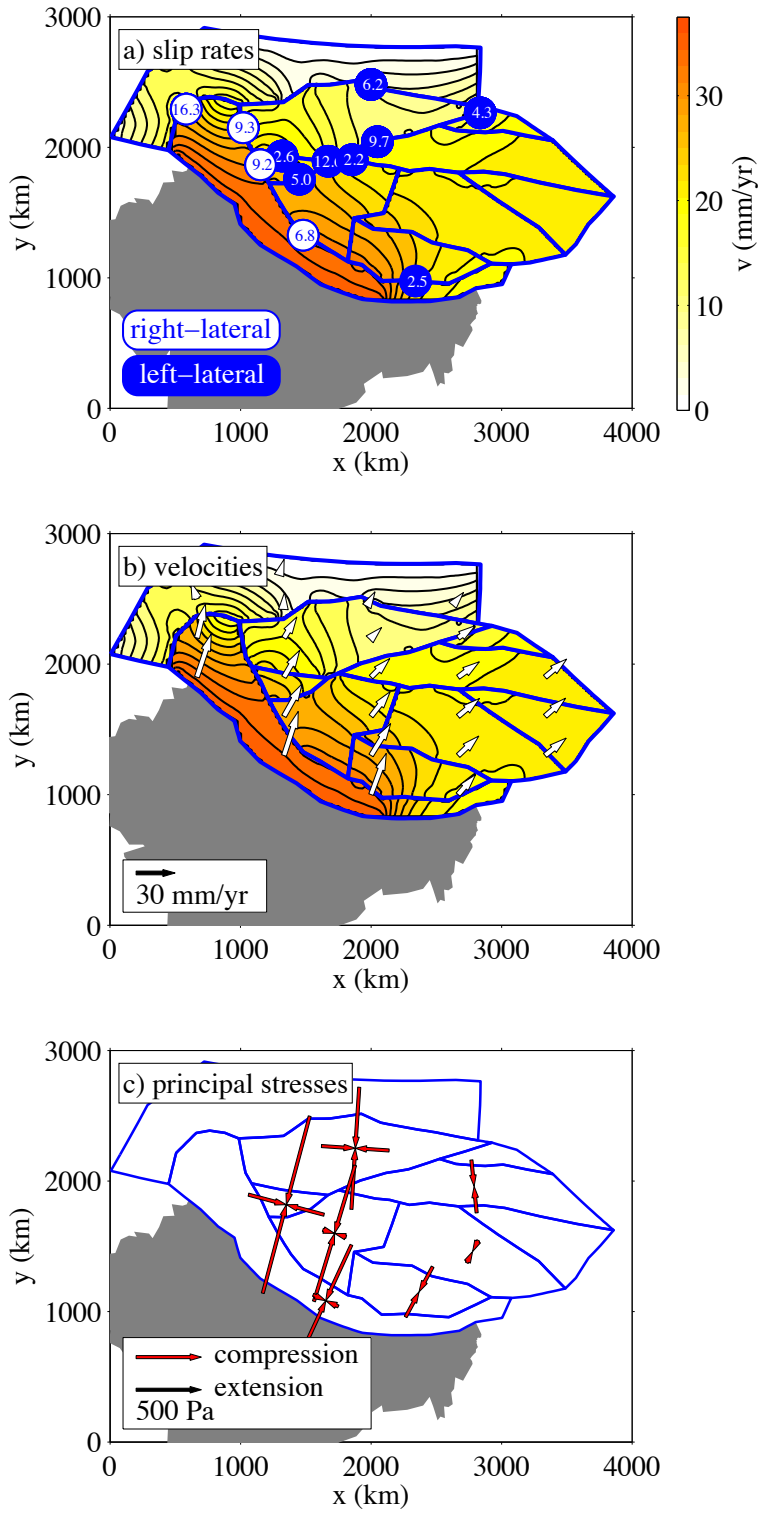

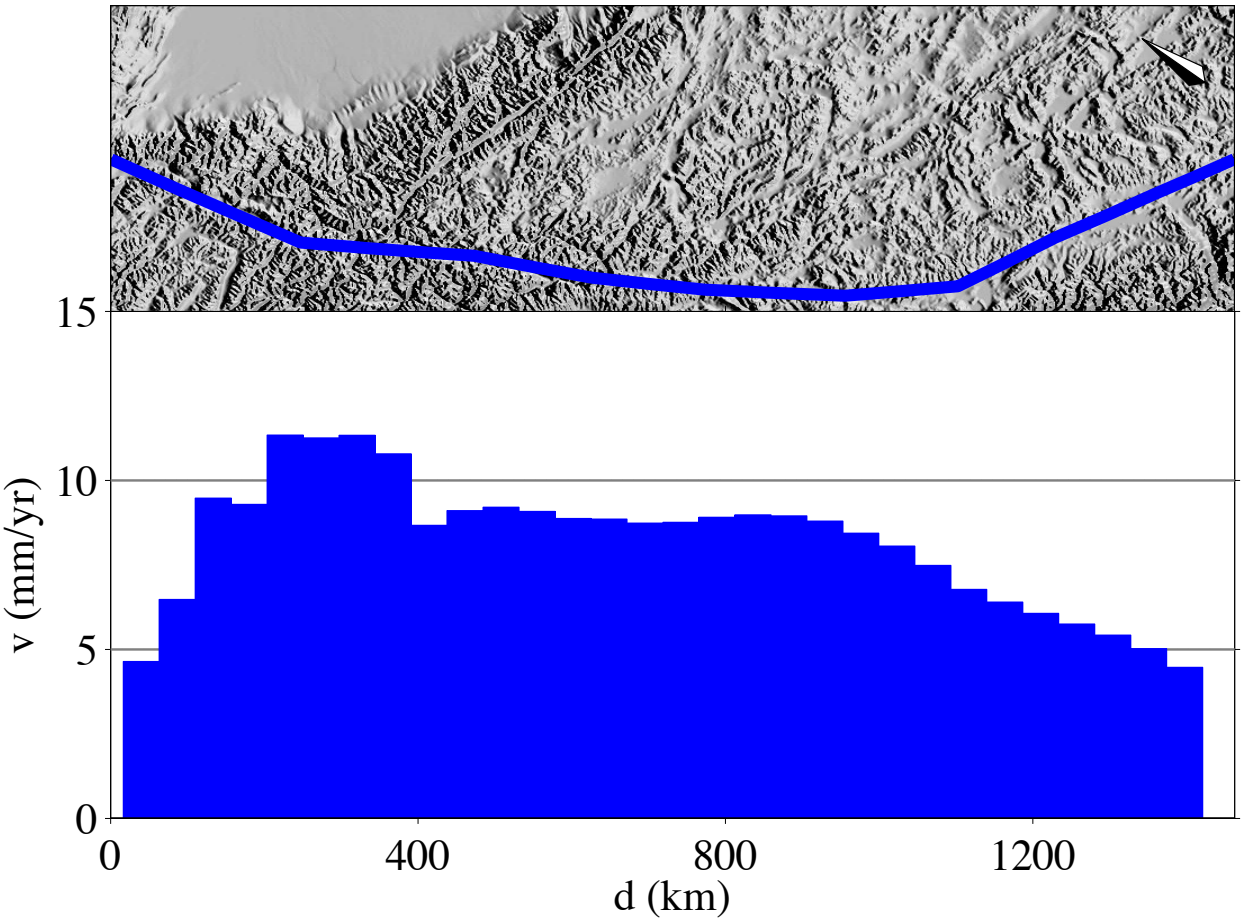

Figure 3.16: Along-strike slip variation for the Karakorum fault at the western boundary of the Tibetan Plateau predicted by DM model T3. The upper panel shows the rotated fault trace and topography within 200 km of the fault endpoints. The compass rose points north. Right-lateral slip rates predicted by model T3 are shown as blue fill and positive values. Slip is lowest (∼4 mm/yr) on the northern and southern ends of the fault and highest (∼12 mm/yr) just south of the intersection with the Altyn Tagh. The predicted slip rate holds steady at ∼8 mm/yr for the ∼500 km south of the intersection with the Altyn Tagh. The peak slip rate is slightly higher than geologic observations of 10.7 ± 0.7 mm/yr (Chevalier et al., 2005), while the northern and southern extremes of the fault are consistent with other geologic (4 ± 1 mm/yr, Brown et al., 2002) and InSAR (1 ± 3 mm/yr, Wright et al., 2004) estimates.

The maximum slip rate, as with models T1 and T2, occurs just east of the intersection with the Karakorum fault but is ∼2 mm/yr higher than in previous modeling approaches. Significantly, model T3 slip rates are slightly lower on the eastern portion of the fault (∼4 mm/yr) and, unlike models T1 and T2, are consistent with block model estimates of 3 ± 2 mm/yr on this portion of the fault.

Like models T1 and T2, the sense of slip on the Kunlun fault (Figure 3.18) changes along strike and does not accurately capture documented slip rates for the Kunlun. Maximum left-lateral slip rates occur in the west, with maximum slip rates of ∼4 mm/yr. Slip decreases along strike, becoming briefly right-lateral (< 0.5 mm/yr), and then is again left-lateral with a very low magnitude (∼1 mm/yr) rate. At ∼ 1000 km, slip becomes right-lateral (∼1 mm/yr) for the eastern 1000 km of the fault. As with models T1 and T2, these results are inconsistent with the well documented left-lateral slip ranging from 1.6–17.8 mm/yr (Kirby et al., 2007; Meade, 2007; Van der Woerd et al., 2002b) reported on this portion of the fault.

Unlike models T1 and T2, model T3 predicts entirely left-lateral slip on the Xianshuihe fault (Figure 3.19). While the sense of slip is consistent with block model and geologic estimates (Allen et al., 1991; He et al., 2006; Meade, 2007; Wang et al., 2009), model predictions of < 1 mm/yr everywhere along strike are lower than the geologic and geodetic estimates.

Model T3 predicts right-lateral motion on the Jiali fault (Figure 3.20) on the eastern and western end points of the fault (up to ∼1 mm/yr) but left-lateral slip (∼0–2 mm/yr) for the central ∼750 km of the fault. This change in the sense of slip on the fault is distinct from the results from models T1 and T2, which predicted entirely right-lateral slip on the fault, and is inconsistent with geologic and block model results (Armijo et al., 1989; Meade, 2007).

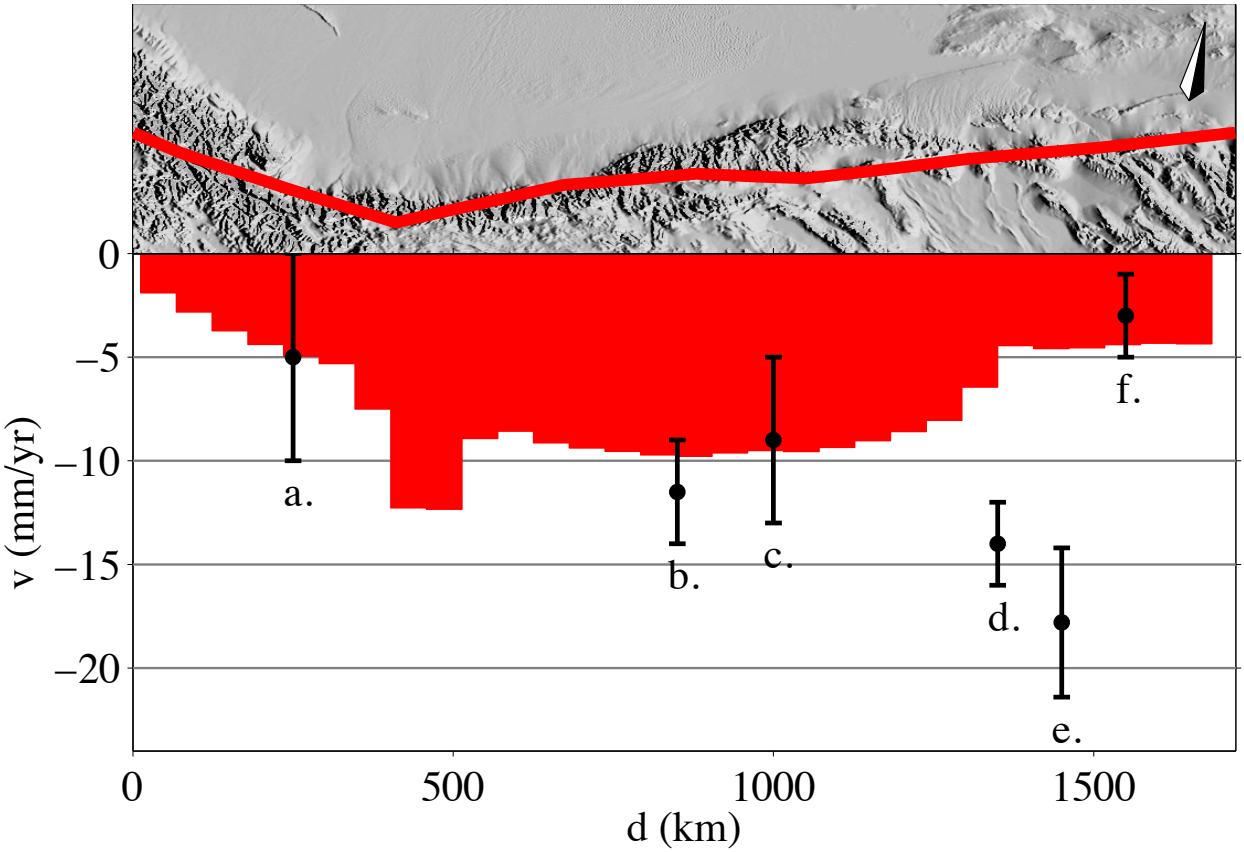

Figure 3.17: Slip rate variation predicted by DM model T3 along the Altyn Tagh-Karakash fault system at the northern boundary of the Tibetan plateau. The upper panel shows the rotated fault trace and topography within 200 km of the fault endpoints with the compass rose pointing north. Slip rates predicted by T3 are shown as the red fill in the lower panel with geologic and geodetic fault slip rate estimates shown as black circles with reported 1-sigma error bars. Negative numbers and red colors indicate left-lateral motion. Model T3 predicts peak slip rates on the central portion of the fault (up to ∼12 mm/yr). The slip rate reaches a minimum on the western extent of the fault (∼2 mm/yr) and is ∼4 mm/yr on the eastern tip. Slip rates inferred from geologic and geodetic data are from west to east: a. 5 ± 5 mm/yr, Wright et al. (2004), b. 11.5 ± 2.5 mm/yr, Cowgill et al. (2009), c. 9 ± 4 mm/yr, Wallace et al. (2004), d. 14 ± 2 mm/yr, Yue et al. (2001), e. 17.8 ± 3.6 mm/yr, Mériaux et al. (2005), and f. 3 ± 2 mm/yr, Meade (2007).

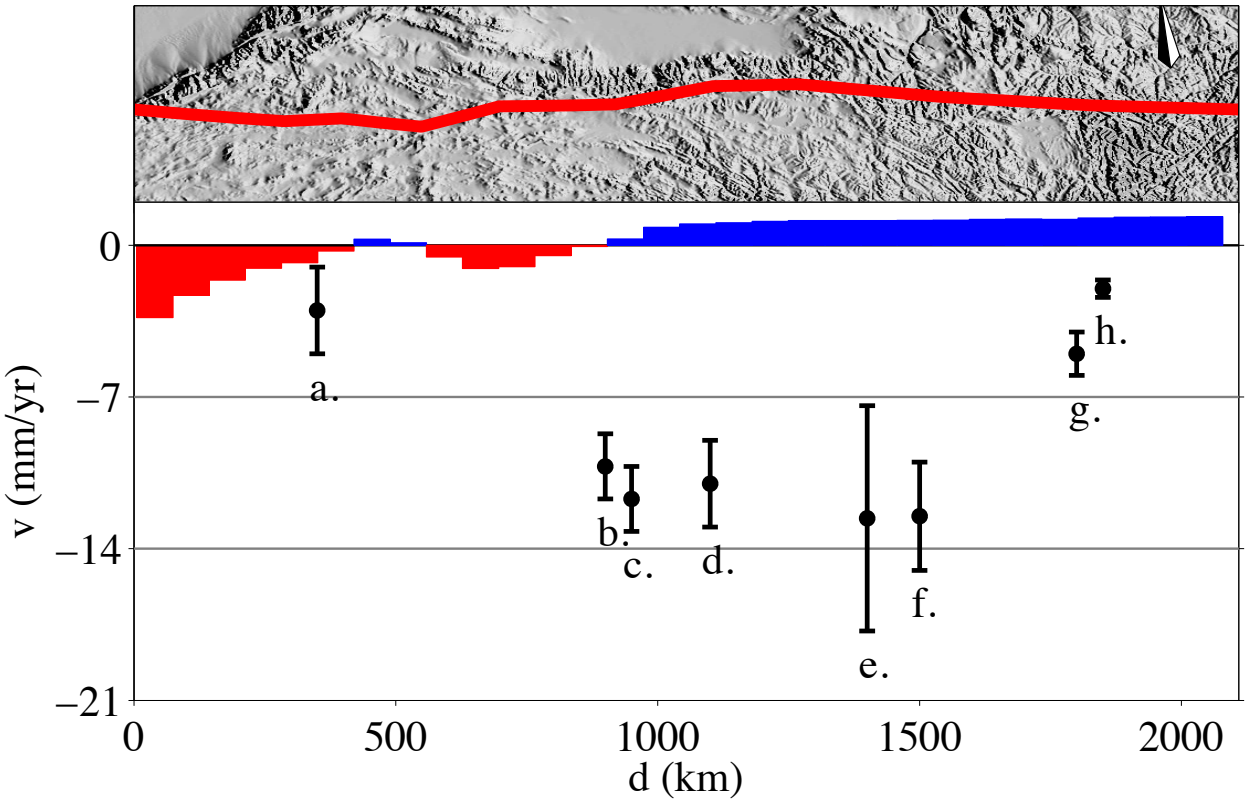

Figure 3.18: Slip rate variation predicted by DM model T3 along the east-west trending Kunlun fault system. The upper panel shows the rotated fault trace and topography within 200 km of the fault endpoints with the compass rose pointing north. Slip rates predicted by T3 are shown as the red and blue fill in the lower panel with geologic and geodetic fault slip rate estimates shown as black circles with reported 1-sigma error bars. Red colors and negative numbers indicate left-lateral motion, blue colors and positive numbers indicate right-lateral motion. The fault is left-lateral on the western portion of the fault (with a slip rate of ∼4 mm/yr) and then is very briefly right-lateral (the slip rate is very low magnitude and is <0.3 mm/yr). For the next ∼400 km the fault is again left-lateral (∼2 mm/yr) and then the sense of slip again becomes right-lateral for the last ∼1000 km along strike (∼1 mm/yr). These predictions are in poor agreement with well documented left-lateral slip on the fault (shown in black above). Slip rates inferred from geologic and geodetic data are from west to east: a. 3 ± 2 mm/yr, Bell et al. (2011), b. 10.2 ± 1.5 mm/yr, Hilley et al. (2005), c. 11.7 ± 1.5 mm/yr (at ∼94°E), Van der Woerd et al. (2002b), d. 11 ± 2 mm/yr, Meade (2007), e. 12.6 ± 5.2 mm/yr (at ∼99°E), Van der Woerd et al. (2002b), f. 12.5 ± 2.5 mm/yr (at ∼100.5°E), Van der Woerd et al. (2002b), g. 5 ± 1 mm/yr at (∼101.5°E), Kirby et al. (2007), and h. 2.0 ± 0.4 mm/yr (at ∼101.75°E), Kirby et al. (2007).

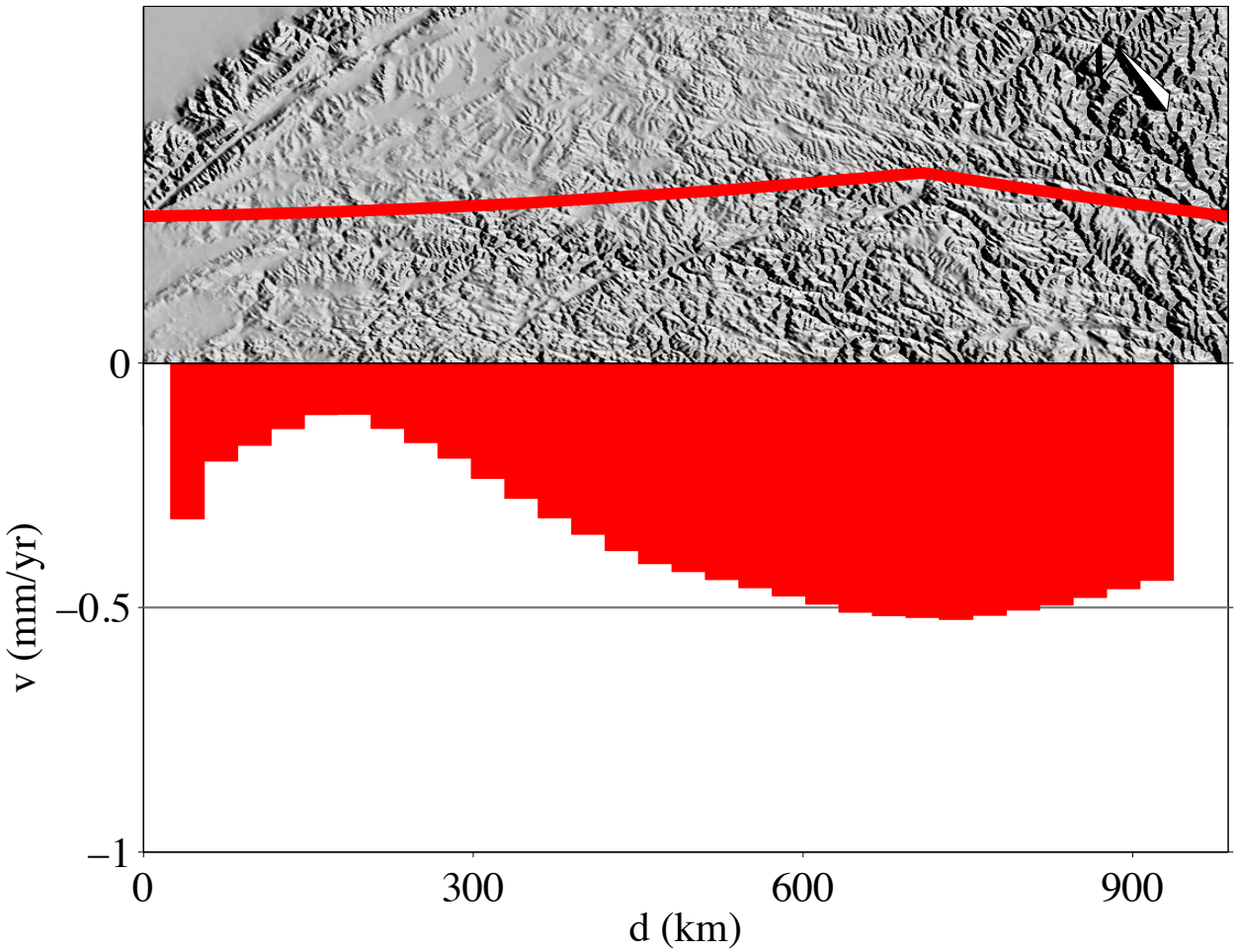

Figure 3.19: Slip rate variation predicted by DM model T3 along the Xianshuihe fault in eastern Tibet. The upper panel shows the rotated fault trace and topography within 200 km of the fault endpoints. The compass rose points north. Model T3 predicts an entirely left-lateral Xianshuihe fault, with maximum slip rates <1 mm/yr. These predictions are close to block models estimates of 3 ± 2 mm/yr on the eastern portion of the fault (Meade, 2007) but well below sinisteral slip estimates of ∼15 mm/yr from geology (Allen et al., 1991; He et al., 2006), 9-12 mm/yr from InSAR (Wang et al., 2009), and ∼20 mm/yr from geodetically constrained block models (Meade, 2007).

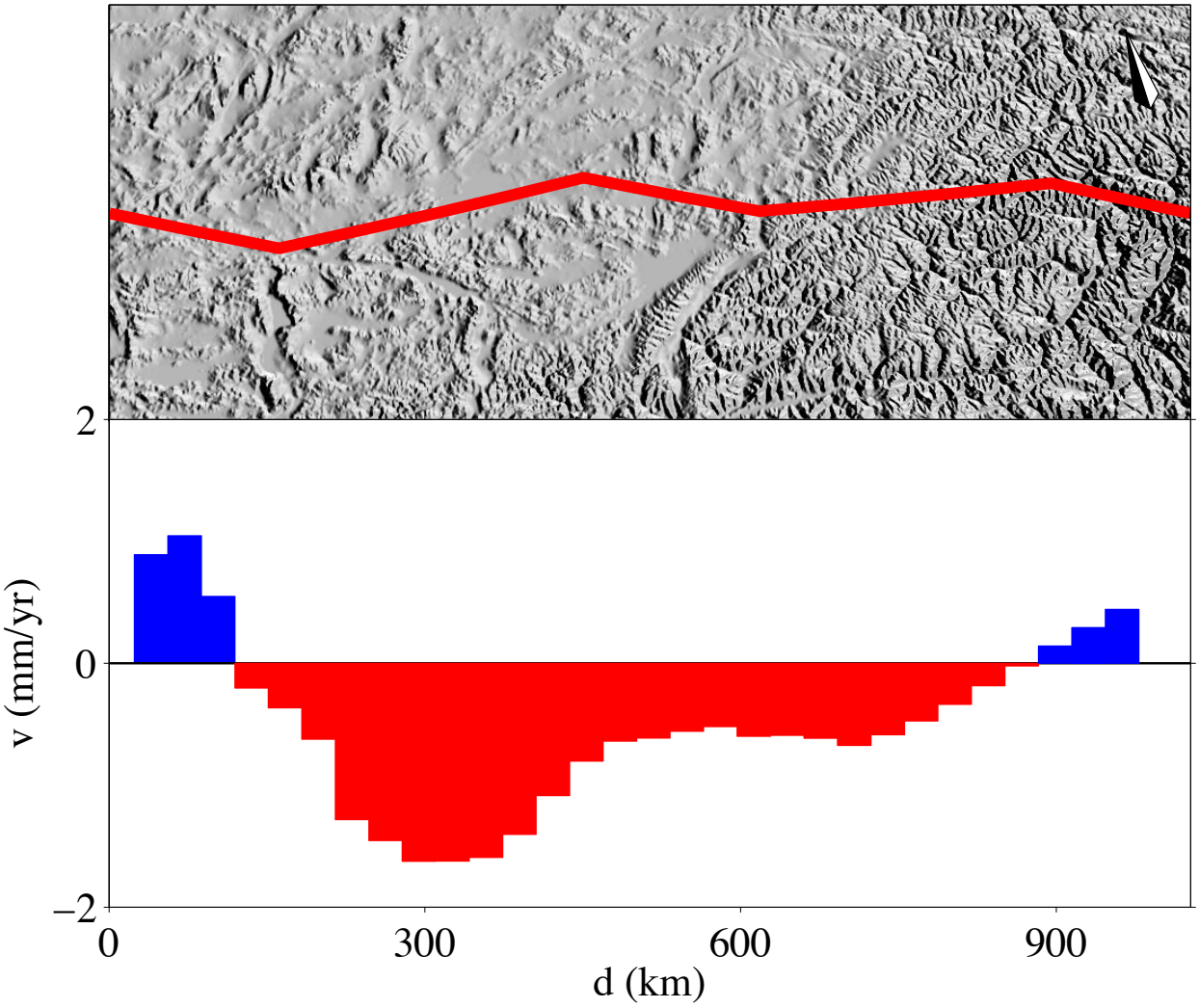

Figure 3.20: Along-strike slip rate variations predicted by DM model T3 for the Jiali fault in southeastern Tibet. The upper panel shows the rotated fault trace and topography within 200 km of the fault endpoints. The compass rose points north. Right-lateral slip rates are plotted as blue fill and positive values while left-lateral slip rates are plotted as red fill and negative values. Model T3 predicts right-lateral slip for ∼100 km (∼1 mm/yr) and then left-lateral slip for the central ∼800 km of fault (reaching ∼2 mm/yr). The sense of slip reverses again to right-lateral for the eastern ∼100 km along strike (<1 mm/yr). Geologic and geodetic data suggest a right-lateral structure, and geologic estimates range from 10-20 mm/yr (Armijo et al., 1989), while block models estimate 3-4 mm/yr of dexteral motion (Meade, 2007).

Internal microplate principal stress axes for model T3 (Figure 3.15) are very similar to those for model T1, however the stress magnitudes in the eastern portion of the model are smaller (in this area the largest principal stress is often <100 Pa). Smaller stresses in the eastern microplates are likely a result of the ¾ convergence boundary on the Himalayan range front.

Model T4: ¾ Himalayan range front convergence and fixed Longmen Shan

In an effort to force eastern extrusion of the Tibetan plateau, we combine the ¾ convergence condition on the Himalayan range front with the zero-slip condition on the Longmen Shan block applied in model T2. Internal microplate deformation is highest along the Himalayan range front where the convergence boundary is applied (Figure 3.21), but the zero-slip displacement condition on the Longmen Shan block results in very small displacements in the eastern microplates, which is inconsistent with Tibetan crustal extrusion.

Slip rates on the Karakorum (Figure 3.22) and Altyn Tagh (Figure 3.23) faults remain robust to any changes in boundary conditions and are nearly identical to all previous models discussed (and particularly to model T3). The slip rate varies from 3–12 mm/yr of dexteral slip on the Karakorum and 1–12 mm/yr of sinisteral motion on the Altyn Tagh. The slip rate on the Haiyuan ranges from 2–5 mm/yr of left-lateral motion along strike (Table 3.1).

The predicted slip rates for the Kunlun fault (Figure 3.24) are similar to the other models discussed: the slip rate is left-lateral (∼3 mm/yr) on the western Manyi splay of the fault, becomes briefly right-lateral (<0.5 mm/yr), and then returns to left-lateral motion for ∼500 km on the central portion of the fault. At ∼1000 km the fault becomes right-lateral for the eastern ∼1000 km along strike. The fixed Longmen Shan condition appears to augment this

Figure 3.21 *(following page)*: Slip rates, velocities, and principal stresses from DM model T4, with ¾ Himalayan range front convergence and a fixed Longmen Shan. In all figures microplate boundaries are shown as blue lines and the Indian sub-continent is shaded in gray. Panel a) shows fault slip rates with left-lateral rates shown as white text in blue circles and right-lateral text shown as blue text in white circles. For clarity, only representative slip rates are shown here. Color shading shows velocity magnitudes, where redder colors indicate faster velocities. Maximum velocities equal the differential motion between India and Eurasia. Here the Altyn Tagh is the fastest left-lateral fault and the Karakorum is the fastest right-lateral fault. The Kunlun and Jiali faults switch from right-lateral to left-lateral along strike. Panel b) shows velocity vectors (white arrows) superimposed over the velocity magnitude field. Velocity azimuths are dominantly north-northeast, consistent with the imposed convergence boundary condition on the HRF. Panel c) shows the principal stresses. Principal stresses are largely convergent (compression) and are broadly consistent with the oblique direction of convergence. Microplates in the eastern portion of the model have slightly rotated principal stress axes, consistent with the zero-slip boundary condition on the Longmen Shan block.

Figure 3.21: (continued)

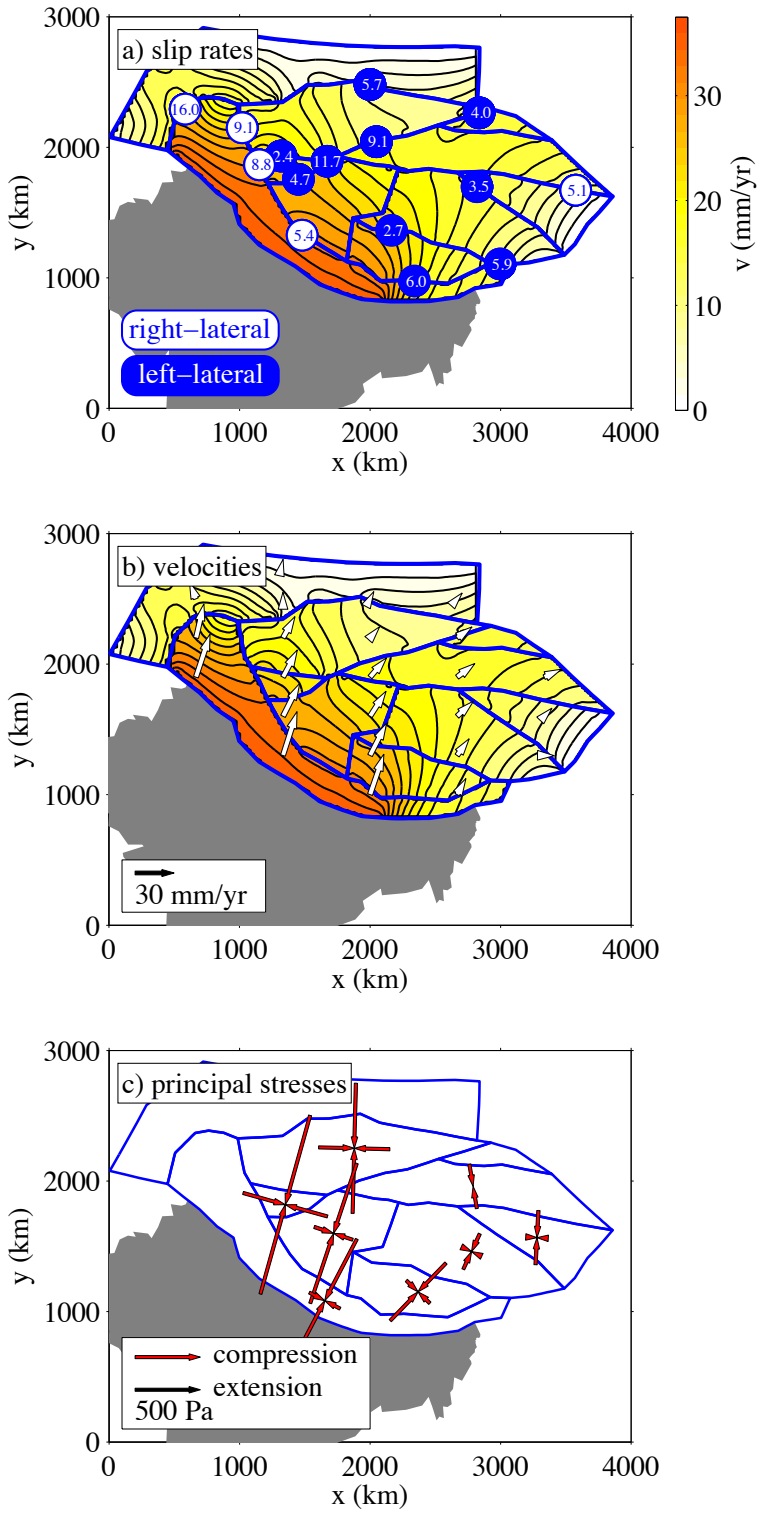

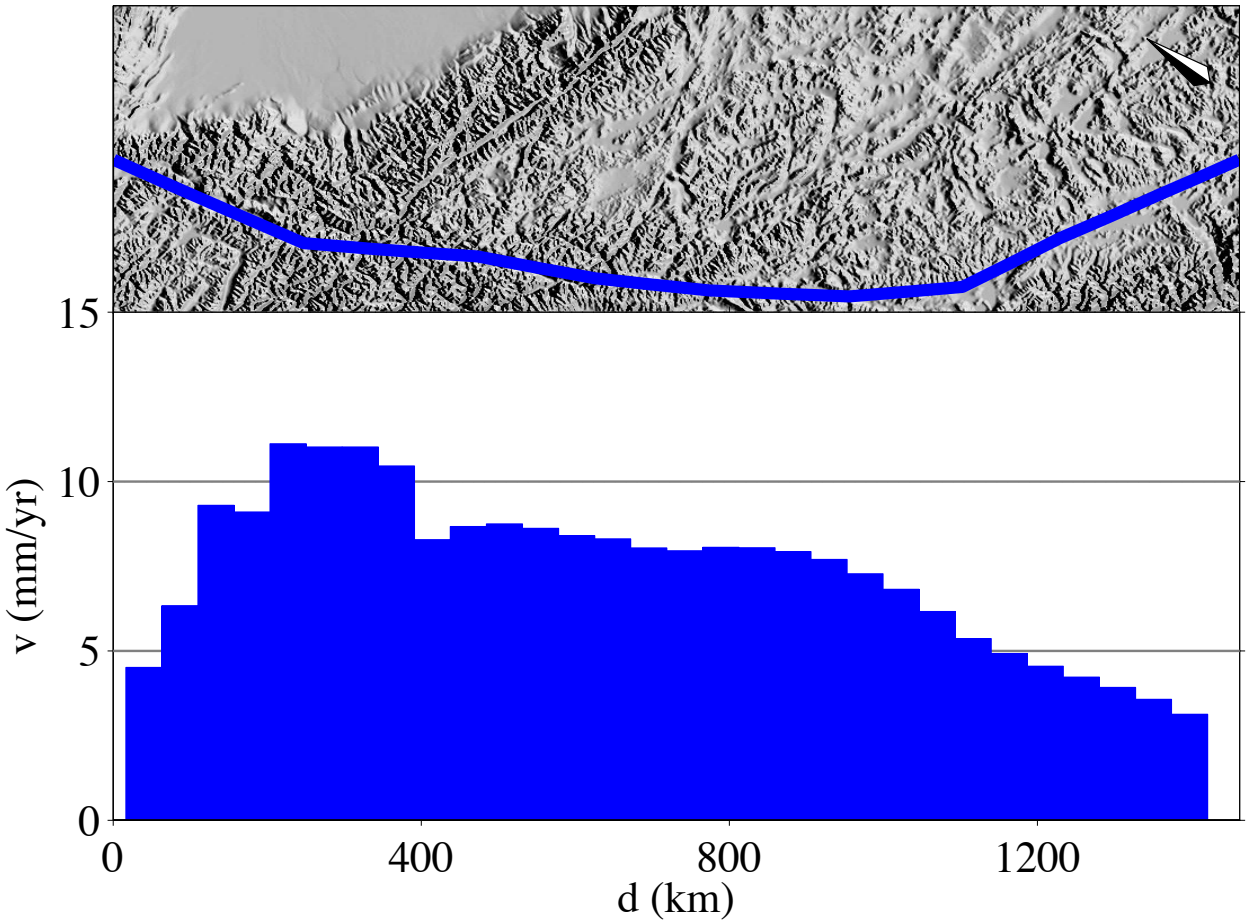

Figure 3.22: Along-strike slip variation for the Karakorum fault at the western boundary of the Tibetan Plateau predicted by DM model T4. The upper panel shows the rotated fault trace and topography within 200 km of the fault endpoints. The compass rose points north. Right-lateral slip rates predicted by model T4 are shown as blue fill and positive values. Slip is lowest (∼3 mm/yr) on the southern end of the fault and highest (∼12 mm/yr) just south of the intersection with the Altyn Tagh. The predicted slip rate holds steady at ∼7-8 mm/yr for the ∼500 km south of the intersection with the Altyn Tagh. The peak slip rate is slightly higher than geologic observations of 10.7 ± 0.7 mm/yr (Chevalier et al., 2005) while the northern and southern extremes of the fault are consistant with other geologic (4 ± 1 mm/yr, Brown et al., 2002) and InSAR (1 ± 3 mm/yr, Wright et al., 2004) estimates.

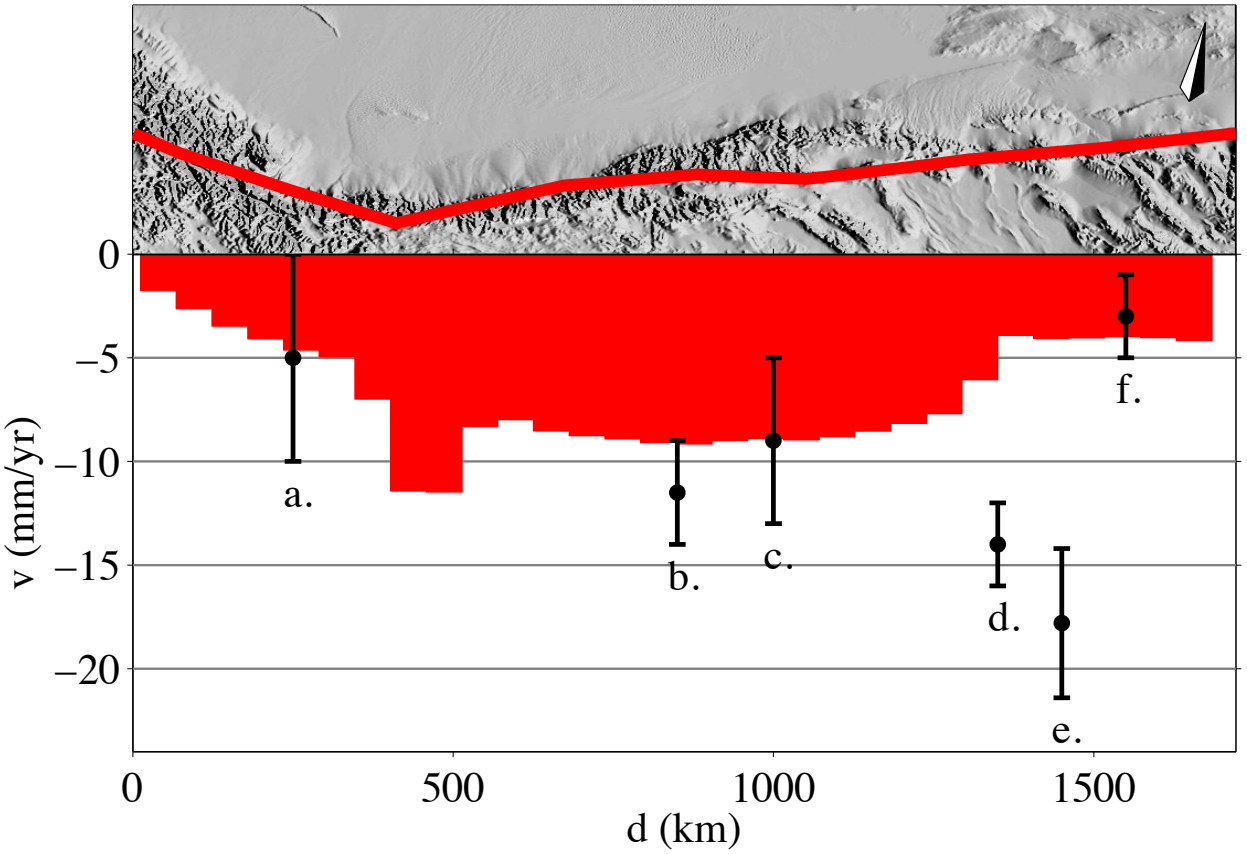

Figure 3.23: Slip rate variation predicted by DM model T4 along the Altyn Tagh-Karakash fault system at the northern boundary of the Tibetan plateau. The upper panel shows the rotated fault trace and topography within 200 km of the fault endpoints with the compass rose pointing north. Slip rates predicted by T4 are shown as the red fill in the lower panel with geologic and geodetic fault slip rate estimates shown as black circles with reported 1-sigma error bars. Negative numbers and red colors indicate left-lateral motion. Model T4 predicts peak slip rates on the central portion of the fault (up to ∼12 mm/yr). The slip rate reaches a minimum on the western extent of the fault (∼1 mm/yr) and is ∼4 mm/yr on the eastern tip. Slip rates inferred from geologic and geodetic data are from west to east: a. 5 ± 5 mm/yr, Wright et al. (2004), b. 11.5 ± 2.5 mm/yr, Cowgill et al. (2009), c. 9 ± 4 mm/yr, Wallace et al. (2004), d. 14 ± 2 mm/yr, Yue et al. (2001), e. 17.8 ± 3.6 mm/yr, Mériaux et al. (2005), and f. 3 ± 2 mm/yr, Meade (2007).

behavior: where in model T3 right-lateral motion reached only 1 mm/yr, model T4 predicts 8 mm/yr of dexteral motion at the far east of the fault. These predictions are inconsistent with the geologic and geodetic sampling of the fault (Kirby et al., 2007; Meade, 2007; Van der Woerd et al., 2002b) and we do not consider model T4 to be an accurate predictor of Tibetan fault slip rates.

Model T4 predicts entirely left-lateral slip on the Xianshuihe fault (Figure 3.25). Slip rates are lowest on the western portion of the fault (∼2 mm/yr) and increase along strike to the east, reaching ∼8 mm/yr at the western fault tip. These predictions are higher than block model estimates of ∼ 3 mm/yr sinisteral slip on the eastern portion of the fault (Meade, 2007) and are below the geologic (∼15 mm/yr; Allen et al., 1991), InSAR (9–12 mm/yr; Wang et al., 2009), and western block model (∼20 mm/yr; Meade, 2007) measurements.

Like the Kunlun fault, model T4 predicts an along-strike reversal in the sense of slip on the Jiali fault (Figure 3.26). The Jiali fault, which geologic and geodetic sampling indicates is right-lateral (Armijo et al., 1989; Meade, 2007), is only predicted by model T4 to be right-lateral for the first ∼100 km (with a slip rate of ∼1 mm/yr). The remainder of the fault is left-lateral, and slip rates reach ∼3 mm/yr.

Internal microplate principal stress axes are dominated by contraction in all but the Haiyuan block (Figure 3.21) and are larger in magnitude than in model T3 (in all blocks but the Haiyuan block the largest principal stress is >150 Pa). Unlike model T2, where principal stress orientations in the Longmen Shan block were oriented ∼45 degrees from the x-axis, the principal stress axes in the Longmen Shan microplate for model T4 approximately align with the x-y plane. This orientation is likely a result of the ¾ condition on the Himalayan range

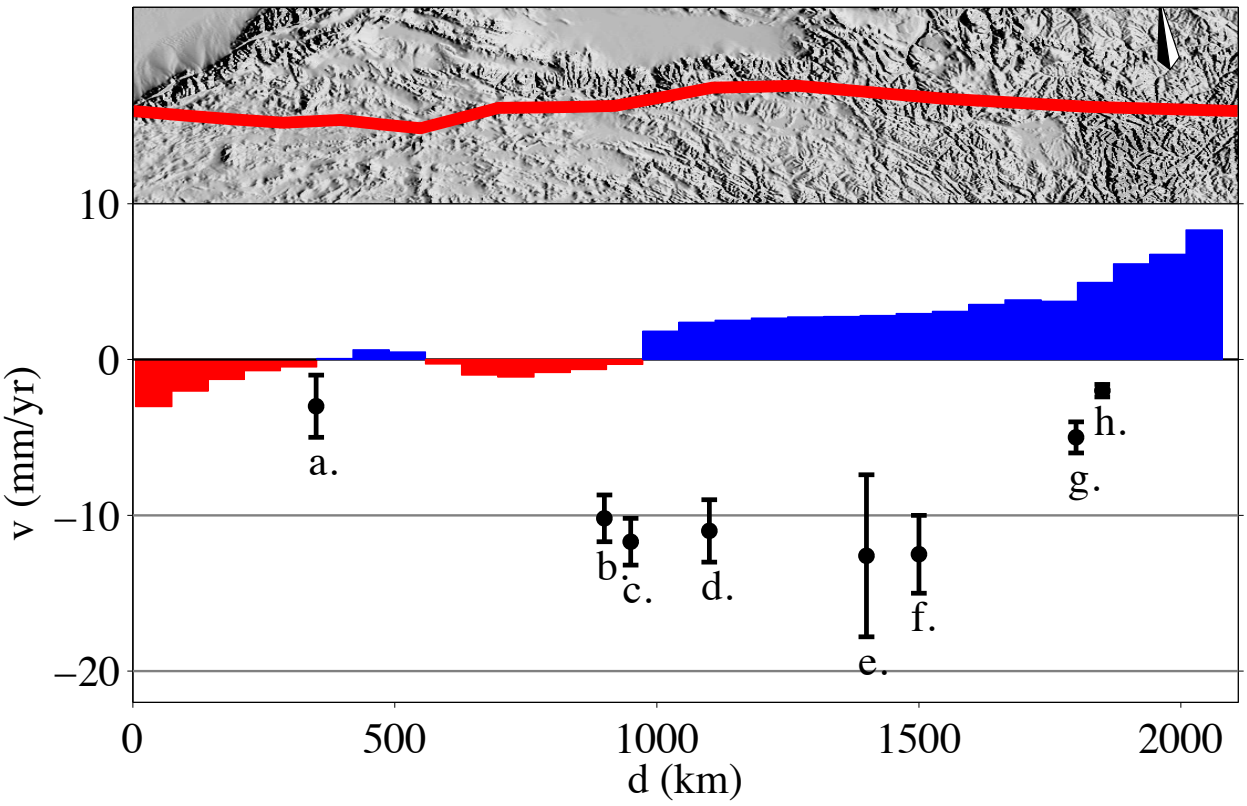

Figure 3.24: Slip rate variation predicted by DM model T4 along the east-west trending Kunlun fault system. The upper panel shows the rotated fault trace and topography within 200 km of the fault endpoints with the compass rose pointing north. Slip rates predicted by T4 are shown as the red and blue fill in the lower panel with geologic and geodetic fault slip rate estimates shown as black circles with reported 1-sigma error bars. Red colors and negative numbers indicate left-lateral motion, blue colors and positive numbers indicate right-lateral motion. The fault is left-lateral on the western portion of the fault (with a slip rate of ∼3 mm/yr) and then is very briefly right-lateral (the slip rate is very low magnitude and is <1 mm/yr). For the next ∼400 km the fault is again left-lateral (∼2 mm/yr) and then the sense of slip again becomes right-lateral for the last ∼1000 km along strike. The zero-slip condition on the Longmen Shan block appears to magnify right-lateral slip on the eastern portion of the fault: here dexteral slip rates reach ∼8 mm/yr. These predictions are in poor agreement with well documented left-lateral slip on the fault (shown in black above). Slip rates inferred from geologic and geodetic data are from west to east: a. 3 ± 2 mm/yr, Bell et al. (2011), b. 10.2 ± 1.5 mm/yr, Hilley et al. (2005), c. 11.7 ± 1.5 mm/yr (at ∼94°E), Van der Woerd et al. (2002b), d. 11 ± 2 mm/yr, Meade (2007), e. 12.6 ± 5.2 mm/yr (at ∼99°E), Van der Woerd et al. (2002b), f. 12.5 ± 2.5 mm/yr (at ∼100.5°E), Van der Woerd et al. (2002b), g. 5 ± 1 mm/yr at (∼101.5°E), Kirby et al. (2007), and h. 2.0 ± 0.4 mm/yr (at ∼101.75°E), Kirby et al. (2007).

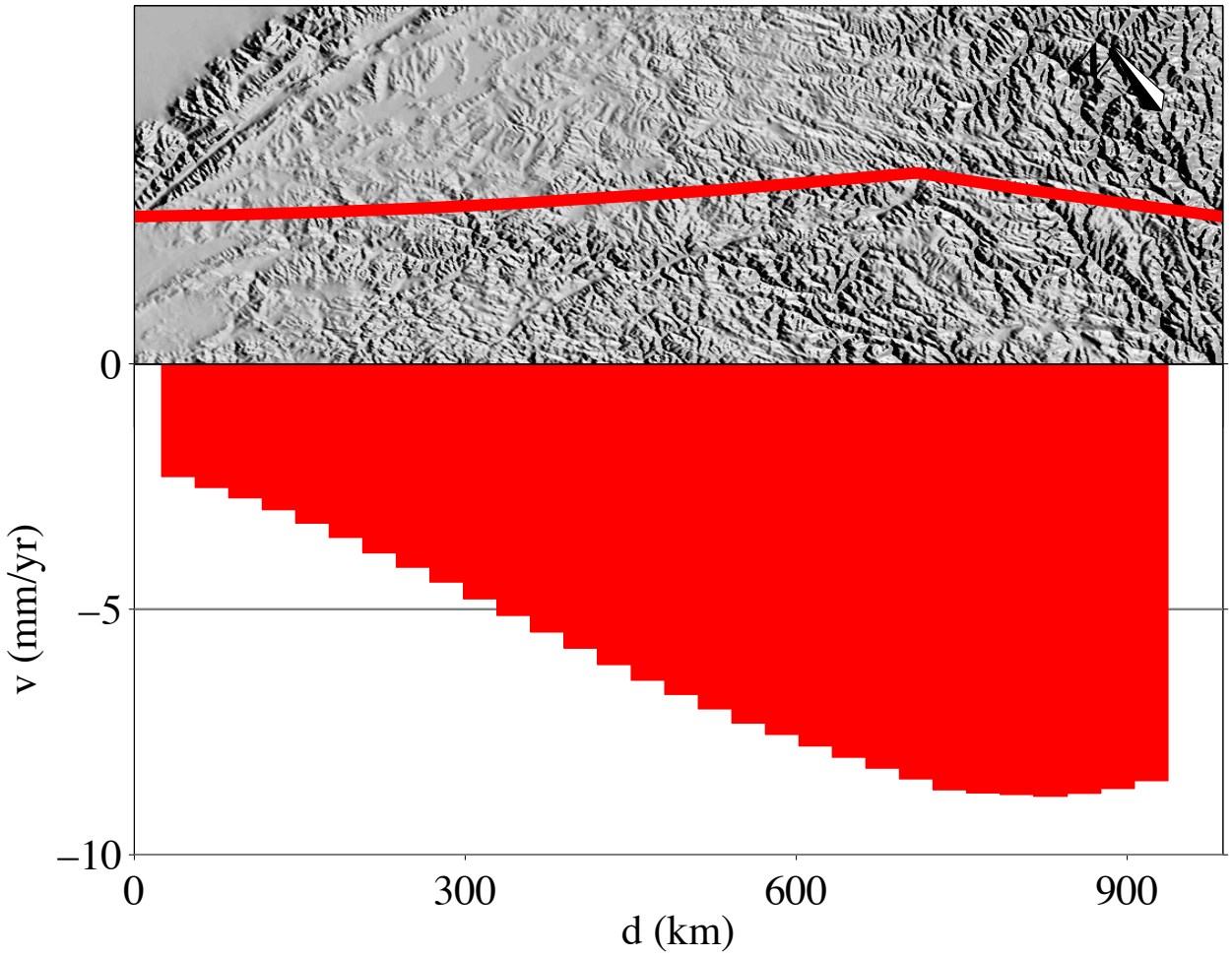

Figure 3.25: Slip rate variation predicted by DM model T4 along the Xianshuihe fault in eastern Tibet. The upper panel shows the rotated fault trace and topography within 200 km of the fault endpoints. The compass rose points north. Model T4 predicts an entirely left-lateral Xianshuihe fault, with slip rates increasing form west (∼2 mm/yr) to east (∼8 mm/yr). These predictions are higher than block models estimates of 3 ± 2 mm/yr on the eastern portion of the fault (Meade, 2007) and below estimates of ∼15 mm/yr from geology (Allen et al., 1991; He et al., 2006), 9-12 mm/yr from InSAR (Wang et al., 2009), and ∼20 mm/yr from geodetically constrained block models (Meade, 2007).

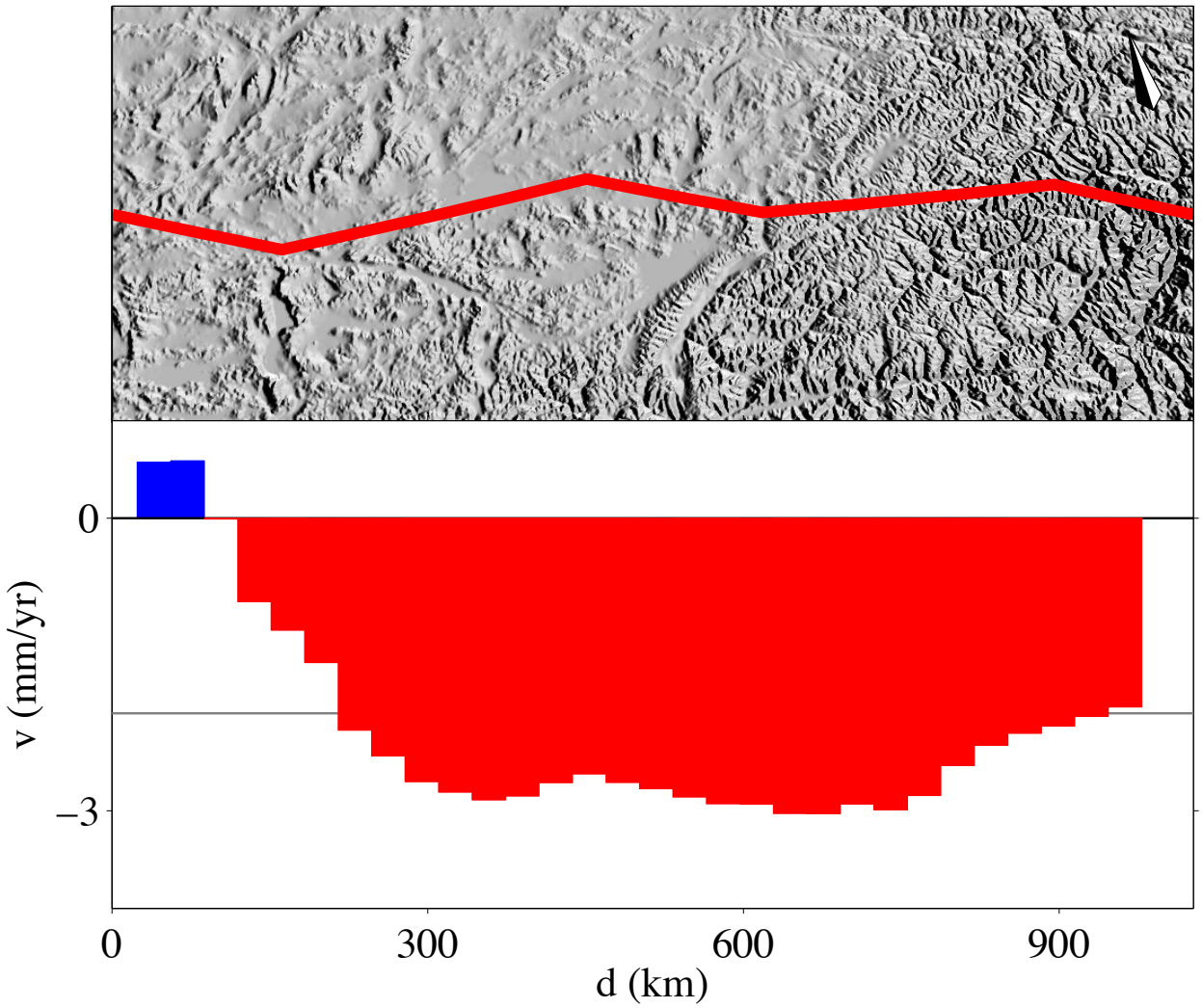

Figure 3.26: Along-strike slip rate variations predicted by DM model T4 for the Jiali fault in southeastern Tibet. The upper panel shows the rotated fault trace and topography within 200 km of the fault endpoints. The compass rose points north. Right-lateral slip rates are plotted as blue fill and positive values while left-lateral slip rates are plotted as red fill and negative values. Model T4 predicts an almost completely left-lateral Jiali (up to ∼3 mm/yr) with right-lateral displacements only on the western <100 km (1 mm/yr). Geologic and geodetic data suggest a right-lateral structure, and geologic estimates range from 10-20 mm/yr (Armijo et al., 1989), while block models estimate 3-4 mm/yr of dexteral motion (Meade, 2007).

front, which places the Longmen Shan block further from the convergent boundary. Thus, the zero-slip condition on the edge of the Longmen Shan block poses a greater influence on the internal microplate principal stress.

Model T5: Full Himalayan range front convergence and southeast Asia force boundary condition

Models T1 to T4 have shown the failure of Dirichlet (displacement) boundary conditions to predict left-lateral slip rates on the Kunlun fault and the southeastern extrusion of Tibetan crustal material. Model T5 combines the full Himalayan front convergence condition with a 1500 N/m southeast-directed force condition on the southeast Asia boundary (Figure 3.2). Internal microplate deformation for model T5 (Figure 3.27) is highest where boundary conditions are applied on the Himalayan range front and in the Longmen Shan block, just north of the force boundary condition. Displacement in the eastern portion of the model is higher than in previous models discussed but is oriented to the northeast and does not match the southeastern extrusion observed (Meade, 2007).

Model T5 predicted slip rates on the Karakorum (Figure 3.28) and Altyn Tagh (Figure 3.29) faults are very similar to the predictions from models T1 to T4. The Karakorum slip rates range from 4–12 mm/yr of right-lateral slip along strike and the Altyn Tagh predictions range from 1–12 mm/yr of left-lateral slip. Like models T1 and T2, the slip rate on the eastern portion of the Altyn Tagh is $\sim$7 mm/yr and exceeds the 3 ± 2 mm/yr estimate from Meade (2007). The Haiyuan slip rate prediction is relatively stable along strike: 1–2 mm/yr of left-lateral slip.

Model T5 predictions for the Kunlun fault (Figure 3.30) are very different from those of

Figure 3.27 *(following page)*: Slip rates, velocities, and principal stresses from DM model T5. In all figures microplate boundaries are shown as blue lines and the Indian sub-continent is shaded in gray. Panel a) shows fault slip rates with left-lateral rates shown as white text in blue circles and right-lateral text shown as blue text in white circiles. For clarity, only representative slip rates are shown here. Color shading shows velocity magnitudes, where redder colors indicate faster velocities. Maximum velocities equal the differential motion between India and Eurasia. Here the Altyn Tagh is the fastest left-lateral fault and the Karakorum is the fastest right-lateral fault. The Kunlun switches from right-lateral to left-lateral from west to east along strike. Panel b) shows velocity vectors (white arrows) superimposed over the velocity magnitude field. Velocity azimuths are dominantly north-northeast, consistent with the imposed convergence boundary condition on the HRF. Panel c) shows the principal stresses. Principal stresses are dominantly convergent (compression) and are broadly consistent with the direction of convergence.

Figure 3.27: (continued)

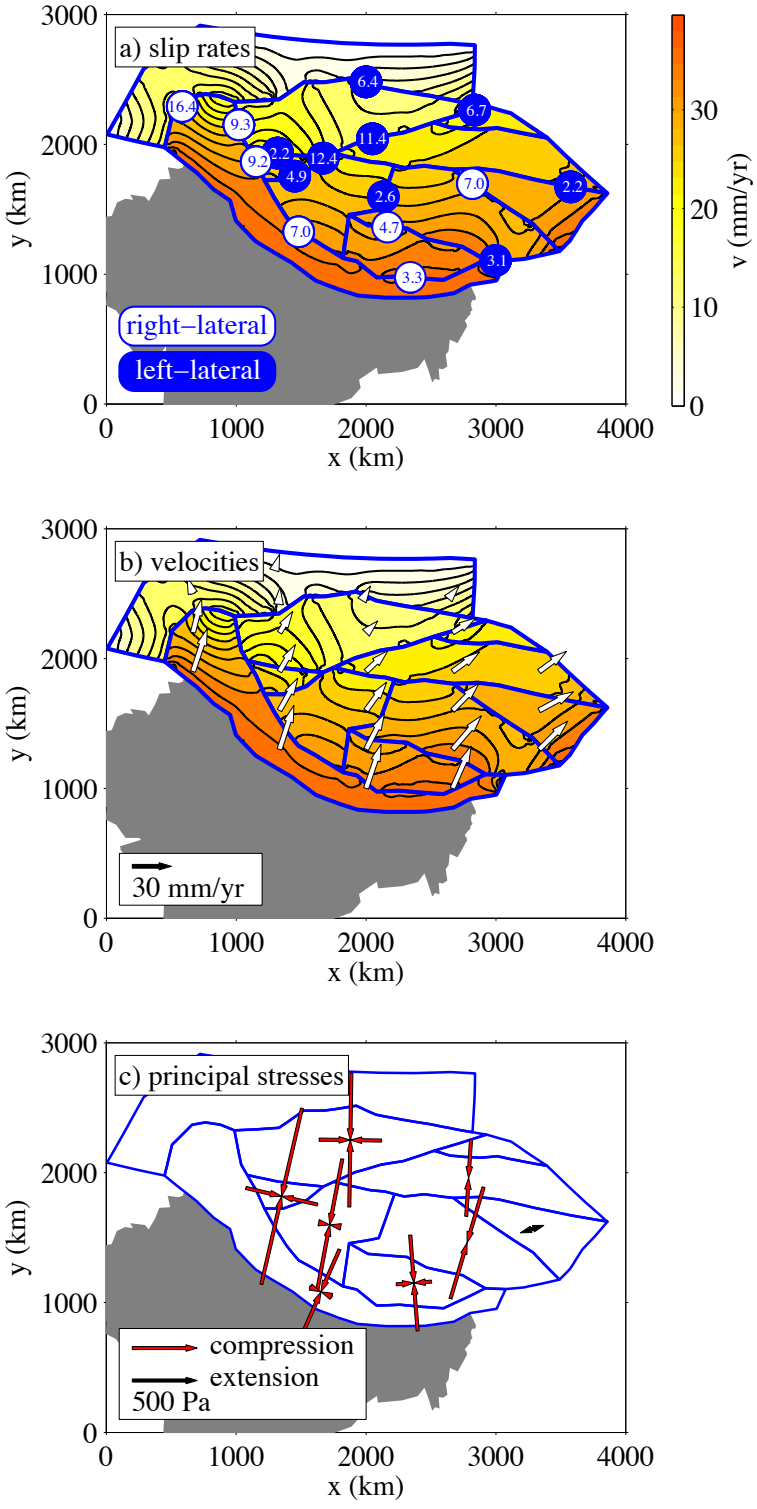

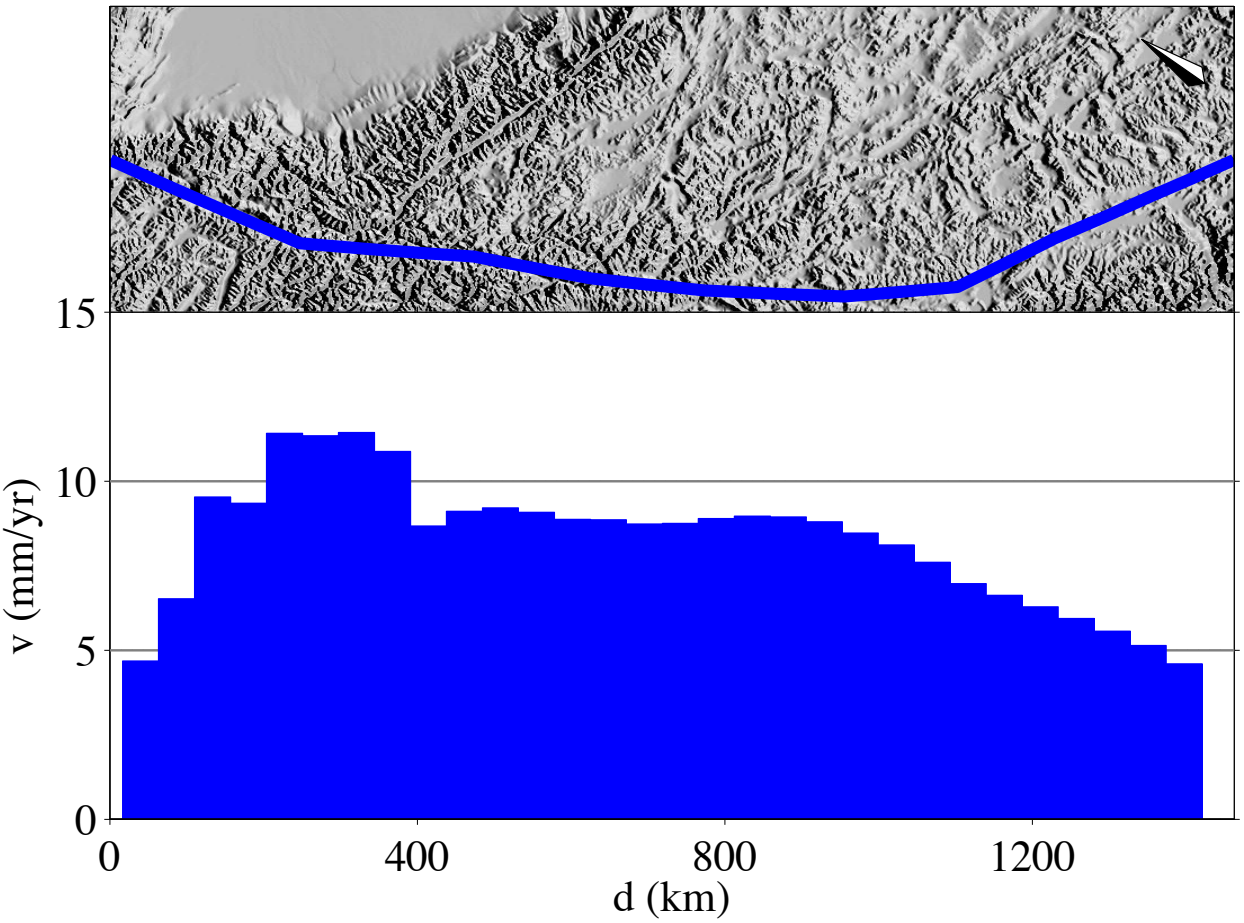

Figure 3.28: Along-strike slip variation for the Karakorum fault at the western boundary of the Tibetan Plateau predicted by DM model T5. The upper panel shows the rotated fault trace and topography within 200 km of the fault endpoints. The compass rose points north. Right-lateral slip rates predicted by model T5 are shown as blue fill and positive values. Slip is lowest (∼4 mm/yr) on the northern and southern ends of the fault and highest (∼12 mm/yr) just south of the intersection with the Altyn Tagh. The predicted slip rate holds steady at ∼8 mm/yr for the ∼500 km south of the intersection with the Altyn Tagh. The peak slip rate is slightly higher than geologic observations of 10.7 ± 0.7 mm/yr (Chevalier et al., 2005) while the northern and southern extremes of the fault are consistant with other geologic (4 ± 1 mm/yr, Brown et al., 2002) and InSAR (1 ± 3 mm/yr, Wright et al., 2004) estimates.

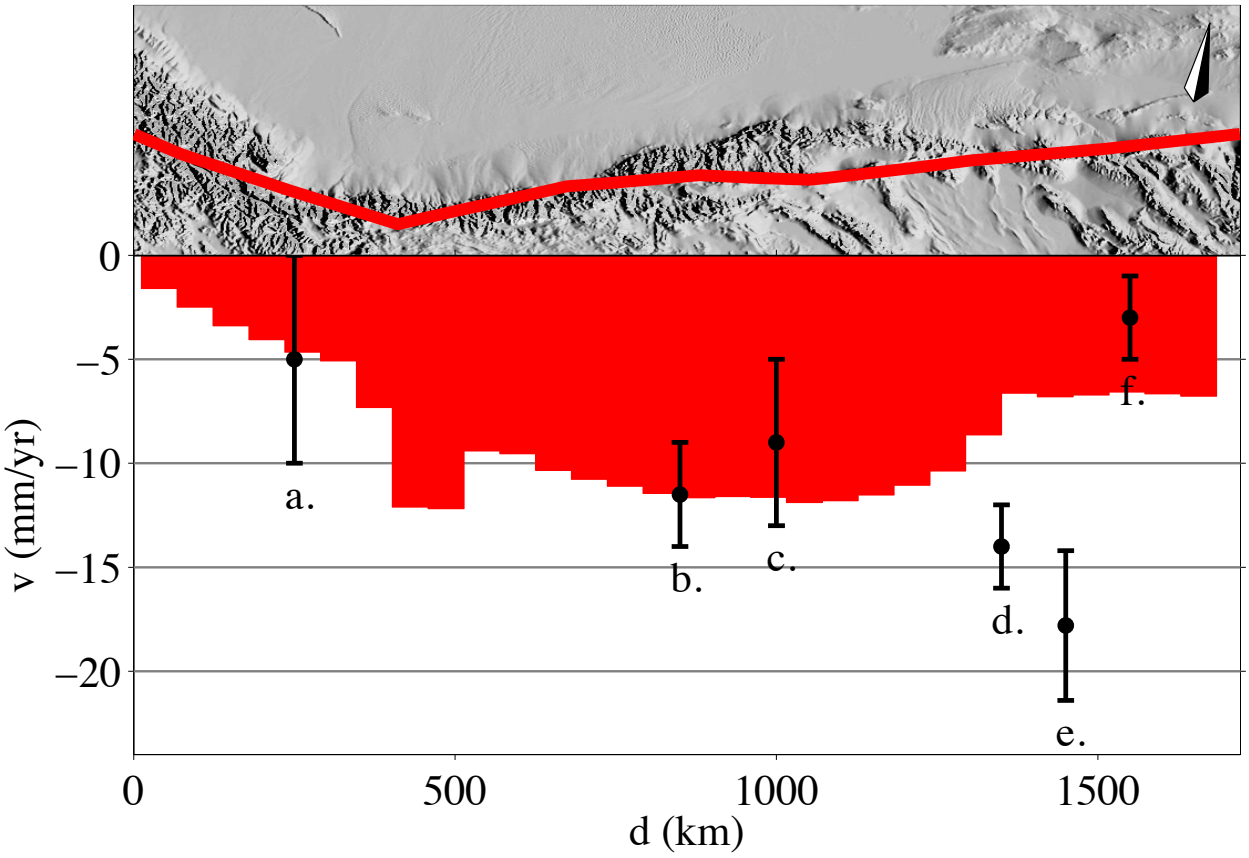

Figure 3.29: Slip rate variation predicted by DM model T5 along the Altyn Tagh-Karakash fault system at the northern boundary of the Tibetan plateau. The upper panel shows the rotated fault trace and topography within 200 km of the fault endpoints with the compass rose pointing north. Slip rates predicted by T5 are shown as the red fill in the lower panel with geologic and geodetic fault slip rate estimates shown as black circles with reported 1-sigma error bars. Negative numbers and red colors indicate left-lateral motion. Model T5 predicts peak slip rates on the central portion of the fault (up to ∼12 mm/yr). The slip rate reaches a minimum on the western extent of the fault (∼1 mm/yr) and is ∼7 mm/yr on the eastern tip. Slip rates inferred from geologic and geodetic data are from west to east: a. 5 ± 5 mm/yr, Wright et al. (2004), b. 11.5 ± 2.5 mm/yr, Cowgill et al. (2009), c. 9 ± 4 mm/yr, Wallace et al. (2004), d. 14 ± 2 mm/yr, Yue et al. (2001), e. 17.8 ± 3.6 mm/yr, Mériaux et al. (2005), and f. 3 ± 2 mm/yr, Meade (2007).

previous models but still fail to predict a fully left-lateral fault. Like previous models, the sense of slip varies along strike: left-lateral at ∼2 mm/yr for the western ∼250 km, right-lateral up to ∼2 mm/yr for ∼750 km, and then left-lateral again (up to ∼3 mm/yr) for the eastern ∼1000 km along strike. The majority of geologic and geodetic slip rate estimates are inconsistent with this data (Kirby et al., 2007; Meade, 2007; Van der Woerd et al., 2002b), but model predictions fall within the range of the easternmost predictions from Kirby et al. (2007) of 2.0 ± 0.4 mm/yr.

Slip rates along strike for the Xianshuihe fault (Figure 3.31) are right-lateral and range from 4–13 mm/yr. The rate increases from west to east along strike. These right-lateral slip rates are in contrast to geologically and geodetically documented left-lateral slip on this fault (Allen et al., 1991; He et al., 2006; Meade, 2007; Wang et al., 2009). Model T5 also predicts entirely right-lateral slip on the Jiali fault (Figure 3.32). Here the slip rate is lowest in the west (∼2 mm/yr) and increases to a maximum of 9 mm/yr on the central portion of the fault before falling off to ∼7 mm/yr in the east. The predicted slip rate in the east is consistent with block model estimates of ∼3–4 mm/yr (Meade, 2007), but even the maximum rate is lower than the 10–20 mm/yr geologic estimate (Armijo et al., 1989).

The internal microplate principal stress axes for model T5 (Figure 3.27) are largely consistent with previous models. Significantly, the largest principal stress in the Longmen Shan block is tensional. This result follows from the southeasterly directed force boundary condition in southeast Asia; however, it is somewhat surprising that it is the Longmen Shan block (north of the applied force boundary condition) that reflects tensional stress axes. This result may reflect the full Himalayan range front convergence condition: the southeast Asia

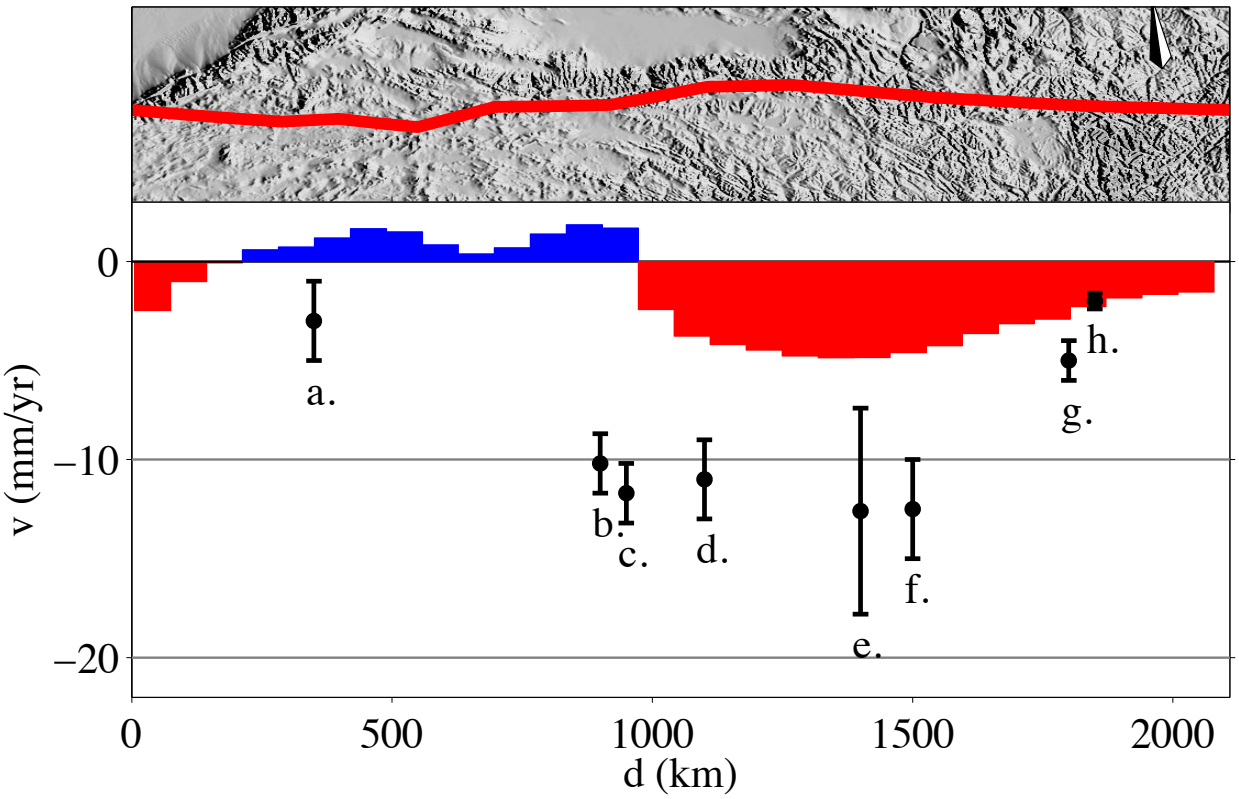

Figure 3.30: Slip rate variation predicted by DM model T5 along the east-west trending Kunlun fault system. The upper panel shows the rotated fault trace and topography within 200 km of the fault endpoints with the compass rose pointing north. Slip rates predicted by T5 are shown as the red and blue fill in the lower panel with geologic and geodetic fault slip rate estimates shown as black circles with reported 1-sigma error bars. Red colors and negative numbers indicate left-lateral motion, blue colors and positive numbers indicate right-lateral motion. The fault is left-lateral on the western portion of the fault (with a slip rate of ∼2 mm/yr) and then is right-lateral for ∼750 km (∼2 mm/yr). Displacements reverse to left-lateral for the remaining ∼1000 km along strike, reaching a maximum slip rate of ∼3 mm/yr. In general, these slip rates do not agree with left-lateral slip rates (shown in black) on the fault, but the model predictions of ∼2 mm/yr on the far eastern portion of the fault fall within the range of 2.0 ± 0.4 mm/yr estimated by Kirby et al. (2007) in that region. Slip rates inferred from geologic and geodetic data are from west to east: a. 3 ± 2 mm/yr, Bell et al. (2011), b. 10.2 ± 1.5 mm/yr, Hilley et al. (2005), c. 11.7 ± 1.5 mm/yr (at ∼94°E), Van der Woerd et al. (2002b), d. 11 ± 2 mm/yr, Meade (2007), e. 12.6 ± 5.2 mm/yr (at ∼99°E), Van der Woerd et al. (2002b), f. 12.5 ± 2.5 mm/yr (at ∼100.5° E) Van der Woerd et al. (2002b), g. 5 ± 1 mm/yr at (∼101.5°E) Kirby et al. (2007), and h. 2.0 ± 0.4 mm/yr (at ∼101.75°E), Kirby et al. (2007).

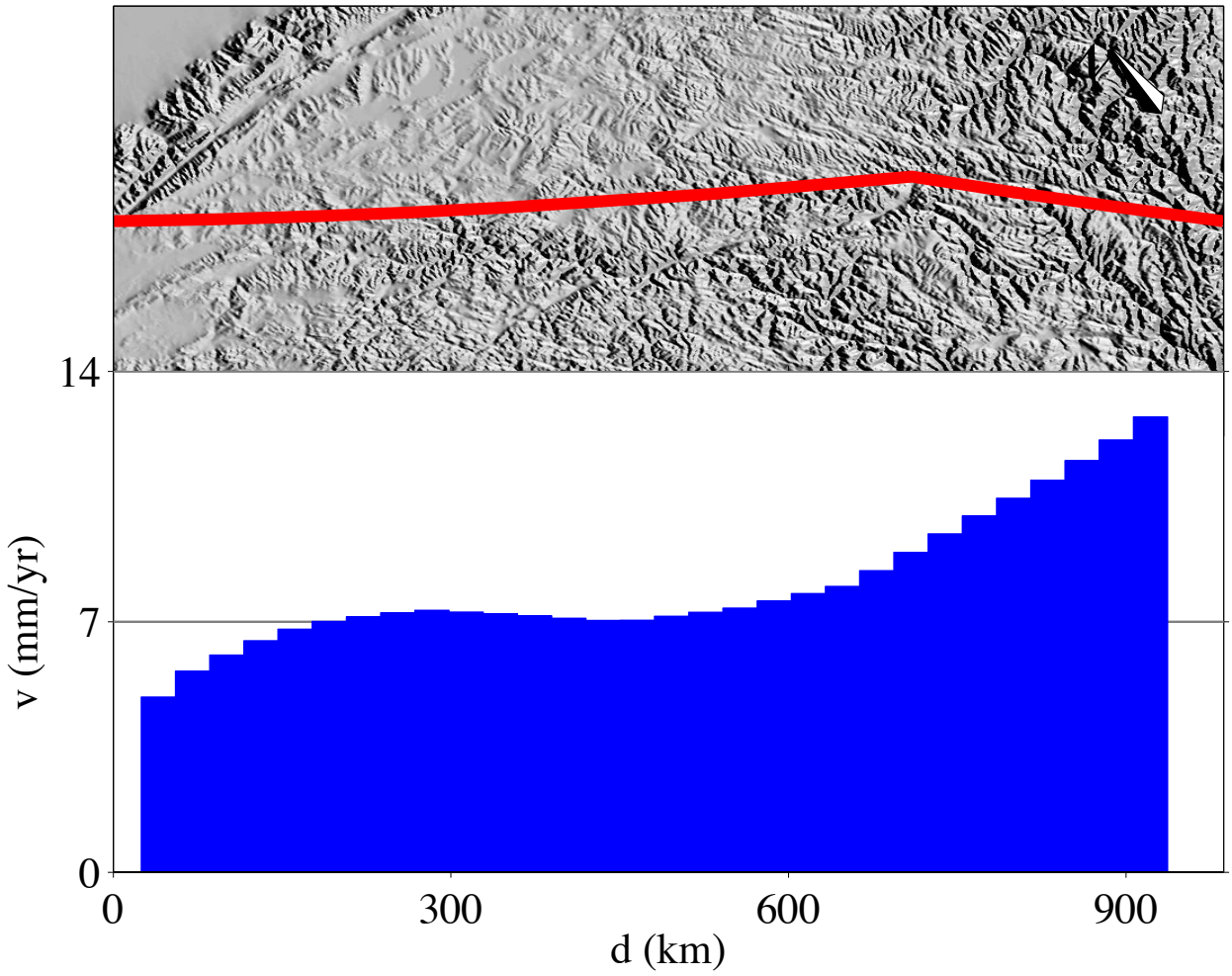

Figure 3.31: Slip rate variation predicted by DM model T5 along the Xianshuihe fault in eastern Tibet. The upper panel shows the rotated fault trace and topography within 200 km of the fault endpoints. The compass rose points north. Model T5 predicts an entirely right-lateral Xianshuihe fault, with slip rates increasing form west (∼4 mm/yr) to east (∼13 mm/yr). These predictions are inconsistent with geologic and geodetic data that suggest left-lateral displacement everywhere along strike: block models estimates of 3 ± 2 mm/yr on the eastern portion of the fault (Meade, 2007), geologic estimates of ∼15 mm/yr (Allen et al., 1991; He et al., 2006), InSAR calculations of 9-12 mm/yr, (Wang et al., 2009), and block model estimates of ∼20 mm/yr on the western portion of the fault (Meade, 2007).

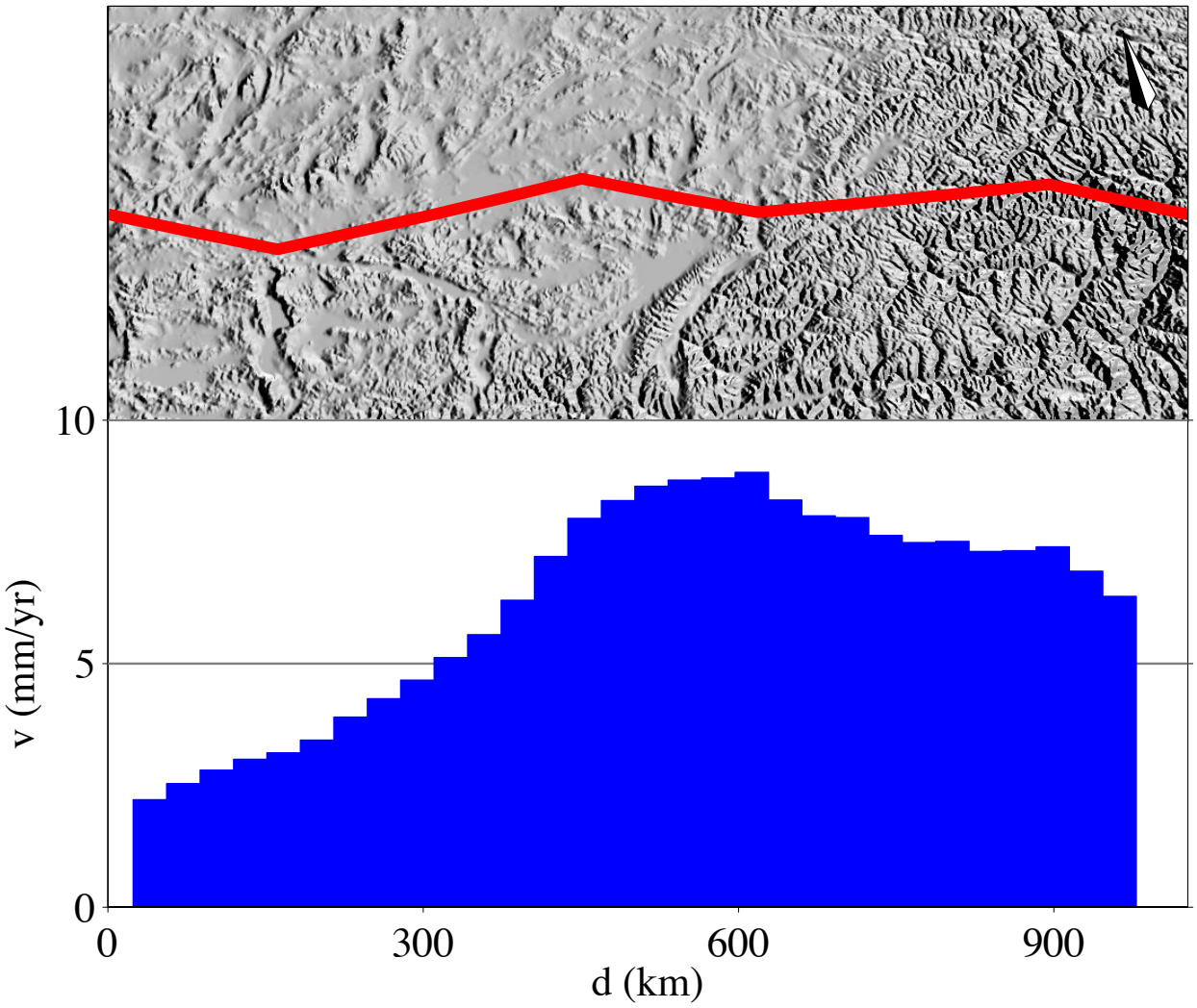

Figure 3.32: Along-strike slip rate variations predicted by DM model T5 for the Jiali fault in southeastern Tibet. The upper panel shows the rotated fault trace and topography within 200 km of the fault endpoints. The compass rose points north. Model T5 predicts entirely right-lateral slip on the Jiali fault, with a minimum in the west (∼2 mm/yr) and a maximum on the central portion of the fault (∼9 mm/yr). Geologic and geodetic data are consistent with a right-lateral structure, but T5 predictions are below geologic estimates of 10-20 mm/yr (Armijo et al., 1989). T5 predicts a slip rate on the western ∼200 km of the fault that is consistent with block models estimate 3-4 mm/yr of dexteral motion (Meade, 2007).

block is closer to this convergence, while the Longmen Shan block is further and may be more influenced by the force boundary condition.

Model T6: ¾ Himalayan range front convergence and southeast Asia force boundary condition

Of the suite of models described, model T6 (Table 3.1), with convergence displacement boundary conditions isolated to the western ¾ of the Himalayan range front and force boundary conditions of 1500 N/m applied along the southeast Asia boundary (Figure 3.2), best explains geologically and geodetically inferred slip rates (Figures 3.33–3.40, Table 3.1).

In DM model T6 extensive internal block compression is complemented by strike-slip faulting, enabling the continued northward penetration of the Pamir and Hindu Kush at the western edge of the model. Further, model T6 accommodates the extrusion of upper crustal material into southeast Asia at the eastern edge of the model domain (Figure 3.33). The eastern extrusion of the Longmen Shan block, in particular, is consistent with geodetically observed stretching in this region (Gan et al., 2007). Additionally, Model T6 is consistent with observations of entirely left-lateral slip along the Altyn Tagh (1–14 mm/yr), Kunlun (3–10 mm/yr), and Haiyuan (3–5 mm/yr) faults as well as exclusively right-lateral slip along the Karakoram fault (5–12 mm/yr).

Model T6 slip rate results for the Karakoram fault (Figure 3.34) are slightly higher than geologic and geodetic observations suggest. Slip on the Karakorum is slowest (5 mm/yr) in the northwest $\sim$ 200 km from the intersection with the Altyn Tagh fault, but quickly increase to a maximum rate of 12 mm/yr just south of this junction. Slip rates then stabilize at $\sim$10 mm/yr for $\sim$600 km along strike before tapering to 7 mm/yr along the southwestern-most

Figure 3.33 *(following page)*: Slip rates and velocities from DM model T6 (Table 3.1) with convergence on the western ¾ of the Himalayan Range Front and a force boundary condition in southeast Asia. In all figures microplate boundaries are shown as blue lines and the Indian sub-continent is shaded gray. Panel a) shows fault slip rates with left-lateral rates shown as white text in blue circles and right-lateral slip rates shown as blue text in white circles. For clarity, only representative slip rates are shown here. The fastest left- and right-lateral slip rates are along the central Altyn Tagh and Karakoram faults, respectively. Color shading shows velocity magnitudes where redder colors indicate faster velocities, with maximum velocities equal to the differential motion between India and Eurasia. Velocities are continuous within each microplate, representing distributed deformation, and discontinuous at microplate boundaries, indicated fault slip. Panel b) shows velocity vectors (white arrows) superimposed over the velocity magnitude field. Velocity azimuths rotate from north-northeast to east-southeast around the eastern syntaxis. Panel c) Representative principal stress orientations for model microplates, where red arrows indicate compression and black arrows indicate extension. Western microplates feature dominantly compressive principal stresses, but eastern microplates feature an extensional component.

Figure 3.33: (continued)

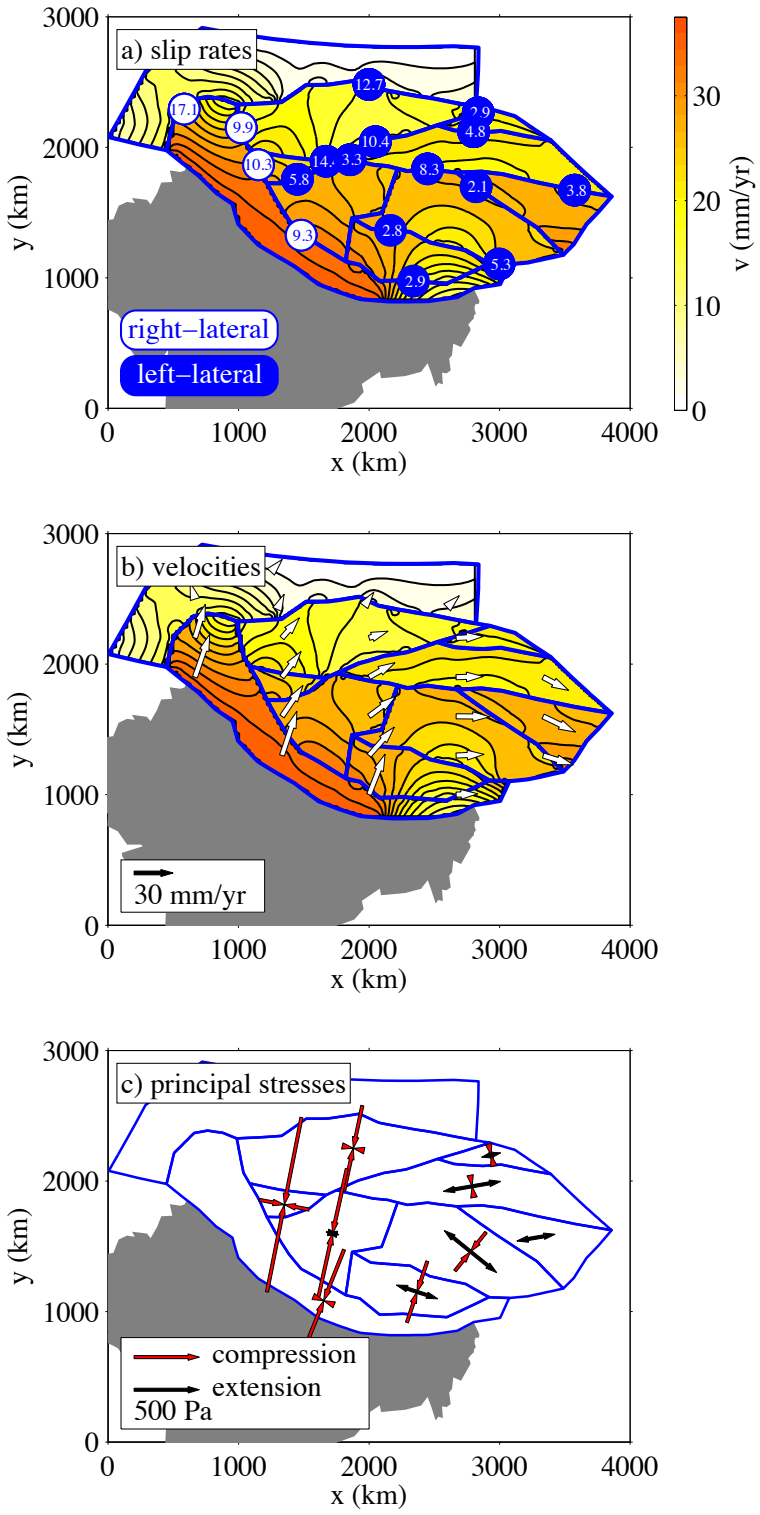

extent of the fault. These results are consistent with the geologic estimates of 10.7 ± 0.7 mm/yr (Chevalier et al., 2005) from the central and southern portion of the Karakorum, but are significantly higher than geologic (4 ± 1 mm/yr, Brown et al., 2002) and InSAR (1 ± 3 mm/yr, Wright et al., 2004) observations from similar regions.

Model T6 predictions for slip along the Haiyuan fault are relatively stable between 3–5 mm/yr. These results are consistent with geologic observations of 4.5 ± 1.1 mm/yr (Li et al., 2009) and InSAR estimates of 6.3 ± 2 mm/yr (Cavalié et al., 2008). Block model results are in agreement with DM predictions in the eastern portion of the fault (∼4 mm/yr, Meade, 2007), but are significantly higher than DM results on the Western portion of the fault (∼9 mm/yr, Meade, 2007).

Slip rate predictions for the Altyn Tagh fault vary by an order of magnitude along strike and are in good agreement with most geologic and geodetic measurements of slip (Figure 3.35). Slip rates peak at 14 mm/yr in the central western portion of the fault just south of the Tarim Basin and fall below 5 mm/yr at the western and eastern extremes of the fault trace, in agreement with InSAR observations of 5 ± 5 mm/yr in the west (Wright et al., 2004) and block model predictions of 3 ± 2 mm/yr in the east (Meade, 2007). Slip on the central ∼500 km of the fault is relatively constant at ∼10 mm/yr, in accord with geologic observations of 11.5 ± 2.5 mm/yr (Cowgill et al., 2009) and geodetic measurements of 9 ± 4 mm/yr (Wallace et al., 2004) for this portion of the fault. Notably, T6 model predictions are not in agreement with geologic observations of 14 ± 2 mm/yr (Yue et al., 2001) and 17.8 ± 3.6 mm/yr (Mériaux et al., 2005) along the eastern third of the Altyn Tagh fault.

One of the primary reasons DM model T6 is the preferred model for describing strike-slip

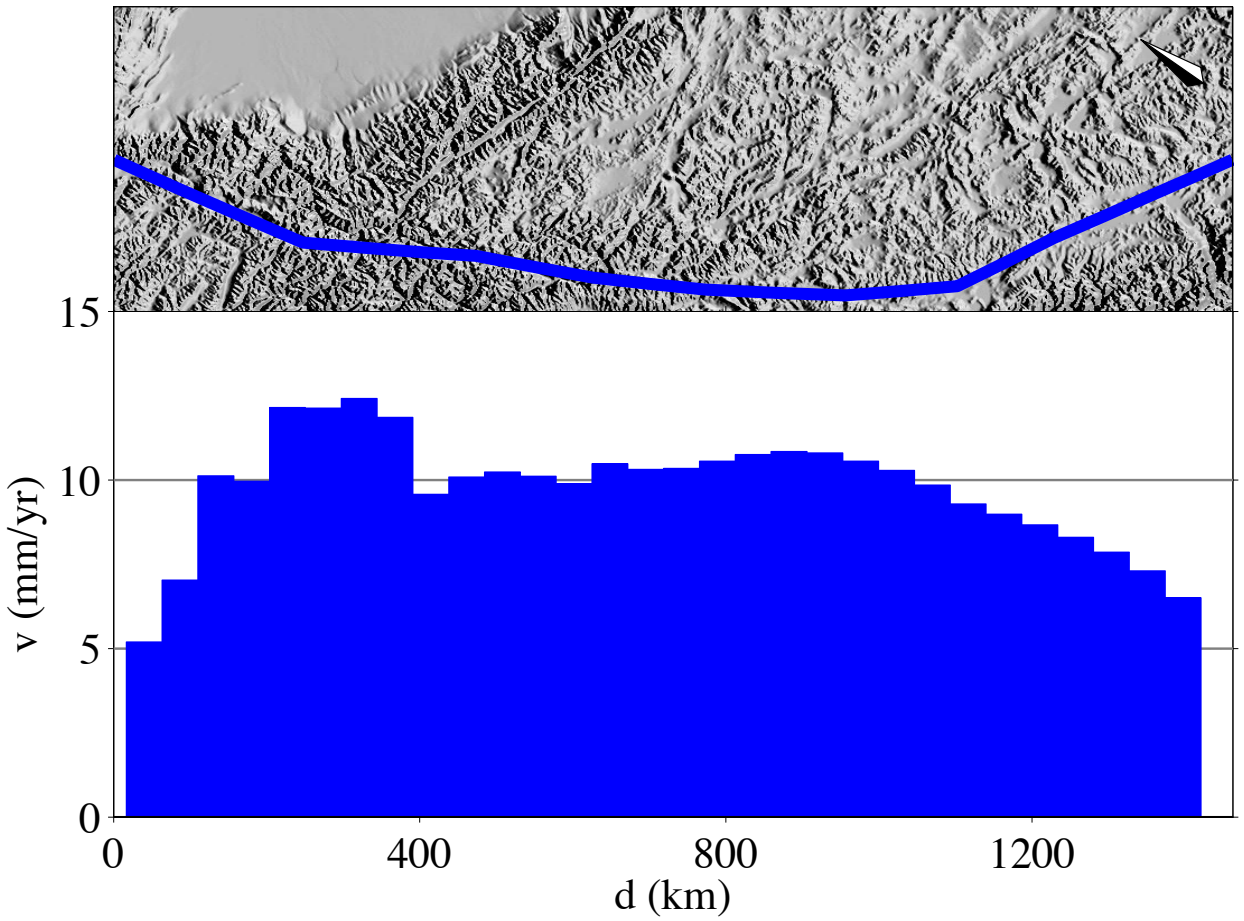

Figure 3.34: Along-strike slip variation for the Karakorum fault at the western boundary of the Tibetan Plateau. The upper panel shows the rotated fault trace and topography within 200 km of the fault endpoints. The compass rose points north. Right-lateral slip rates predicted by DM model T6 are shown as blue fill. Slip is lowest in the north, near the intersection with the Altyn Tagh fault, but reaches a maximum value (12 mm/yr) just south of this junction. Slip is relatively constant at ∼10 mm/yr on the central portion of the fault before tapering to 7 mm/yr at the southern extreme. These estimates are consistent with geologic observations of 10.7 ± 0.7 mm/yr (Chevalier et al., 2005) but are significantly higher than other geologic (4 ± 1 mm/yr, Brown et al., 2002) and InSAR (1 ± 3 mm/yr, Wright et al., 2004) estimates.

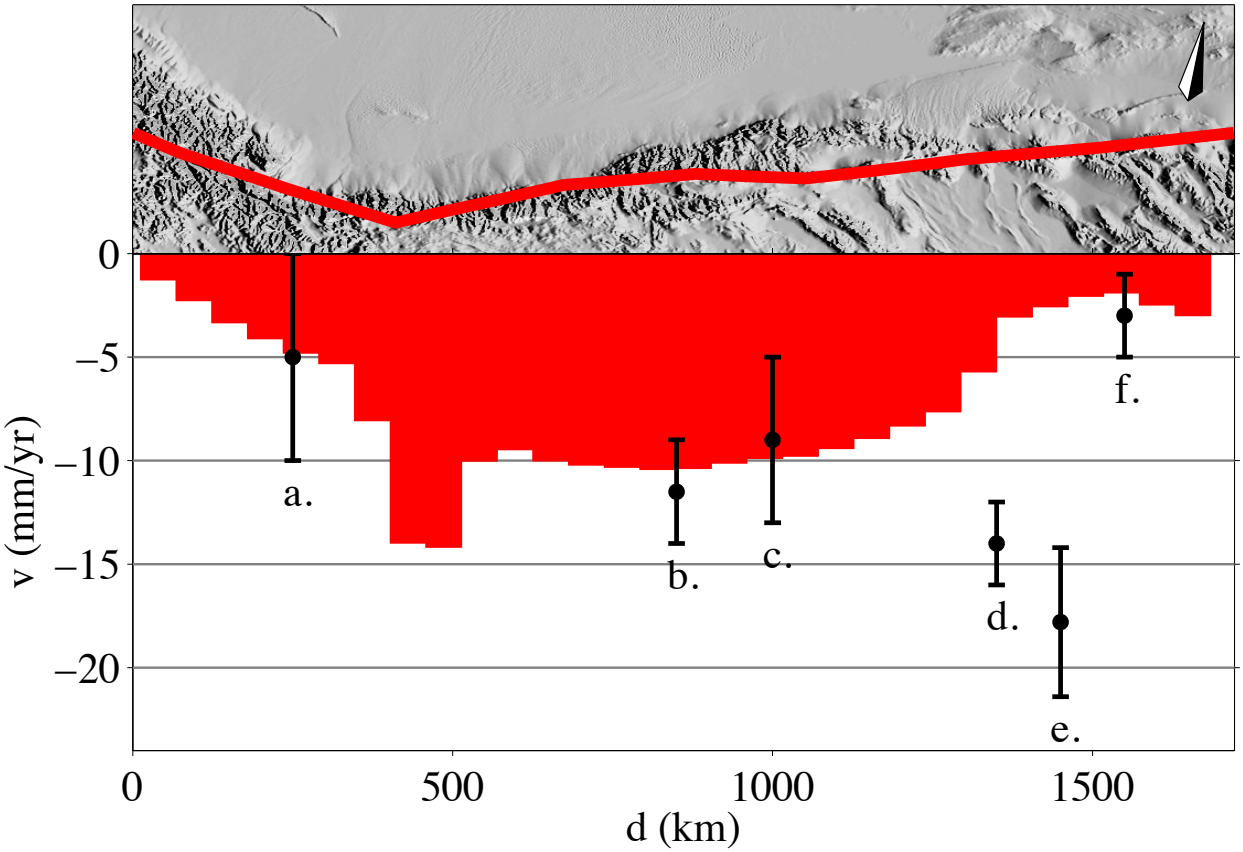

Figure 3.35: Slip rate variation along the Altyn Tagh-Karakash fault system at the northern boundary of the Tibetan plateau predicted by DM model T6. The upper panel shows the rotated fault trace and topography within 200 km of the fault endpoints with the compass rose pointing north. Slip rates predicted by T6 are shown as the red fill in the lower panel with geologic and geodetic fault slip rate estimates shown as black circles with reported 1-sigma error bars. Both observations and model predictions show a peak in fault slip along the central Altyn Tagh fault, reaching up to 14 mm/yr and decreasing to <5 mm/yr to both the east and west. Slip rates inferred from geologic and geodetic data are from west to east: a. 5 ± 5 mm/yr,Wright et al. (2004), b. 11.5 ± 2.5 mm/yr, Cowgill et al. (2009), c. 9 ± 4 mm/yr, Wallace et al. (2004), d. 14 ± 2 mm/yr, Yue et al. (2001), e. 17.8 ± 3.6 mm/yr, Mériaux et al. (2005), and f. 3 ± 2 mm/yr, Meade (2007).

faulting in Tibet is because it accurately predicts an entirely left-lateral Kunlun fault. None of the other DM models considered here correctly predict the sense of slip everywhere on this structure. DM model agreement is critical for validating the efficacy of the dynamic microplate method because geologic and geodetic slip estimates for the Kunlun fault are not isolated to a single point but rather are distributed broadly along more than 1200 km of the fault's length. Model predictions peak at 10 mm/yr along the central segment of the fault and decrease below 5 mm/yr to the east and west (Figure 3.36). This trend is in good agreement with geologic and geodetic observations of slip, which similarly peak towards the center of the fault and are likewise <5 mm/yr at the eastern and western extremes. In particular, model slip rate gradients along the Kunlun fault are consistent with inferences from InSAR data of 3 ± 2 mm/yr on the western Manyi splay (Bell et al., 2011) as well as block-model inference of 11 ± 2 mm/yr (Meade, 2007) on the central portion of the structure. DM model T6 results also fall within range of geologic estimates from Van der Woerd et al. (2002b) at ∼99°E (12.6 ± 5.2 mm/yr), but fall just below similar calculations from ∼94°E (11.7 ± 1.5 mm/yr) and ∼100.5°E (12.5 ± 2.5 mm/yr) of the same study. Similarly, model predictions are consistent with estimates from Kirby et al. (2007) at ∼101.5°E (5 ± 1 mm/yr) while the eastern-most observations at ∼101.75°E (2.0 ± 0.4 mm/yr), fall slightly below model predictions.

Slip rates for the Altyn Tagh and Kunlun faults are extremely sensitive to the magnitude of force applied at the SEA boundary (Figures 3.37 and 3.38). A five-fold increase in force boundary conditions (7500 N/m) results in a 50% increase in maximum left-lateral slip on the Altyn Tagh and an along-strike reversal in sense-of slip. In these models, the eastern

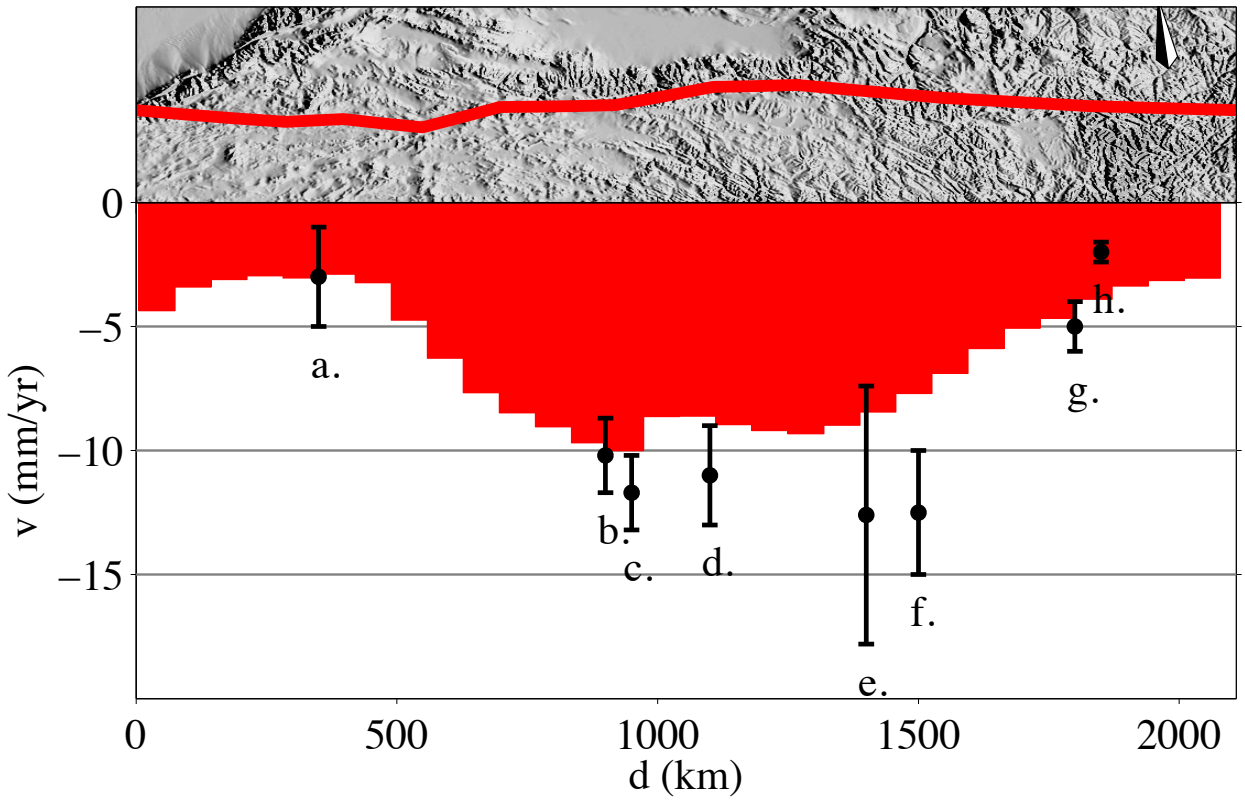

Figure 3.36: Slip rate variation along the east-west trending Kunlun fault system predicted by DM model T6. The upper panel shows the rotated fault trace and topography within 200 km of the fault endpoints with the compass rose pointing north. Slip rates predicted by T6 are shown as the red fill in the lower panel with geologic and geodetic fault slip rate estimates shown as black circles with reported 1-sigma error bars. Both observations and model predictions show a peak in fault slip along the central Kunlun fault reaching up to 10 mm/yr and decreasing to <5 mm/yr to both the east and west. Slip rates inferred from geologic and geodetic data are from west to east: a. 3 ± 2 mm/yr, Bell et al. (2011), b. 10.2 ± 1.5 mm/yr, Hilley et al. (2005), c. 11.7 ± 1.5 mm/yr (at ∼94° E) Van der Woerd et al. (2002b), d. 11 ± 2 mm/yr, Meade (2007), e. 12.6 ± 5.2 mm/yr (at ∼99°E), Van der Woerd et al. (2002b), f. 12.5 ± 2.5 mm/yr (at ∼100.5°E), Van der Woerd et al. (2002b), g. 5 ± 1 mm/yr at (∼101.5°E), Kirby et al. (2007), and h. 2.0 ± 0.4 mm/yr (at ∼101.75°E), Kirby et al. (2007).

Altyn Tagh is heavily right-lateral (maximum dexteral slip reaches >8 mm/yr). Similarly, maximum slip on the Kunlun fault is more than 500% higher than model T6 estimates (∼52 mm/yr) when the SEA force boundary condition is five times higher. Further, reducing the SEA boundary condition by a factor of five (300 N/m) only slightly reduces Altyn Tagh fault slip rates, but reverses the sense of motion on the eastern Kunlun fault to ∼0.5 mm/yr of right-lateral slip.

Although DM model T6 is consistent with geologic and geodetic measurements for the majority of Tibetan faults and satisfies geodetically observed eastward extrusion of continental material, model predictions are inconsistent with previously inferred slip rates for the Xianshuihe and Jiali faults. DM model T6 finds low magnitude (∼3 mm/yr) left-lateral slip on the northern Xianshuihe fault (Figure 3.39) decreasing along strike to 0 mm/yr in the center. Here the sense of slip reverses and the fault becomes strongly right-lateral, reaching 11 mm/yr of dextral motion at the southern extreme. All documented slip on the Xianshuihe is decisively left-lateral, and while northern Xianshuihe model results are consistent with block model predictions of 3 mm/yr, block model predictions increase to 20 mm/yr of sinisteral slip for the southern portion of the fault (Meade, 2007). Geologic estimates of left-lateral slip are ∼15 mm/yr (Allen et al., 1991; He et al., 2006), and InSAR measurements range from 9–12 mm/yr (Wang et al., 2009).

Like the Xianshuihe fault to the northwest, DM model T6 predicts (Figure 3.40) an along-strike reversal in the sense of slip for the Jiali fault. In this case, the Jiali fault is right-lateral in the western corner of the fault with a slip rate 2 mm/yr, but it quickly becomes left-lateral, achieving sinisteral slip rates of 5 mm/yr in the east. Slip rate estimates for the Jiali

fault are sparse, but model predictions do not agree with geologic estimates of 10–20 mm/yr of right-lateral slip (Armijo et al., 1989) or block model estimates of 3–4 mm/yr of dexteral motion (Meade, 2007). More realistic model representations of the complex geometry in the vicinity of the eastern syntaxis may allow more significant eastward extrusion between the Jaili and Xianshuihe faults. Despite the challenges in satisfying previously inferred slip rates on the Xianshuihe and Jiali faults, DM model T6 remains the preferred model because of the good agreement between model predictions and all other major Tibetan faults. Significantly, model T6 is the only model that satisfies geodetic and geologic observations on the densely sampled Kunlun fault and is the only model that captures the eastern extrusion of Tibetan crustal material.

Internal microplate principal stresses (Figure 3.33) calculated from Model T6 are dominantly compressive through the western ∼2000 km of the model, consistent with the oblique convergence displacement boundary condition on the western ¾ of the HRF. Principal stresses in the eastern half of the model domain feature an extensional component. These results are broadly consistent with the tectonic context of the region, as normal faulting in central and eastern Tibet is well documented (e.g., Blisniuk et al., 2001; Coleman and Hodges, 1995; Harrrison et al., 1995)

3.3 Discussion

While comparisons between DM model slip rate predictions and observationally constrained slip rate estimates offer a direct means of assessing model efficacy, DM models also predict pervasive non-localized deformation interior to microplates. This distributed

deformation may be considered a coarse parameterization of faulting and folding at smaller scales or as non-brittle deformation processes. Observationally, quantifying diffuse deformation may be challenging due to the difficulty in identifying small deformation gradients distributed over large spatial extents. However, the relative amount of total deformation associated with localized or diffuse deformation can be quantified by calculating the potency (geometric moment) rates associated with each. Localized deformation on faults has a potency rate, P_f, given as the product of fault area, A, and slip rate magnitude, s, such that $P_f = A|s|$. Fault potency for individual microplates is divided by two to ensure that cumulative fault potency rates are equal to the global (entire model) sum of on-fault potency (Loveless and Meade, 2011a). For microplate interiors, potency rates are calculated from Kostrovs formula as, $P_b = 2V\sqrt{\dot{\boldsymbol{\epsilon}} : \dot{\boldsymbol{\epsilon}}}$, where V is the microplate volume and $\dot{\boldsymbol{\epsilon}}$ is the strain rate tensor. In DM models strain rates vary within microplates, thus strain rates are summed over each of the triangular regions that constitute the finite element mesh. The potency partitioning ratio, $\phi = P_b/(P_b + P_f)$ (Loveless and Meade, 2011a), quantifies the relative magnitudes of localized and diffuse deformation ranging from completely localized ($\phi = 0$) to entirely distributed ($\phi = 1$). For the microplates in DM model T6, potency partitioning ratios range from 0.28 in the microplate bounded by the Kunlun and Haiyuan faults in the northeast, to 0.79 in the block bounded by the Jaili and Xianshuihe faults in the southeast. The mean potency partitioning ratio in model T6 is 0.54 (Figure 3.41a). The approximate equipartitioning of localized and distributed deformation is an inherent part of the elastic rheology assumed in the model and represents a hybrid view between idealized models of rigid continental microplates bounded by major faults (e.g., Avouac and

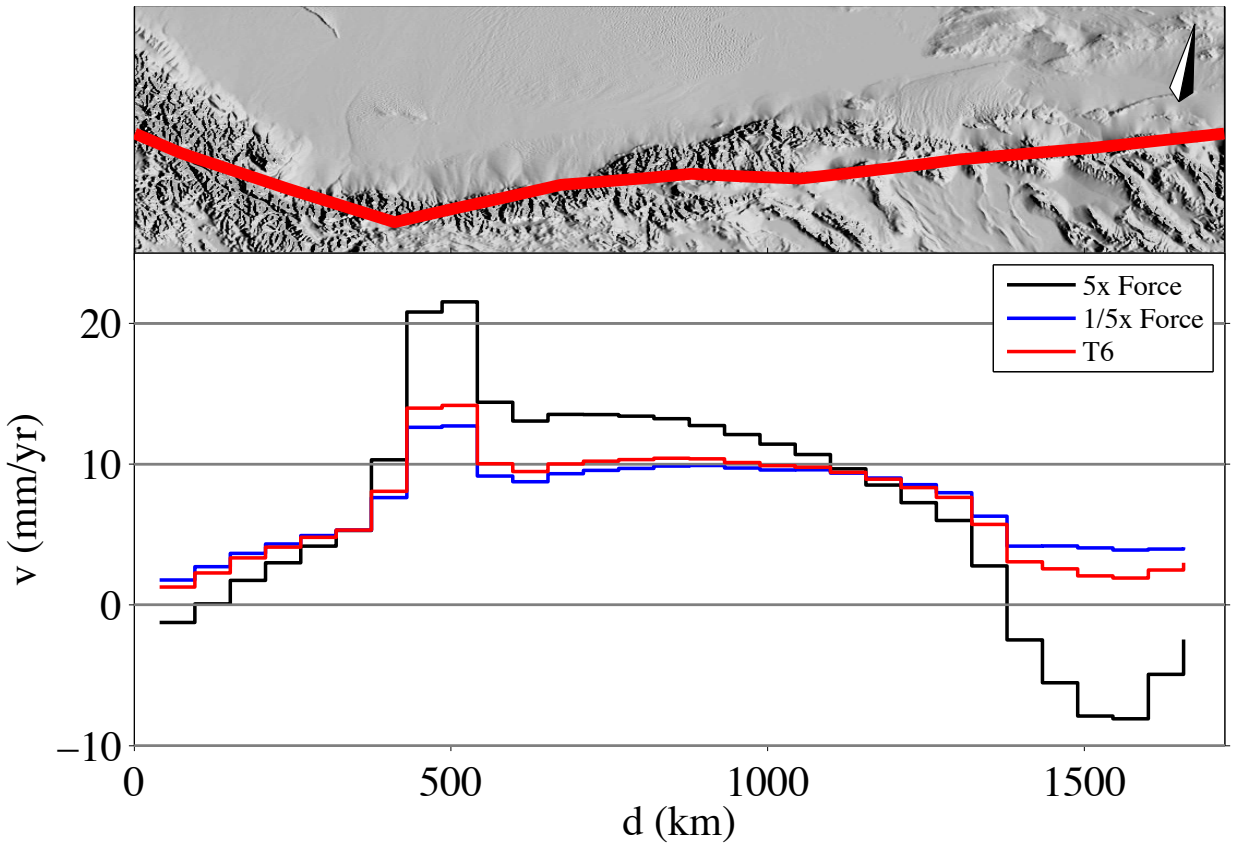

Figure 3.37: Along-strike slip rate variations for the Altyn Tagh fault for models with different magnitude SEA force boundary conditions. The upper panel shows the rotated fault trace and topography within 200 km of the fault endpoints. The compass rose points north. Here positive slip-rates indicate left-lateral motion and negative slip rates connote right-lateral displacements. Results from DM model T6, with a force boundary condition of 1500 N/m, are plotted in red. Results for models with force boundary conditions five-times larger (7500 N/m; black line) and five-times smaller (300 N/m; blue line) are also shown. Larger magnitude force boundary conditions result in a 50% increase in peak left-lateral slip rate over T6 predictions (to 21.5 mm/yr) and an along-strike reversal in sense of slip to right-lateral along the eastern quarter of the fault. Smaller SEA force boundary conditions do not significantly impact slip rate estimates. Though peak left-lateral slip is ∼1 mm/yr less than predicted in T6 and eastern Altyn Tagh slip rates are ∼1 mm/yr higher.

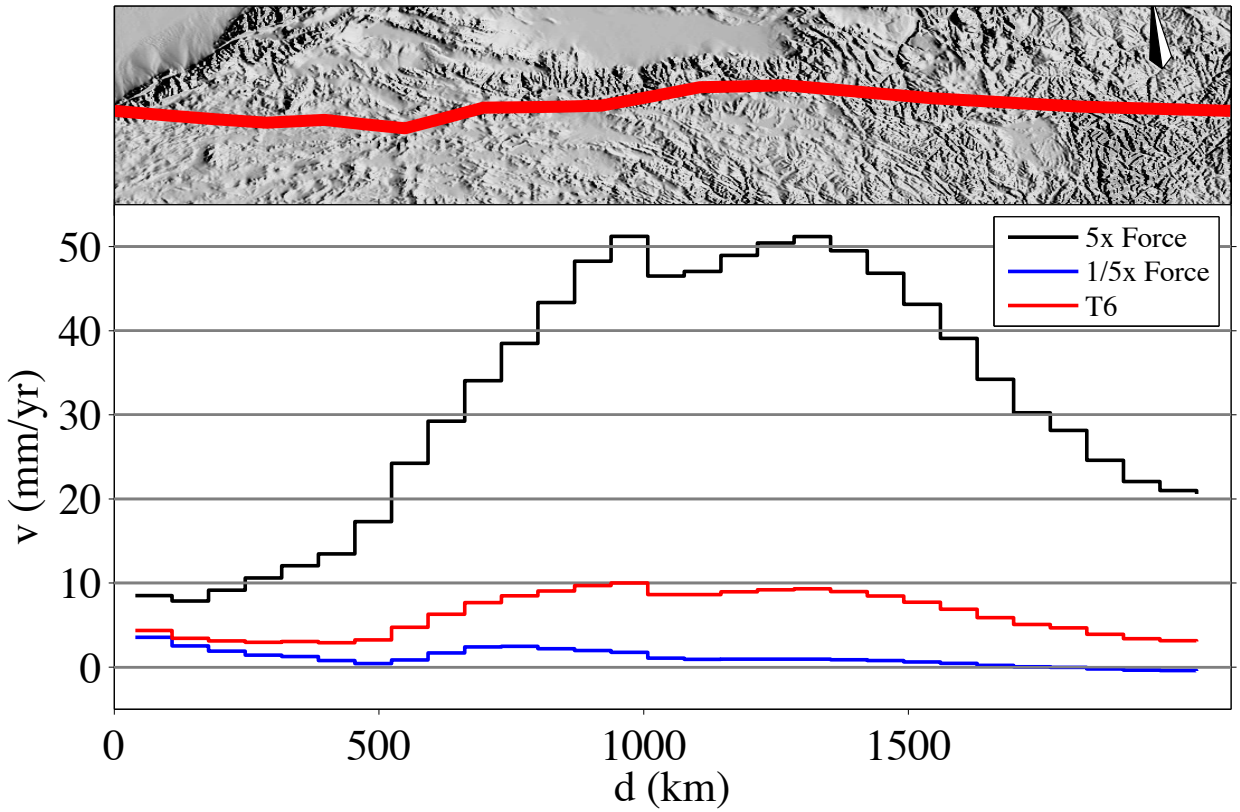

Figure 3.38: Along-strike slip rate variations for the Kunlun fault for models with different magnitude SEA force boundary conditions. The upper panel shows the rotated fault trace and topography within 200 km of the fault endpoints. The compass rose points north. Here positive slip-rates indicate left-lateral motion and negative slip rates connote right-lateral displacements. Results from DM model T6, with a force boundary condition of 1500 N/m, are plotted in red. Results for models with force boundary conditions five-times larger (7500 N/m; black line) and five-times smaller (300 N/m; blue line) are also shown. Larger magnitude SEA force boundary conditions correspond to a five-fold increase in left-lateral slip rate on the Kunlun of T6 model predictions, with peak slip predictions reaching 52 mm/yr. Models with smaller magnitude SEA force boundary conditions have peak slip rates that are more than three times smaller than T6 results ($\sim$4 mm/yr). These models also feature a change in the sense of slip to right-lateral for the eastern Kunlun, with peak dexteral slip rates of 0.5 mm/yr.

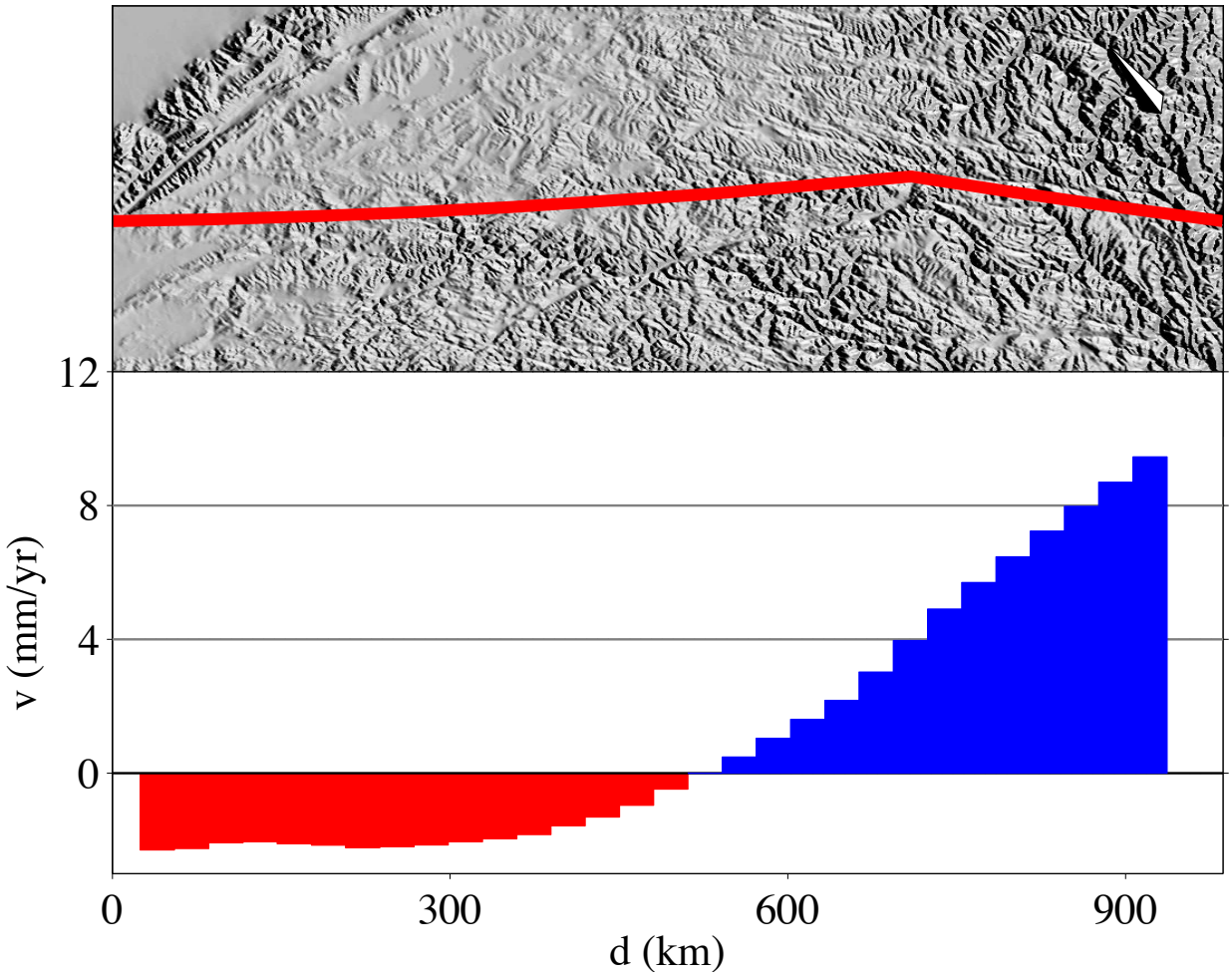

Figure 3.39: Slip rate variation along the Xianshuihe fault in eastern Tibet predicted by DM model T6. The upper panel shows the rotated fault trace and topography within 200 km of the fault endpoints. The compass rose points north. T6 model predictions of low magnitude ($\sim$3 mm/yr) left-lateral slip rates are plotted as red fill. The predicted sense of slip changes to right-lateral in the center of the fault, and dexteral slip rates, achieving magnitudes of 11 mm/yr, are plotted as blue fill. While western left-lateral slip of 3 mm/yr is consistent with block model predictions of 3 $\pm$ 2 mm/yr on this portion of the fault, geologic and geodetic observations suggest a left-lateral Xianshuihe. In particular, model T6 predictions are in contradiction with sinisteral slip estimates of $\sim$15 mm/yr from geologic estimates (Allen et al., 1991; He et al., 2006), 9-12 mm/yr inferred from InSAR observations (Wang et al., 2009), and $\sim$20 mm/yr from geodetically constrained block models (Meade, 2007).

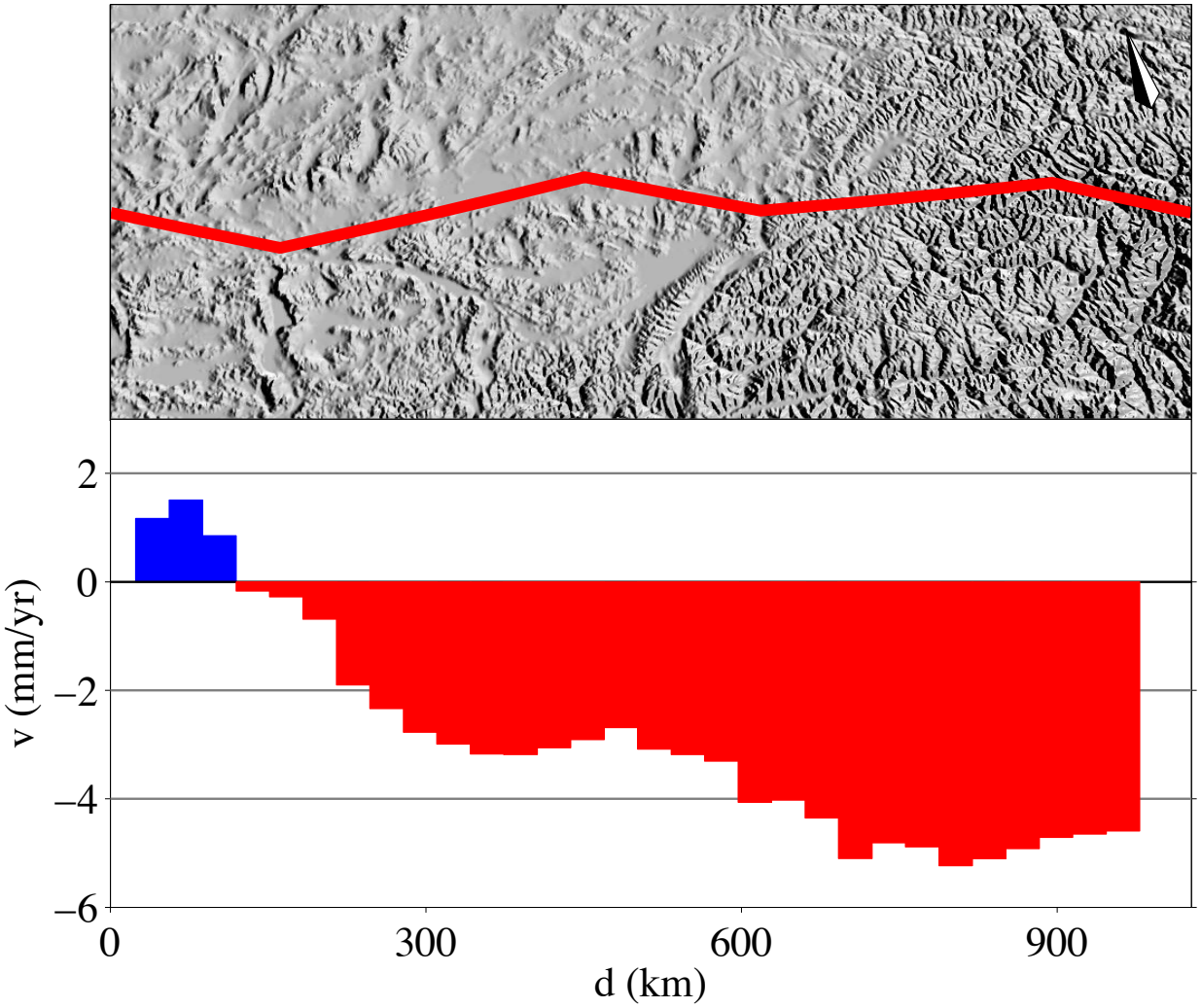

Figure 3.40: Along-strike slip rate variations for the Jiali fault in southeastern Tibet predicted by DM model T6. The upper panel shows the rotated fault trace and topography within 200 km of the fault endpoints. The compass rose points north. Right-lateral slip rates are plotted as blue fill and left-lateral slip rates as red fill. Model T6 predicts that the Jiali is right-lateral only on the far-western portion of the fault. Slip rates then become left-lateral, reaching 5 mm/yr of sinisteral motion. Although geologic and geodetic data are sparse for this structure, these results are in poor agreement with geologic observations of 10-20 mm/yr of right-lateral slip (Armijo et al., 1989) and block model estimates of 3-4 mm/yr of dexteral motion (Meade, 2007).

Figure 3.41 *(following page)*: a) Potency partitioning ratios and locations of earthquakes away from major faults. Color shading gives the value of the potency partitioning ratio, ϕ, with redder colors indicating more distributed deformation. Earthquakes from the Global CMT catalog are shown with areas proportional to moment and compressional quadrants shaded blue. b) Correlation between potency partitioning ratio, ϕ, and number of earthquakes interior to each microplate. Earthquakes are limited to those in the Global CMT catalog at depths shallower than 40 km and more than 25.1 km away from any microplate boundary. The number of earthquakes is positively correlated with high potency partitioning ratios with a Pearson correlation coefficient of 0.72 ± 18 (67% confidence).

Figure 3.41: (continued)

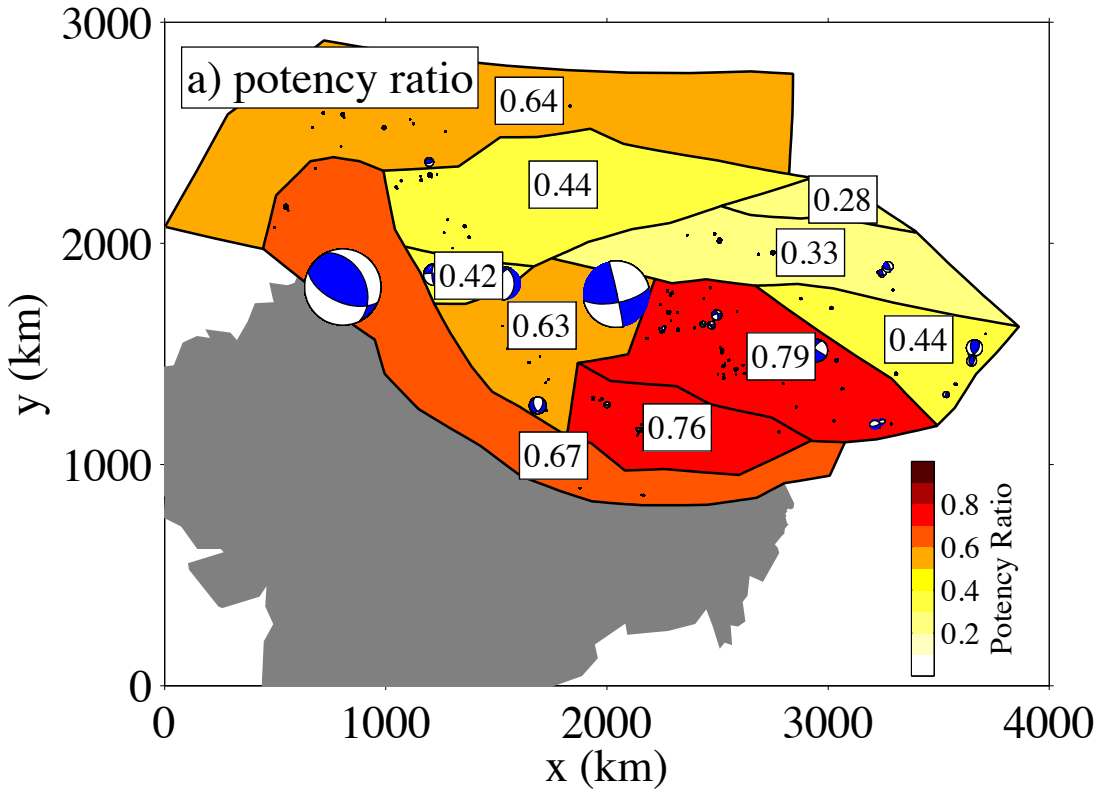

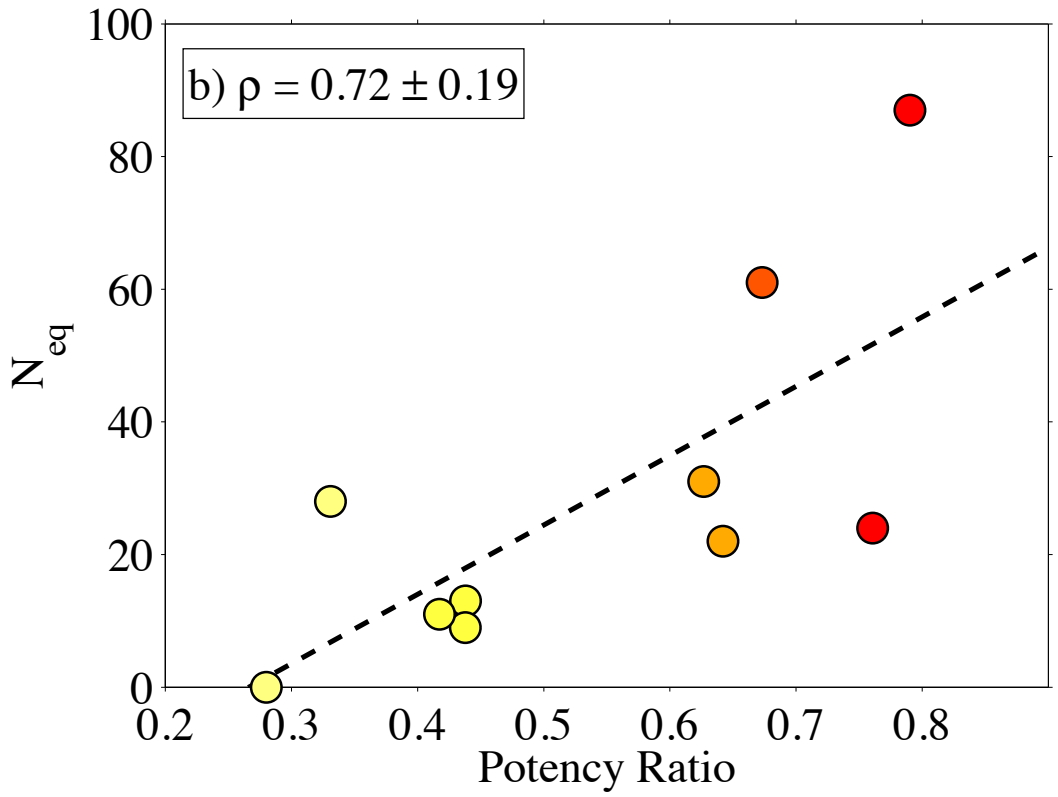

Tapponnier, 1993; Thatcher, 2007; Zhen-Kang et al., 2005) and models of a homogenous and continuously deforming lithosphere (e.g., England and McKenzie, 1982; England and Molnar, 1997, 2005; Flesch et al., 2001; Holt et al., 2000).

The geometrically and rheologically controlled microplate potency partitioning ratios can be compared against macroscale seismicity across the Tibetan plateau to assess whether or not microplates with the highest fraction of distributed internal deformation are characterized by relative high levels of internal seismicity. We take earthquake locations from the Global CMT (www.globalcmt.org) catalog between 69°–108°E longitude and 23°–45°N latitude with hypocenter depths shallower than 40 km. Here we consider earthquakes that are not likely to have occurred on the major faults bounding continental microplates. Thus we filter the earthquake catalog to eliminate all earthquakes occurring at a distance <25.1 km from model microplate boundaries (Figure 3.41a). Approximately 90% of the total Tibetan moment release in the historical earthquake record has occurred within 25.1 km of major faults (Loveless and Meade, 2011a), which is within the approximate location uncertainty of CMT estimates (Lohman and Simons, 2005). The Pearson correlation coefficient describing the linear relationship between the microplate potency partitioning ratios and the number of earthquakes interior to each microplate is 0.72 ± 19 (67% confidence, Figure 3.41b). This result suggests that the microplates predicted to have the greatest internal deformation (e.g. highest potency partitioning ratios) are indeed those with the highest internal seismicity rates. Because the selected earthquakes in the global CMT catalog are only those exceeding $M_W = 4.6$, this correlation is not a reflection of microscale seismicity associated with non-tectonic processes. Additionally, the duration of the CMT catalog (∼42 years) is much

less than the typical recurrence time for large earthquakes on major faults in Tibet (e.g., Van der Woerd et al., 2002a). As a result, this comparison may be biased due to sampling only a small fraction of a single earthquake cycle.

As described above, of the six DM models considered here, model T6 explains the slip rate observables best with two key boundary conditions: 1) convergence at 37 mm/yr along the western ¾ of the HRF west of the Shilong plateau, and 2) a southeasterly directed force of 1500 N/m acting on the SEA boundary (Figures 3.2, 3.33). These boundary conditions are motivated by variability in geologic structure along the strike of the HRF and geodetic observations, respectively.

Bounded by the Brahmaputra river to the north and west, the Shillong plateau emerges from the Indian subcontinent at 90°E and is an actively growing foreland structure. North-south oriented shortening is manifest not only geologically, but also in the occurrence of the $M_W = 8.1$ Assam 1897 earthquake, which contributed to the uplift of this structure by slipping as much as 11 m on the south-southwest dipping Oldham fault at the northern edge of the plateau (Bilham and England, 2001). In addition to seismic activity, geodetic data further indicate that east of 90°E deformation is partitioned, at least partially, from the HRF to the Shillong plateau bounding structures. Interseismic GPS data indicate 6.8 ± 3.8 mm/yr of differential motion between the northern edge of the Shillong plateau and the nominally stable Indian subcontinent (Paul et al., 2001). Taken at face value, this convergence south of the HRF would reduce the shortening rate across the easternmost HRF by at most ∼10 mm/yr, or about 30% of the overall tectonic convergence rate. While GPS data near major faults may be significantly modified throughout the earthquake cycle processes (e.g., time

dependent viscoelastic relaxation at depth), even quasi-static models of thrust faults suggest that neglecting earthquake cycle effects gives rise to minimum shortening rate estimates unless both sides of a fault are spanned by GPS stations out to several hundred kilometers (Feldl and Bilham, 2006; Savage, 1983). Results from DM model T6, which best predicts observed Tibetan strike-slip rates and has no applied convergent displacement conditions north of Shillong plateau, are consistent with greater magnitude shortening in this region than has previously been suggested.

Force boundary conditions along SEA are particularly critical for explaining observed slip rate gradients along the Kunlun fault (Table 3.1, Figure 3.36). The observational motivation for this boundary condition is the apparent geodetic extrusion of material into southeast Asia between the left-lateral Xianshuihe and right-lateral Jiali faults (Figure 3.1b). Assuming that these GPS velocities do not entirely result from transient earthquake cycle processes (e.g., large magnitude viscoelastic relaxation), the velocity at this boundary is $\sim$15 mm/yr south-southeast, relative to stable Eurasia. The mechanism driving this deformation is less clear. Models T2 and T4 (Table 3.1) show that the southeastern extrusion of Tibetan crustal material is neither a necessary consequence of simple boundary conditions satisfying convergence at the HRF and confinement of Asia north of the Tien Shan, nor does it result from additional displacement conditions such as fixing the LMS boundary. Instead, both $^3/_4$ HRF convergence and a southeastward-directed SEA force condition are needed to successfully replicate the geodetically observed extrusion towards Burma, Laos, and Vietnam. Candidate mechanisms for local driving forces in southeast Asia include both channelized lower crustal flow and basal tractions associated with mantle flow induced by the westward

rollback of the Indo-Burman slab (Royden et al., 2008).

3.4 Conclusions

Dynamic microplate models integrate the localized faulting of kinematic block models with the predictive ability of models driven exclusively by far-field boundary conditions. We suggest that DM models provide a mechanical basis for understanding along strike variation in fault slip rates at ∼1000 km length scales. Current slip rate gradients can be explained as the response of elastic upper crustal microplates deforming to accommodate the interseismic deformation of fault networks rather than resulting from lateral variations in crustal strength or thickness (e.g., Chéry, 2008). Applied to two-dimensional models of strike-slip faults in the Tibetan plateau, we can predict slip rates along the Altyn Tagh-Karakash (1–14 mm/yr), and Karakoram (5–12 mm/yr) faults as well as an eastward decrease in fault slip rate along the Kunlun fault (3–10 mm/yr). Geologically and geodetically inferred slip rate gradients along the Kunlun fault may plausibly result from the application of simple displacement and force boundary conditions applied to the edges of a discontinuous elastic model. In particular, the application of convergent displacement boundary conditions along the western ¾ of the Himalayan range front and an active force dragging upper crustal material toward southeast Asia appear as critical elements in explaining geologically and geodetically inferred fault slip rates. Although these edge-driven models explain strike-slip fault slip rates along the Altyn Tagh, Kunlun, and Karakoram faults, there is no inference that precludes a role for local gravitationally induced body forces. Many continuum models are predicated on the assumption that body forces are a driving factor in continental tectonics (England and

Molnar, 1997, 2005; Flesch et al., 2001). The efficacy of DM models with edge and body forces for explaining fault slip rates at the India-Asia boundary is a question for future work.

Potency rates for DM models associated with internal block and on-fault deformation are approximately equipartitioned. This result is rheology-dependent and may change significantly with the addition of non-zero coefficients of fault friction or the implementation of a more incompressible bulk crustal material. Further geologic constraints on Tibetan fault slip rates are necessary to constrain the extent of localized and distributed deformation and will be vital in determining the potential of known faults for future great earthquakes. While the DM models presented here effectively describe both geologically and geodetically inferred fault slip rates across Tibet, directly testing these models against geodetic data will require the development of representations of earthquake cycle processes. Further, DM models predict slip rate gradients along faults in the absence of mechanical heterogeneities within microplates. This result suggests that inferences of structural segmentation on faults, based exclusively on observations of along-strike slip rate variability, may be poor indicators of geometric limits to large earthquake ruptures.

Chapter 4

Slip Rate Variations on the San Andreas Fault Driven by Deformable Microplate Models

The San Andreas fault (SAF) marks the primary transform boundary between the Pacific and North American plates and has been studied intensively to determine the recurrence intervals of large earthquakes. Dense geologic and geodetic sampling along the SAF has revealed substantial variability in the slip rate along strike, with maxima approaching 40 mm/yr to the north and south of Los Angeles. In contrast, the San Bernardino segment of the SAF appears to slip at only 5–13 mm/yr, representing just 13–33% of the maximum SAF slip rate. Here we suggest that this spatial variation in slip rate may be explained by the interactions of deformable microplates driven by a combination of far-field plate motion boundary conditions and localized slip beneath the SAF. We find that the observed slip rate variations may be best described by models with 75% of Pacific-North America plate motion localized as slip beneath the SAF and 25% applied at the edges of the deforming plate boundary zone region. These models provide a mechanical explanation for why slip rates vary so significantly along the SAF and suggest a hybrid view of crustal deformation

in southern California in which relative plate motion is accommodated by a combination of both localized and distributed deformation.

4.1 Introduction

The southern California fault system accommodates ∼50 mm/yr of relative plate motion (DeMets et al., 1994; DeMets and Stein, 1990) between the North American and Pacific plates. The dominant feature of this system, the San Andreas fault (SAF), extends from the Gulf of California to the Mendocino triple junction and poses a significant seismic threat to both Los Angeles and San Francisco (Weldon et al., 2005; Working Group on California Earthquake Probabilities, 1995).

Geologic and geodetic studies of the southern SAF suggest a significant along-strike gradient in fault slip rate (Figure 4.1). To the north, on the Parkfield and Carrizo segments, slip rate estimates range from 27–41 mm/yr (54%–82% of the total relative plate motion) (Chuang and Johnson, 2011; Loveless and Meade, 2011b; Meade and Hager, 2005; Murray et al., 2001; Savage and Burford, 1973; Schmalzle et al., 2006; Segall, 2002; Sieh and Jahns, 1984). Both geologic and geodetic estimates of SAF slip rates suggest a minimum slip rate occurs on the San Bernardino segment ∼100 km east of Los Angeles, where estimates range from 2.9–18.5 mm/yr (6%–37% of total relative plate motion) (Chuang and Johnson, 2011; Loveless and Meade, 2011b; McGill et al., 2013; Meade and Hager, 2005). Further south, slip rate estimates increase sharply (35–42 mm/yr; 71%–83% total relative plate motion) on the Imperial and Cerro Prieto faults (Loveless and Meade, 2011b; Meade and Hager, 2005).

Many previous models of deformation in southern California may be effectively classified

as one of two distinct end–member models. The first class of model assumes that deformation occurs as localized slip on major faults. This hypothesis has served as the foundation for block models, which treat continental deformation as the rigid body rotation of a finite number of microplates and incorporate geologic and geodetic data to determine fault slip rates (e.g., Baldock and Stern, 2005; Bennett et al., 1996; Bird and Rosenstock, 1984; Cheng et al., 1987; Chuang and Johnson, 2011; Loveless and Meade, 2011b; Meade and Hager, 2005; Weldon and Humphreys, 1986). A second modeling approach draws on observations of diffuse seismicity and regional moment magnitude deficits to hypothesize that continental deformation is broadly distributed over the entirety of the Pacific-North America boundary zone (Ekström and England, 1989). Distributed deformation models may treat the lithosphere as a thin viscous sheet (e.g., Flesch et al., 2010) or as a finite number of crustal blocks subject to basal tractions (e.g., Bourne et al., 1998).

Here we present results from a suite of deformable microplate models (e.g., Langstaff and Meade, 2013) that combine both localized and distributed deformation to make testable slip rate predictions for major faults in southern California. This approach is complimentary to the boundary element models described by Marshall et al. (2009) and Cooke and Dair (2011). While those approaches feature a three-dimensional linear halfspace partially cut by faults, the models presented here are two-dimensional and are composed of fully disaggregated microplates. In both approaches faults are frictionless, and both models make testable predictions for fault slip rates. The Marshall et al. (2009) and Cooke and Dair (2011) studies consider only the Los Angeles region, whereas the deformable microplate models presented here describe the entire southern California region as a whole.

Figure 4.1 *(following page)*: Predicted along-strike slip rate for the San Andreas fault in southern California. The upper panel shows the rotated fault trace (red) and model microplate boundaries (blue). Topography within 300 km of the SAF is shaded in gray. Model-predicted slip rates are shown in the lower panel with fault segment names indicated at the top (SB - San Bernardino and CP - Cerro Prieto). The bold red line indicates our best-fit hybrid model slip rate predictions, with ∼36 mm/yr localized as deep slip beneath the SAF and ∼14 mm/yr of distributed deformation applied on the western boundary of the model domain. End-member models of purely distributed deformation (bottom dotted line) and entirely localized deep slip beneath the SAF (top dotted line) are also shown. Geologic and geodetic fault slip rate estimates are shown as black circles with reported 1-sigma error bars or as white circles when error estimates are not reported. Both observations and model predictions have maxima on the northern and southern segments of the model domain and both reach a minimum on the San Bernardino segment. Slip rates inferred from geologic and geodetic data are taken from: a. Savage and Burford, 1973; b. Meade and Hager, 2005; c. Murray et al., 2001; d. Segall, 2002; e. Loveless and Meade, 2011b; f. Schmalzle et al., 2006; g. Chuang and Johnson, 2011; h. Sieh and Jahns, 1984; i. Matmon et al., 2005; j. Matmon et al., 2005; k. Weldon and Sieh, 1985; l. McGill et al., 2013; m. Van der Woerd et al., 2006; n. Fialko, 2006.

Figure 4.1: (continued)

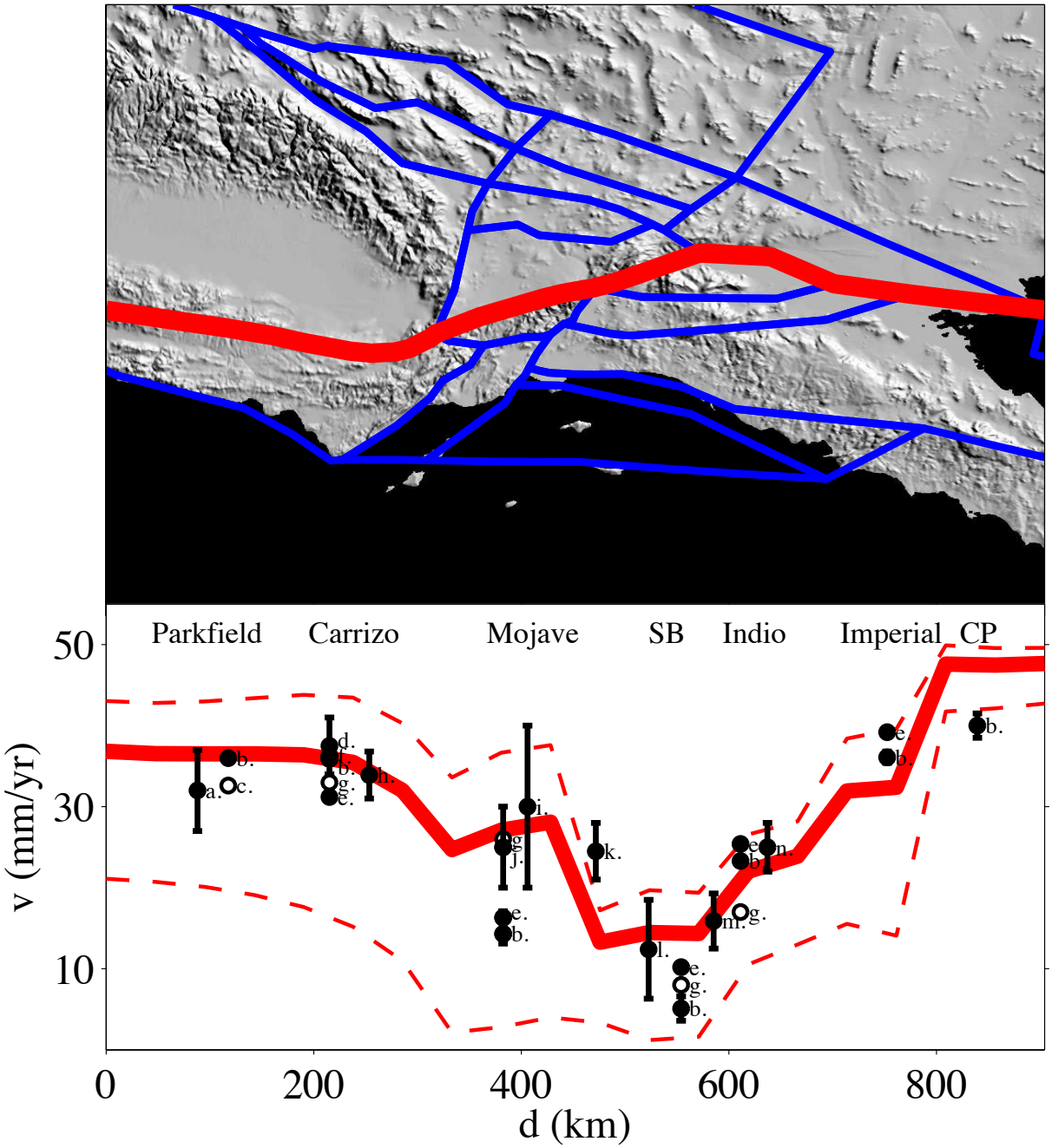

4.2 Deformable microplate models for southern California

Deformable microplate models are based on a two-dimensional, elastic, two-step finite element approach. In these models, elastic deformation accrues within microplate interiors and discrete slip occurs at microplate boundaries (faults). For the purposes of the models described below, all faults are assumed to be frictionless. Initially, microplate boundaries are defined and microplates are individually meshed. Next, a global mesh is constructed that encompasses the entire model domain. In the first finite element step, displacement boundary conditions are applied to the global mesh. Advected microplate boundaries (faults) are interpolated from the resulting global displacement field. In the second finite element step, individual finite element solutions are calculated for each microplate using the advected boundaries as displacement boundary conditions. In this way we maintain geometric compliance and prevent unrealistic gaps and overlaps of tectonic microplates. Given the two-dimensional nature of these models, all faults represented are purely strike-slip. Deformable microplate modeling is more fully discussed in Chapter 2 of this text and in Langstaff and Meade (2013).

Microplate boundaries in southern California are based on the locations of major mapped faults from the Southern California Earthquake Center Community Fault Model (Figure 4.1; Plesch et al., 2007). Together, this fault network forms 19 microplates constituting an idealized representation of the Pacific-North America plate boundary in southern California. The microplates used for the deformable models presented here range in size from ∼4,000 km^2 to ∼200,000 km^2, with a maximum block edge length of ∼1000 km (the North America block). In all models, the eastern boundary of the North America block is subject to a

zero-displacement boundary condition, approximating the nominally stable North American continent.

In addition to the North America boundary condition, we explore a series of boundary conditions motivated by two previous modeling approaches used to explain the driving mechanisms at transform plate boundary zones. In the first, continental transform tectonics are treated as a broad region of distributed shear subject to mantle tractions or far-field displacement conditions (e.g., Lamb, 1994a,b). The second approach draws from the suggestion of deeply routed and spatially constrained slip zones beneath major strike-slip faults (e.g., Corsini et al., 1991; Pili et al., 1997; West and Hubbard, 1997) and 15–40 km wide zones of mantle shear beneath such structures (e.g., Herquel et al., 1999; Moore et al., 2002; Rümpker et al., 2003; Thatcher and England, 1998) (though some authors have suggested shear zones of >100 km; Baldock and Stern, 2005) to suggest that transform motion occurs within localized lithospheric shear zones beneath large-scale strike slip faults such as the SAF (Platt and Becker, 2010; Platt et al., 2008). To test the relative contribution of each mechanism in producing observed slip rates on major southern California faults, we develop a suite of deformable microplate models for the region.

Distributed deformation end-member models are subject to 50 mm/yr displacement boundary conditions on the western edge of the model domain (Figure 4.2a), consistent with relative plate motion estimates from DeMets et al. (1994). Because of the assumed elastic rheology, in the absence of faulting these models predict smoothly varying displacement rates across the plate boundary zone. In contrast, localized lithospheric shear zone models apply all 50 mm/yr of relative plate motion as slip beneath the SAF (Figure 4.2b).

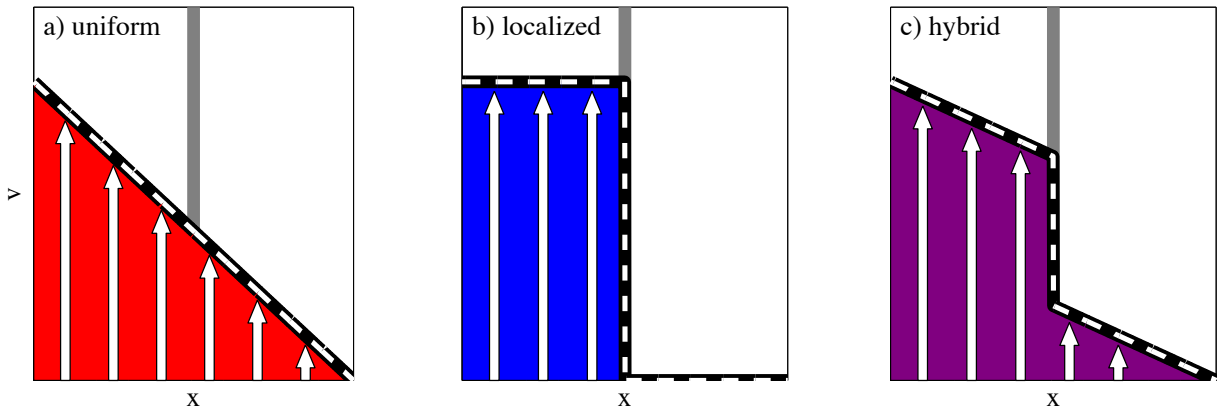

Figure 4.2: Velocity (v) versus distance (x) for idealized representations of end-member and hybrid elastically deformable microplate models. In all cases, the gray line indicates an idealized SAF and the eastern boundary of the model is fixed with a zero-displacement boundary condition. a) In the uniform (distributed) end-member, all relative motion between the Pacific and North American plates is applied to the western boundary of the model domain. Velocities decrease smoothly as distance from the western boundary increases. b) For end-member models where all slip is localized beneath the SAF, all relative motion between the Pacific and North American plates occurs on the SAF. In this idealized case, all points west of the SAF move at the same velocity as Pacific-North America plate motion while all points east of the SAF have no displacement. c) The hybrid approach incorporates both end-member behaviors. Here 50% of Pacific-North America plate motion occurs as deep slip beneath the SAF (as with the localized model) and 50% is applied on the western boundary (distributed approach). Velocities decrease smoothly to the east of the western boundary before dropping sharply at the SAF. East of the SAF, velocities smoothly decay to zero.

In the context of the models presented here, this condition is implemented as an applied displacement along the SAF before geometric compliance is enforced. We also consider hybrid models (e.g., Figure 4.2c), in which localized slip beneath the SAF increases incrementally, to find the combination of distributed deformation and localized deep slip that best match southern California slip rate estimates.

Model goodness-of-fit is assessed by comparing model-predicted SAF slip rates with along-strike geologic and geodetic slip rate estimates using the weighted sum of squared residuals (WSSR; Figure 4.3). Residuals are calculated as the difference between the geo-

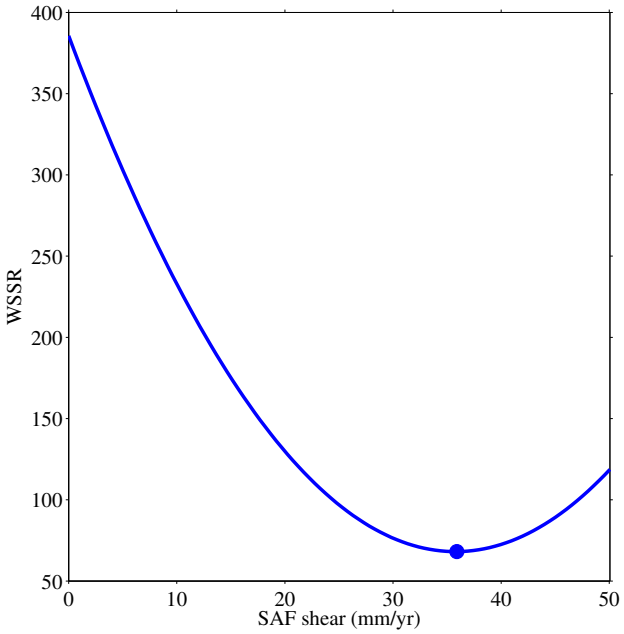

Figure 4.3: Weighted sum of squared residuals (WSSR) for all models considered as a function of the localized shear on the SAF in each model. WSSR values are highest for the end-member model with only distributed deformation (0 mm/yr of shear on the SAF) and decrease to a minimum WSSR value when ∼36 mm/yr of shear is localized on the SAF. The minimum WSSR value, plotted as the blue circle, is taken as the best-fit deformable microplate model for predicting SAF slip rates. The WSSR value increases again with additional shear localization on the SAF and is >100 for the purely localized SAF shear model.

logic or geodetic estimate and the model-predicted slip rate from the same location along strike. Residuals are then weighted by the error or the spread associated with each observation and squared. End-member models that are purely edge driven (0 mm/yr slip beneath the SAF) and those where all displacements conditions are confined to the SAF (50 mm/yr slip beneath the SAF) have high WSSR values, suggesting neither give SAF slip rate predictions that are a good fit to geologic and geodetic estimates. Entirely edge driven models have WSSR values >350, and SAF slip rate predictions are consistently below geologic and geodetic estimates (Figure 4.1). Models where deformation is entirely driven by localized slip beneath the SAF have WSSR values >100 and over predict SAF slip rates (Figure 4.1).

Fault Name	Distributed End-Member (mm/yr)	Localized End-Member (mm/yr)	Best-Fit Model (mm/yr)
SAF - Parkfield	(16 - 21)	(43 - 44)	(37)
SAF - Carrizo	(9 - 16)	(39 - 44)	(32 - 36)
SAF - Mojave	(2- 4)	(23 - 39)	(25 - 28)
SAF - San Bernardino	(1 - 2)	(13 - 20)	(10 - 14)
SAF - Indio	(8 - 13)	(22 - 29)	(21 - 24)
Imperial	(12 - 16)	(37 - 41)	(30 - 34)
Cerro Prieto	(42 - 43)	(50)	(48)
Garlock	0 - 3	(1) - 5	0 - 5
San Jacinto	(2 - 6)	(11 - 17)	(9 - 13)
Elsinore	(4 - 26)	(1 - 10)	(2 - 13)

Table 4.1: Predicted slip rates (mm/yr) for the SAF, Imperial, Cerro Prieto, Garlock, San Jacinto, and Elsinore faults from the distributed deformation end-member model, the localized slip end-member model, and the best-fit hybrid distributed deformation-localized shear model with $\sim$36 mm/yr of slip localized on the SAF. Right-lateral slip rates are denoted with parentheses while left-lateral slip rates are not. In general the distributed deformation end-member model underpredicts slip rates on the SAF, while the localized slip end-member model overpredicts them. In the purely localized slip case, the sense of slip on the Garlock fault changes direction along strike.

Notably, even in end-member models that localize all deformation on the SAF, slip rates along the central portion of the fault (e.g. the Mojave and San Bernardino segments) are <50 mm/yr, suggesting that the complex fault network in these regions plays a crucial role in partitioning deformation. In these regions, the SAF slips slower than the deep slip rate because of the curvilinear nature of the fault: here, SAF-bounding microplates must deform to satisfy the geometric compliance constraint and the equilibrium equations. These results suggest that a hybrid distributed deformation-localized slip model is required to explain the SAF slip rate. Slip rate predictions from the end-member and best-fit models are summarized in Table 4.1.

4.2.1 Distributed deformation end-member model

The distributed end-member model (Figures 4.1, 4.4, and 4.5 and Table 4.1), where all 50 mm/yr of displacement is applied on the western boundary of the model, predicts the correct sense of slip on all major southern Californian faults but significantly under predicts the slip rate on the SAF. SAF slip rates are highest in the east and west: the distributed deformation model predicts 16–21 mm/yr of right–lateral motion on the Parkfield segment, but slip rates fall to 9–16 mm/yr on the Carrizo segment and 2–4 mm/yr on the Mojave segment before reaching a minimum of 1–2 mm/yr on the San Bernardino portion of the fault. These results are one-and-a-half to three times less than geologic and geodetic estimates for Parkfield and Carrizo (Chuang and Johnson, 2011; Loveless and Meade, 2011b; Meade and Hager, 2005; Murray et al., 2001; Savage and Burford, 1973; Schmalzle et al., 2006; Segall, 2002; Sieh and Jahns, 1984) and up to five times less than geologic and geodetic estimates for the Mojave and San Bernardino segments (Chuang and Johnson, 2011; Loveless and

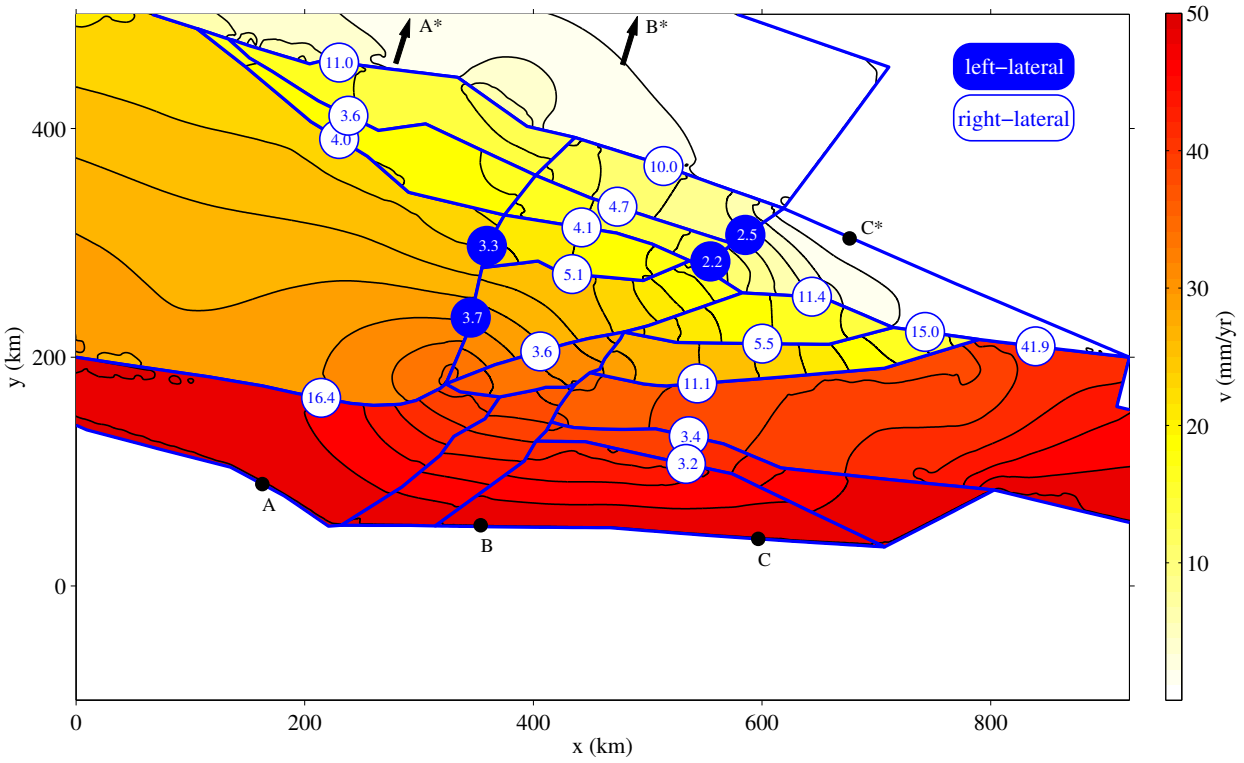

Figure 4.4: Slip rates and velocities from the distributed deformation end-member model. Microplate boundaries are shown as blue lines. Points A, A*, B, B*, C, and C* indicate end points for velocity profiles shown in Figure 4.5. Right-lateral slip rates are shown as white circles with blue text and left-lateral slip rates as blue circles with white text. For clarity, only representative slip rates are shown. Color shading shows velocity magnitudes, where redder colors indicate faster velocities. Maximum velocities equal the total relative motion between the Pacific and North American plates.

Meade, 2011b; Matmon et al., 2005; McCaffrey, 2005; McGill et al., 2013; Meade and Hager, 2005). Slip rate predictions increase south of San Bernardino to 8–13 mm/yr on the Indio segment, 12–16 mm/yr on the Imperial fault, and 42–43 mm/yr on the Cerro Prieto fault. Although predictions on the Cerro Prieto are consistent with block model estimates (Loveless and Meade, 2011b; Meade and Hager, 2005), all other predictions fall below geologic and geodetic estimates by a factor of two (Chuang and Johnson, 2011; Fialko, 2006; Loveless and Meade, 2011b; Meade and Hager, 2005).

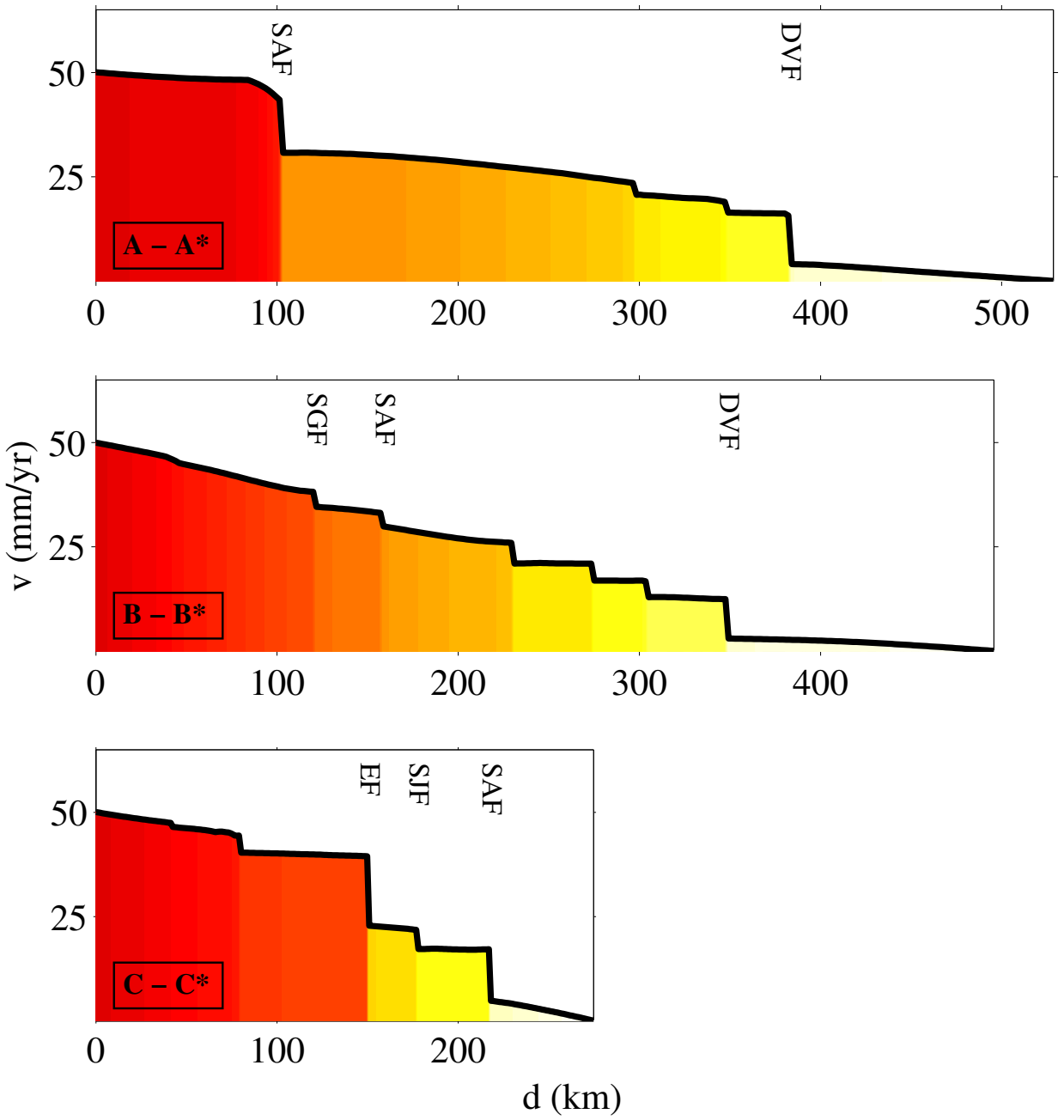

Figure 4.5: Velocity profiles across the northern (A-A*), central (B-B*), and southern (C-C*) extent of the distributed deformation end-member model. Profile endpoints are indicated in Figure 4.4. Color shading indicates velocity magnitudes and corresponds to velocity shading in Figure 4.4. Redder colors indicate faster velocities, with maximum velocities equal to the relative motion between the Pacific and North American plates. Here deformation decreases uniformly from west to east within microplates, though small discontinuities are evident at microplate boundaries (faults). In profile A offsets are the largest at the SAF, but offsets at the Death Valley fault and Elsinore fault are larger in profile B and profile C, respectively. SAF: San Andreas; DVF: Death Valley Fault; SGF: San Gabriel Fault; EF: Elsinore Fault; SJF: San Jacinto Fault.

The distributed deformation end-member model predicts 0–3 mm/yr of left-lateral slip on the Garlock fault and is broadly consistent with some block model calculations ranging from 0–4.7 mm/yr of sinisteral motion (Loveless and Meade, 2011b; Meade and Hager, 2005), but far less than the ∼10 mm/yr from Chuang and Johnson (2011). However, San Jacinto (2–6 mm/yr of right-lateral slip) and Elsinore (4–26 mm/yr of right-lateral slip) fault slip rate predictions fall far below (San Jacinto) and above (Elsinore) geologically and geodetically inferred rates (Chuang and Johnson, 2011; Loveless and Meade, 2011b; Meade and Hager, 2005).

As expected, although localized deformation does occur on faults in this end-member model, the majority of deformation is distributed. We show this by plotting velocity profiles at three transects (north, central, and south) across the model domain (Figure 4.5). Significant distributed deformation is observed in all three profiles: in Profiles A and B, velocities east of the SAF are >25 mm/yr, and in all cases the velocities between fault traces show a smooth, decreasing trend consistent with internal block deformation.

4.2.2 Localized slip end-member model

The localized deformation end-member model (Figures 4.1, 4.6, and 4.7 and Table 4.1) applies the entire 50 mm/yr displacement boundary condition on the SAF and over predicts the slip rate on the fault. Like the distributed deformation end-member, the entirely localized deformation model predicts the highest SAF slip rates on the northern and southern ends of the fault. Predicted slip rates decrease from Parkfield to San Berardino: 43–44 mm/yr on the Parkfield segment, 39–44 mm/yr on the Carrizo segment, 23–39 mm/yr on the Mojave segment, and 13–20 mm/yr on the San Bernardino segment. These results are 6–16 mm/yr

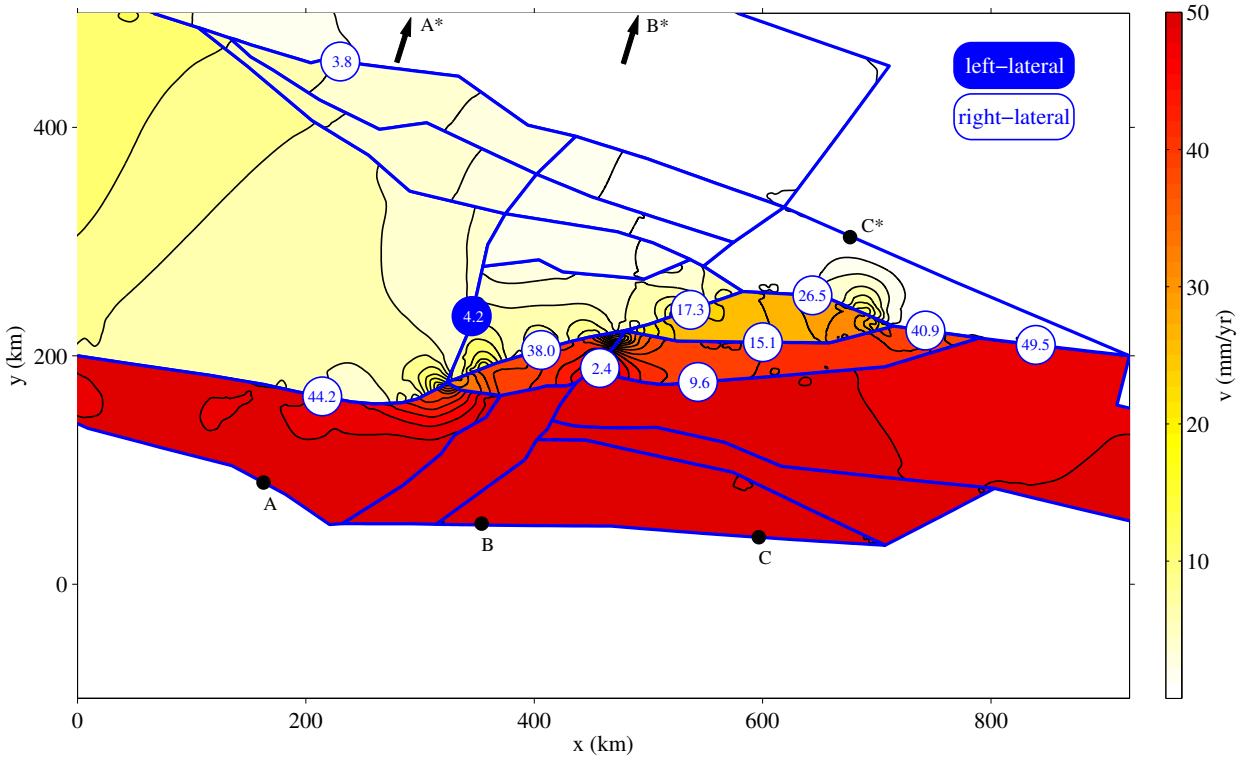

Figure 4.6: Slip rates and velocities from the localized SAF slip end-member model. Microplate boundaries are shown as blue lines. Points A, A*, B, B*, C, and C* indicate end points for velocity profiles shown in Figure 4.7. Right-lateral slip rates are shown as white circles with blue text and left-lateral slip rates as blue circles with white text. For clarity, only representative slip rates are shown. Color shading shows velocity magnitudes, where redder colors indicate faster velocities. Maximum velocities equal the total relative motion between the Pacific and North American plates.

higher than previously reported geologic and geodetic estimates for Parkfield (Meade and Hager, 2005; Murray et al., 2001; Savage and Burford, 1973). On the Carrizo segment, they fall within the range of the largest geodetic estimate (Segall, 2002) but are 8–13 mm/yr higher than other estimates (Chuang and Johnson, 2011; Loveless and Meade, 2011b; Meade and Hager, 2005; Schmalzle et al., 2006; Sieh and Jahns, 1984). The lower Mojave predictions agree with geologic estimates of 20–40 mm/yr (Matmon et al., 2005; McCaffrey, 2005) and block-model results of ∼26 mm/yr (Chuang and Johnson, 2011), but are 6–22 mm/yr higher

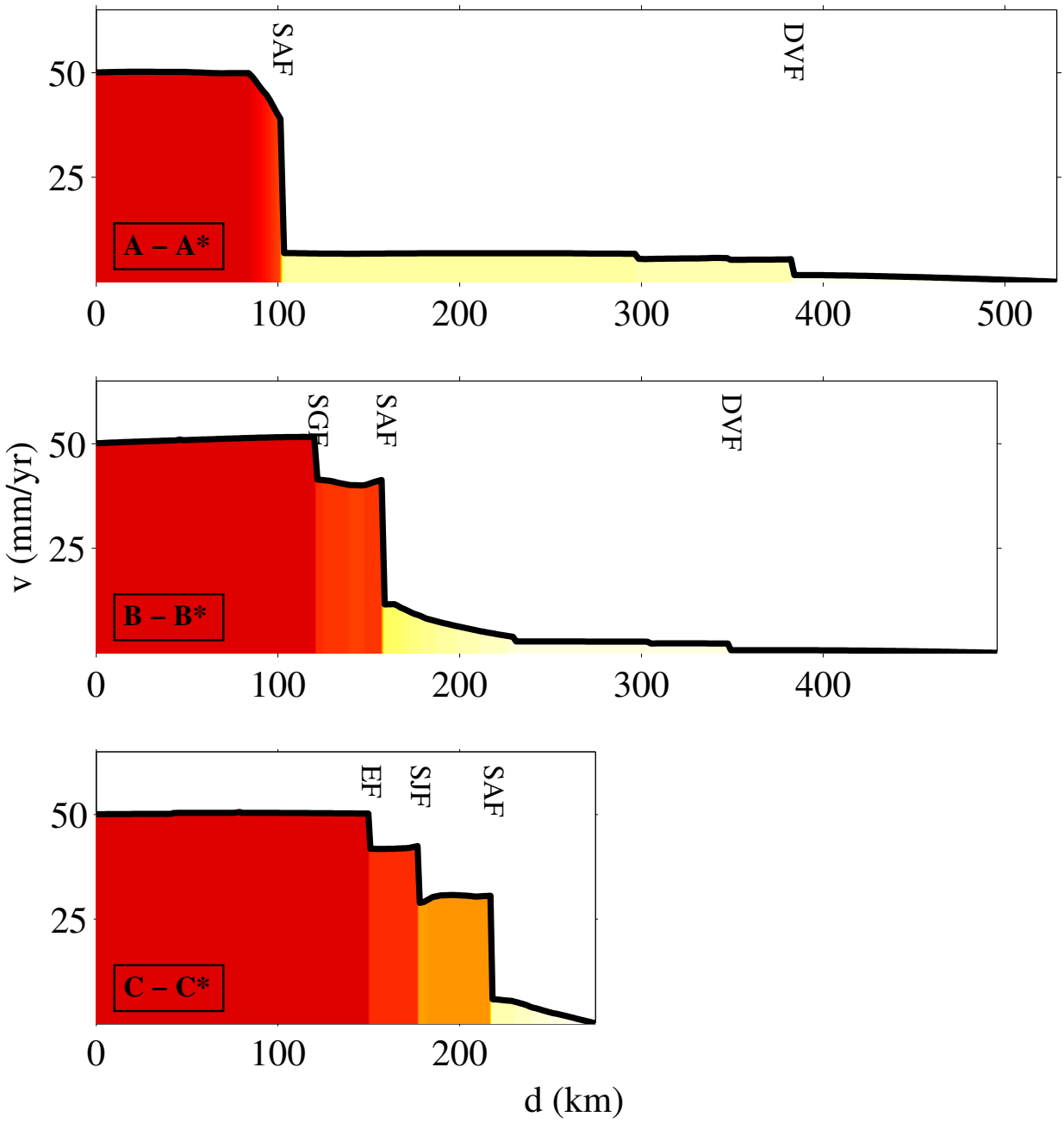

Figure 4.7: Velocity profiles across the northern (A-A*), central (B-B*), and southern (C-C*) extent of the localized SAF slip end-member model. Profile end points are indicated in Figure 4.6. Color shading indicates velocity magnitudes and corresponds to velocity shading in Figure 4.6. Redder colors indicate faster velocities, with maximum velocities equal to the relative motion between the Pacific and North American plates. Here deformation decreases slowly from west to east within microplates, with major discontinuities at microplate boundaries (faults). In all three profiles offsets are >25 mm/yr on the SAF, in keeping with localized displacements of 50 mm/yr on this structure. Velocities east of the SAF are small: <10 mm/yr in all cases. SAF: San Andreas; DVF: Death Valley Fault; SGF: San Gabriel Fault; EF: Elsinore Fault; SJF: San Jacinto Fault.

than other block-model estimates (Loveless and Meade, 2011b; Meade and Hager, 2005). Similarly, the localized end-member predictions on the San Bernardino are within range of geologic measurements (McGill et al., 2013), but higher than all block model calculations (Chuang and Johnson, 2011; Loveless and Meade, 2011b; Meade and Hager, 2005). South of San Bernardino, the model finds higher slip rates: the predicted slip rate on the Indio segment of the SAF is 22–29 mm/yr, in good agreement with InSAR (Fialko, 2006) and with some block model results (Loveless and Meade, 2011b; Meade and Hager, 2005). The predicted slip rate on the Imperial fault is 37–41 mm/yr, and the lower values fall within range of block–model estimates of 35.4–39.6 mm/yr (Loveless and Meade, 2011b; Meade and Hager, 2005); however, the predicted rate on the Cerro Prieto fault is 50 mm/yr of right–lateral motion and is ∼10 mm/yr higher than block model calculations from the same studies.

The localized deformation end-member slip rate predictions for the San Jacinto and Elsinore faults are more consistent with geologic and geodetic observations than the distributed deformation model previously described. Here 11–17 mm/yr of dexteral displacement is predicted for the San Jacinto fault and 1–10 mm/yr for the Elsinore fault. These predictions agree well with block model calculations for the San Jacinto ranging from 10.7–14 mm/yr, and the lower slip rates are consistent with Elsinore slip rates of 2–4 mm/yr (Chuang and Johnson, 2011; Loveless and Meade, 2011b; Meade and Hager, 2005). However, our localized deformation end-member predicts a Garlock fault that is left-lateral in the west (up to ∼5 mm/yr), right-lateral on the central portion (∼1 mm/yr), and then left-lateral again on the eastern end of the fault (∼0.5 mm/yr). These results are inconsistent with geodetic obser-

vations of an entirely left-lateral Garlock fault (Chuang and Johnson, 2011; Loveless and Meade, 2011b; Meade and Hager, 2005).

SAF-perpendicular velocity profiles at three transects (north, central, and south) (Figure 4.7) reflect the localization of slip on the SAF. On all three profiles the largest velocity differential occurs on the SAF, and in each of the profiles the velocities east of the SAF are <10 mm/yr, suggesting limited distributed deformation.

4.2.3 Best-fit model: Hybrid localized and distributed deformation

By minimizing WSSR values (Figure 4.3), we find that models with ∼36 mm/yr of localized slip beneath the SAF and ∼14 mm/yr of additional western-boundary displacement best predict the observed SAF slip rate gradient. This model predicts ∼37 mm/yr of right-lateral slip on the Parkfield segment, consistent with the upper bound of the 32 ± 5 mm/yr geologic estimate from Savage and Burford (1973) and just higher than block model estimates of 36 ± 0.5 mm/yr (Meade and Hager, 2005) and ∼33 mm/yr (Murray et al., 2001). Slip rate predictions of 32–36 mm/yr for the Carrizo segment are also in agreement with geologic and geodetic estimates: these rates are within the range of estimates from Segall (2002; 34–41 mm/yr), Schmalzle et al. (2006; 36.25 ± 1.75 mm/yr), Sieh and Jahns (1984; 33.9 ± 2.9 mm/yr), Meade and Hager (2005; 35.9 ± 0.7 mm/yr), and Chuang and Johnson (2011; ∼33 mm/yr), and just less than block model estimates from and Loveless and Meade (2011b; 31.2 ± 0.2 mm/yr). On the Mojave segment, slip rate predictions of 25–28 mm/yr of dexteral displacement are consistent with geologic measurements of 30 ± 10 mm/yr (Matmon et al., 2005) and geodetic estimates of 25 ± 5 mm/yr (McCaffrey, 2005), and ∼26 mm/yr (Chuang and Johnson, 2011), but are higher than block model estimates of 14.3 ± 1.2

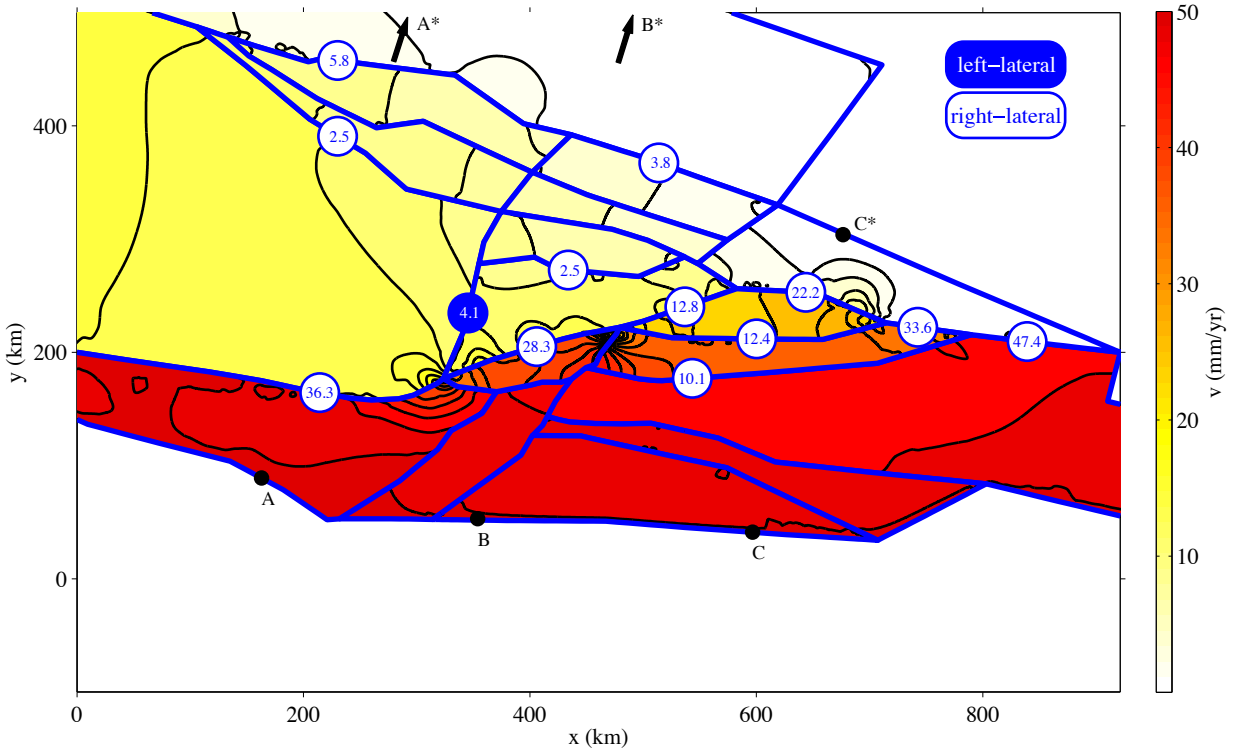

Figure 4.8: Slip rates and velocities for the best-fit hybrid distributed deformation-localized slip model. Microplate boundaries are shown as blue lines. Points A, A*, B, B*, C, and C* indicate endpoints for velocity profiles shown in Figure 4.9. Right-lateral slip rates are shown as white circles with blue text and left-lateral slip rates as blue circles with white text. For clarity, only representative slip rates are shown. Color shading shows velocity magnitudes, where redder colors indicate faster velocities. Maximum velocities equal the total relative motion between the Pacific and North American plates.

(Meade and Hager, 2005) and 16.3 ± 0.8 (Loveless and Meade, 2011b). Slip rate predictions, like geologic and geodetic estimates, reach a minimum on the San Bernardino segment of the SAF, with best-fit models finding 13–14 mm/yr of slip. This rate is consistent with geologic measurements of 12.4 ± 6.1 mm/yr (McGill et al., 2013), but higher than block model estimates, which range from 3.6–10.5 mm/yr (Chuang and Johnson, 2011; Loveless and Meade, 2011b; Meade and Hager, 2005). Moving further south, the slip rate increases again on the Indo segment of the SAF, where best–fit model predictions are 22–24 mm/yr.

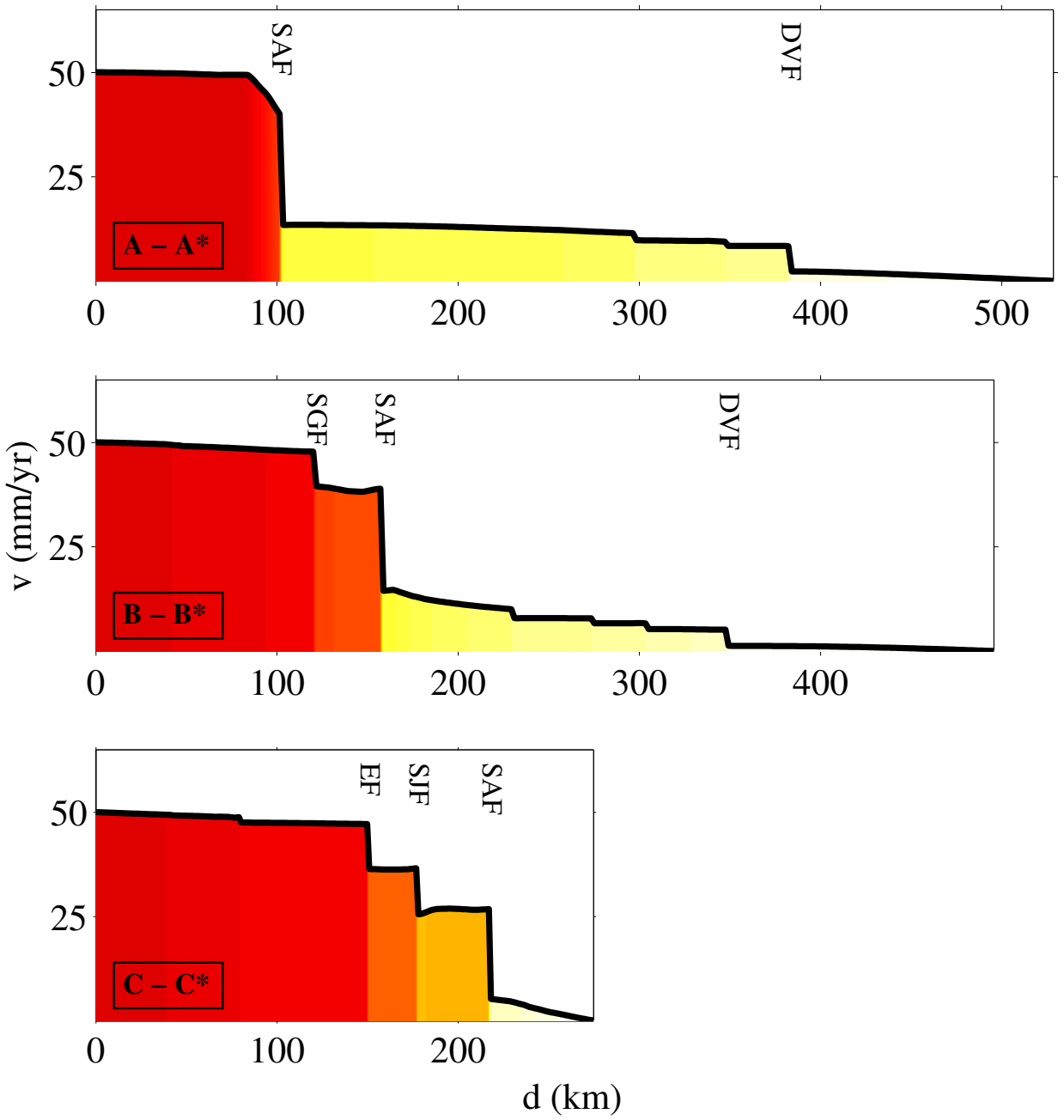

Figure 4.9: Velocity profiles across the northern (A-A*), central (B-B*), and southern (C-C*) extent of the best-fit hybrid distributed deformation-localized slip model. Profile endpoints are indicated in Figure 4.8. Color shading indicates velocity magnitudes and corresponds to velocity shading in Figure 4.8. Redder colors indicate faster velocities, with maximum velocities equal to the relative motion between the Pacific and North American plates. Here deformation decreases uniformly from west to east within microplates, but discontinuities are evident at microplate boundaries (faults). In all three profiles, the largest offsets occur on the SAF, in keeping with localized slip of ∼36 mm/yr on this structure. SAF: San Andreas Fault; DVF: Death Valley Fault; SGF: San Gabriel Fault; EF: Elsinore Fault; SJF: San Jacinto Fault.

Here INSAR results suggest a slip rate of 25 ± 3 mm/yr (Fialko, 2006) and Meade and Hager (2005) estimate 23.3 ± 0.5 mm/yr, but other block models resolve both higher (25.4 ± 0.2 mm/yr; Loveless and Meade, 2011b) and lower (∼17 mm/yr, Chuang and Johnson, 2011) slip rates. Slip rate predictions on the southernmost extension of the SAF, the Imperial (∼32 mm/yr) and Cerro Prieto (∼48 mm/yr) faults are lower (35.4–39.6 mm/yr) and higher (40 ± 1.5 mm/yr) than block model estimates, respectively (Loveless and Meade, 2011b; Meade and Hager, 2005).

The best-fit hybrid distributed deformation-localized SAF slip model also effectively explains the sense of slip and slip rate magnitude on other major southern California structures (Figure 4.8). In particular, San Jacinto slip rates are highest (12–13 mm/yr dexteral motion) on the northern extent of the fault and decrease to 9–10 mm/yr towards the south. These numbers are consistent with right–lateral block model estimates of 11.9 ± 1.2 mm/yr (Meade and Hager, 2005) and ∼11 mm/yr (Chuang and Johnson, 2011) and are slightly less than the ∼14 mm/yr found by Loveless and Meade (2011b). Model results also indicate an entirely left-lateral Garlock fault, with maximum slip rates of ∼5mm/yr in the west decreasing to ∼0.5mm/yr along the eastern portion of the fault. These results are consistent with reported eastward-decreasing slip rate gradients (3.2 ± 1.5 mm/yr to 1.1 ± 1.9 mm/yr, Meade and Hager, 2005) and estimates of ∼2 mm/yr of left-lateral slip (Loveless and Meade, 2011b). Block model estimates from Chuang and Johnson (2011) of ∼10 mm/yr are significantly higher than Garlock slip rate predictions from our best-fit model. Significantly, slip rates on the Elsinore fault are much higher than previously estimated values, ranging from ∼2–8 mm/yr of right-lateral displacement in the north to ∼11–13 mm/yr of dexteral motion in

the south. Typical estimates of slip range from 2–4 mm/yr (Chuang and Johnson, 2011; Loveless and Meade, 2011b; Meade and Hager, 2005).

While discrete slip is localized at block boundaries, distributed deformation is also evident in our best-fit hybrid model. We visualize this partitioning by showing San Andreas-perpendicular velocity profiles along three transects (north, central, and south) across the model domain (Figure 4.9). In all profiles, large velocity discontinuities occur at major faults, indicating localized slip on these structures. The largest velocity offsets occur at the SAF, but significant velocity discontinuities are also observed on the San Jacinto, San Gabriel, Elsinore, and Death Valley faults. In contrast, microplate interiors are characterized by smooth velocity gradients that decrease eastward. Internal microplate strain rates are relatively low, averaging 7×10^{-16} s^{-1} and 2×10^{-15} s^{-1} in the Sierra and western Mojave blocks, respectively.

4.3 Discussion

Unlike Cooke and Dair (2011), who predicted the SAF slip rate gradient along strike from three-dimensional boundary element models, the SAF slip rate predicted here is generated by a two-dimensional modeling approach. Although a fully three-dimensional deformable microplate model might allow for improved accuracy in slip rate predictions, the goodness-of-fit found with the two-dimensional model suggests that along-strike variations in fault geometry is sufficient to reproduce observed slip rate gradients.

The model that best explains SAF slip rate observations, a hybrid approach between distributed deformation and localized slip beneath the SAF, may provide constraints on

the nature of the Pacific-North America plate boundary. While distributed deformation end-member models are consistent with an offshore Pacific plate boundary (west of Los Angeles), end-member approaches with all displacement localized as slip beneath the SAF effectively treat the SAF as the boundary between the Pacific and North American plates. The hybrid nature of our best-fit model may suggest a broad plate boundary zone. Such an explanation would be consistent with traditional interpretations of the Pacific-North America boundary that assume that the SAF forms the definitive structure between the two plates (e.g. Atwater, 1970), but would also allow for forcing from a stable Pacific plate (here the western boundary of our model).

The partitioning of boundary conditions may also reflect the eastern migration of the plate boundary. These observations may be consistent with the hypothesis offered by Nur et al. (1993), which suggests that a new Landers-Mojave fault line is emerging to compete with the SAF in accommodating Pacific-North America motion. Further, the eastward migration of the Pacific-North America plate boundary has previously been hypothesized in Baja California, where Stock and Hodges (1989) have proposed the Pacific plate capture of the Baja California block.

4.4 Conclusions

Deformable microplate models make testable slip rate predictions for the major strike-slip faults in southern California, and may provide a mechanical explanation for observed slip rate gradients on the SAF. Using this approach, we have developed a suite of models ranging from purely distributed deformation (all relative plate motion is applied on the western boundary

of the model domain) to locally driven (where all relative motion is localized beneath the SAF). By minimizing the WSSR, we determine that hybrid models that incorporate $\sim$ 36 mm/yr of deep slip beneath the SAF and $\sim$14 mm/yr of western boundary displacement best describe the geologically and geodetically observed slip rate gradient along the SAF.

Chapter 5

Interseismic modulation of stress orientations in southern California predicted by geodetically constrained block models and regional background stresses

We derive an analytical equation for the interseismic principal stress rotation rate as a function of a tectonic stressing rate, a regional background stress, and time. Parameter sensitivity analyses are shown to constrain the magnitude of principal stress rotations at different background stresses and stressing rates. We then calculate the principal stress rotation rates across an idealized, infinitely long strike-slip fault at different background stresses. Finally, we combine stressing rate estimates from geodetically constrained block models with candidate background stress fields to quantify the temporal evolution of stress over the earthquake cycle in southern California. Observations of principal stress axes rotations have been previously documented both before and after large earthquake events, and post-mainshock seismicity has indicated ~ 1.5 degree/yr of principal stress axes rotation in

the vicinities of the Landers, Northridge, Elmore Ranch and Superstition Hills, and Ridgecrest earthquakes. We compare the model-predicted principal stress axes rotation rates to those previously reported in southern California to constrain the regional background stress magnitudes that may be consistent with the inferred principal stress rotations. These models of time-dependent stress orientations also provide mechanical constraints on the range of stress variability possible through a simple earthquake cycle, including the orientation of stresses just prior to large ruptures.

5.1 Introduction

The southern California fault system accommodates ∼50 mm/yr of relative plate motion between the Pacific and North American plates (DeMets and Dixon, 1999; DeMets and Stein, 1990). Previous research has characterized the regional stress field, and the associated principal stress field orientations, within which the fault system operates: borehole breakout measurements of stress have suggested that the stress field may be heterogeneous, with maximum horizontal principal stress values ranging from N0° to N59° over six regions in southern California (Wilde and Stock, 1997). Borehole measurements at the Cajon Pass and San Andreas Fault Observatory at Depth (SAFOD) sites on the San Berardino and Parkfield segment of the SAF, respectively, have revealed stress orientations that vary by up to 92°-100° over 2.6-1.71 km in the Cajon Pass and by 44° over 1.2 km at the SAFOD borehole (Hickman and Zoback, 2004; Shamir and Zoback, 1992; Townend and Zoback, 2004; Zoback and Healy, 1992; Zoback et al., 1987). Other analyses of the SAFOD borehole have

suggested that principal stresses are oriented at high angles to the San Andreas Fault (SAF) (Boness and Zoback, 2004; Zoback et al., 2011), and measurements of fault core gauge from 2.7 km depth may suggest the fault material is very weak (Carpenter et al., 2011; Lockner et al., 2011).

Beyond the in situ borehole observations, regional characterizations of the southern California stress field have been obtained through inversions of earthquake first motions and focal mechanisms (e.g., Gephart and Forsyth, 1984; Hardebeck and Hauksson, 2001; Hardebeck and Michael, 2006; Hauksson, 1994; Jones, 1988; Michael, 1987; Yang and Hauksson, 2013; Zhao et al., 1997). While regional principal stresses cannot be constrained by a single fault plane solution (McKenzie, 1969), a variety of different focal mechanisms may be used to infer the orientation and relative magnitude of the principal stresses (Bott, 1959). Focal mechanism and first motion studies for southern California have variously suggested that the stress field may be either regionally homogeneous ($< 20^\circ$ misfit) (Abers and Gephart, 2001; Gephart and Forsyth, 1984; Hardebeck, 2010; Hardebeck and Michael, 2006) or heterogeneous ($> 20^\circ$ misfit) (Hardebeck and Hauksson, 2001; Hardebeck and Michael, 2006; Hauksson, 1990, 1994; Rivera and Kanamori, 2002; Yang and Hauksson, 2013). Focal mechanism inversion studies have also suggested an interseismic rotation rate of the maximum compressive stress orientation of up to 2 degrees/yr (Hardebeck and Hauksson, 2001), and principal stress rotations near the San Bernardino segment of the San Andreas fault since the 1857 Fort Tejon earthquake have been proposed from focal mechanism data (Jones, 1988). Here, Jones (1988) observes both a change from reverse to normal faulting at the Mojave-San Bernardino boundary and a coincident decrease in stress magnitude (calculated

from focal mechanisms) at the termination point of the Fort Tejon earthquake. Jones (1988) hypothesizes that the 1857 stress field on the San Bernardino segment may have stalled the rupture but argues that the current stress field, which, from focal mechanisms, features a small angle (∼43 degrees) between the maximum horizontal stress and the SAF, has rotated to be particularly favorable to rupture propagation.

The role of earthquakes in modulating the total regional stress field is similarly debated: some focal mechanism inversions suggest that the pre- and post-Landers regional stress fields are aligned and represent the regional background stress state (Hardebeck, 2010; Townend and Zoback, 2004). However, other studies have documented 7°-20° of rotation after the same event (Hardebeck and Hauksson, 2001; Hauksson, 1994), suggesting the earthquake significantly altered the regional stress field. Similarly, ∼10°-15° of rotation in the maximum compressive stress orientation was observed following the 1983 M_W = 6.7 Coalinga earthquake (Hardebeck and Michael, 2006; Michael, 1987), and ∼14° of rotation was inferred after the M_W = 6.1 Joshua Tree earthquake (Hauksson, 1994). P-wave polarity data indicates a 17° p-axis rotation in the two weeks following the 1994 Northridge earthquake, however, stress orientations recovered to their pre-earthquake state within two years of the mainshock (Zhao et al., 1997). Others have inferred from focal mechanism studies that stress fields are locally (∼30-50 km) homogenous (Abers and Gephart, 2001; Gephart and Forsyth, 1984). However, focal mechanism inversions of aftershocks in the Landers region are inconsistent with a homogeneous stress field and may reflect stress field modulation by the large mainshock (Abers and Gephart, 2001).

Differences in estimates of earthquake modulation of stress over the earthquake cycle

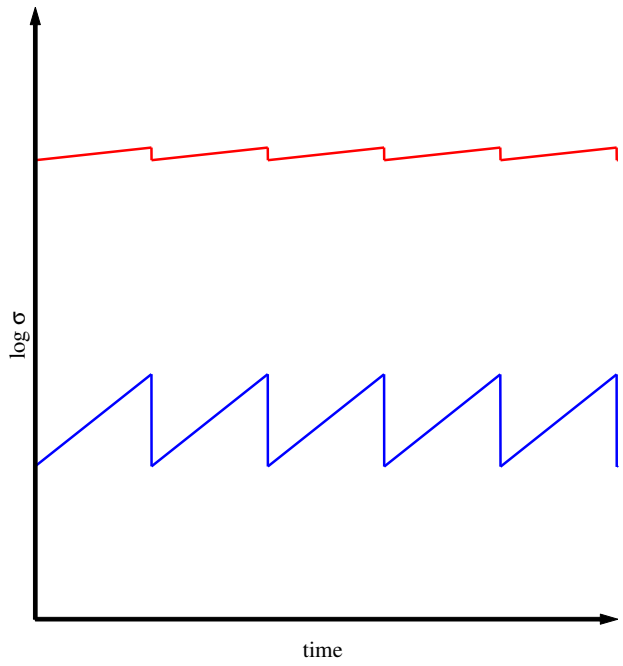

Figure 5.1: Idealized representation of total stress versus time for high (red) and low (blue) background stresses over five earthquake cycles. Here the total stress is a function of the background stress and the tectonic stress that is accumulated and relieved over the earthquake cycle. The tectonic stress accumulation rate is equal for the two models shown here and tectonic stress is released in equally sized stress drops. Tectonic stress accumulation and earthquake stress drops result in large modulations of the total stress for the low background stress case. For the high background stress case, the magnitude of the background stress is much larger than the tectonic stress accumulation and earthquake stress drop, and the relative change of the total stress is smaller.

bear on the uncertainty regarding the magnitude of the background stress field in southern California (Figure 5.1). If large earthquakes do not change the regional stress field, then the magnitude of the background stress may be much larger than the earthquake stress drops (Figure 5.1). However, if large earthquakes result in a rotation of the regional stress field (Hardebeck and Michael, 2006; Smith and Heaton, 2011), then the ratio between the background stress and the earthquake stress drop must be much smaller. In these cases, we may expect the orientation of the maximum principal stress to evolve over the course of the earthquake cycle (e.g., Hardebeck and Hauksson, 2001; Jones, 1988). Here we analyze interseismic stressing rate models to constrain the range of background stresses consistent with interseismic p-axis rotations inferred from focal mechanism studies.

5.2 Analytical solution for the principal stress axes rotation rate

If the stress drops associated with large earthquakes significantly alter regional stress fields (e.g., Hardebeck and Michael, 2006; Hauksson, 1994; Smith and Heaton, 2011), then we may reasonably expect stress orientations to evolve during the intersiesmic loading period of the earthquake cycle (e.g., Hardebeck and Hauksson, 2001; Jones, 1988). If, for example, an earthquake has a median stress drop of 4 MPa (Allmann and Shearer, 2009), then the regional background stress may only be ∼10-1000 times smaller or larger than the stress drop. If the background stress is too high, the earthquake stress drop will be small relative to the background stress and will not be resolved. If the background stress is too low, the stress drop will be small compared to the tectonic loading rate ($\sim 10^3 - 10^4$ Pa/yr; Loveless and Meade, 2011b) and stress will very quickly (e.g., months to one year) realign with the

accumulated tectonic stress. If 10° of stress field rotation was observed after the Coalinga mainshock (Hardebeck and Michael, 2006), then we may expect to observe ∼10° of stress field rotation during the interseismic period as the fault experiences elastic reloading.

To constrain the tectonic conditions under which rotations in the orientations of the principal stress tensor may occur, we use an analytical equation derived from Mohr's circle that describes the angle, θ, between the maximum principal stress and the normal vector to the fault:

$$\theta = \frac{1}{2}\tan^{-1}\left(\frac{2\sigma_{xy}^{T}}{\sigma_{xx}^{T} - \sigma_{yy}^{T}}\right), \tag{5.1}$$

where σ_{xx}^{T}, σ_{yy}^{T}, and σ_{xy}^{T} are components of $\boldsymbol{\sigma}^{\mathbf{T}}$, the total stress tensor. Here we define the total stress tensor, $\boldsymbol{\sigma}^{\mathbf{T}}$, to be,

$$\boldsymbol{\sigma}^{\mathbf{T}} = \boldsymbol{\sigma}^{\mathbf{b}} + \dot{\boldsymbol{\sigma}}t \tag{5.2}$$

where $\boldsymbol{\sigma}^{\mathbf{b}}$ is the constant background stress, $\dot{\boldsymbol{\sigma}}$ is the interseismic stressing rate, and t is time. By substituting the total stress equation (5.2) into the Mohr's circle equation (5.1) for θ and taking the derivative with respect to time, we can find an analytical equation for the rotation rate, $\dot{\theta}$, of the orientation of the principal stresses:

$$\dot{\theta} = \frac{\dfrac{2\dot{\sigma}_{xy}}{\sigma_{xx}^{b} - \sigma_{yy}^{b} + \dot{\sigma}_{xx}t - \dot{\sigma}_{yy}t} - \dfrac{(2\sigma_{xy}^{b} + \dot{\sigma}_{xy}t)(\dot{\sigma}_{xx} - \dot{\sigma}_{yy})}{(\sigma_{xx}^{b} - \sigma_{yy}^{b} + \dot{\sigma}_{xx}t - \dot{\sigma}_{yy}t)^{2}}}{2\left(\dfrac{(2\sigma_{xy}^{b} + 2\dot{\sigma}_{xy}t)^{2}}{(\sigma_{xx}^{b} - \sigma_{yy}^{b} + \dot{\sigma}_{xx}t - \dot{\sigma}_{yy}t)^{2}} + 1\right)}. \tag{5.3}$$

We can further simplify this equation such that,

$$\dot{\theta} = -\frac{\dot{\sigma}_{xx}\sigma^b_{xy} - \dot{\sigma}_{xy}\sigma^b_{xx} + \dot{\sigma}_{xy}\sigma^b_{yy} - \dot{\sigma}_{yy}\sigma^b_{xy}}{\left(\frac{4(\sigma^b_{xy} + \dot{\sigma}_{xy}t)^2}{(\sigma^b_{xx} - \sigma^b_{yy} + \dot{\sigma}_{xx}t - \dot{\sigma}_{yy}t)^2} + 1\right)(\sigma^b_{xx} - \sigma^b_{yy} + \dot{\sigma}_{xx}t - \dot{\sigma}_{yy}t)^2}. \tag{5.4}$$

5.3 Deviatoric stress rotation rate

Focal mechanism studies of regional stress rely on earthquake first motion data, and, consequently, can only describe the deviatoric portion of the stress tensor (Michael, 1984). Focal mechanisms provide information on the earthquake slip and therefore cannot constrain the isotropic (i.e. volumetric change) portion of the stress tensor. In focal mechanism inversion studies only the relative magnitudes of the deviatoric (i.e. distortion) component of the stress tensor are found (Michael, 1984; Zang and Stephansson, 2010). Reported principal stress orientations and principal stress rotation rates (e.g., Hardebeck and Hauksson, 2001) are thus describing the rotations in the deviatoric stress tensor. The Mohr's circle is a representation of total stress, but we can show that rotations in the deviatoric stress tensor are equal to rotations in the axis of the principal stresses. For the two-dimensional case the mean background stress, σ^b_m, and mean stressing rate, $\dot{\sigma}_m$, are:

$$\sigma^b_m = \frac{\sigma^b_{xx} + \sigma^b_{yy}}{2} \tag{5.5}$$

and

$$\dot{\sigma}_m = \frac{\dot{\sigma}_{xx} + \dot{\sigma}_{yy}}{2}. \tag{5.6}$$

The deviatoric background stress tensor is defined as,

$$\partial\boldsymbol{\sigma}^{\mathrm{b}} = \begin{bmatrix} \sigma^b_{xx} - \sigma^b_m & \sigma^b_{xy} \\ \sigma^b_{xy} & \sigma^b_{yy} - \sigma^b_m \end{bmatrix} \tag{5.7}$$

and the deviatoric stressing rate is,

$$\partial\dot{\boldsymbol{\sigma}} = \begin{bmatrix} \dot{\sigma}_{xx} - \dot{\sigma}_m & \dot{\sigma}_{xy} \\ \dot{\sigma}_{xy} & \dot{\sigma}_{yy} - \dot{\sigma}_m \end{bmatrix}. \tag{5.8}$$

We can then find the deviatoric rotation rate as follows:

$$\partial\dot{\theta} = -\frac{(\dot{\sigma}_{xx} - \dot{\sigma}_m)\sigma^b_{xy} - \dot{\sigma}_{xy}(\sigma^b_{xx} - \sigma^b_m) + \dot{\sigma}_{xy}(\sigma^b_{yy} - \sigma^b_m) - (\dot{\sigma}_{yy} - \dot{\sigma}_m)\sigma^b_{xy}}{\left(\dfrac{4(\sigma^b_{xy} + \dot{\sigma}_{xy}t)^2}{\lambda} + 1\right)\lambda} \tag{5.9}$$

where

$$\lambda = [\sigma^b_{xx} - \sigma^b_m - (\sigma^b_{yy} - \sigma^b_m) + (\dot{\sigma}_{xx} - \dot{\sigma}_m)t - (\dot{\sigma}_{yy} - \dot{\sigma}_m)t]^2. \tag{5.10}$$

Grouping similar terms together,

$$\lambda = [(\sigma^b_{xx} - \sigma^b_{yy}) + (\sigma^b_m - \sigma^b_m) + (\dot{\sigma}_{xx} - \dot{\sigma}_{yy})t + (\dot{\sigma}_m - \dot{\sigma}_m)]^2, \tag{5.11}$$

and $\partial\dot{\theta}$ becomes

$$\partial\dot{\theta} = -\frac{(\dot{\sigma}_{xx} - \dot{\sigma}_{yy})\sigma^b_{xy} + (\dot{\sigma}_m - \dot{\sigma}_m)\sigma^b_{xy} + (\sigma^b_{yy} - \sigma^b_{xx})\dot{\sigma}_{xy} + (\sigma^b_m - \sigma^b_m)\dot{\sigma}_{xy}}{\left(\dfrac{4(\sigma^b_{xy} + \dot{\sigma}_{xy}t)^2}{\lambda} + 1\right)\lambda}. \tag{5.12}$$

The σ^b_m and $\dot{\sigma}_m$ terms cancel such that:

$$\partial\dot{\theta} = -\frac{\dot{\sigma}_{xx}\sigma^b_{xy} - \dot{\sigma}_{xy}\sigma^b_{xx} + \dot{\sigma}_{xy}\sigma^b_{yy} - \dot{\sigma}_{yy}\sigma^b_{xy}}{\left(\dfrac{4(\sigma^b_{xy} + \dot{\sigma}_{xy}t)^2}{(\sigma^b_{xx} - \sigma^b_{yy} + \dot{\sigma}_{xx}t - \dot{\sigma}_{yy}t)^2} + 1\right)(\sigma^b_{xx} - \sigma^b_{yy} + \dot{\sigma}_{xx}t - \dot{\sigma}_{yy}t)^2}, \tag{5.13}$$

or

$$\partial\dot{\theta} = \dot{\theta}. \tag{5.14}$$

Results from an analysis of $\dot{\theta}$ can therefore be directly compared to regional focal mechanism and earthquake first motion inversions.

5.4 Rotation rate sensitivity analysis

Before we can constrain the range of regional background stresses required to generate intersiesmic rotations in the principal stresses in California, it is useful to understand the rotation rate sensitivity to the regional background stress, stressing rate, and time parameters. We construct an idealized one hundred year interseismic model where the background stress satisfies the condition $\sigma^b_{xx} = \sigma^b_{yy} = \sigma^b_{xy} = \sigma^*$, $\dot{\sigma}_{xy} = 0$, and $\dot{\sigma_{xx}}/\dot{\sigma}_{yy} = 2$. These assumptions allow us to simplify the rotation rate equation:

$$\dot{\theta} = -\frac{\sigma^*\dot{\sigma}_{xx}}{8\sigma^{*2} + \dot{\sigma}^2_{xx}t^2}. \tag{5.15}$$

We explore values for the principal stress rotation rate where $\sigma^* = \pm 10^1$ Pa to $\pm 10^{12}$ Pa and $\dot{\sigma}_{xx} = \pm 10^1$ Pa/yr to $\pm 10^6$ Pa/yr. Values for background stress were chosen to encompass the entire spectrum of possible background stresses and to extend well beyond the

rupture model stress approximations (Fliss et al., 2005; Pelties et al., 2012). Stressing rates up to $\pm 10^6$ Pa/yr encompass the block-model derived stressing rates inferred for southern California (Loveless and Meade, 2011b). The geodetically constrained block model is used to calculate fault slip rates (or slip deficit rates) and stressing rates on each fault are calculated from Okada (1992). The total stressing rate is the stress at each point calculated from the slip deficit for all faults considered in the southern California fault system (Loveless and Meade, 2011b). Using Equation 5.15 for the rotation rate, we can show analytically that,

$$\lim_{\sigma^* \to 0} \dot{\theta} = -\frac{0}{0 + \dot{\sigma}_{xx}^2 t^2} = 0 \tag{5.16}$$

and

$$\lim_{\sigma^* \to \infty} \dot{\theta} = -\frac{\infty}{\infty^2 + \dot{\sigma}_{xx}^2 t^2} = 0. \tag{5.17}$$

Similarly, we can show:

$$\lim_{t \to 0} \dot{\theta} = -\frac{\sigma^* \dot{\sigma}_{xx}}{8\sigma^{*2}} \tag{5.18}$$

and

$$\lim_{t \to \infty} \dot{\theta} = -\frac{\sigma^* \dot{\sigma}_{xx}}{8\sigma^{*2} + \infty} = 0. \tag{5.19}$$

Figure 5.2 shows rotation rate contours as a function of the stressing rate and background stress for a given time. Here only positive background stress and stressing rate values are shown on a log-log scale. Rotation rates have the same magnitude but are multiplied by a factor of negative one when the background stress or stressing rate parameters are negative.

When both the background stress and the stressing rate are negative the principal stress rotation rate is equal to those shown. The maximum rotation rate occurs in year 1 and is -14.32 degrees/yr. The order of magnitude of the rotation rate decreases by a factor of ten with each tenfold increase in time, with maximum rotation rate values of -1.43 degrees/yr in year 10 and -0.14 degrees in year 100. Maximum rotation rate values also correspond to higher order background stresses later in the earthquake cycle. The slope of the rotation rate contours remains the same over the course of the earthquake cycle but the contours are shifted to right, a result that follows from the rotation rate dependence on $1/t^2$ (Equation 5.15).

Rotation rate contours for the background stress versus time at given stressing rates are shown in Figure 5.3. For plotting purposes only positive background stress values are shown, but rotation rates for negative background stresses are equivalent to the rotation rates at the positive background stress multiplied by negative one. Maximum rotation rate values shift to higher background stress magnitudes as the stressing rate magnitude increases. For all stressing rates, there are background stress values such that the rotation rate remains relatively constant over the earthquake cycle, e.g., when $\dot{\sigma}_{xx} = 10^4$ Pa/yr background stress values of $\sigma^* \sim 10^6$ Pa give rotation rates that are relatively constant over the 100 year earthquake cycle shown. These values are typically <0.3 degrees/yr, and are most often <0.1 degrees/yr, and would amount to a total rotation in the principal stress axes of <30 degrees over a 100 year interseismic period. For lower background stress values (e.g., $\sigma^* < 10^3$ Pa when $\dot{\sigma}_{xx} = 10^4$ Pa/yr) the rotation rate reaches ~ 14 degrees/yr early in the earthquake cycle (first year after an earthquake) and approaches zero within 25 years.

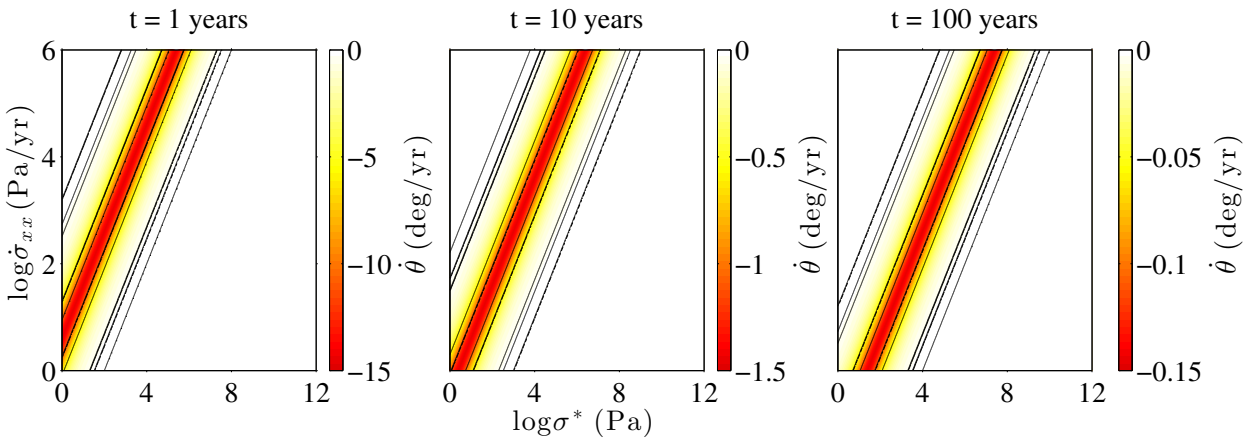

Figure 5.2: Parameter sensitivity analysis of the rotation rate ($\dot{\theta}$, color contours) of the maximum principal stress orientation at given time, t, in the earthquake cycle as a function of the log of the background stress, σ^*, and the log of the stressing rate, $\dot{\sigma}_{xx}$, where $\dot{\sigma}_{xx}/\dot{\sigma}_{yy} = 2$. Redder colors indicate faster rotation. Only positive values of σ^* and $\dot{\sigma}_{xx}$ are shown here, but values are symmetric about the σ^* and $\dot{\sigma}_{xx}$. Rotation rates are positive in quadrants 1 (shown) and 3, and negative in quadrants 2 and 4. The magnitude of $\dot{\theta}$ decreases by an order of magnitude with each order of magnitude increase in t. $\dot{\theta}$ contours exhibit the same slope across the earthquake cycle, but the maximum $\dot{\theta}$ values shift to higher background stresses over the course of the earthquake cycle.

Figure 5.4 shows rotation rate contours as a function of the stressing rate and time for a given background stress. As with previous figures, only the positive values of the background stress and stressing rate are shown, and stressing rate is plotted as the logarithm of the stressing rate value. As with Figure 5.3, maximum principal stress rotation rates (14.32 degrees/yr) occur in the first year of the earthquake cycle and when $\sigma^* < 10^5$ Pa. When $\sigma^* = 10^6$ Pa, the maximum rotation rate is 6.74 degrees/yr and occurs in the first year of the earthquake cycle. With $\sigma^* \geq 10^7$ Pa, the absolute value of the rotation rate is < 1 degree/yr and occurs one year after the last earthquake. With $\sigma^* = 10^9$ Pa, the fastest rotation rate is -0.0072 degrees/yr. Even if the rotation rate remains constant over the entire 100 year earthquake cycle, the total rotation in the principal stress axes would be < 1 degree. At

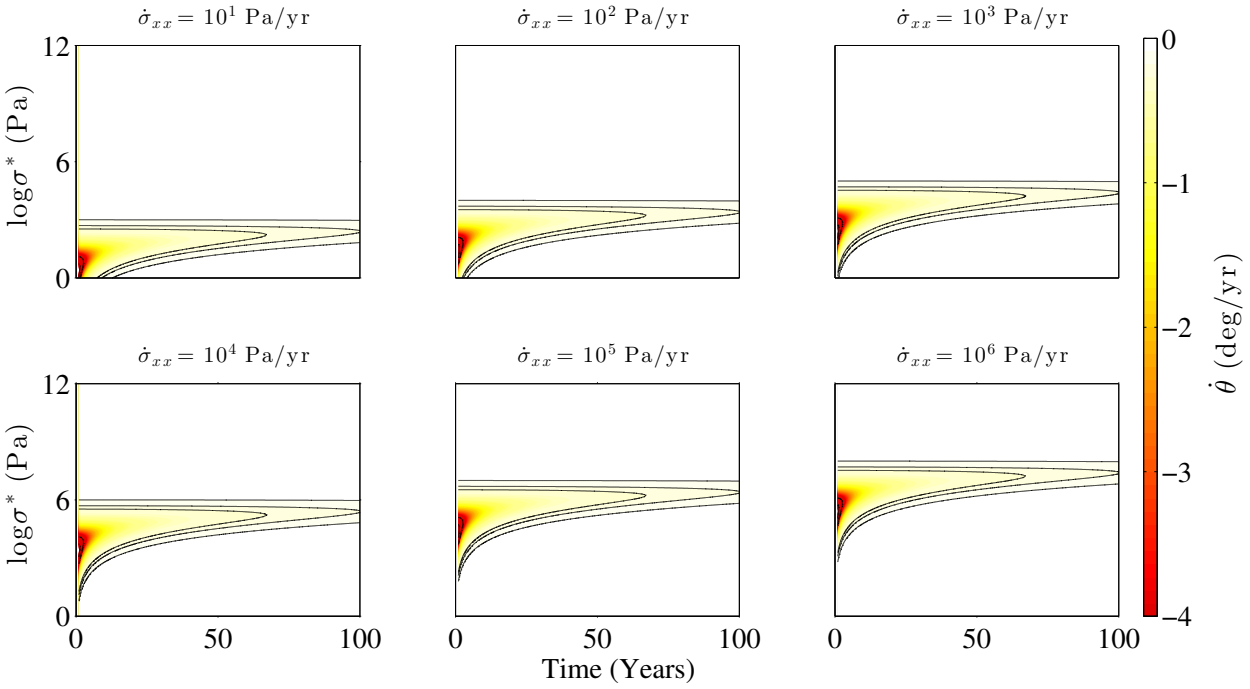

Figure 5.3: Parameter sensitivity analysis of the rotation rate, $\dot{\theta}$, as a function of the background stress, σ^*, and time for given stressing rates, $\dot{\sigma}_{xx}$. As with Figure 5.2, only positive values for $\dot{\sigma}_{xx}$ and σ^* are shown. $\dot{\theta}$ results are identical for negative values of σ^* but are multiplied by negative one. Similarly, $\dot{\theta}$ values are identical but multiplied by negative one for negative values of $\dot{\sigma}_{xx}$. Models with negative values of both $\dot{\sigma}_{xx}$ and σ^* have rotation rates identical to the ones shown above. $\dot{\theta}$ contours retain the same shape and scale across all stressing rates, but maximum values of $\dot{\theta}$ shift to higher magnitude σ^* as the magnitude of the stressing rate increases. In each case, a range of background stresses exist such that $\dot{\theta}$ remains relatively constant over the earthquake cycle. Conversely, at each stressing rate there is a range of background stresses such that values of $\dot{\theta}$ range from the maximum value to $\sim$0 degrees/year within the first 10 years of the earthquake cycle.

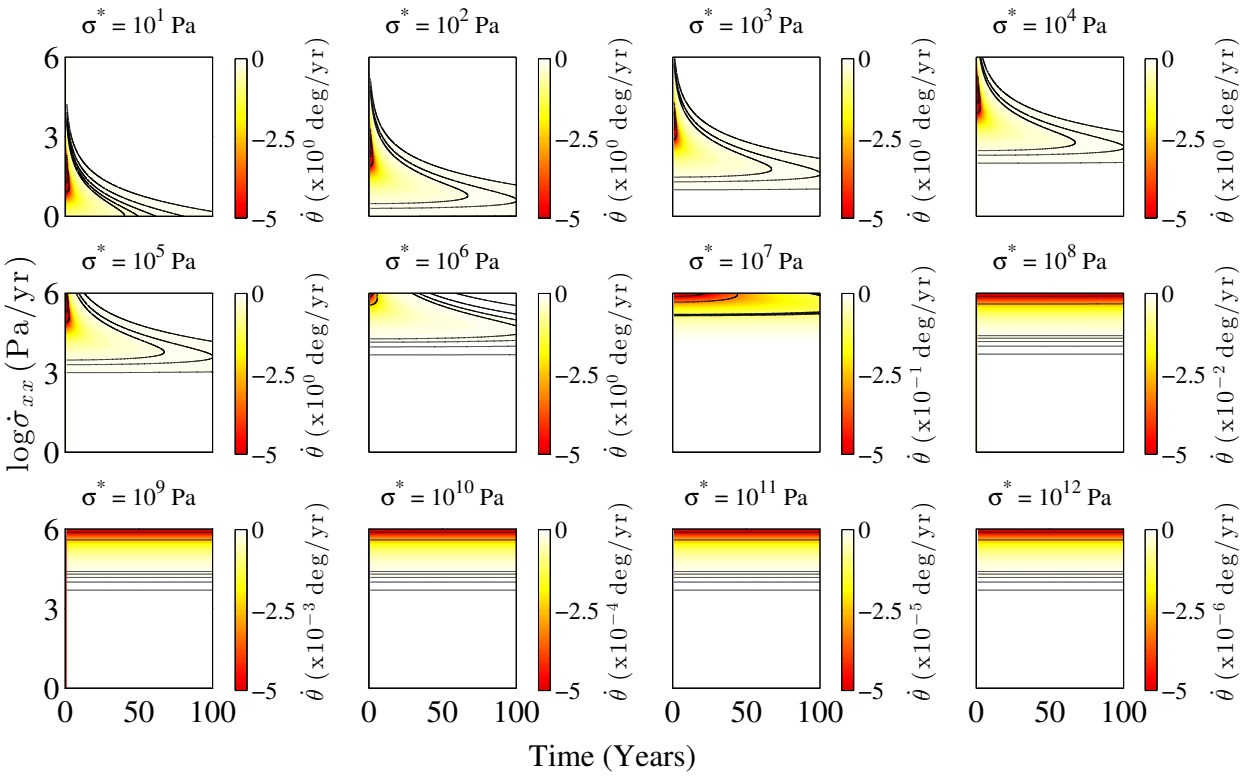

Figure 5.4: Parameter sensitivity analysis of the rotation rate ($\dot{\theta}$, color contours) as a function of the stressing rate, $\dot{\sigma}_{xx}$, and time for given background stresses, σ^*. As with Figures 5.2 and 5.3, only positive values of $\dot{\sigma}_{xx}$ and σ^* are shown, but negative values give values of $\dot{\theta}$ equal to those above multiplied by negative one. For background stresses between $\sigma^* = 10^1 - 10^6$ Pa, contours retain the same shape and scale (values of $\dot{\theta}$ range from $\sim -14 - 0$ degrees/yr), but maximum values of $\dot{\theta}$ shift to larger magnitude values of $\dot{\sigma}_{xx}$. For $\sigma^* \geq 10^7$ Pa, the background stresses are no longer large enough to allow for the same range of $\dot{\theta}$, and $\dot{\theta}$ decreases by an order of magnitude for each order of magnitude increase in σ^*, with maximum rotation rates at higher values of $\dot{\sigma}_{xx}$.

these background stresses, measurement techniques that can record stress orientations to within a tenth of a degree or smaller would be required.

5.5 Interseismic principal stress rotation rates near an infinitely long strike-slip fault

To further explore the temporal evolution of the principal stress rotation rate over the earthquake cycle, we apply a regional background stress to an infinitely long strike-slip fault in an homogeneous elastic half-space (Savage and Burford, 1973). At high viscosities this solution is identical to the classical two-layer approach with an elastic upper layer underlain by a viscoelastic half-space (e.g., Hetland and Hager, 2005; Savage and Prescott, 1978; Savage and Lisowski, 1998). Steady state interseismic velocities are given by:

$$v = \frac{s}{\pi}\tan^{-1}\left(\frac{x}{D}\right), \tag{5.20}$$

where v is the displacement, s is the slip rate, x is the distance from the fault, and D is the locking depth. The strain rate, $\dot{\epsilon}_{xy}$, is therefore:

$$\dot{\epsilon}_{xy} = \frac{sD}{2\pi(x^2 + D^2)}. \tag{5.21}$$

Using Hooke's Law, the stressing rate as a function of distance from the fault is:

$$\dot{\sigma}_{xy} = 2\mu\dot{\epsilon}_{xy}, \tag{5.22}$$

where μ is the shear modulus. In the models shown here, we take $\mu = 30$ GPa.

Models discussed here are for an idealized approximation of the San Andreas Fault (SAF), the dominant feature of the Pacific-North American plate boundary (Atwater, 1970; Meade and Hager, 2005; Savage and Burford, 1973). To calculate the stressing rate from the equation above, we use a slip rate, s, of 33.9 $\pm$ 2.9 mm/yr, consistent with geologic estimates from the Carrizo region of the San Andreas (Sieh and Jahns, 1984). We assume a locking depth of 20 km (e.g., Smith-Konter and Sandwell, 2009) and calculate the stressing rate, $\dot{\sigma}_{xy}$, for a profile that stretches 50 km from the fault in either direction. Figure 5.5 shows the calculated displacement rate, strain rate, and stressing rate for the idealized fault model. Displacement rates are zero at the locked fault, but strain and stress rates reach maximums of 2.67×10^{-6} yr^{-1} and 1.60×10^{5} Pa/yr, respectively, at the fault.

For the purposes of these calculations we assume that $\dot{\sigma}_{xx} = \dot{\sigma}_{yy} = 0$. To test the temporal evolution of the principal stress orientations within a north-south deviatoric stress regime, we define the background stress, $\boldsymbol{\sigma}^{\mathbf{b}}$, to be:

$$\boldsymbol{\sigma}^{\mathbf{b}} = \begin{bmatrix} \sigma^* & 0 \\ 0 & -\sigma^* \end{bmatrix} \tag{5.23}$$

and thus the total stress, $\boldsymbol{\sigma}^{\mathbf{T}}$, is:

$$\boldsymbol{\sigma}^{\mathbf{T}} = \begin{bmatrix} \sigma^* & \dot{\sigma}_{xy}t \\ \dot{\sigma}_{xy}t & -\sigma^* \end{bmatrix}, \tag{5.24}$$

where $\dot{\sigma}_{xy}$ is the shear stressing rate and t is time since the last earthquake. We test values

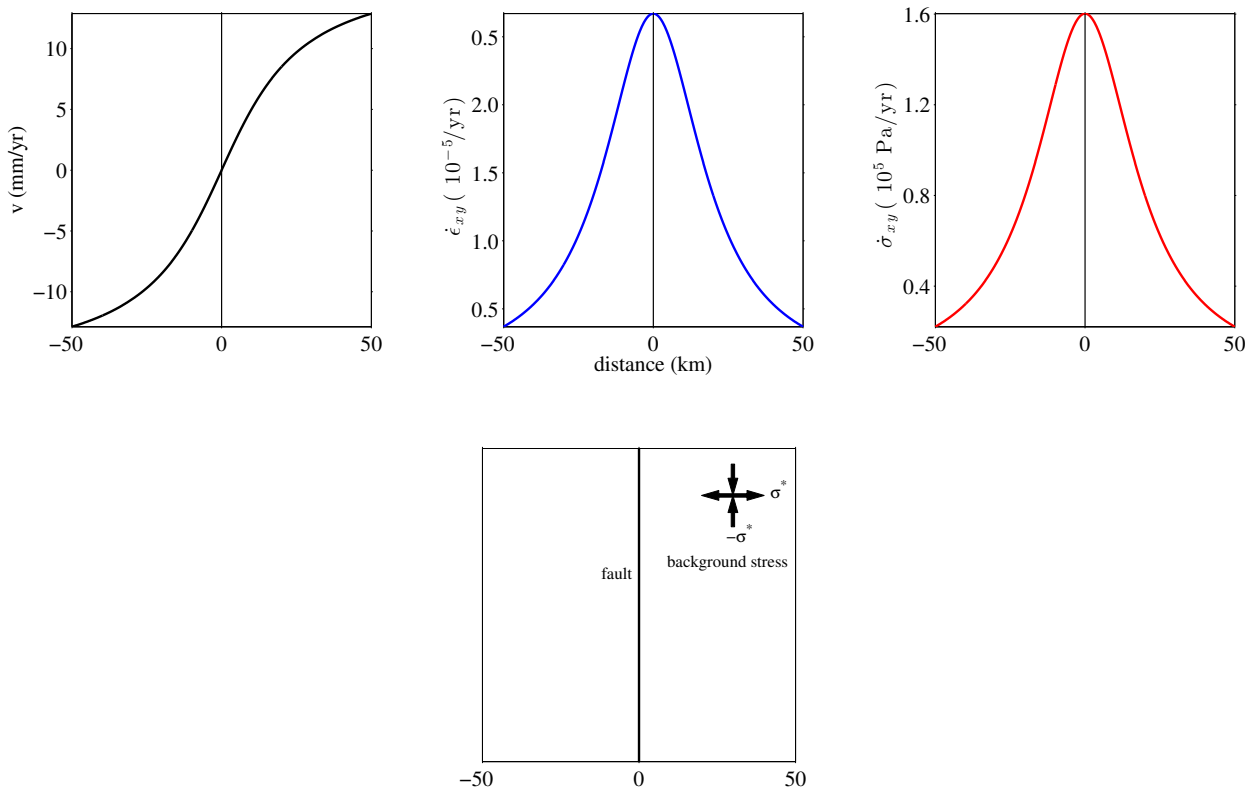

Figure 5.5: Displacement rate (v), strain rate ($\dot{\epsilon}_{xy}$), and stress rate ($\dot{\sigma}_{xy}$), calculated from an idealized fault model. Equations are from the analytical solution for an infinitely long strike-slip fault in a homogeneous elastic half-space (Savage and Burford, 1973), but for a high-viscosity limit these equations are identical to a two layer model with an elastic layer underlain by a viscoelastic layer (Savage and Prescott, 1978). Here the slip rate is assumed to be 34 mm/yr and the locking depth 20 km, consistent with an idealized San Andreas Fault (Sieh and Jahns, 1984). The fault trace is plotted as the black vertical line at 0 km in each figure. The background stress is a deviatoric approximation and is indicated black arrows. Displacement rates (black) follow an arctangent function centered on the fault trace. Strain (blue) and stress (red) rates are highest at the fault and decay away with distance.

of σ^* between 10^4 Pa and 10^9 Pa, which is the range of σ^* from the parameter sensitivity analysis (described above) for which we may expect to see rotations in the orientation of the maximum principal stresses. Thus the rotation rate equation becomes:

$$\dot{\theta} = -\frac{\dot{\sigma}_{xy}\sigma^*}{2(\dot{\sigma}_{xy}^2 t^2 + \sigma^{*2})}. \tag{5.25}$$

This approach is distinct from Scholz (2000), who combines Mohr's circle-derived equations for the shear stress on a fault with the Coulomb failure stress equation and observations of ψ, the angle between the maximum horizontal stress and the SAF (Hardebeck and Hauksson, 1999). Scholz (2000) predicts a range of values for the frictional coefficient, μ, and the shear stress, τ_{xy}^0, by assuming Anderson-Byerlee mechanics and hydrostatic pore fluid pressure. He incorporates these predictions into the Turcotte and Spence (1974) model of a deep ductile shear zone beneath the SAF to show that the model-predicted values of ψ are a good fit to the Hardebeck and Hauksson (1999) data and infers that the SAF is a strong fault. Scholz (2000) assumes that the angle between the maximum horizontal stress and the SAF remains constant over the earthquake cycle. We are interested in identifying the conditions under which the principal stresses will rotate. Unlike Scholz (2000), our goal is not to fit data, but rather to define a range of expectations given different initial southern California stress states.

Rotation rates for values of σ^* between 10^4 Pa and 10^7 Pa show considerable evolution over the earthquake cycle (Figure 5.6). When the background stress is of comparable magnitude to the interseismic stressing rate ($\sigma^* = 10^5$ Pa) maximum rates of 14.32 degrees/yr are observed in the first year of the earthquake cycle, but maximum rotation rates drop to 1.08 degrees/yr at year ten, 0.05 degrees/yr at year 50, and are $\sim$0 degrees/yr at later stages

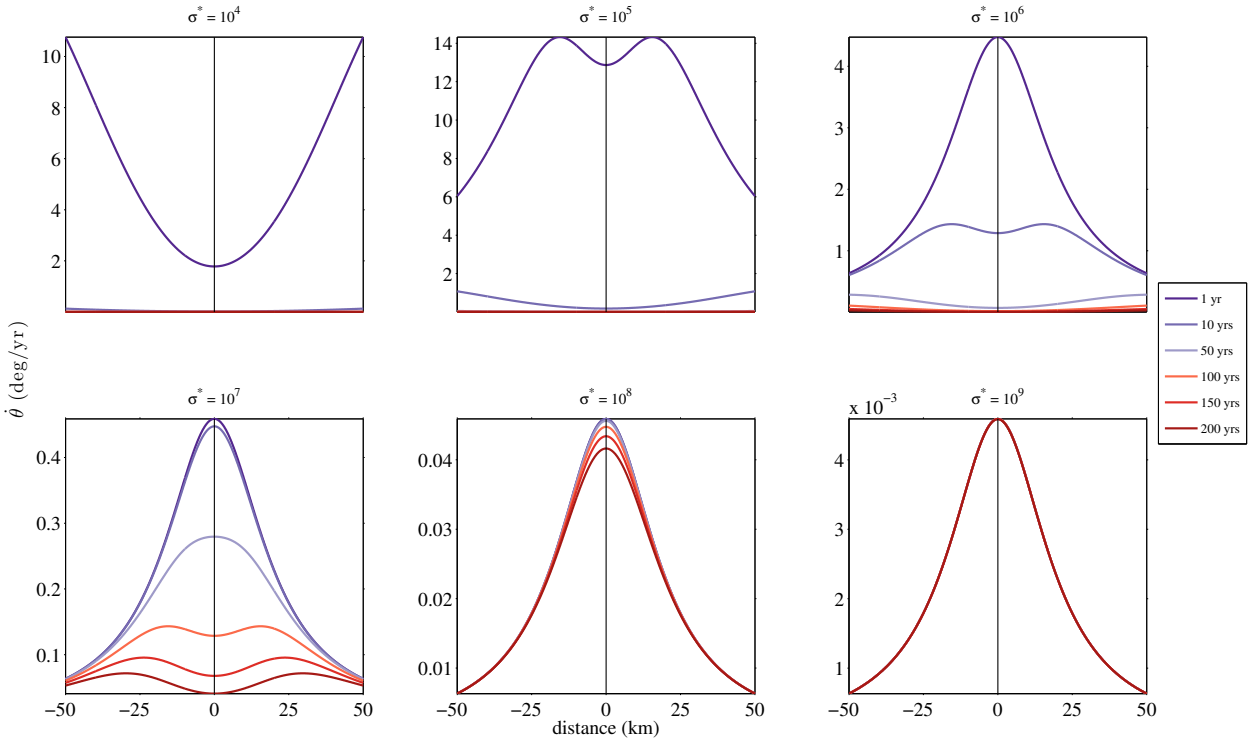

Figure 5.6: Principal stress rotation rates ($\dot{\theta}$ as a function of distance from the fault and time in the earthquake cycle at different background stresses, σ^*, for the idealized fault described in Figure 5.5. Colors correspond to time in the earthquake cycle, with bluer colors indicating earlier in the earthquake cycle (1, 10, and 50 years) and redder colors indicating later in the earthquake cycle (100, 150, and 200 years). The vertical thin black line indicates the location of the fault. For $\sigma^* = 10^4$ Pa, maximum values of $\dot{\theta}$ occur at year 1 of the earthquake cycle are ∼11 degrees/yr and at the edges of the model domain. $\dot{\theta}$ values for later years in the earthquake cycle are ∼0 degrees/year. At $\sigma^* = 10^5$ Pa, the maximum rotation rate is ∼14 degrees/yr at year 1 of the earthquake cycle and occurs at ±15.5 km from the fault trace. Rotation rates at this background stress decay quickly, and the maximum value in year 10 is ∼1 degree/yr and is at the edge of the model domain. When t > 10 years, the rotation rate is ∼ 0 degrees/yr. For $\sigma^* = 10^6 - 10^7$ Pa, rotation rates are highest at the fault until the accumulated interseismic stress exceeds the background stress, after which maximum rotation rates move away from the fault to locations where the accumulated interseismic stress has not yet exceeded the background stress. For $\sigma^* \geq 10^5$ Pa, the $\dot{\theta}$ order of magnitude decreases with the increase in σ^*. For $\sigma^* = 10^8 - 10^9$ Pa, the background stress is greater than the accumulated interseismic stress over the entire earthquake cycle and values of $\dot{\theta}$ are $\ll$ 1 degree/yr and are always highest at the fault.

of the earthquake cycle. At $\sigma^* = 10^4$ Pa and $t = 1$ year, minimum rotation rates (1.78 degrees/yr) are observed at the fault and maximum rotation rates occur beyond the model domain. At the fault trace the stressing rate is 1.60×10^5 Pa/yr. With a background stress of $\sigma^* = 10^4$ Pa, it will take much less than one year for the interseismic stress accumulation to dominate the total stress tensor and for the maximum principal stress orientations to align with the stressing rate tensor.

For background stress $\sigma^* = 10^5$ Pa, rotation rates of 12.88 degrees/yr occur at the fault when $t = 1$. Here the accumulated interseismic stress at the fault is ∼160% of the background stress and is the dominant feature of the total stress tensor. The stressing rate decays away from the fault and is $\sim 10^5$ Pa/yr at $\sim \pm 15.5$ km from the fault (Figure 5.6), consistent with the location of the maximum rotation rate. At $t = 10$ years the maximum rotation rate is 1.08 degrees/yr and occurs at $\pm$ 50 km from the fault trace, or at the edge of the model domain. Rotation rates are ∼0 degrees/yr later in the earthquake cycle.

At $\sigma^* = 10^6$ Pa, the background stress is an order of magnitude higher than the stressing rate and the total stress tensor is a combination of the regional background stress and the accumulated interseismic stress. At $t = 10$ years the accumulated interseismic stress at the fault is 1.60×10^6 Pa (the calculated stressing rate at the fault trace multiplied by 10 years), or approximately the same as the background stress. At $t = 10$ years, the maximum rotation rate begins moving away from the fault as the accumulated interseismic stress near the fault exceeds σ^* and the principal stress orientations align with the interseismic stress. Thus the maximum rotation rate (4.48 degrees/yr) in the first year of the earthquake cycle occurs at the fault trace, but at year ten the maximum rotation rate (1.43 degrees/yr) occurs

at $\pm\sim$15.5 km from the fault. At year fifty the maximum accumulated tectonic stress is 8.01×10^6 Pa, or approximately eight times the background stress, and the accumulated tectonic stress dominates the total stress tensor. At $t = 50$ years, the maximum rotation rate (0.29 degrees/yr) occurs at the edge of the model domain, and later in the earthquake cycle ($t > 50$ years) the rotation rate is $\sim$0 degrees/yr.

For background stresses of $\sigma^* = 10^7$ Pa, the peak rotation rates occur on the fault trace at $t = 1$, 10, and 50 years (maximum rotation rates of 0.46 degrees/yr, 0.45 degrees/yr, and 0.28 degrees/yr, respectively). The location of the maximum rotation rate begins to migrate away from the fault after year 50 and is located at $\pm$ 15.5 km from the fault. As with before, the location of the maximum rotation rate is not surprising: at $\pm$15.5 km the tectonic stressing rate is $\sim 1.0 \times 10^5$ Pa. After 100 years the accumulated tectonic stress is $\sim 1.0 \times 10^7$ Pa, or the same size as the background stress. At 150 years the maximum rotation rate is located $\pm$23.7 km from the fault and is 0.10 degrees/yr, and at 200 years the maximum is at $\pm$29.7 km and is 0.07 degrees/yr.

Between $\sigma^* = 10^6$ Pa and $\sigma^* = 10^9$ Pa, the maximum rotation rate at any point in the earthquake cycle decreases by approximately an order of magnitude with each order of magnitude increase in σ^*, a result which follows from the rotation rate equation above. For background stresses $\sigma^* = 10^8$ Pa and $\sigma^* = 10^9$ Pa, the background stress exceeds the interseismic stress accumulation over the course of the entire earthquake cycle and the total stress tensor is dominated by the σ^* term. Thus principal stresses are largely aligned with the background stress throughout the earthquake cycle and rotations in the principal stress axes are $\ll 1$ degree/yr (between 0-0.05 degrees/yr when $\sigma^* = 10^8$ Pa and $\sim$ 0.005 degrees/yr

when $\sigma^* = 10^9$ Pa).

5.6 Southern California stressing rates

To constrain the range of background stresses in southern California for which rotations in the principal stress axes may be observed, we combine regional background stress tensors with the stressing rate calculations from the Loveless and Meade (2011b) block model. The Loveless and Meade (2011b) block model combines strain accumulation due to interseismic locking of faults with microplate rotations and explicitly satisfies conservation of momentum. Elastic deformation rates are calculated from the analytical solution for a displacement field due to a dislocation in a uniform elastic half space (Okada, 1992). Stressing rates are calculated using the fault slip rates (or slip deficit rates Okada, 1992) and the stressing rate at each point is a result of the slip deficit on each fault in the southern California fault system. To make our study most comparable to previous San Andreas focused studies, we limit our study to the region ∼50 km from the SAF fault trace, extending from the Indio segment in the south to the Parkfield segment in the north. Stressing rates from 22,244 points within this model domain are used, representing a spatial density of one point every ∼2 km. The model geometry and major southern California earthquakes since 1990 are shown in Figure 5.7.

5.6.1 Principal stressing rate azimuths

Principal stressing rate azimuths for depths 1, 5, 9, and 15 km are shown in Figure 5.8. These depths are chosen to allow for easy comparison to focal mechanism inversion studies (e.g., Hardebeck and Hauksson, 2001) that report stress azimuths at several seismogenic

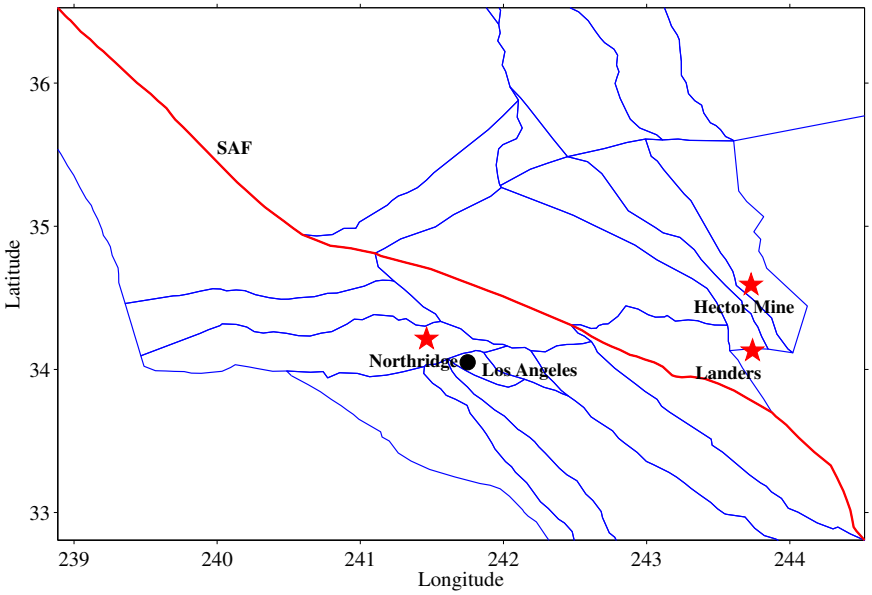

Figure 5.7: Model geometry used in this study, as derived from the Loveless and Meade (2011b) block model. Blue lines indicate faults. The red line indicates the portion of the SAF we are considering in this study. Red stars show the epicenters of the June 28, 1992 $M_W = 7.3$ Landers earthquake, the January 17, 1994 $M_W = 6.7$ Northridge earthquake, and the October 16, 1999 $M_W = 7.1$ Hector Mine earthquake. The black circle indicates the city of Los Angeles.

depths. The value, θ, is equivalent to the angle used in the stress rotation calculations described above. No background stress is added, and θ is the orientation of the tectonic stress that accumulates over the earthquake cycle. All values of θ are reported in degrees from north, where positive values indicate degrees east of north and negative values indicate degrees west of north.

At 1 km depth, azimuths range from ± 90 degrees, with a median value of 33.19 degrees and a mean value of 27.44 degrees (Figure 5.8). As these values suggest, azimuths are dominantly northeast trending. More than 46% of all calculated points have azimuths between 30-45 degrees. This result may not be surprising: an azimuth of $\sim$45 degrees is broadly consistent with the direction of relative motion between California and North America (DeMets

and Dixon, 1999; DeMets and Stein, 1990) and the strike of the SAF. These results are inconsistent with the maximum horizontal compressive stress orientations reported by Hardebeck and Hauksson (2001), which have a mean orientation of 7 degrees and range from -30 degrees to 45 degrees. At 1 km depth, stressing rate orientations along the SAF are almost exclusively positive (northeastern) and typically range from $\sim 30-40$ degrees on the San Bernardino and southern Mojave segments and $\sim 40-50$ degrees on the Carrizo and northern Mojave segments. Estimates of the maximum horizontal compressive stress direction from the Cajon Pass drilling site on the San Bernardino fault are consistent with the stressing rate azimuths and range from 57 ± 19 degrees at depths of $1.75-3.5$ km. The two largest exceptions to the dominant northeastern azimuth trend occur in the north on the Parkfield segment and in the south on the Indio segment, where stressing rates have negative azimuths. At Parkfield, stressing rate azimuths just east of the fault are subhorizontal and range from -70 to -90 degrees before quickly reversing direction to 70 to 90 degrees. West of the SAF trace azimuths are negative and range from $-50-0$ degrees. SAFOD estimates of maximum horizontal stress orientations are not consistent with the Parkfield stressing rate azimuths and are subvertical, making a 50 ± 17 degree angle with the SAF (corresponding to an azimuth of $\sim$7-20 degrees) at depths of $0.8-2.2$ km. Just east of the southern portion of the Indio segment azimuths are again northwestern and range from $-15-0$ degrees. In contrast, Hardebeck and Hauksson (2001) report significant spatial heterogeneity in the maximum horizontal compressive stress orientations along the SAF. Values range from $\sim -30-0$ (on the Carrizo and San Bernardino segments) to $\sim$15 degrees on the Mojave and parts of the Indio segments. Hardebeck and Hauksson (2001) report maximum

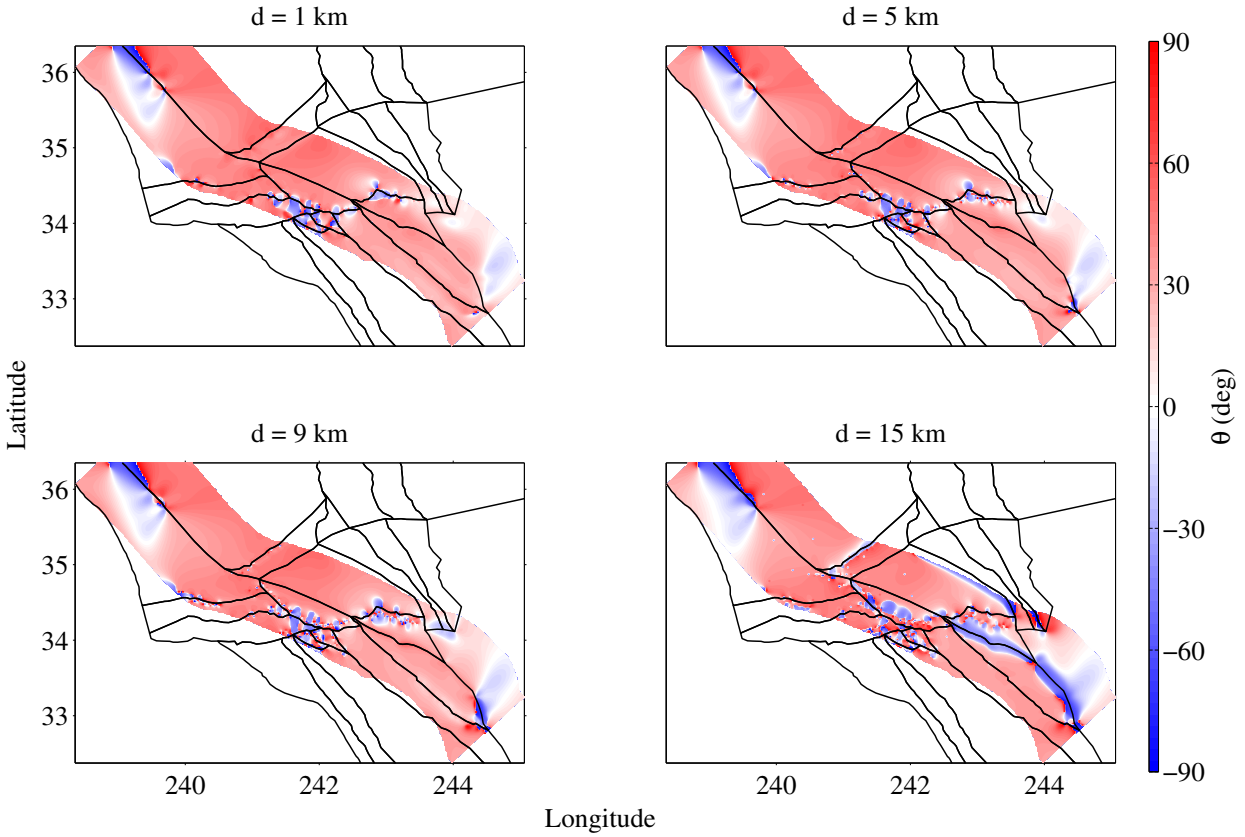

Figure 5.8: Principal stressing rate azimuths, θ, for 1, 5, 9, and 15 km depth. Azimuths are calculated in degrees east from north, where north is 0 degrees. At all depths azimuths range from ± 90 degrees. Here red colors indicate positive (western) azimuths and blue colors indicate negative (eastern) azimuths.

compressive stresses of $\sim 20 - 45$ degrees. Our study area considers only the eastern portion of this region, but typical stressing rate azimuths are lower than the mean and range from $0 - 20$ degrees. However, just east of the Indio segment azimuths range from $20 - 40$ degrees and are consistent with Hardebeck and Hauksson (2001) results. Loveless and Meade (2011b) stressing rate azimuths north of the White Wolf fault and south of the Garlock fault are typically $40 - 50$ degrees, in contrast to the $\sim 0 - 15$ degrees reported by Hardebeck and Hauksson (2001). Like Hardebeck and Hauksson (2001), we observe considerable heterogeneity in stressing rate azimuths in the Transverse Ranges and Los Angeles Basin, with

azimuths trending both in the northeastern and northwestern direction such that, in general, $|\theta| \geq 30$ degrees. (Hardebeck and Hauksson (2001) find maximum compressive stress azimuths ranging from $-30 - 45$ degrees.) However, borehole breakouts from this region are also heterogeneous, ranging from -59 ± 23 degrees in the eastern Los Angeles Basin to 0 ± 14 degrees in the western Los Angeles Basin, 46 ± 16 degrees in the East Ventura Basin/Central Transverse Ranges, 47 ± 22 degrees in the Central Ventura Basin, 20 ± 4 degrees in the Upper Ojai Valley just east of the San Gabriel fault, and 13 ± 9 degrees in the Santa Barbara region (Wilde and Stock, 1997).

Principal stressing rate azimuths at 5 km depth (Figure 5.8) are nearly identical to those at 1 km depth. Azimuths values range from ± 90 degrees with a median value of 32.84 degrees and a mean value of 27.11 degrees. Azimuths on the SAF are largely positive (northeastern), but on the Parkfield segment there is a large ($\sim$100 km by $\sim$50 km) region with negative principal stress azimuths on the west side of the fault. Like at 1 km depth, the eastern side of the Indio segment also has negative stressing rate azimuths. Hardebeck and Hauksson (2001) maximum horizontal compressive stress azimuths at 5 km are also nearly identical to those reported at 0 km and are typically negative ($-30 - 0$ degrees) on the Carrizo and San Bernardino segments and positive ($\sim$15 degrees) on the Mojave and parts of the Indio segments. Stressing rate azimuths on the Mojave segment of the SAF and between the White Wolf and Garlock faults range between $40 - 50$ degrees, in contrast to the $-30 - 20$ degrees that Hardebeck and Hauksson (2001) find for the maximum horizontal compressive stress for the same region. In the Transverse Ranges and the Los Angeles Basin there are significant heterogeneities in the stressing rate azimuths, and regions switch from positive

(>40 degrees) to negative (<-40 degrees) over ∼5-20 km length scales.

At 9 km depth, the principal stress azimuths once again range between ±90 degrees (Figure 5.8). The median azimuth is 32.43 degrees and the mean azimuth is 25.56 degrees. At 9 km depth the transition from positve principal stress azimuths to negative azimuths on the Parkfield segment of the SAF remains a robust feature. As with previous depths, negative principal stress azimuths on the fault trace are < -40 degrees, while negative azimuths on the west side range from $-30 - 0$ degrees, with higher values occurring closer to the SAF. Principal stress azimuths on the Indio segment of the SAF are more northwestern than at previous depths: on the fault trace, azimuths range from -50 to -90 degrees, and west of the fault, azimuths range from $\sim -30 - 0$ degrees. Azimuths on the Mojave and Carrizo segments of the SAF between the White Wolf and Garlock faults are between $40 - 50$ degrees, and significant spatial heterogeneity in the Transverse Ranges and Los Angeles Basin is again observed (with $|\theta|$ >30 degrees and changing sign at length scales of $\sim 5 - 20$ km). We can compare these results to those from Hardebeck and Hauksson (2001) at 10 km depth. Maximum horizontal compressive stress orientations are nearly indistinguishable from previous depths and are generally in poor agreement with the stressing rate azimuths described above.

Principal stress azimuths at 15 km range from ± 90 degrees with a median value of 32.60 degrees and a mean of 20.15 degrees (Figure 5.8). Negative azimuths are more common at this depth, as reflected in the mean azimuth value and in Figure 5.8. As with previous depths there is a region of negative azimuths on the Parkfield segment of the SAF (< -70 degrees $\sim 2-10$ km east of the fault and then >70 degrees for the next $\sim 2-10$ km; $-40-0$ degrees

for the ∼60 km west of the fault). West of the SAF negative principal stress azimuths range from $-50-0$ degrees, with more negative (western) values closer to the fault. Principal stress azimuths are also negative on the San Bernardino and Indio segments of the SAF, ranging -20 to -50 degrees and -30 to -90 degrees, respectively, on the fault strike and extending east of Indio with values ranging from $-20-0$ degrees. Principal stressing rate azimuths are positive and range from $20-40$ degrees on the Carrizo and Mojave segments of the SAF. As with previously discussed depths, the reported maximum horizontal compressive stress orientations from Hardebeck and Hauksson (2001) are unchanged at 15 km depth. As a result there is some overlap between the Loveless and Meade (2011b) stressing rate azimuths and the lower bound of $-30-10$ degrees reported by Hardebeck and Hauksson (2001) on the San Bernardino segment. At 15 km depth, the principal stress azimuths within $\sim 2-5$ km of the White Wolf fault are negative and range from -30 to -10 degrees. These results are somewhat consistent with the Hardebeck and Hauksson (2001) observations of maximum horizontal compressive stress orientations of $\sim -30-0$ degrees on the central portion of this fault but inconsistent with their observed positive orientations on the western and eastern edges. Stressing rate azimuths on the Garlock and between the Garlock and White Wolf faults are positive and range from $30-50$ degrees, much higher than Hardebeck and Hauksson (2001) observations of $\sim -25-20$ degrees. In the Transverse Ranges and the Los Angeles Basin, stressing rate azimuths are heterogeneous ($|\theta| > 30$ degrees) and change sign over $\sim 5-20$ km length scales. Hardebeck and Hauksson (2001) find only positive maximum horizontal compressive stresses in this region, but locations where these orientations are $\sim 20-45$ degrees are consistent with some stressing rate azimuths while

inferences of $\sim 0-15$ degrees are not.

Other focal mechanism inversion estimates of maximum horizontal compressive stress orientations in southern California do not differentiate between seismogenic depths. Yang and Hauksson (2013) find dominantly northwestern ($\sim -30-0$ degrees) maximum horizontal compressive stresses near the SAF (though azimuths are positive and range from $0-30$ degrees on the Indio segment). These results are not consistent with the principal stressing rate azimuths described above, which are dominantly northeastern at all depths. Hardebeck and Michael (2006) and Hardebeck and Michael (2004) report subvertical maximum horizontal compressive stresses over nearly their entire southern California study area (and specifically near the SAF), though trends are slightly northwestern on the San Bernardino segments and slightly northeastern on the Indio segment. In general, these azimuths are in poor agreement with the principal stressing rate orientations which, at 5 km depth, are only subvertical ($|\theta| = 0-10$ degrees) ~2-30 km west of Parkfield and $\sim 2-60$ km east of Indio as well as in the vicinity of the Landers earthquake and sporadically in the Transverse Ranges and the Los Angeles Basin.

5.6.2 Stressing rate magnitudes

Figure 5.9 shows the stressing rate magnitudes at 1, 5, 9, and 15 km depth. Magnitudes are calculated using the equation:

$$||\dot{\boldsymbol{\sigma}}|| = \sqrt{\dot{\boldsymbol{\sigma}} : \dot{\boldsymbol{\sigma}}} = \sqrt{\dot{\sigma}_{xx}\dot{\sigma}_{xx} + 2\dot{\sigma}_{xy}\dot{\sigma}_{xy} + \dot{\sigma}_{yy}\dot{\sigma}_{yy}} \tag{5.26}$$

At 1 km depth, magnitudes range from 317.38 Pa/yr to 3.73×10^5 Pa/yr and have a

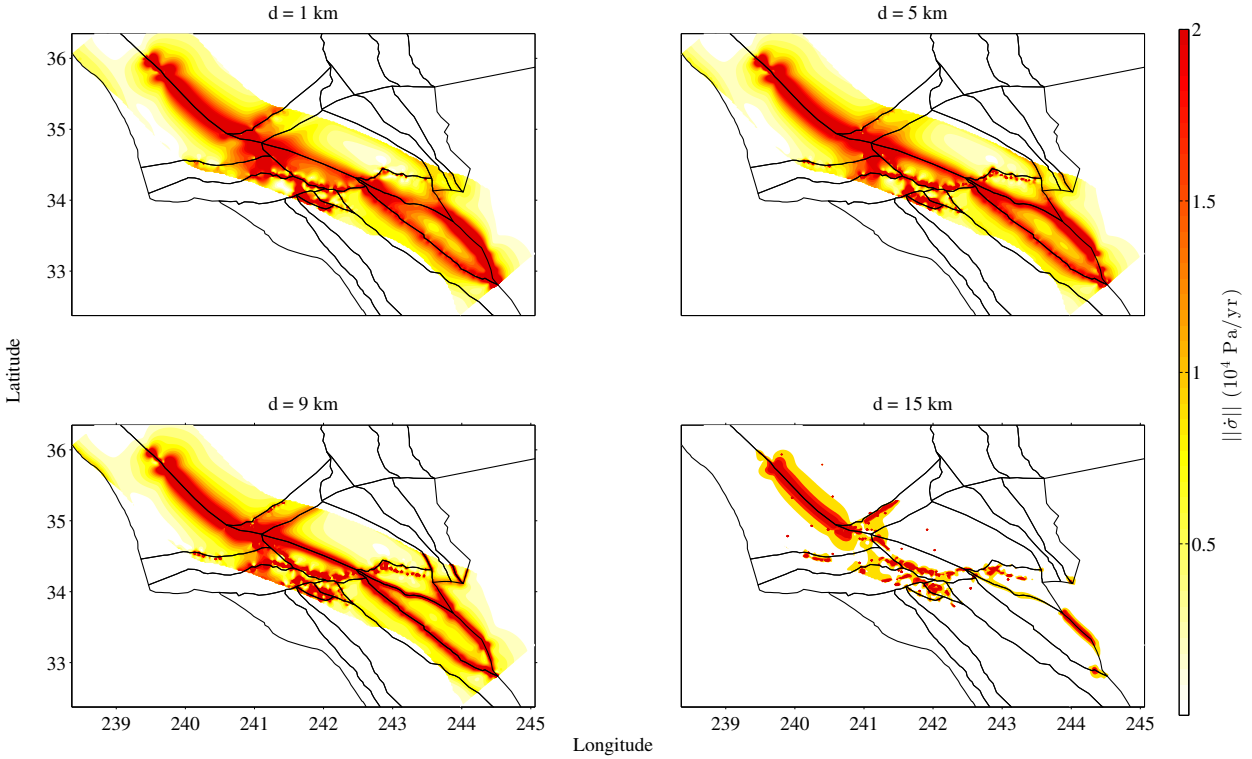

Figure 5.9: Stressing rate magnitudes calculated from Loveless and Meade (2011b) for 1, 5, 9, and 15 km depth. Redder colors indicate higher magnitudes and white indicates low magnitudes. Colors saturate at 2×10^4 Pa/yr. At 1, 5, and 9 km depth the highest stressing rate magnitudes occur along faults, and particularly on the Parkfield and Indio segments of the SAF. At 15 km depth stressing rate magnitudes on the Mojave and San Berardino segments are smaller and high stressing rate magnitudes are concentrated on the Parkfield, Carrizo, and Indio segments of the SAF, as well as on the San Gabriel and White Wolf faults.

median value of 8.78×10^3 Pa/yr and a mean value of 1.15×10^4 Pa/yr. Magnitudes are highest on faults, with magnitudes $> 10^5$ Pa/yr occurring on the SAF fault trace on the Parkfield and southern Indio segments and intermittently on the San Gabriel block and on the small scale structures in the Los Angeles Basin. Stressing rate magnitudes are $> 2 \times 10^4$ Pa/yr within $\sim$10 km of the SAF on all segments except for the Mojave and central San Bernardino segments, and magnitudes are $> 1 \times 10^4$ Pa/yr within $\sim 5 - 20$ km of nearly all faults considered in the model.

Stressing rate magnitudes at 5 km depth are similar to those at 1 km depth: the magnitudes range from 313.16 Pa/yr to 3.98×10^5 Pa/yr with a median value of 8.39×10^3 Pa/yr. Magnitudes $> 10^5$ Pa/yr occur at isolated points on the Parkfield and southern Indio segments of the SAF as well as on at select locations on the San Gabriel block, in the Los Angeles Basin, and on the eastern structures in the model. Stressing rate magnitudes are $> 2 \times 10^4$ Pa/yr within $\sim 5 - 10$ km of the SAF everywhere but the Mojave segment, on the San Gabriel fault, throughout much of the Los Angles Basin, and on the northern San Jacinto fault. Stressing rate magnitudes are $> 1 \times 10^4$ Pa/yr on all major structures in the model, with the exception of the eastern Garlock fault.

At 9 km depth, stressing rate magnitudes range from 279.43 Pa/yr to 4.52×10^5 Pa/yr and have a median of 7.61×10^3 Pa/yr and a mean of 1.14×10^4 Pa/yr. Stressing rate magnitudes are $> 10^5$ Pa/yr within $\sim 2 - 3$ km of the northern Indio segment of the SAF and at isolated locations on the Parkfield segment, the San Gabriel block, the Los Angeles Basin, and the southern San Jacinto fault. Unlike previous depths, stressing rate magnitudes are $> 2 \times 10^4$ Pa/yr within $\sim 2 - 10$ km everywhere on the SAF and San Jacinto faults, as well as on the eastern side of the San Gabriel and through much of the Los Angles Basin.

Stressing rate magnitudes at 15 km depth show slightly different patterns than those at previously described depths. Magnitudes represent a broader range: from 192.32 Pa/yr to 2.18×10^6 Pa/yr, but the median (4.32×10^3 Pa/yr) and mean (8.88×10^3 Pa/yr) are lower than at shallower depths. Here stressing rate magnitudes $> 10^5$ Pa/yr are concentrated on the San Gabriel fault and on the western half of the Garlock block, as well as scattered throughout the Los Angeles Basin and on a $\sim$5 km by $\sim$5 km portion of the Parkfield

segment of the SAF. Stressing rate magnitudes are only $> 2 \times 10^4$ Pa/yr on the Parkfield and northern Indio segments of the SAF, and stressing rate magnitudes on the San Berardino segment fall between $1 - 2 \times 10^4$ Pa/yr. Magnitudes on the San Jacinto block are largely between 5×10^3 Pa/yr and 1×10^4 Pa/yr, and the magnitudes on the Mojave segment of the SAF largely fall between $1 - 5 \times 10^3$ Pa/yr.

5.7 Southern California principal stress rotations for a deviatoric background stress

To constrain the principal stress rotation rates in southern California we combine the simple north-south stress regime (described in Equation 5.23) with the Loveless and Meade (2011b) block model-derived southern California stressing rates. The total stress tensor becomes:

$$\boldsymbol{\sigma}^{\mathbf{T}} = \begin{bmatrix} \sigma^* + \dot{\sigma}_{xx}t & \dot{\sigma}_{xy}t \\ \dot{\sigma}_{xy}t & -\sigma^* + \dot{\sigma}_{yy}t \end{bmatrix}. \tag{5.27}$$

The generalized principal stress rotation rate equation (Equation 5.4) reduces to:

$$\dot{\theta} = -\frac{2\dot{\sigma}_{xy}\sigma^*}{4\dot{\sigma}_{xy}^2 t^2 + (2\sigma^* + \dot{\sigma}_{xx}t - \dot{\sigma}_{yy}t)^2}. \tag{5.28}$$

We apply simple north-south and east-west background stresses (Equation 5.23) ranging from $\sigma^* = \pm 10^4$ Pa to $\sigma^* = \pm 10^9$ Pa. To allow for direct comparison to rotation rates from Hardebeck and Hauksson (2001) and stress rotations observed after the Landers and Northridge earthquake main shocks (e.g., Hauksson, 1994; Zhao et al., 1997), we calculate principal stress rotation rates at 5 km depth. This depth is also well within the seismogenic

region for aftershocks from these earthquakes (Hardebeck and Hauksson, 1997, 2001; Mori et al., 2003; Sieh and Jahns, 1984).

5.7.1 Median principal stress rotation rates as a function of the background stress

Rotation rates are dominantly positive (counterclockwise) when $\sigma^* > 0$ and dominantly negative (clockwise) when $\sigma^* < 0$ (Figure 5.10), a result which follows from the largely negative values of $\dot{\sigma}_{xx}$ and $\dot{\sigma}_{yy}$ stressing rates at 5 km depth (consistent with southern California compression) and from Equation 5.28. Positive values of σ^* suggest extension in the x-direction and contraction in the y-direction. Maximum median rotation rates for the entire southern California region (Figure 5.10) decrease with higher magnitude background stresses and over the course of the earthquake cycle. As demonstrated in plots of σ^* versus the rotation rate, $\dot{\theta}$, (Figure 5.10), at the six times in the earthquake cycle considered ($t = 1$, 10, 50, 100, 150, and 200 years) the maximum rotation rate shifts to the right, corresponding to higher magnitude background stresses (Table 5.1). For positive values of σ^*, the fastest median southern California rotation rate in the first year of the earthquake cycle occurs when $\sigma^* = 10^4$ Pa and is 11.82 degrees/yr. In year 10 of the earthquake cycle the fastest rotation rate falls to 1.28 degrees/yr and occurs when $\sigma^* = 10^{4.87}$ Pa. By year 200 the fastest median rotation rate is 0.06 degrees/yr and occurs when $\sigma^* = 10^{6.17}$ Pa. When σ^* is negative the median rotation rates are also negative and the fastest rotation rates are somewhat smaller in magnitude and occur at slightly smaller background stresses (Table 5.1). Like the positive σ^* case, in year one of the earthquake cycle the fastest counterclockwise rotations occur when $\sigma^* = -10^4$ Pa, but the rates are only -7.27 degrees/yr. In year 10 of the earthquake

cycle, the fastest median rotation rate occurs when $\sigma^* = -10^{4.83}$ Pa and is -0.78 degrees/yr. By year 200, the fastest median rotation rate is only -0.04 degrees/yr and occurs when $\sigma^* = -10^{6.13}$ Pa. A complete list of the fastest median clockwise (positive rotation rates) and counterclockwise (negative rotation rates) and the corresponding values of σ^* for years 1, 10, 50, 100, 150, and 200 in the earthquake cycle is provided in Table 5.1.

5.7.2 Regional southern California principal stress rotation rates at various background stresses

We also investigate the regional southern California principal stress axes rotation rates as a function of twelve background stresses ranging from $\sigma^* = \pm 10^4 - \pm 10^9$ Pa (Figures 5.10-5.22; Table 5.2). Median rotation rates at these background stresses and for the six timesteps (t = 1, 10, 50, 100, 150, 200 years) are summarized in Table 5.2. When $\sigma^* = 10^4$ Pa (Figure 5.11, Table 5.2), principal stress axes rotations occur almost entirely in the first year of the earthquake cycle. At year one, the maximum rotation rate is 281.75 degrees/yr and the minimum rotation rate is -351.55 degrees/yr. The median rotation rate is 11.82 degrees/yr and the mean is 10.74 degrees/yr. Only ∼0.2% of all points in the model have $|\dot{\theta}| > 100$ degrees/yr. These points are located on isolated portions of the Parkfield and Indio segments of the SAF and on the North Frontal faults east of the San Bernardino segment of the SAF. $|\dot{\theta}| > 20$ degrees/yr occur to the east and west of the Parkfield, San Bernardino, and Indio segments of the SAF, but not within $\sim 5 - 10$ km of the fault trace. $|\dot{\theta}| > 20$ degrees/yr occurs across the SAF on the boundary between the San Bernardino and Mojave segment. $|\dot{\theta}|$ is > 10 degrees/yr for 61% of the modeled region, consistent with median stressing rate magnitudes of $\sim 10^3$ Pa/yr. At a backgrounds stress of $\sigma^* = 10^4$

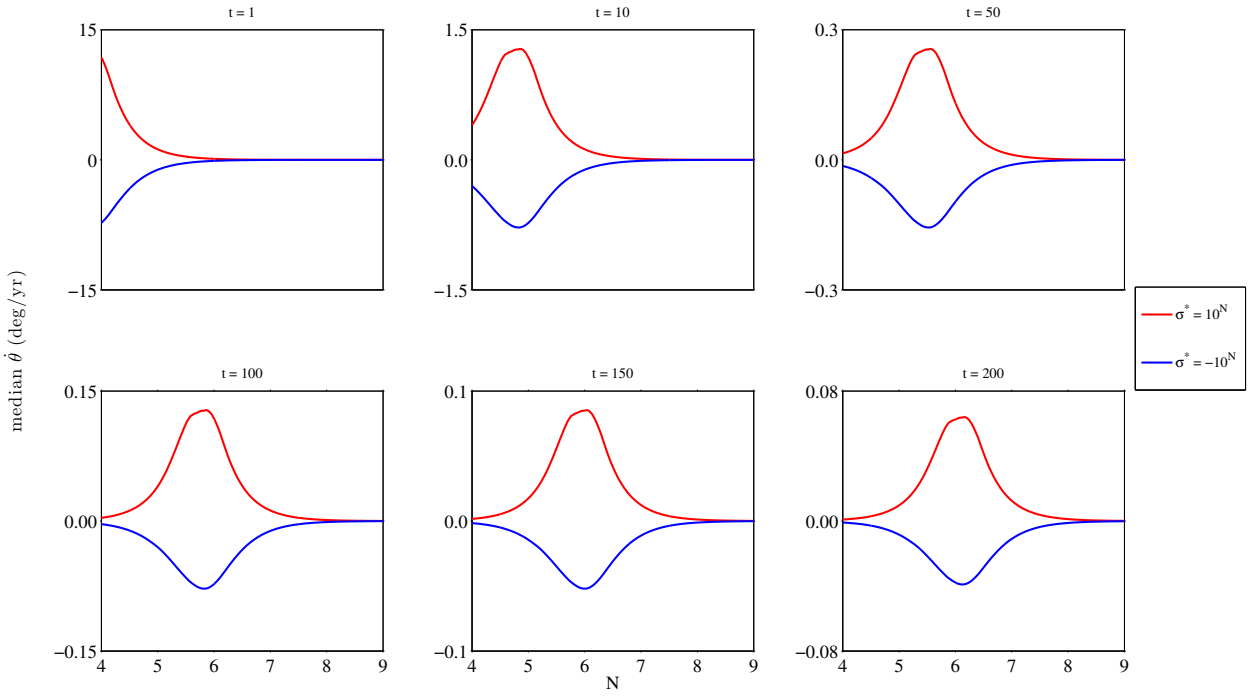

Figure 5.10: N versus the regional southern California median principal stress axes rotation rate, $\dot{\theta}$ at six different times in the earthquake cycle (t = 1, 10, 50, 100, 150, and 200 years), where $\sigma^* = 10^N$ Pa (red lines) or $\sigma^* = -10^N$ Pa (blue lines). As with the idealized case, with each factor of 10 increase in time (t = 1, 10, 100), the magnitude of the rotation rate decreases by 1. The fastest rotation rate shifts to higher values of N over the earthquake cycle. Negative values σ^* (blue lines) have consistently smaller rotation rates than positive values of σ^* at every time in the earthquake cycle.

Pa the accumulated tectonic stress is already a large proportion of the total stress tensor in the first year of the earthquake cycle and the principal stress axes rotate to reflect this component. By year 10, principal stress rotation rates are much smaller, ranging from 104.80 degrees/yr to -49.00 degrees/yr with a median value of 0.40 degrees/yr and a mean value of 0.58 degrees/yr. The fastest rotation rates have moved away from fault traces: instances where $|\dot{\theta}| > 10$ degrees occur $\sim 30 - 50$ km from the Parkfield and Indio segments of the SAF and represent $< 0.5\%$ of all model points. By year 50 of the earthquake cycle, the maximum rotation rate is 5.73 degrees/yr, the minimum is -3.19 degrees/yr, the median

Earthquake Cycle (Years)	t = 1	t = 10	t = 50	t = 100	t = 150	t = 200
Max. Clockwise Median Rotation Rate (deg/yr)	11.82	1.28	0.26	0.13	0.09	0.06
Max. Clockwise σ* (Pa)	$10^{4.00}$	$10^{4.87}$	$10^{5.56}$	$10^{5.87}$	$10^{6.05}$	$10^{6.17}$
Max. Counterclockwise Median Rotation Rate (deg/yr)	-7.27	-0.78	-0.16	-0.08	-0.05	-0.04
Max. Counterclockwise σ* (Pa)	$-10^{4.00}$	$-10^{4.83}$	$-10^{5.53}$	$-10^{5.83}$	$-10^{6.01}$	$-10^{6.13}$

Table 5.1: Table of the fastest clockwise (positive) and counterclockwise (negative) median regional southern California rotation rate (from Figure 5.10) and the corresponding value of σ^* for t =1, 10, 50, 100, 150, and 200 years in the earthquake cycle. As shown in Figure 5.10, rotation rates decrease by approximately an order of magnitude with each factor of 10 increase in time. The fastest median rotation rates occur at higher exponent values of σ^* as time increases. The fastest counterclockwise rotations are $\sim 60\%$ of the fastest clockwise rotations and, with the exception of the first year in the earthquake cycle, occur at slightly smaller magnitudes of σ^*.

is 0.01 degrees/yr, and the mean is 0.02 degrees/yr. In year 100 the maximum rotation rate is 0.55 degrees/yr, the minimum -1.14 degrees/yr, and the mean and median are $\sim$0 degrees/yr. Rotation rates become increasingly smaller as the earthquake cycle progresses.

For $\sigma^* = 10^5$ Pa (Figure 5.12, Table 5.2), principal stress rotations are fastest through the first 10 years of the earthquake cycle before becoming smaller as the earthquake cycle progresses. In the first year, $\dot{\theta}$ ranges from $-53.76 - 27.61$ degrees/yr with a median value of 1.22 degrees/yr and a mean of 1.55 degrees/yr. $|\dot{\theta}|$ is > 5 degrees/yr within $\sim$5 km of the Parkfield, Carrizo, northern San Bernardino, and Indio segments of the SAF, as well as at several locations on the San Gabriel, Santa Susana, Sierra Madre, and Cucamonga faults (bordering the San Gabriel block) and in the Transverse Ranges, the Los Angeles Basin, and at isolated locations on the North Frontal fault. This result is consistent with locations where stressing rate magnitudes are $\sim 10^5$ Pa/yr. At these locations the background stress

median rotation rate (degrees/yr)							median total rotation (degrees)
σ* (Pa)	t = 1 year	t = 10 years	t = 50 years	t = 100 years	t = 150 years	t = 200 years	1 - 200 years
10^4	11.82	0.40	0.01	< 0.01	< 0.01	<< 0.01	32.89
10^5	1.22	1.18	0.16	0.04	0.02	0.01	36.83
10^6	0.12	0.12	0.13	0.12	0.09	0.06	21.42
10^7	0.01	0.01	0.01	0.01	0.01	0.01	2.43
10^8	< 0.01	< 0.01	< 0.01	< 0.01	< 0.01	< 0.01	0.24
10^9	<< 0.01	<< 0.01	<< 0.01	<< 0.01	<< 0.01	<< 0.01	0.02
-10^4	-7.27	-0.30	-0.01	> -0.01	> -0.01	>> -0.01	-21.20
-10^5	-1.14	-0.73	-0.10	-0.03	-0.01	-0.01	-24.64
-10^6	-0.10	-0.10	-0.10	-0.07	-0.05	-0.04	-14.90
-10^7	-0.01	-0.01	-0.01	-0.01	-0.01	-0.01	-2.29
-10^8	> -0.01	> -0.01	> -0.01	> -0.01	> -0.01	> -0.01	-0.24
-10^9	>> -0.01	>> -0.01	>> -0.01	>> -0.01	>> -0.01	>> -0.01	-0.02

Table 5.2: Median rotation rate (degrees/yr) for background stresses $\sigma^* = \pm 10^4 - \pm 10^9$ Pa at six different times in the earthquake cycle (t = 1, 10, 50, 100, 150, 200 years). For $\sigma^* = 10^8$ Pa and $\sigma^* = 10^9$ Pa, the median rotation rates are positive but less than 0.01 degrees/yr. For $\sigma^* = -10^8$ Pa and $\sigma^* = -10^9$ Pa, the rotation rates are negative but larger than -0.01 degrees/yr. The right column gives the median total rotation (in degrees) for the entire earthquake cycle (years 1-200) for the corresponding values of σ^*.

and the accumulated tectonic stress contribute equally to the total stress tensor and we expect the fastest rotations. In year 10 of the earthquake cycle, principal stress rotations range from $-146.00 - 111.83$ degrees/yr (median: 1.18 degrees/yr; mean: 1.07 degrees/yr). $|\dot{\theta}|$ is > 2 degrees/yr $\sim$5-20 km west (and east in the south) of the Parkfield segment and on either side of the San Bernardino and Indio segments, suggesting that peak rotation rates are moving away from the SAF fault trace to locations where the stressing rate magnitude is smaller. $\dot{\theta} = 2 - 3$ degrees/yr on and within $\sim$5 km of the San Jacinto fault, where stressing rate magnitudes are lower than the SAF. At year 50 of the earthquake cycle, rotation rates range from $-14.85 - 22.45$ degrees/yr and median and mean values are 0.16 degrees/yr and 0.18 degrees/yr, respectively. Here locations where $\dot{\theta} > 1$ degree/yr are concentrated $\sim$50-80 km west of Parkfield and east of Indio. At year 100 of the earthquake cycle, the median and mean rotation rates are 0.04 degrees/yr and 0.06 degrees/yr respectively (with a range of $-4.90 - 10.48$ degrees/yr), and $\dot{\theta} > 0.5$ degree/yr occur $\sim$65-90 km west of the Parkfield and east of the Indio traces. Rotation rates become increasingly smaller as the earthquake cycle progresses, though maximum and minimum values are always such that $\dot{\theta} > 3$ degrees (though the median and mean values fall to $<$0.02 degrees/yr for each).

Background stress such that $\sigma^* = 10^6$ Pa (Figure 5.13, Table 5.2) is the first background stress considered that is larger than the stressing rate magnitude everywhere in the model. In the first year of the earthquake cycle, rotation rates range from $-7.81 - 4.20$ degrees/yr and median and mean values are 0.12 degrees/yr and 0.15 degrees/yr, respectively. $|\dot{\theta}| >$ 0.5 degrees/yr occur within $\sim$2-10 km of the northern Parkfield, Carrizo, northern San Bernardino, and Indio segments of the SAF. $|\dot{\theta}| > 0.5$ also occur on the faults bounding

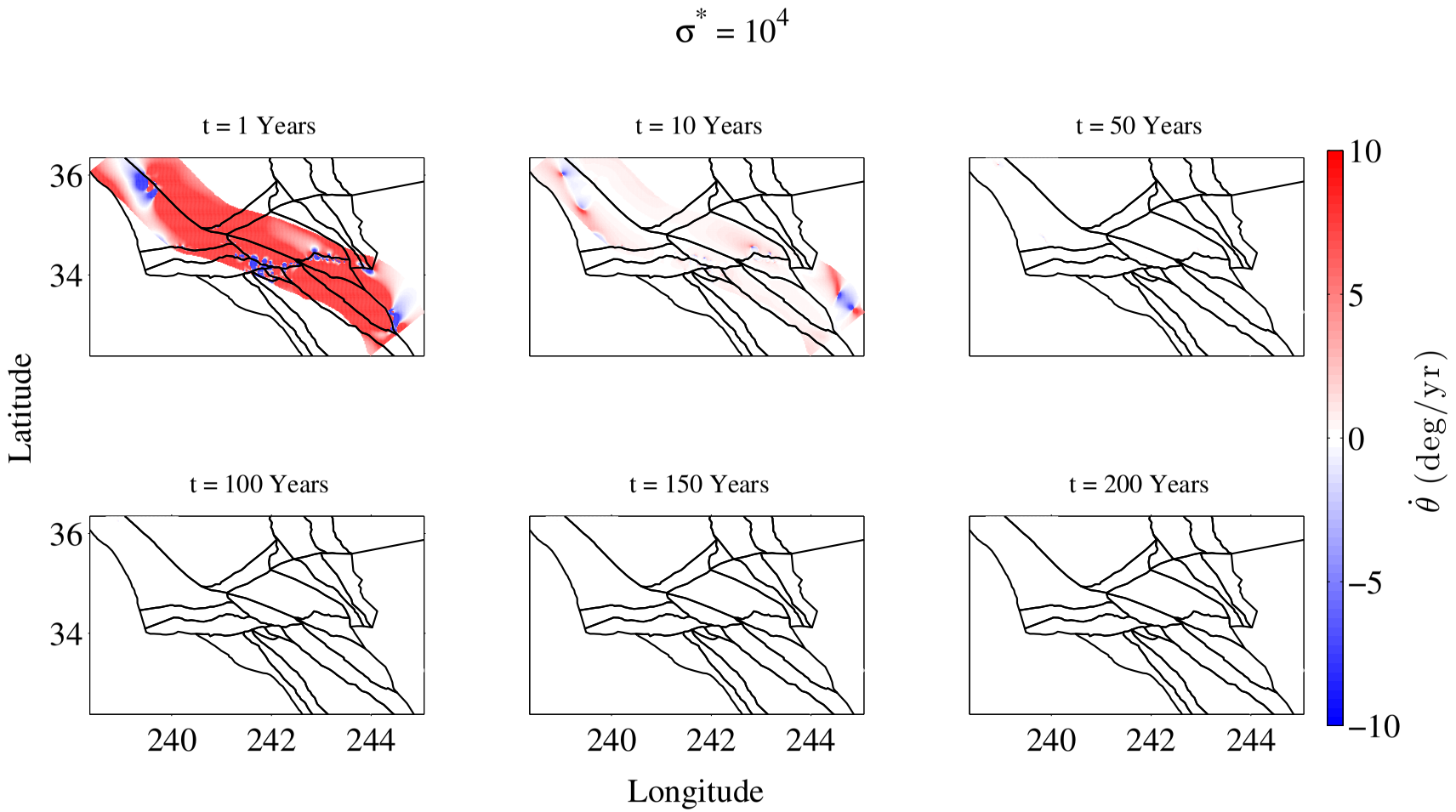

Figure 5.11: Principal stress axes rotation rates at 5 km depth for a deviatoric background stress where $\sigma^b_{xx} = -\sigma^b_{yy} = \sigma^* = 10^4$ Pa. Here red colors indicate positive rotation rates and blue colors indicate negative rotation rates. Colors saturate at ± 10 degrees/yr. At this background stress principal stress axes rotate quickly in the first year of the earthquake cycle but are much smaller at year 10 and negligible in subsequent time frames.

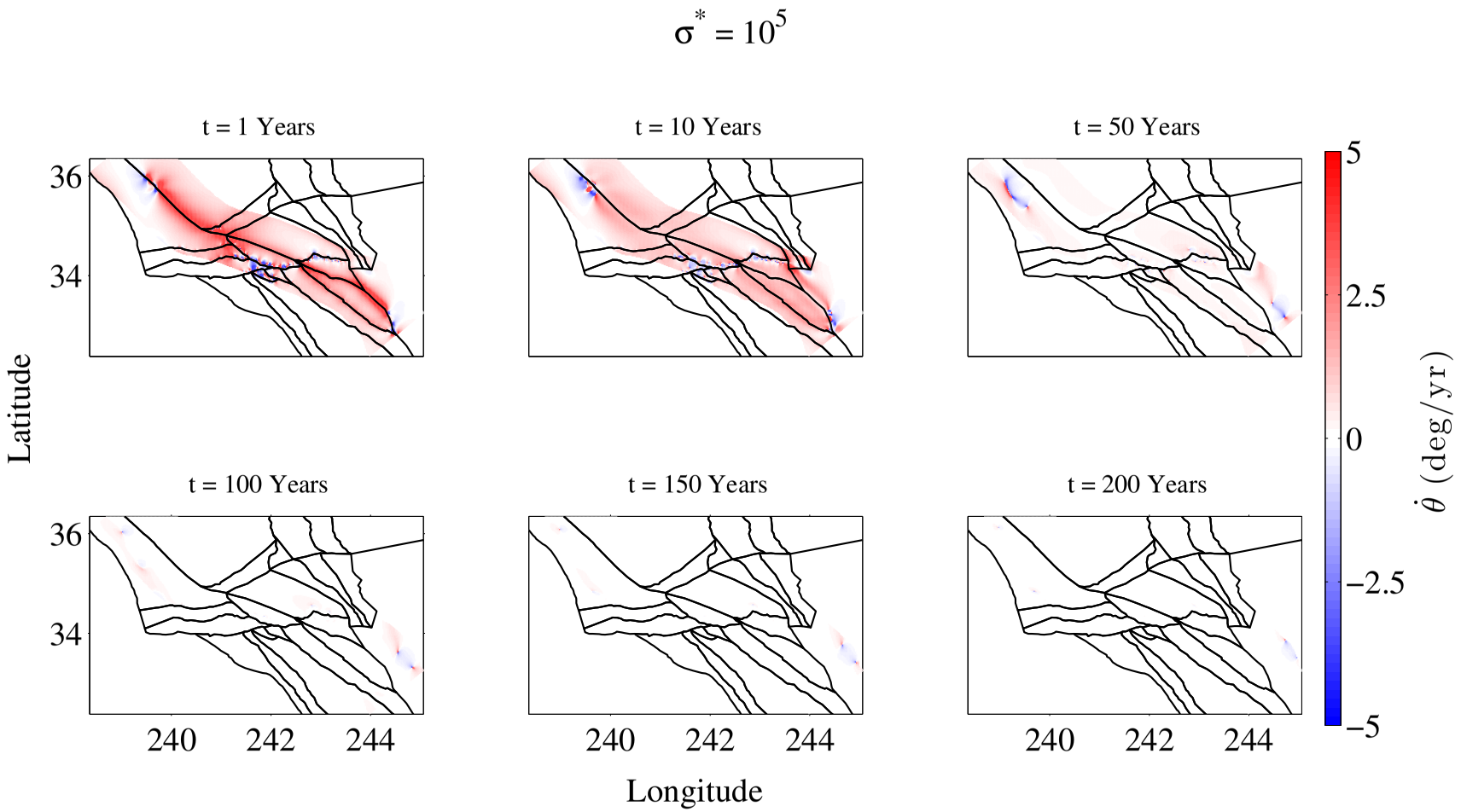

Figure 5.12: Principal stress axes rotation rates at 5 km depth for a deviatoric background stress where $\sigma^b_{xx} = -\sigma^b_{yy} = \sigma^* = 10^5$ Pa. Here red colors indicate positive rotation rates and blue colors indicate negative rotation rates. Colors saturate at ± 5 degrees/yr. At this background stress principal stress axes rotate fastest in year 1 of the earthquake cycle. In year 10 median rotation rates are still > 1 degree/yr, but fall to 0.15 degrees/yr by year 50 and are < 0.1 degrees/yr in subsequent time frames.

the San Gabriel block, in the Transverse Ranges, and in the Los Angeles Basin. In year 10 of the earthquake cycle, rotation rates range from $-5.38 - 2.76$ degrees/yr (the median value is 0.12 degrees/yr and the mean value is 0.16 degrees/yr). $|\dot{\theta}| > 0.5$ occur in nearly identical locations: now within ∼2-10 km of the entire Parkfield segment, as well as on the Carrizo, northern San Bernardino, and Indio segments of the SAF, Rotation rates are also $|\dot{\theta}| > 0.5$ degrees/yr at at the boundary of the San Gabriel block, in the Transverse Ranges, and on structures in the Los Angeles Basin. In year 50 of the earthquake cycle, rotation rates range from $-4.80 - 3.30$ degrees/yr (with a median value of 0.13 degrees/yr and a mean value of 0.14 degrees/yr). Rotation rates with $|\dot{\theta}| > 0.5$ degree/yr now start ∼2 km west of northern Parkfield and ∼2 km east of Indio (as well as at locations close to or on the bounding structures of the San Gabriel block, in the Transverse Ranges, and in the Los Angeles Basin). Rotation rates are $\dot{\theta} = 0.3 - 0.5$ degrees/yr at all locations within ∼15 km of the Parkfield, Indio, and northern San Bernardino segments, as well as within 5-10 km of the San Jacinto, San Gabriel, Transverse Ranges, and Los Angles Basin faults. In year 50 of the earthquake cycle, the maximum rotation rates are moving away from the SAF as the accumulated tectonic stress becomes an equal or dominant contributor to the total stress tensor. Rotation rates on the SAF, however, are not zero because of the nontrivial contribution of the background stress to the total stress tensor. In year 100 of the earthquake cycle, principal stress rotation rates range from $-14.60 - 11.18$ degrees/yr. Median and mean rotation rate values are 0.12 degrees/yr and 0.11 degrees/yr, respectively. The majority of locations where $|\dot{\theta}| > 0.5$ degree/yr occur ∼15-0 km west of Parkfield and east of Indio (though $|\dot{\theta}| > 0.5$ degree/yr at select locations on the North Frontal fault and

in the vicinity of the 1992 Landers earthquake). Similarly, locations with $\dot{\theta} = 0.3 - 0.5$ degrees/yr are concentrated ∼5-20 km west of Parkfield and east of Indio as well as in the southern Eastern California Shear Zone. $\dot{\theta} = 0.2 - 0.3$ degrees/yr occur on either side ($\sim 5 - 30$ km from the fault trace) of Parkfield and Indio, on the east side of northern and southern San Bernardino, and on the San Jacinto fault. Rotation rates range from $-3.07 - 9.21$ degrees/yr in year 150 of the earthquake cycle (here the median value is 0.09 degrees/yr and the mean value is 0.08 degrees/yr). Values of $|\dot{\theta}| > 0.5$ degrees/yr continue to move away from the SAF (now $\sim 10 - 30$ km east of Parkfield and west of Indio as well as ∼5-10 km from northwest-southeast trending faults in the southern Eastern California Shear Zone), $\dot{\theta} = 0.1 - 0.5$ degrees/yr does not occur within ∼5 km of either the SAF or the San Jacinto fault, suggesting that principal stress axes near these fault traces have aligned with the accumulated tectonic stress.

When $\sigma^* = 10^7$ Pa (Figure 5.14, Table 5.2), principal stress rotation rates are small: over 200 years maximum rotation rate values range from $0.28 - 0.51$ degrees/yr (smallest values occur in years 50 and 100 and highest values in year 200) and minimum values range from -1.37 to -0.37 degrees/yr (here the fastest negative rate occurs in year 200). At all times the median rotation rate is 0.01 degrees/yr and the mean rotation rate is 0.02 degrees/yr. In every year of the earthquake cycle the fastest rotation rates ($|\dot{\theta}| > 0.1$ degrees/yr) are concentrated on the Parkfield and Indio segments of the SAF and at points bounding the San Gabriel block and faults in the Los Angeles Basin. Points achieving these rotation rates account for $0.6 - 0.9\%$ of all points in the model. This result is consistent with the stressing rate magnitudes at 5 km depth: maximum stressing rate magnitudes occur on the trace

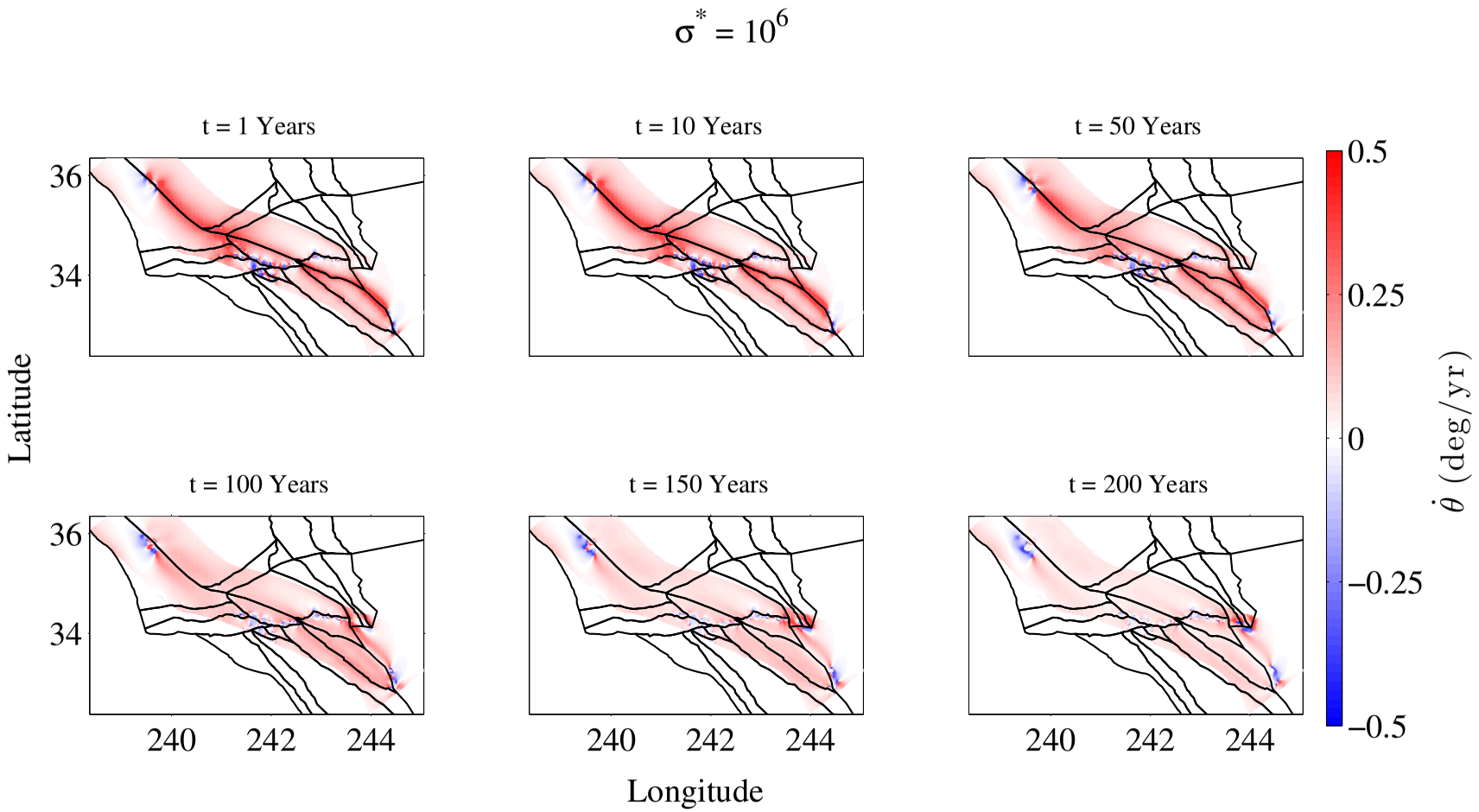

Figure 5.13: Principal stress axes rotation rates at 5 km depth for a deviatoric background stress where $\sigma^b_{xx} = -\sigma^b_{yy} = \sigma^* = 10^6$ Pa. Here red colors indicate positive rotation rates and blue colors indicate negative rotation rates. Colors saturate at ± 0.5 degrees/yr. At this background stress principal median principal stress axes rotation rates are 0.12-0.14 degrees/yr for years 1-100 of the earthquake cycle and then fall to 0.06 degrees/yr by year 200. Rotation rates are fastest on the fault traces in the first 10 years but move away from the SAF as the earthquake cycle progresses.

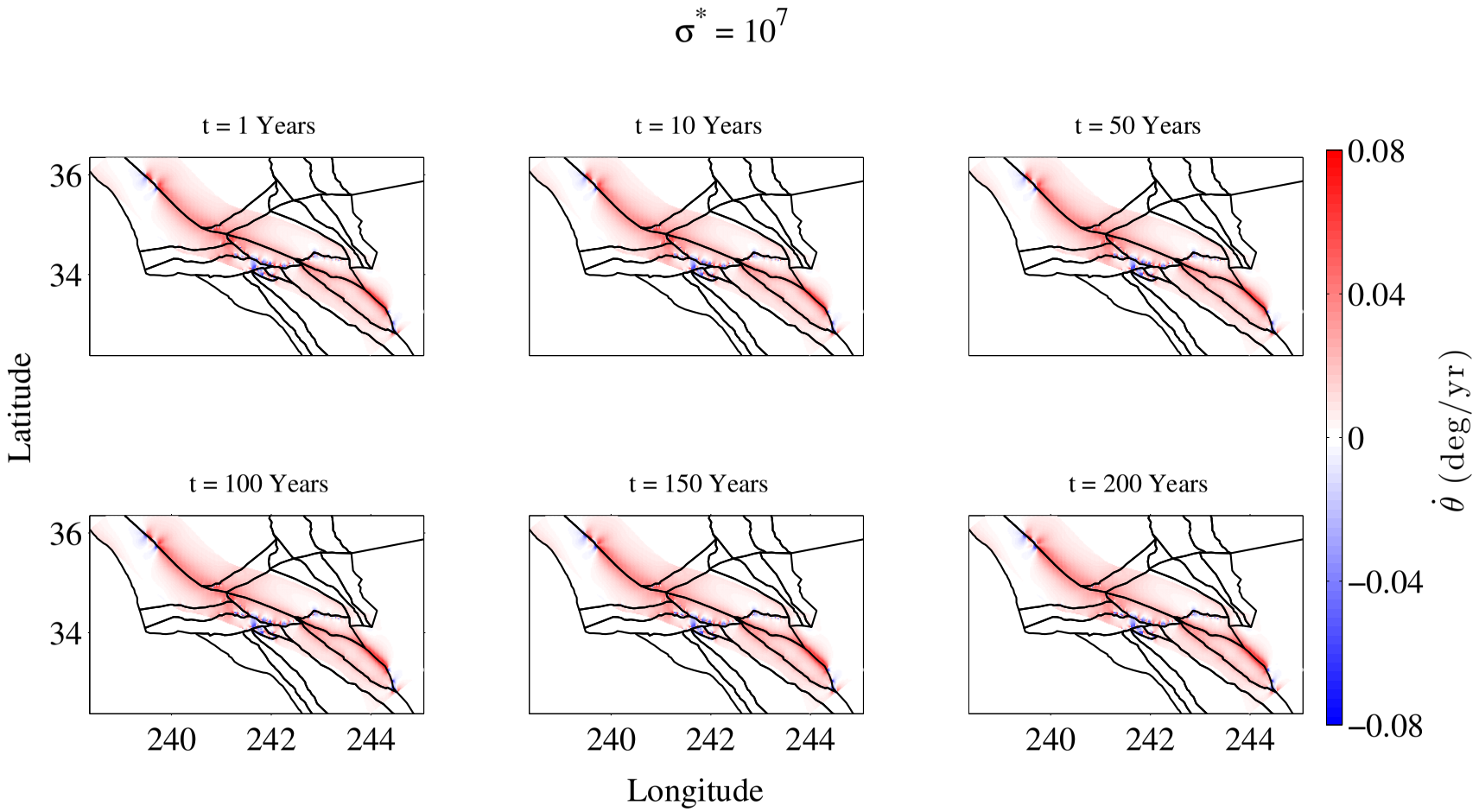

Figure 5.14: Principal stress axes rotation rates at 5 km depth for a deviatoric background stress where $\sigma^b_{xx} = -\sigma^b_{yy} = \sigma^* = 10^7$ Pa. Here red colors indicate positive rotation rates and blue colors indicate negative rotation rates. Colors saturate at ± 0.08 degrees/yr. At this background stress the median rotation rate is 0.01 degrees/yr over the entire earthquake cycle and maximum rotation rates occur almost exclusively at fault traces at every time interval.

of the Parkfield and Indio segments of the SAF and are $\sim 10^5$ Pa/yr. At a background stress of $\sigma^* = 10^7$ Pa it will take ∼100 years for the accumulated tectonic stress to be an approximately equal contributor to the total stress tensor at these locations, and even longer (∼1000 years) for it to become the dominant stress term. Thus principal stress rotations will continue even at locations that experience maximum stressing rate magnitudes over the entire 200 years we are considering here.

Similar behavior is observed for $\sigma^* = 10^8$ Pa (Figure 5.15, Table 5.2) and $\sigma^* = 10^9$ Pa (Figure 5.16, Table 5.2) but principal stress rotation rates are smaller. When $\sigma^* = 10^8$ Pa, rotation rates range from $-0.08 - 0.04$ degrees/yr. At $\sigma^* = 10^9$ Pa, $\dot{\theta} < 0.01$ degrees/yr. At both background stresses the median and mean principal stress rotation rates are ∼0 degrees/yr. The fastest rotation rates are concentrated at fault traces (and, in particular, on the Parkfield and Indio segments of the SAF).

Principal stress rotations follow a similar pattern for negative values of σ^*, which indicate x-direction contraction and y-direction extension. When $\sigma^* = -10^4$ Pa (Figure 5.17, Table 5.2), principal stress axes rotation rates are highest in the first year of the earthquake cycle, ranging from $-144.47 - 136.25$ degrees/yr with a median rotation rate of -7.27 degrees/yr and a mean rotation rate of -6.53 degrees/yr. Rotation rates ($|\dot{\theta}| > 15$ degrees/yr) are highest on the central western portion of the White Wolf fault and at isolated locations on the structures bounding the San Gabriel block and in the Transverse Ranges and Los Angeles Basin. $\dot{\theta} < -15$ degrees/yr also occur $\sim 5 - 30$ km east of northern Parkfield. At this location on the fault trace the stressing rate magnitudes are $\sim 10^5$ Pa/yr and the accumulated tectonic stress is already the dominant term in the stress tensor. It takes $\ll 1$

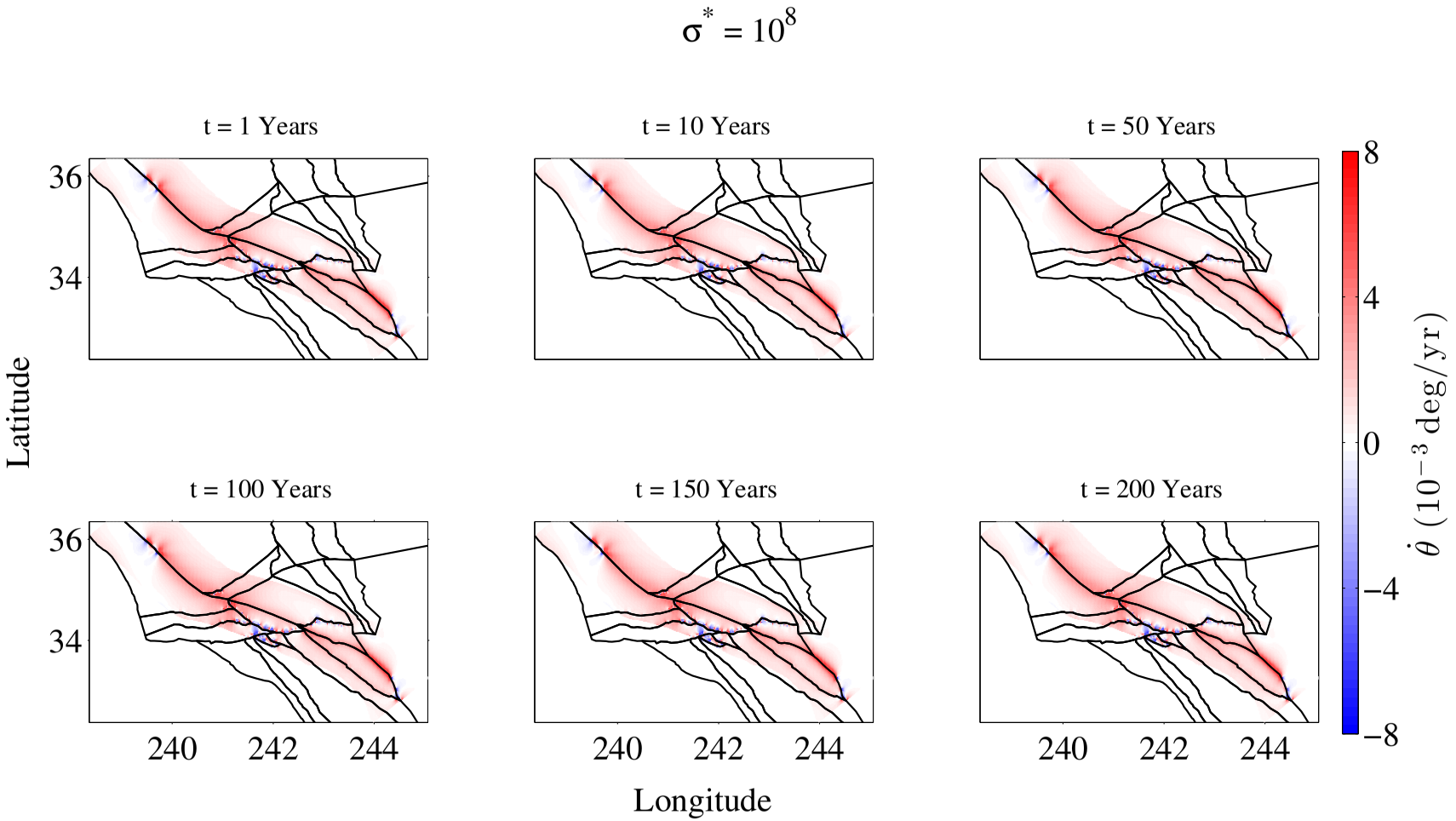

Figure 5.15: Principal stress axes rotation rates at 5 km depth for a deviatoric background stress where $\sigma^b_{xx} = -\sigma^b_{yy} = \sigma^* = 10^8$ Pa. Here red colors indicate positive rotation rates and blue colors indicate negative rotation rates. Colors saturate at ± 0.008 degrees/yr. At this background stress the median rotation rate is 0.001 degrees/yr over the entire earthquake cycle and maximum rotation rates occur exclusively at fault traces at every time interval.

year for principal stress axes to align with the tectonic component, and they will not continue to rotate through the earthquake cycle. Principal stress axis rotations are $|\dot{\theta}| > 10$ degrees/yr on the Carrizo, Mojave, and much of the San Bernardino segments of the SAF as well as on the Garlock fault. By year 10 of the earthquake cycle, rotation rates are much smaller: while they range from $-15.64 - 38.55$ degrees/yr, the median is -0.30 degrees/yr and the average is -0.32 degrees/yr. Rotation rates on the northernmost SAF points in the model (north Parkfield) are positive and range from $1 - 5$ degrees/yr, but $|\dot{\theta}| > 1$ degrees/yr account for only 4.6% of all points in the model. The largest concentration occurs $\sim 40 - 50$ km east of Parkfield. By year 50 in the earthquake cycle, only 7.6% of rotation rates are $|\dot{\theta}| > 0.05$ degrees/yr.

For $\sigma^* = -10^5$ Pa (Figure 5.18, Table 5.2), principal stress rotations persist through the first 10 years of the earthquake cycle and, to a smaller degree, through year 50. In the first year rotation rates range from $-40.23 - 74.93$ degrees/yr and have a median value of -1.14 degrees/yr and a mean value of -1.42 degrees/yr. $\sim$0.4% of points have stress rotations $|\dot{\theta}| > 10$ degrees/yr, and these occur on the trace of the northern Parkfield and southern Indio segments of the SAF and at isolated locations bounding the San Gabriel block and in the Los Angeles Basin. $|\dot{\theta}| = 5 - 10$ degrees/yr on the northern Parkfield, Carrizo, and Indio segments of the SAF. Rotation rates of this magnitude also occur on the faults bounding the San Gabriel block, in the Transverse Ranges, and in the Los Angeles Basin. During the first year of the earthquake cycle, rotation rates of $|\dot{\theta}| > 1$ degrees/yr occur on all faults in the model. In year 10 of the earthquake cycle rotation rates range from $-45.32 - 63.97$ degrees/yr and have a median and mean value of -0.73 degrees/yr and -0.65 degrees/yr, respectively.

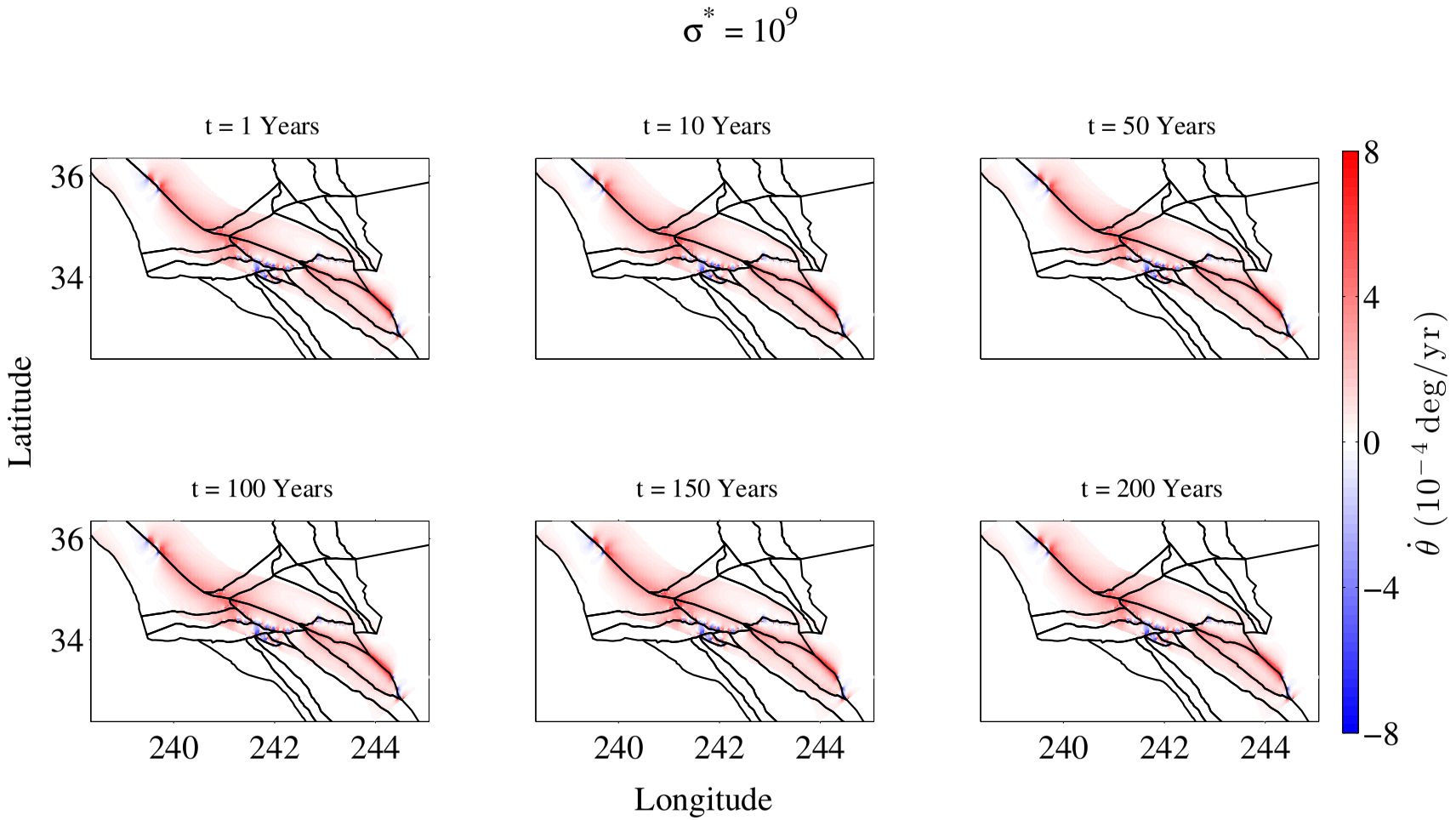

Figure 5.16: Principal stress axes rotation rates at 5 km depth for a deviatoric background stress where $\sigma^b_{xx} = -\sigma^b_{yy} = \sigma^* = 10^9$ Pa. Here red colors indicate positive rotation rates and blue colors indicate negative rotation rates. Colors saturate at 8×10^{-4} degrees/yr. At this background stress the median rotation rate is 0.001 degrees/yr over the entire earthquake cycle and maximum rotation rates occur exclusively at fault traces at every time interval.

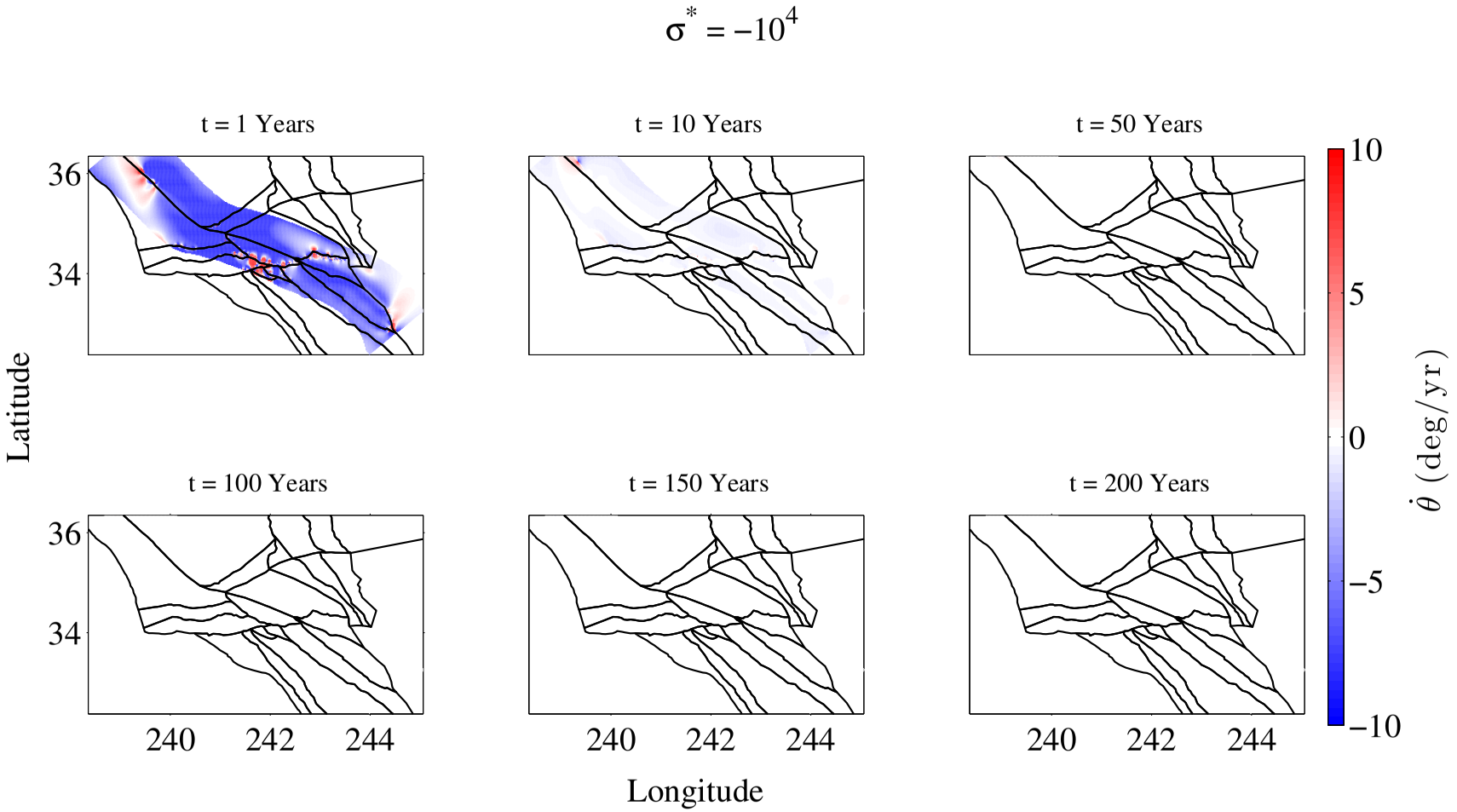

Figure 5.17: Principal stress axes rotation rates at 5 km depth for a deviatoric background stress where $\sigma^b_{xx} = -\sigma^b_{yy} = \sigma^* = -10^4$ Pa. Here red colors indicate positive rotation rates and blue colors indicate negative rotation rates. Colors saturate at ±10 degrees/yr. At this background stress principal stress axes rotate quickly (the median rotation rate is -7.53 degrees/yr) in the first year of the earthquake cycle but are much smaller (the median is -0.30 degrees/yr) at year 10 and negligible in subsequent time frames.

Here principal stress axes rotation rates $|\dot{\theta}| > 2$ degrees/yr account for $< 0.7\%$ of all points (the largest concentration is east of the Parkfield segment of the SAF, but there are also isolated points on the Indio segment, on the bounding faults of the San Gabriel fault, in the Los Angeles Basin, and on the North Frontal fault), but rates $|\dot{\theta}| > 1$ degrees/yr account for $\sim$28% of all points. Rotation rates $|\dot{\theta}| > 1 - 2$ degrees/yr occur $\sim 2 - 40$ km from the trace of the Parkfield and northern Carrizo segments of the SAF, as well as on the remainder of the Carrizo segment, the Mojave and San Bernardino segments, the Garlock and White Wolf faults, and on structures bounding the San Gabriel fault and in the Transverse Ranges and Los Angeles Basin. At year 50, rotation rates range from $-2.80 - 3.32$ degrees/yr and the median and mean are both equal to -0.10 degrees/yr. Rotation rates $|\dot{\theta}| > 0.3$ account for just $\sim$3% of all points, but 53% of points satisfy $|\dot{\theta}| > 0.1$ degrees/yr. The majority of points for which $\dot{\theta} = 0.3 - 0.5$ occur east of the Parkfield trace. $|\dot{\theta}| > 0.1$ degrees/yr also occurs $\geq$10 km from the San Jacinto fault trace. These results are consistent with the calculated stressing rate magnitudes and $\sigma^* = -10^5$ Pa: near the SAF, where stressing rate magnitudes are highest, the accumulated tectonic stress will become the dominant term in the total stress tensor after $\sim$10 years and principal stresses at the fault will stop rotating (as they become aligned with the tectonic stress direction). Maximum stress rotations will migrate away from the fault.

When $\sigma^* = -10^6$ Pa (Figure 5.19, Table 5.2), small-scale principal stress rotations occur throughout the earthquake cycle. In the first year, rotation rates range from $-4.33 - 6.38$ degrees/yr (median and mean values are -0.12 degrees/yr and -0.15 degrees/yr, respectively). Rotation rates such that $|\dot{\theta}| > 0.5$ degrees/yr occur on the trace of the northern Parkfield,

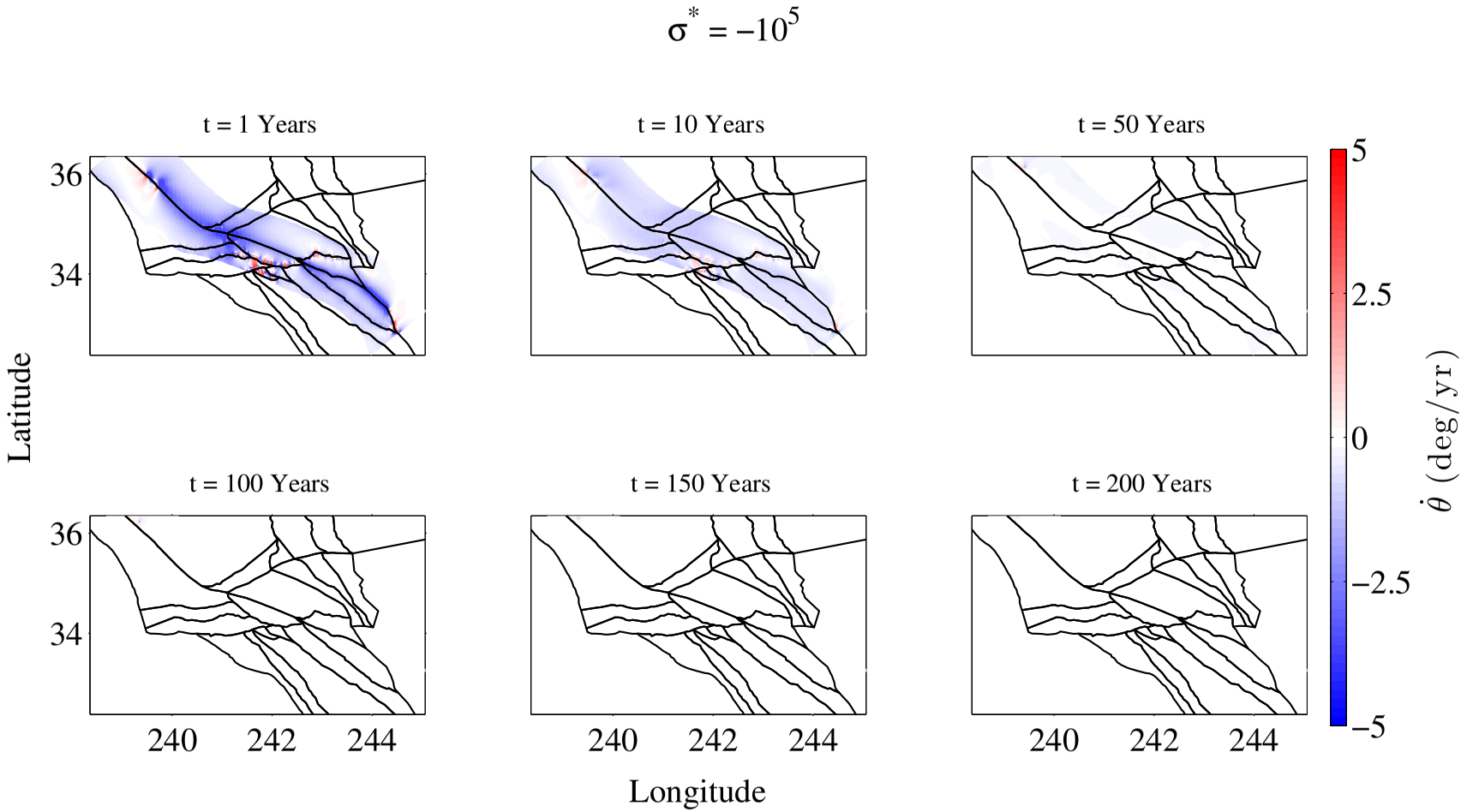

Figure 5.18: Principal stress axes rotation rates at 5 km depth for a deviatoric background stress where $\sigma^b_{xx} = -\sigma^b_{yy} = \sigma^* = -10^5$ Pa. Here red colors indicate positive rotation rates and blue colors indicate negative rotation rates. Colors saturate at ± 5 degrees/yr. At this background stress principal stress axes rotate fastest in year 1 of the earthquake cycle (the median rotation rate is -1.22 degrees/yr). In year 10, median rotation rates are -0.75 degrees/yr, and fall to -0.10 degrees/yr by year 50 and are < 0.05 degrees/yr in subsequent time frames.

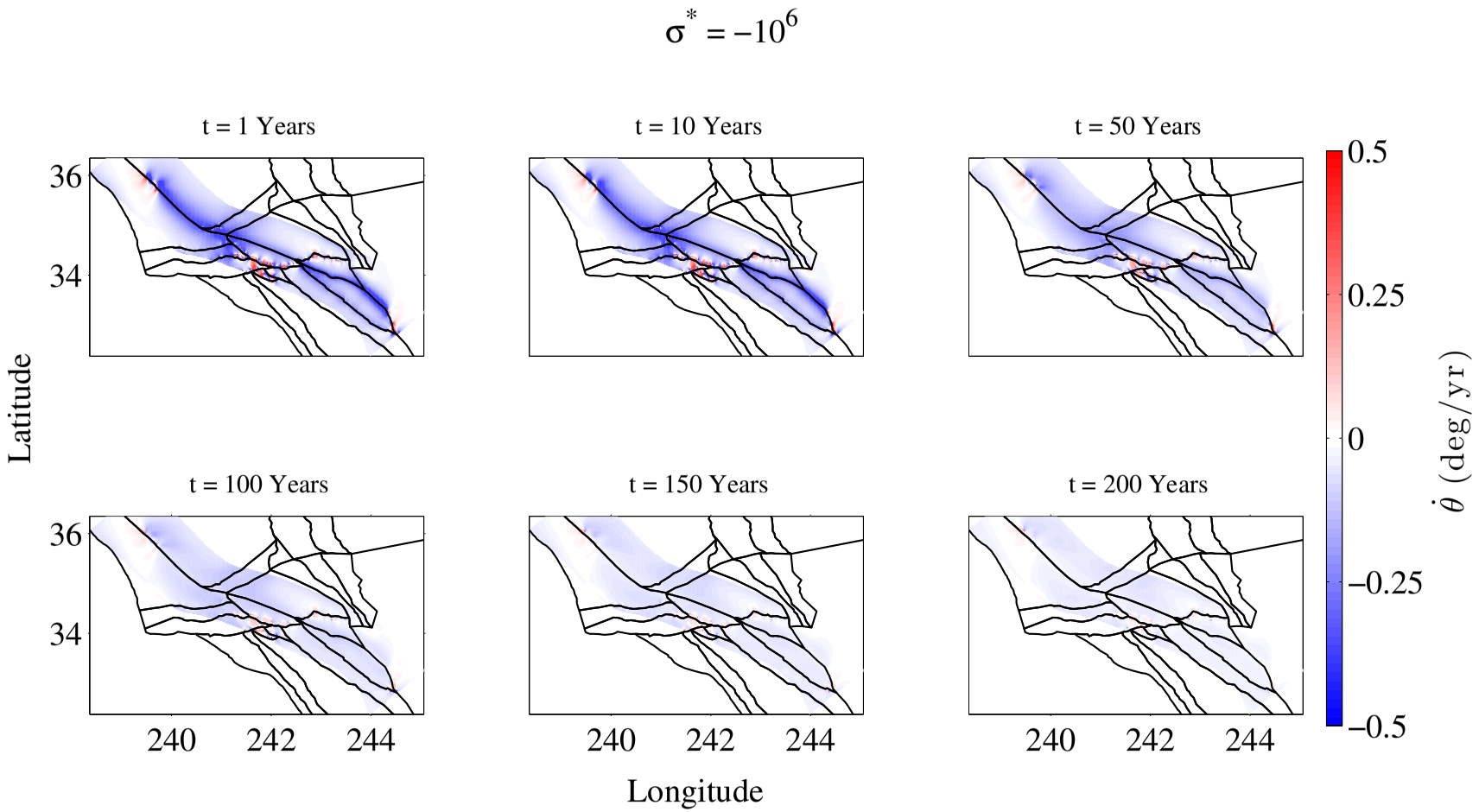

Figure 5.19: Principal stress axes rotation rates at 5 km depth for a deviatoric background stress where $\sigma^b_{xx} = -\sigma^b_{yy} = \sigma^* = -10^6$ Pa. Here red colors indicate positive rotation rates and blue colors indicate negative rotation rates. Colors saturate at ± 0.5 degrees/yr. At this background stress principal median principal stress axes rotation rates are -0.10-0.12 degrees/yr for years 1-50 of the earthquake cycle and then fall to -0.04 degrees/yr by year 200. Rotation rates are fastest on the fault traces in the first 10 years but move away from the SAF as the earthquake cycle progresses.

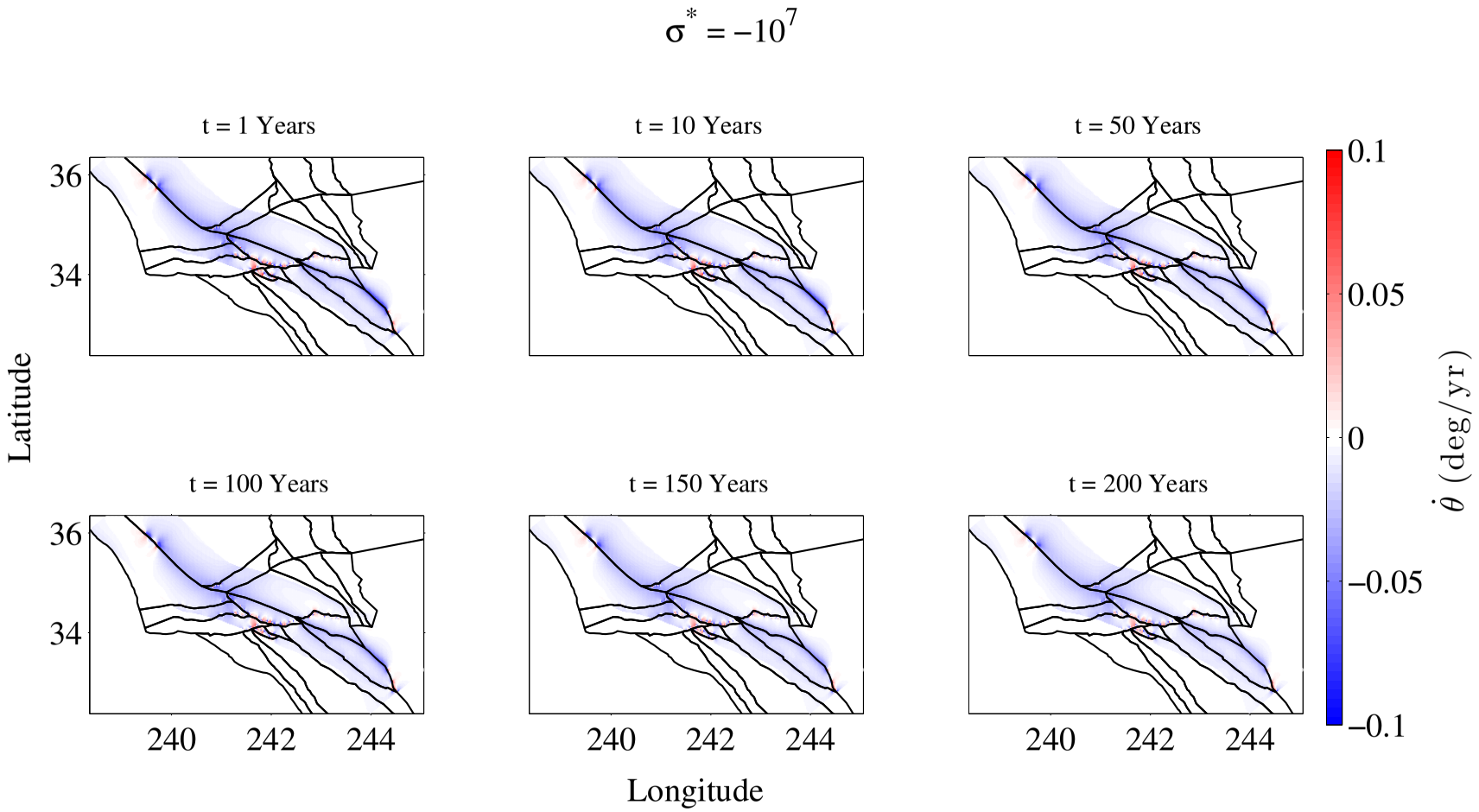

Figure 5.20: Principal stress axes rotation rates at 5 km depth for a deviatoric background stress where $\sigma^b_{xx} = -\sigma^b_{yy} = \sigma^* = -10^7$ Pa. Here red colors indicate positive rotation rates and blue colors indicate negative rotation rates. Colors saturate at ± 0.1 degrees/yr. At this background stress the median rotation rate is -0.01 degrees/yr over the entire earthquake cycle and maximum rotation rates occur almost exclusively at fault traces at every time interval.

Carrizo, northern San Bernardino, and Indio segments of the SAF and on the boundaries of the San Gabriel block, the Transverse Ranges, and the Los Angeles Basin. $|\dot{\theta}| > 0.2$ degrees/yr occur everywhere on the SAF, San Jacinto, and San Gabriel block faults as well as through much of the Transverse Ranges and Los Angeles Basin. Rotation rates in year 10 of the earthquake cycle are similar: they range from $-4.02 - 7.49$ degrees/yr with median and mean values of-0.11 degrees/yr and -0.14 degrees/yr, respectively. Slightly fewer points have rotation rates $|\dot{\theta}| > 0.5$ degrees/yr, but they occur in the same locations as in year 1 of the earthquake cycle. As with year 1 of the earthquake cycle, $|\dot{\theta}|$ is > 0.2 degrees/yr everywhere on the SAF, San Jacinto, and San Gabriel block boundaries, and through much of the Transverse Ranges and the Los Angeles Basin. In year 50, rotation rates are again similar in range: from $-4.59 - 1.74$ degrees/yr. Median and mean values are both -0.10 degrees/yr. $|\dot{\theta}| > 0.3$ degrees/yr are rare and occur on and near the northern Parkfield segment of the SAF, on the boundaries of the San Gabriel block, and in the Los Angeles Basin. $|\dot{\theta}| > 0.2$ degrees/yr occur on the Mojave, Carrizo, and San Bernardino traces of the SAF, on the boundaries of the San Gabriel fault, and in the Transverse Ranges and Los Angeles Basin. Rotation rates with these magnitudes also occur $\sim 2 - 20$ km east of the Parkfield segment and at select locations on the North Frontal fault trace. Principal stress rotation rates slow in year 100 of the earthquake cycle, and range from $-4.53 - 6.40$ degrees/yr (median and mean rotation rate values are both -0.07 degrees/yr). $|\dot{\theta}| > 0.2$ degrees/yr account for $\sim$0.6% of all ponts, but $|\dot{\theta}| > 0.1$ degrees/yr make up $\sim$28% of all modeled points $|\dot{\theta}| > 0.1 - 0.2$ degrees/yr occur $2 - 40$ km east of Parkfield. $|\dot{\theta}| > 0.1 - 0.2$ degrees/yr on the Carrizo, Mojave, and San Bernardino segments of the SAF and at many locations

along the North Frontal and San Gabriel block-bounding faults. As with the $\sigma^* = 10^6$ Pa case, by year 100 the accumulated tectonic stress has likely become the dominant term in the total stress tensor and the principal stress axes have stopped rotating. Rotations occur where the accumulated tectonic stress is smaller and the principal stress axes continue to be a function of both the region background stress and the tectonic stress.

For background stresses such that $\sigma^* = -10^7$ Pa (Figure 5.20, Table 5.2), $\sigma^* = -10^8$ Pa (Figure 5.21, Table 5.2), and $\sigma^* = -10^9$ Pa (Figure 5.22, Table 5.2), it takes much longer than the 200-year earthquake cycle considered here for the accumulated tectonic stresses to dominate ($\sim$1000, 10,000, and 100,000 years, respectively, given maximum stressing rate magnitudes of $\sim 10^5$ Pa/yr). As a result, maximum principal stress rotation rates are typically at locations with the highest stressing rate magnitudes (typically on the northern Parkfield, Carrizo, and Indio segments of the SAF and at points bounding the San Gabriel block and in the Transverse Ranges and Los Angeles Basin). For $\sigma^* = -10^7$ Pa, rotation rate values at these points are typically $|\dot{\theta}| = 0.05 - 0.1$ degrees/yr for all faults in the model. Rotation rates are a factor 10 smaller when $\sigma^* = -10^8$ Pa. Here the fastest rotation rates are typically $|\dot{\theta}| = 0.005 - 0.01$ degrees/yr and, again, occur on the northern Parkfield, Carrizo, and Indio traces of the SAF, on boundaries of the San Gabriel block, and in the Transverse Ranges and Los Angeles Basin. For $\sigma^* = -10^9$ Pa, rotation rates again decrease by an order of magnitude (maximum $|\dot{\theta}| = 0.0005 - 0.001$ degrees/yr and occur in the same locations described above).

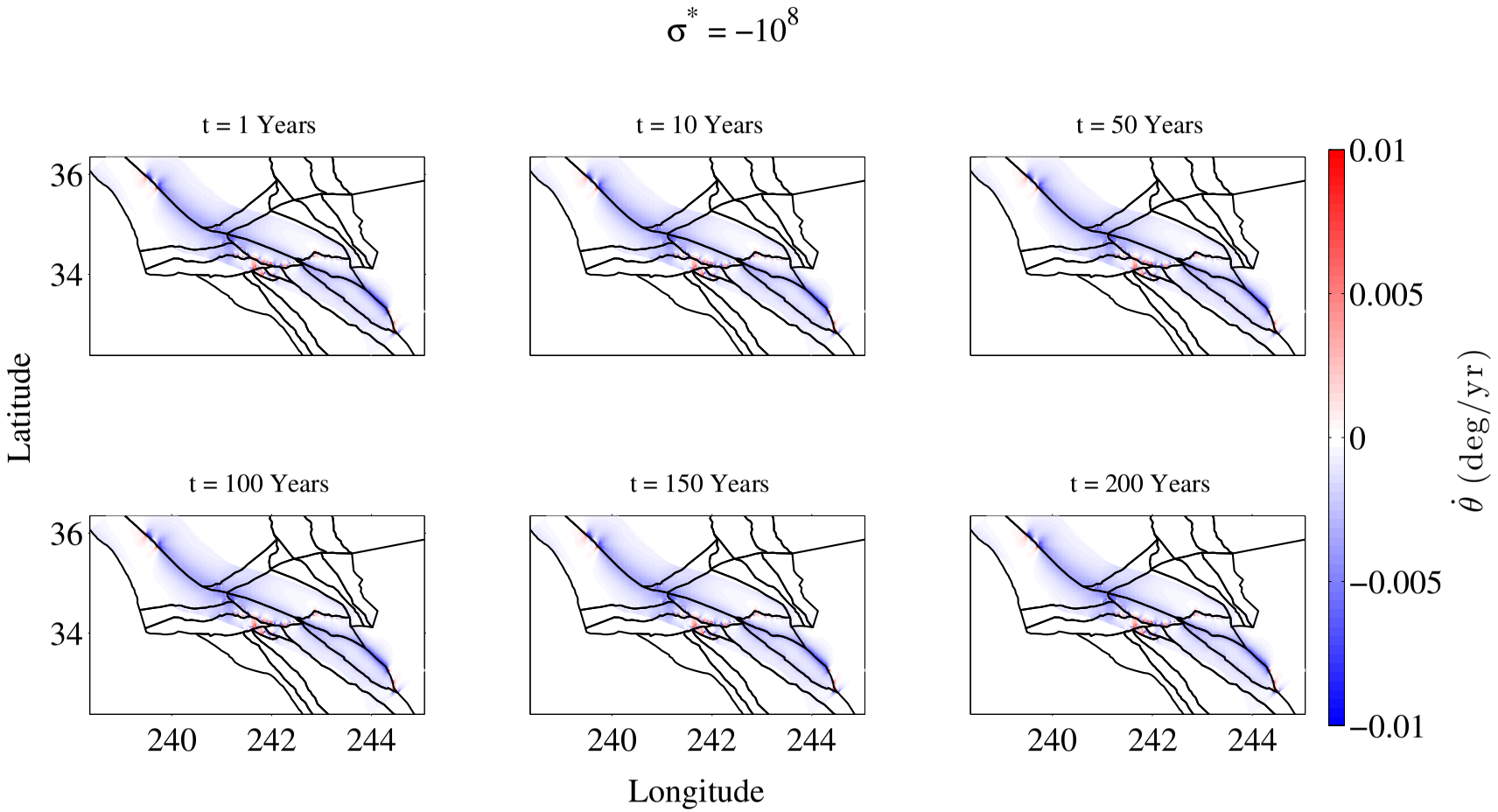

Figure 5.21: Principal stress axes rotation rates at 5 km depth for a deviatoric background stress where $\sigma^b_{xx} = -\sigma^b_{yy} = \sigma^* = -10^8$ Pa. Here red colors indicate positive rotation rates and blue colors indicate negative rotation rates. Colors saturate at ± 0.01 degrees/yr. At this background stress the median rotation rate is -0.001 degrees/yr over the entire earthquake cycle and maximum rotation rates occur exclusively at fault traces at every time interval.

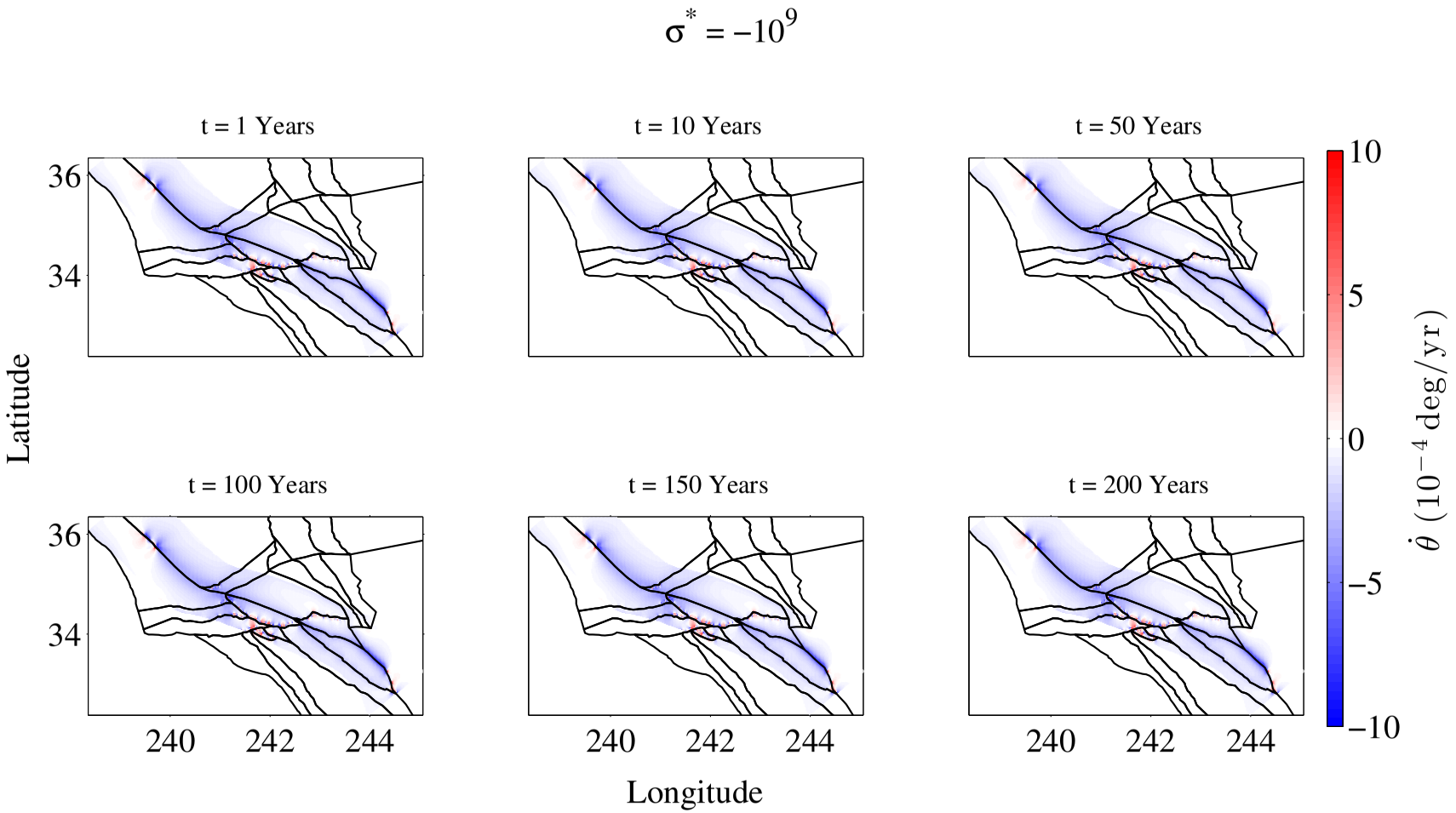

Figure 5.22: Principal stress axes rotation rates at 5 km depth for a deviatoric background stress where $\sigma^b_{xx} = -\sigma^b_{yy} = \sigma^* = -10^9$ Pa. Here red colors indicate positive rotation rates and blue colors indicate negative rotation rates. Colors saturate at ± 0.001 degrees/yr. At this background stress the median rotation rate is 1×10^{-4} degrees/yr over the entire earthquake cycle and maximum rotation rates occur exclusively at fault traces at every time interval.

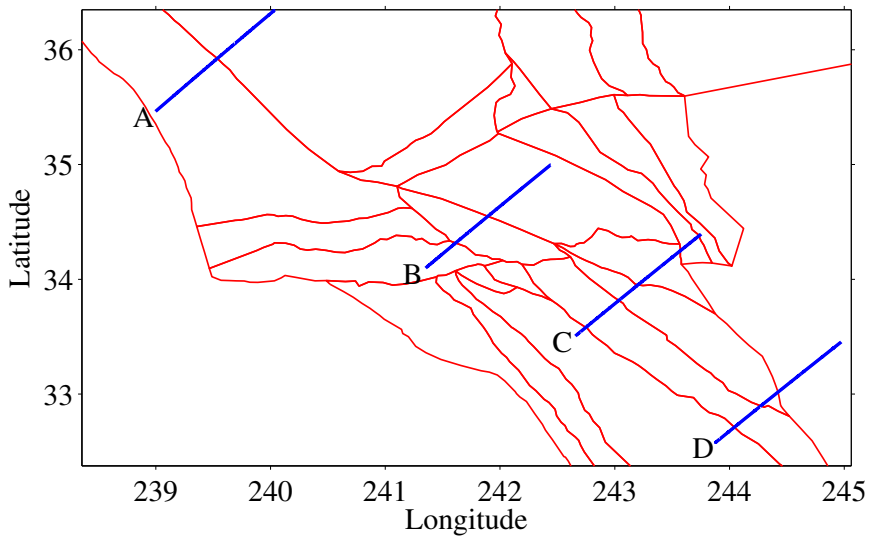

Figure 5.23: Locations of the four rotation rate profiles (blue) across the SAF. The model blocks, from Loveless and Meade (2011b) are shown in red. Profile A crosses the SAF at the Parkfield segment, Profile B at the Mojave segment, Profile C at the San Bernardino segment, and Profile D at the Indio segment.

5.7.3 Principal stress rotation rate profiles across the San Andreas fault

To determine how rotation rates vary across the SAF, we find rotation rates on four profiles across the SAF (Figure 5.23) on the Parkfield (Figure 5.24), Mojave (Figure 5.25), San Bernardino (Figure 5.26), and Indio (Figure 5.27) segments. In all four profiles we consider rotation rates at 5 km depth and within ±70 km from the SAF, background stresses where $\sigma^* = \pm 10^4 - \pm 10^9$ Pa, and times of 1, 10, 50, 100, 150, and 200 years in the earthquake cycle. Across Parkfield (Profile A, Figure 5.24) rotation rates typically change sign across the SAF for background stresses where $\sigma^* = \pm 10^4 - \pm 10^6$ Pa. At these background stresses the location of the maximum rotation rate moves away from the fault as the earthquake cycle progresses. This trend is the most pronounced when $\sigma^* = -10^6$ Pa, and rotation rates are highest (< -1 degree/yr) in the first year of the earthquake cycle right on the fault trace. By year 50, the maximum rotation rate on the east of the fault is ∼10 km from the fault

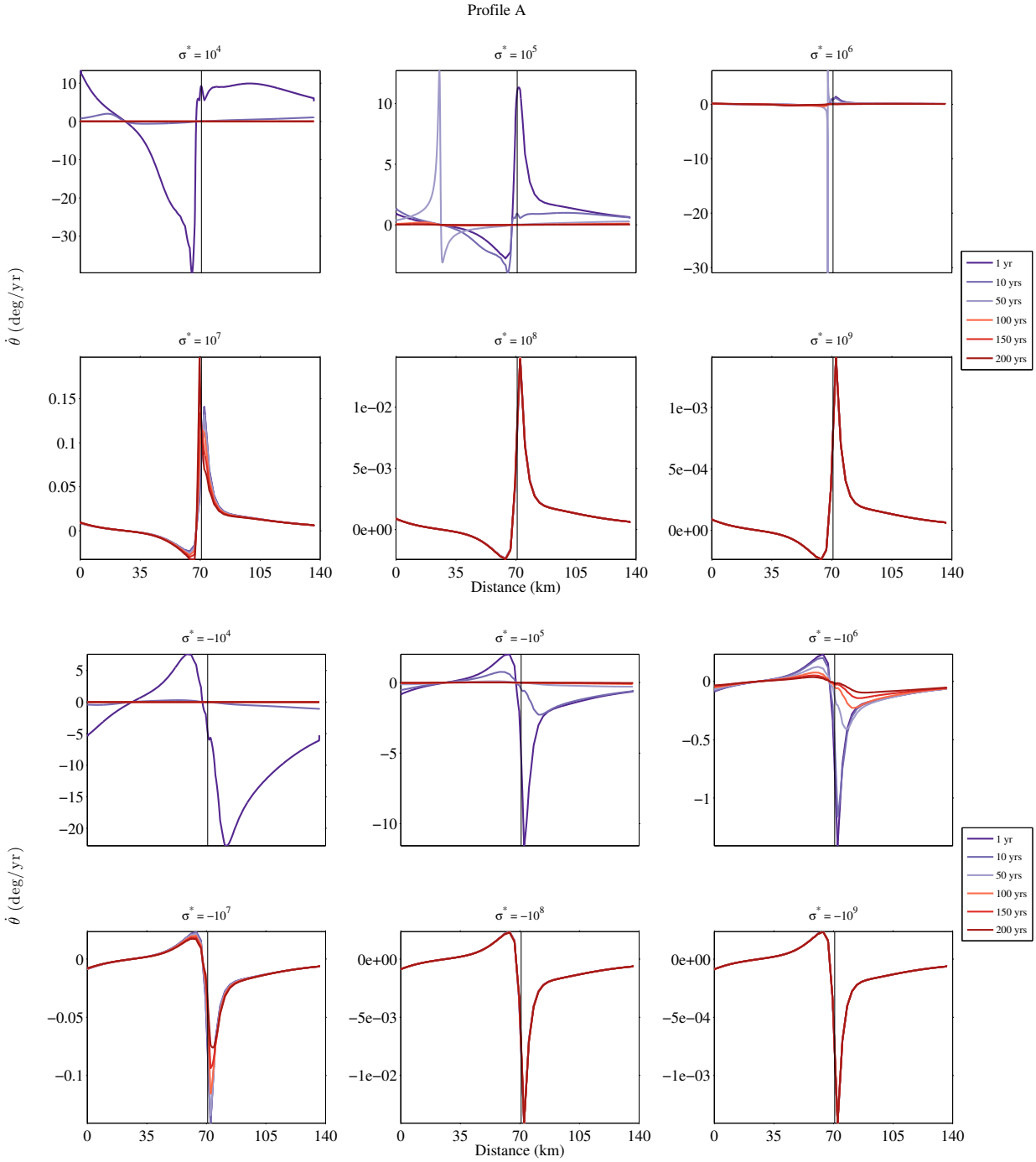

Figure 5.24: Principal stress axes rotation rates (5 km depth), from west to east, for Profile A across the Parkfield segment of the SAF at 1, 10, 50, 100, 150, and 200 years in the earthquake cycle and for backgrounds stresses $\sigma^* = \pm 10^4 - \pm 10^9$ Pa. The x-axis is distance in kilometers. The fault trace is plotted as the thin black vertical line at ∼70 km.

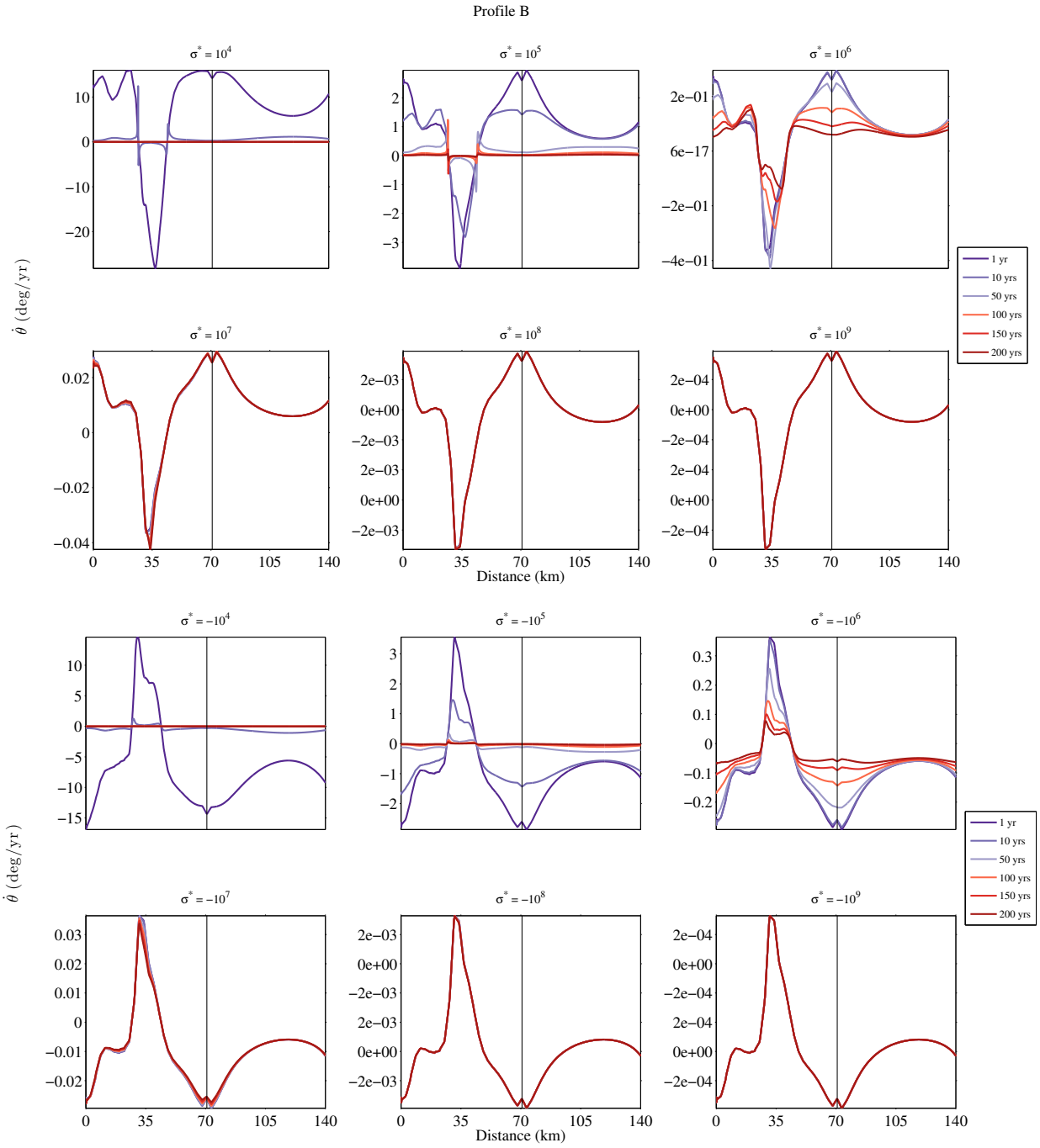

Figure 5.25: Principal stress axes rotation rates (5 km depth), from west to east, for Profile B across the Mojave segment of the SAF at 1, 10, 50, 100, 150, and 200 years in the earthquake cycle and for backgrounds stresses $\sigma^* = \pm 10^4 - \pm 10^9$ Pa. The x-axis is distance in kilometers. The fault trace is plotted as the thin black vertical line at ∼70 km.

trace, and by year 200 it is ∼30 km from the fault trace. When $\sigma^* = \pm 10^7 - \pm 10^9$ Pa the location of the maximum rotation rate does not change relative to the fault trace.

Across the Mojave segment of the SAF (Profile B, Figure 5.25), rotation rates change with time for background stresses where $\sigma^* = \pm 10^4 - \pm 10^6$ Pa, but the location of the maximum rotation rates is approximately the same for all times in the earthquake cycle. Here maximum rotation rates do not occur on the SAF, but rather ∼35 km west of the fault where the profile crosses the Santa Susana fault on the west side of the San Gabriel block (Figure 5.23).

Rotation rates across the San Berardino segment of the SAF (Profile C, Figure 5.26) are extremely complicated. This profile crosses the San Jacinto, SAF, and parts of the southern Eastern California Shear Zone. When $\sigma^* = \pm 10^7 - \pm 10^9$ Pa, rotation rates have a double peak and the fastest rotation rates occur on the SAF trace (the second peak corresponds to the San Jacinto fault trace). For these background stress values the location and magnitude of the maximum rotation rates does not change significantly. When $\sigma^* = 10^4$ Pa, rotation rates have a double peak, located ∼35 from the SAF fault trace, in the first year of the earthquake cycle. Here the magnitude of the accumulated tectonic stress (from the magnitude of the stressing rate) is already larger than σ^*, and the maximum rotation rate has shifted away from the fault. The minimum rotation rate in year 1 occurs on the SAF. When $\sigma^* = 10^5$ Pa, maximum rotation rates occur on the SAF and San Jacinto fault traces in year 1 of the earthquake cycle but shift ∼35 km east in year 10 (with minimum rotation rates in year 10 and year 50 occurring at the SAF fault trace). When $\sigma^* = 10^6$ Pa, maximum rotation rates occur at the SAF and San Jacinto fault traces in years 1 and 10 of the earthquake cycle.

In year 50, maximum rotation rates occur on the San Jacinto fault trace (∼0.4 degrees/yr) and the maximum rotation rates in the vicinity of the SAF occur ∼5 km west of the fault. East of the fault, at a distance of ∼110 km along the profile, rotation rates increase again (∼0.2 degrees/yr). In year 100, the rotation rate resembles the rotation rate from year 1 when $\sigma^* = 10^4$ Pa, with a minimum rotation rate at the SAF and maximum values ∼35 km east and west of the fault. The location of maximum rotation rates continues to move east and west from the SAF with subsequent years in the earthquake cycle. When $\sigma^* = -10^4$ Pa, rotation rates in the first year of the earthquake cycle do not have the same double peak structure and maximum rotation rates occur ∼5 km east of the SAF. For $\sigma^* = -10^5$ Pa, the fastest rotation rates occur on the trace of the SAF and San Jacinto in the first year of the earthquake cycle, but in year 10 the fastest rotation rates occur ∼5 km east of the SAF and becomes slower moving in either direction. When $\sigma^* = -10^6$ Pa, rotation rates are fastest on the San Jacinto and SAF fault traces during the first 10 years of the earthquake cycle. By year 50, the maximum rotation rate has moved slightly (<5km) east of the SAF. In subsequent years, maximum rotation rates continue to move away from the SAF, but much more slowly than when $\sigma^* = 10^6$ Pa.

Rotation rates across the Indio segment of the SAF (Profile D, Figure 5.27) change sign at the SAF trace for all background stresses. When $\sigma^* = 10^4$ Pa, the fastest rotation rates occur ∼15 km west and ∼10 km east of the SAF in year 1 of the earthquake cycle and ∼50 km east of the SAF in year 10. The location of the maximum rotation rate shifts dramatically when $\sigma^* = 10^5$ Pa: from the SAF fault trace in year 1 to $\pm 10 - 15$ km in year 10, ∼35 km to the east in year 50, ∼50 km to the east in year 100, and ∼65 km to the east in year 150.

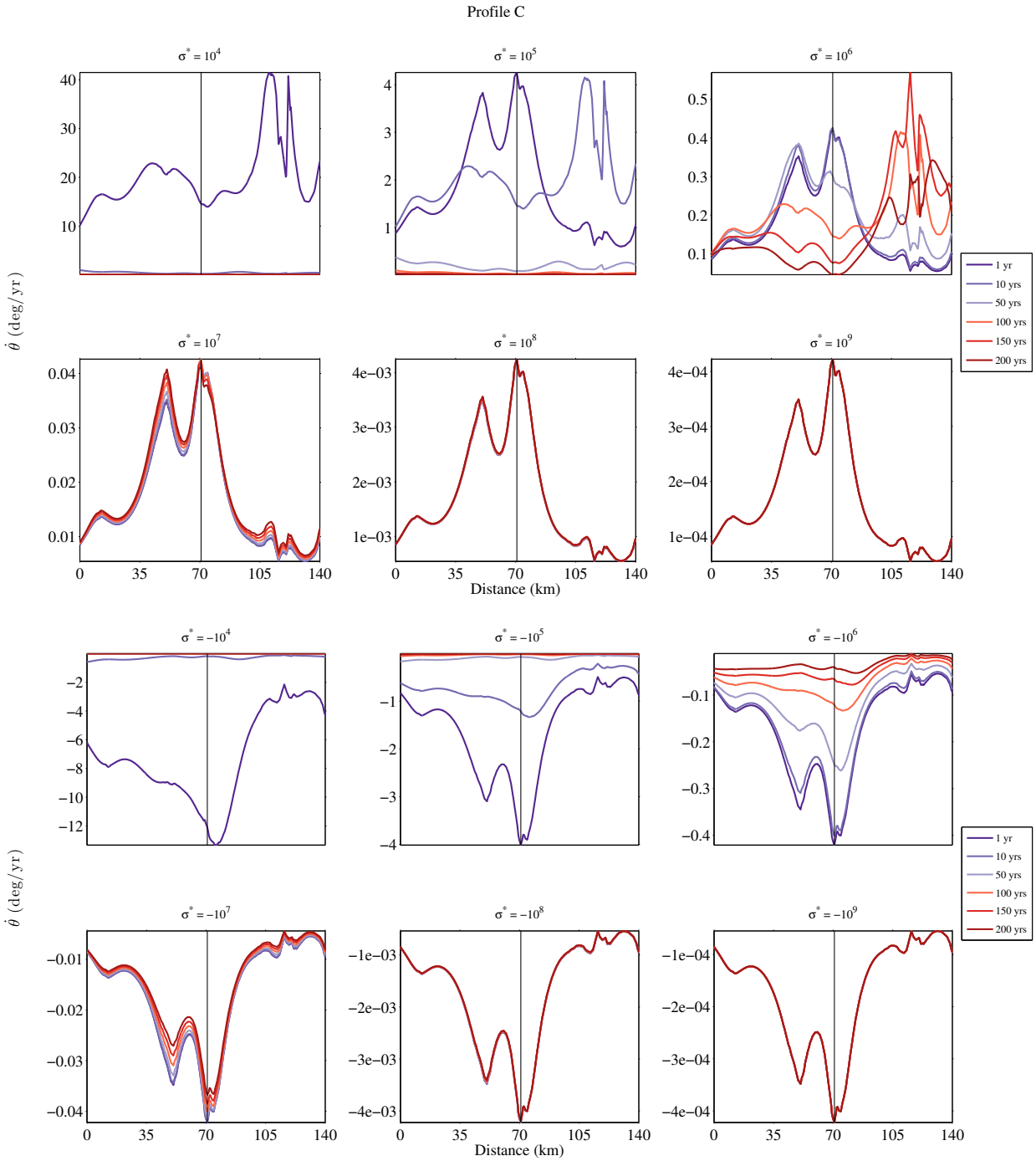

Figure 5.26: Principal stress axes rotation rates (5 km depth), from west to east, for Profile C across the San Bernardino segment of the SAF at 1, 10, 50, 100, 150, and 200 years in the earthquake cycle and for backgrounds stresses $\sigma^* = \pm 10^4 - \pm 10^9$ Pa. The x-axis is distance in kilometers. The fault trace is plotted as the thin black vertical line at ∼70 km.

The rotation rate is ∼0 degree/yr on the fault at every time but year 1. Similar, though less pronounced, migration of the location of the maximum rotation rate occurs when $\sigma^* = 10^6$ Pa: the rotation rate is highest on the SAF trace in years 1 and 10 of the earthquake cycle but moves east and west in subsequent years. Migration of the location of the maximum rotation rate is less pronounced for negative background stresses. When $\sigma^* = -10^4$ Pa, rotation rates are fastest at the SAF and immediately to the west of the fault trace in the first year of the earthquake cycle, but in year 10 the fastest rotation occurs ∼35 km to the west. When $\sigma^* = -10^5$ Pa, rotation rates are again fastest at the fault trace in the first year of the earthquake cycle and move ∼5 km in either direction of the fault trace in year 10. For $\sigma^* = -10^6$ Pa, the maximum rotation rates occur on the SAF for years 1, 10, and 50 in the earthquake cycle before moving ∼5 km east in subsequent years. For background stresses where $\sigma^* = \pm 10^7 - \pm 10^9$ Pa, rotation rates are fastest at the SAF trace and do not change significantly in magnitude or location.

5.8 Comparison to previously reported stress rotation rates

5.8.1 Comparison to regional southern California estimates of stress rotation rates

We can compare our calculated rotation rates to southern California rotation rates derived from focal mechanism inversions (Hardebeck and Hauksson, 2001). Direct, quantitative comparison between Hardebeck and Hauksson (2001) and the calculated results described above is difficult, as Hardebeck and Hauksson (2001) do not provide a detailed quantitative description of their southern California rotation rates.

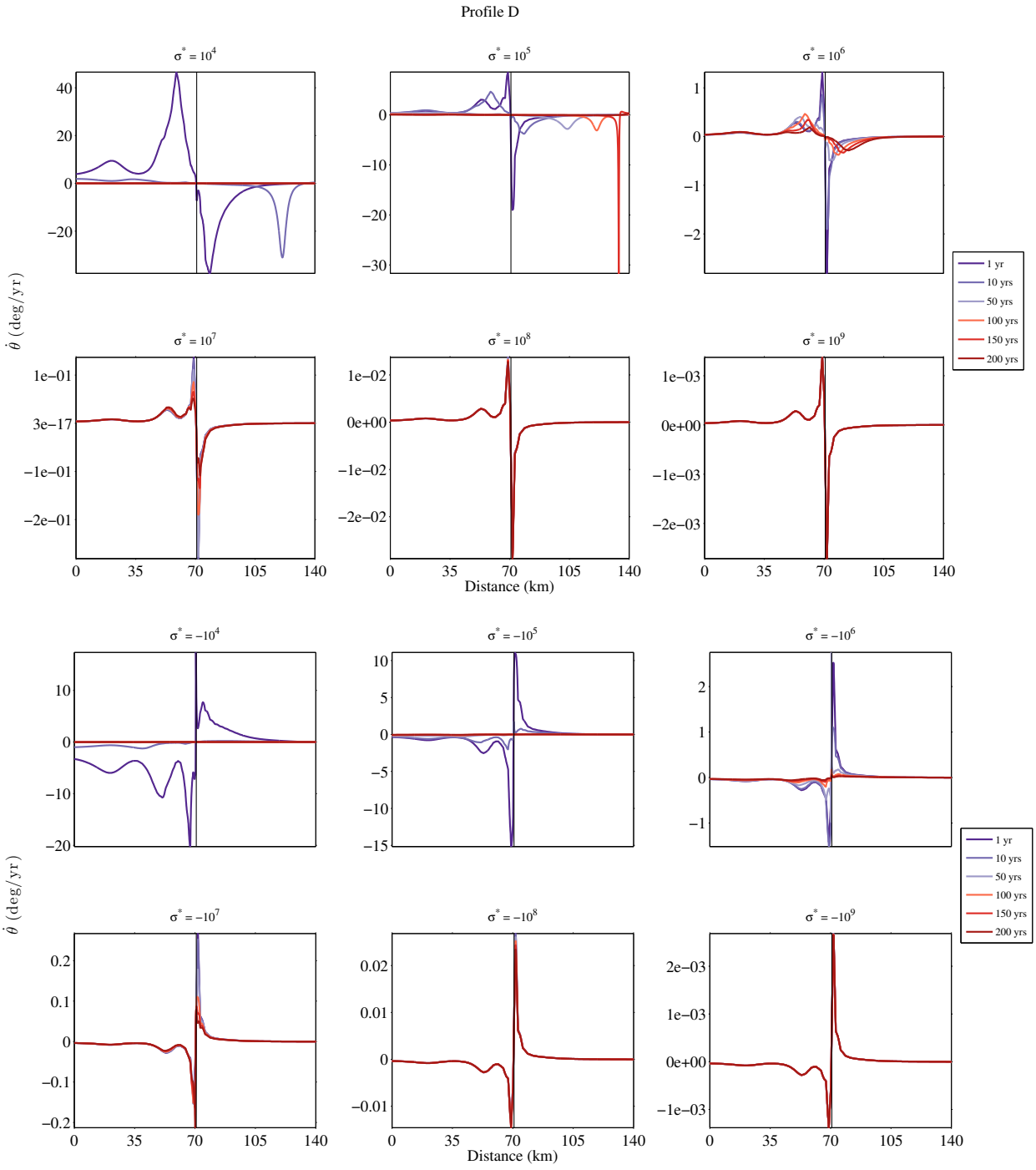

Figure 5.27: Principal stress axes rotation rates (5 km depth), from west to east, for Profile D across the Indio segment of the SAF at 1, 10, 50, 100, 150, and 200 years in the earthquake cycle and for backgrounds stresses $\sigma^* = \pm 10^4 - \pm 10^9$ Pa. The x-axis is distance in kilometers. The fault trace is plotted as the thin black vertical line at ∼70 km.

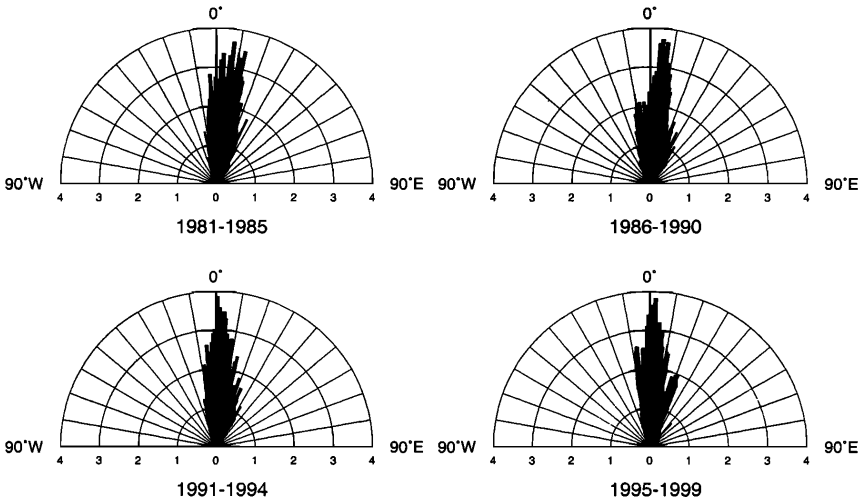

Figure 5.28: Reproduced from Hardebeck and Hauksson (2001), Figure 6. Rose diagrams of σ_H axis orientation during four time intervals. The focal mechanisms of earthquakes during each time interval were inverted using the same technique as in Hardebeck and Hauksson (2001) Plate 1. The length of each sector indicates the percent of grid points at which the inversion result falls within a 1°-wide bin.

$\sigma^* = -10^5$ Pa and the system is early $(0 - 10$ years) in the earthquake cycle.

Hardebeck and Hauksson (2001) also calculate regional rotation rates, inferred from focal mechanisms, over their entire study time frame, which spans the years $1981 - 1999$. Again, an in-depth quantitative comparison is difficult, however, one distinction is striking: where Hardebeck and Hauksson (2001) find significant heterogeneity in the direction (sign) of rotation, typically switching between positive and negative values over less than a quarter degree in longitude or latitude, our calculated rotation rates are much more uniform. While spatial heterogeneity in rotation rate signs does exist in our results, when $\sigma^* > 0$ rotation rates are predominantly positive and when $\sigma^* < 0$ rotation rates are predominantly negative (as evidenced by the median rotation rates described above, in Figure 5.10, and in Table 5.1).

Hardebeck and Hauksson (2001) report rotation rates ranging from $-2.0 - 2.0$ degrees/yr

over the entire region (with the exception of the Mojave dessert, where there are an insufficient number of earthquake events to determine the rotation rate). These rates are most consistent with our results with background stresses such that $\sigma^* = \pm 10^4 - \pm 10^6$ Pa. While Hardebeck and Hauksson (2001) do not provide median or mean rotation rates for southern California, it is clear that when $\sigma^* = \pm 10^4$ Pa rotation rates in the first year of the earthquake cycle are much larger (median $|\dot{\theta}| > 7$ degrees/yr) than the results presented here and are inconsistent with focal mechanism-derived rotation rates. However, in year 10 of the earthquake cycle the median rotation rates are 0.40 degrees/yr (σ^* positive) and -0.30 degrees/yr (σ^* negative) and appear to be broadly consistent with the Hardebeck and Hauksson (2001) results. By year 50 in the earthquake cycle, median rotation rates are more than an order of magnitude smaller (median $|\dot{\theta}| \sim 0.01$ degrees/yr) and are too small to be consistent with the majority of the Hardebeck and Hauksson (2001) rotation rates.

When $\sigma^* = \pm 10^5$ Pa, median rotation rates in year one of the earthquake cycle are 1.22 degrees/yr (σ^* positive) and -1.14 degrees/yr (σ^* negative), and in year 10 of the earthquake cycle median rotation rates are 1.18 degrees/yr (σ^* positive) and -0.73 degrees/yr (σ^* negative). Visual analysis of the Hardebeck and Hauksson (2001) results suggest these values are broadly consistent with the focal mechanism results. In year 50 of the earthquake cycle, median rotation rates are 0.16 degrees/yr (σ^* positive) and -0.10 degrees/yr (σ^* negative) and may be consistent with the smallest focal mechanism-derived rotation rates, but in subsequent time frames (100, 150, 200 years) median rotation rates are an order of magnitude smaller and appear to be much smaller than the majority of the Hardebeck and Hauksson (2001) results.

When $\sigma^* = \pm 10^6$ Pa, median rotation rates are 0.12 degrees/yr (σ^* positive) and -0.12 degrees/yr (σ^* negative) in year 1 of the earthquake cycle, 0.12 degrees/yr and -0.11 degrees/yr in year 10 of the earthquake cycle, 0.13 degrees/yr and -0.10 degrees/yr in year 50, and 0.12 degrees/yr and -0.07 degrees/yr in year 100. By year 150, $|\dot{\theta}|$ is < 0.10 degrees/yr for both positive and negative values of σ^*. Here the median rotation rates from the first $\sim$100 years of the earthquake cycle may be visually consistent with the smaller rotation rates inferred from focal mechanisms (Hardebeck and Hauksson, 2001), but median rotation rates from later in the earthquake cycle appear to be inconsistent with focal mechanism-derived rotation rates.

Because of the spatial heterogeneity in rotation rate sign in Hardebeck and Hauksson (2001) and the large scale rotation rate sign uniformity in our results, it is not possible to say if positive or negative values of σ^* are more consistent with the focal mechanism inversions for $\dot{\theta}$. However, values of σ^* where $|\sigma^*| \geq 10^7$ Pa have median rotation rate values of $|\dot{\theta}| < 0.02$ degrees/yr and appear to be too small to be consistent with the Hardebeck and Hauksson (2001) rotation rates.

5.8.2 Comparison to estimates of stress rotations in the vicinity of the Northridge earthquake

Previous estimates of rotation rates in the vicinity of the 17 January 1994 Northridge earthquake have been inferred from focal mechanism inversions and p-wave polarity studies (Hardebeck and Hauksson, 2001; Zhao et al., 1997). Zhao et al. (1997) report +8 degrees of p-axis rotation between February 1994 and August 1995 and another +8 degrees of rotation between August 1995 and the end of that year, suggesting rotation rates of 5.33 degrees/yr

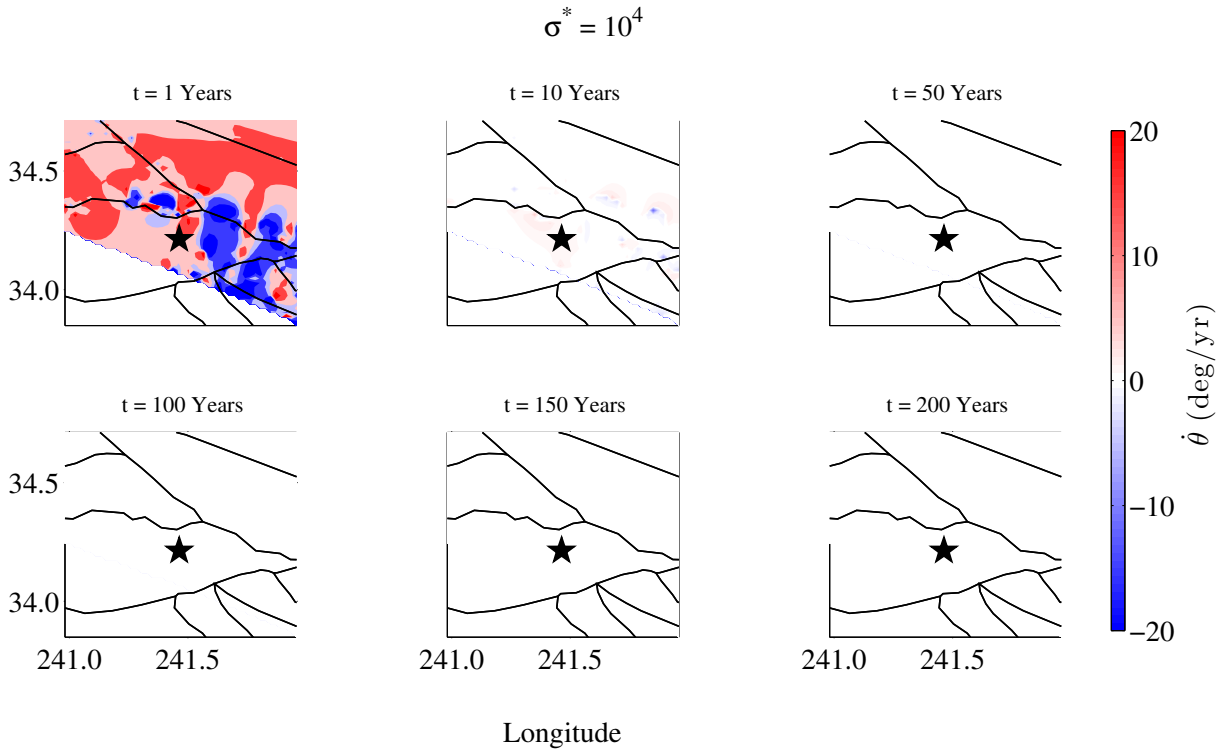

Figure 5.29: Principal stress axes rotation rates at 5 km depth within 0.5° longitude and latitude of the epicenter of the January 17, 1994 $M_W = 6.7$ Northridge earthquake. The background stress is $\sigma^b_{xx} = -\sigma^b_{yy} = \sigma^* = 10^4$ Pa. Here red colors indicate positive rotation rates, blue colors indicate negative rotation rates, and colors saturate at ±20 degrees/yr. The black star indicates the location of the Northridge mainshock. At this background stress rotation rates are very fast in the first year of the earthquake cycle but decay quickly and are ∼0 degrees/yr by year 50.

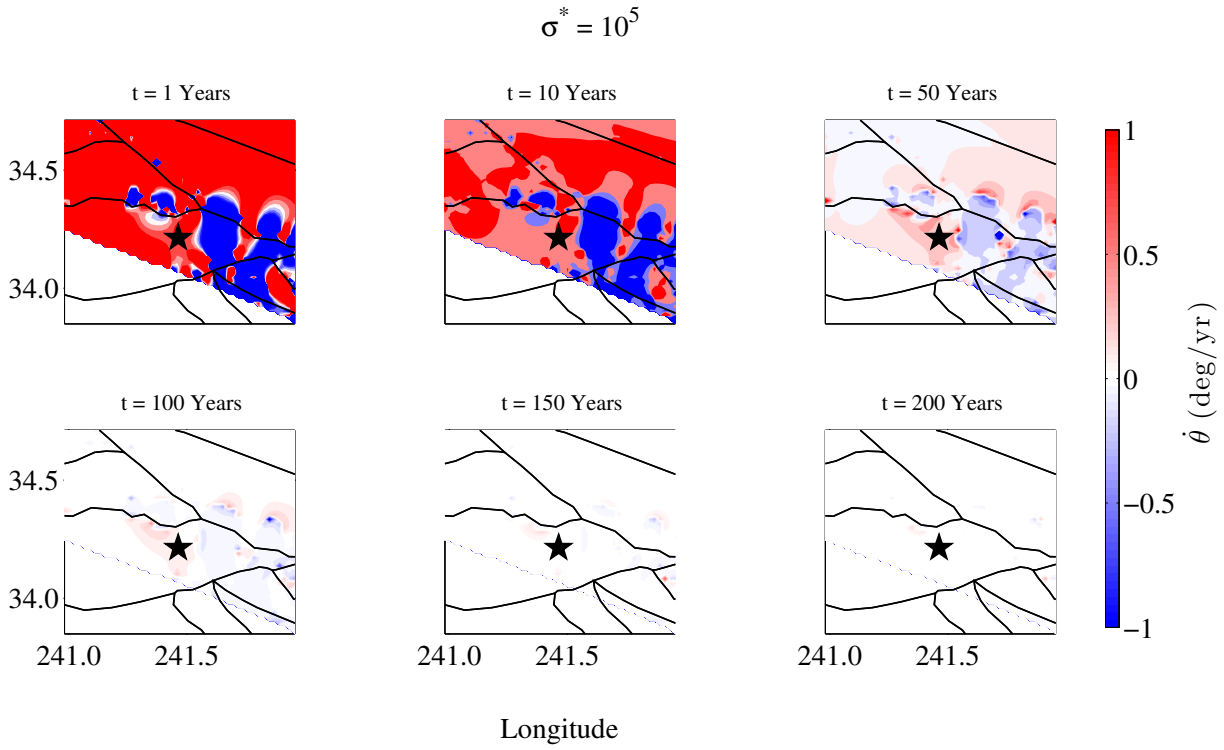

Figure 5.30: Principal stress axes rotation rates at 5 km depth within 0.5° longitude and latitude of the epicenter of the January 17, 1994 $M_W = 6.7$ Northridge earthquake. The background stress is $\sigma^b_{xx} = -\sigma^b_{yy} = \sigma^* = 10^5$ Pa. Here red colors indicate positive rotation rates, blue colors indicate negative rotation rates, and colors saturate at ±1 degrees/yr. The black star indicates the location of the Northridge mainshock. At this background stress rotation rates are nearly all > 1 degree/yr in the first 10 years of the earthquake cycle but are typically < 1 degree/yr by year 50.

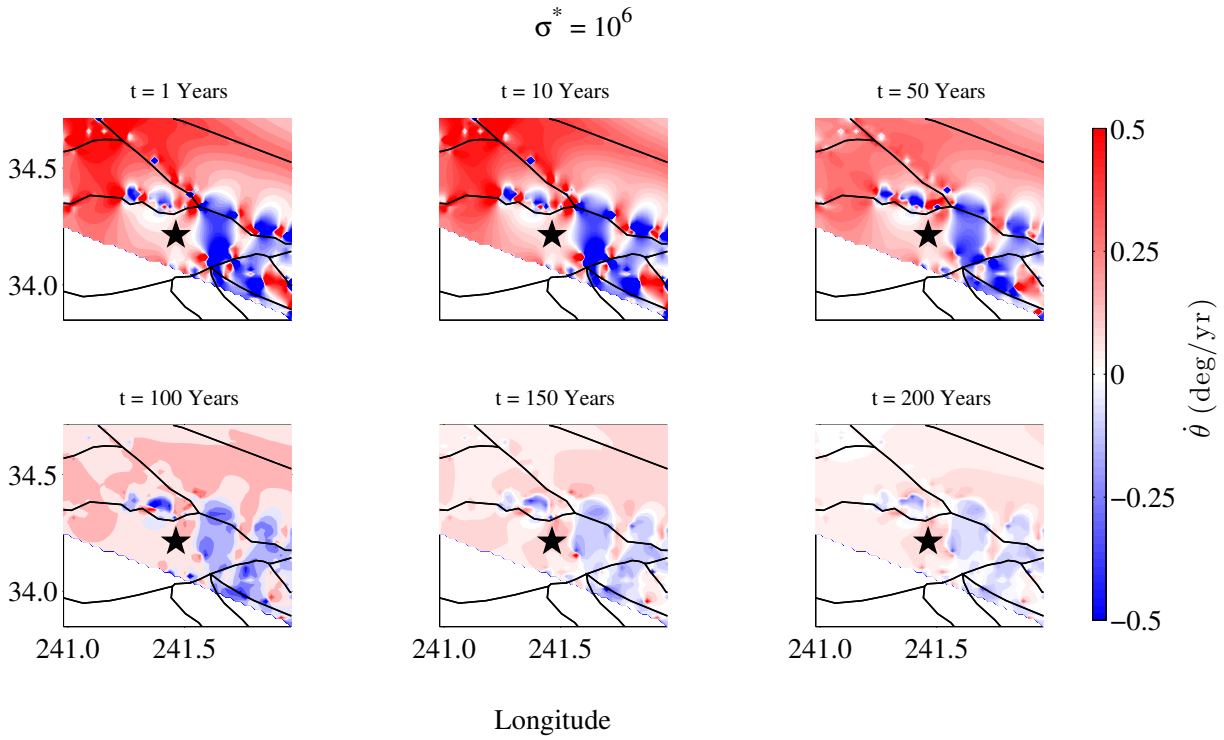

Figure 5.31: Principal stress axes rotation rates at 5 km depth within 0.5° longitude and latitude of the epicenter of the January 17, 1994 $M_W = 6.7$ Northridge earthquake. The background stress is $\sigma^b_{xx} = -\sigma^b_{yy} = \sigma^* = 10^6$ Pa. Here red colors indicate positive rotation rates, blue colors indicate negative rotation rates, and colors saturate at ±0.5 degrees/yr. The black star indicates the location of the Northridge mainshock. Rotation rates are $|\dot{\theta}| = 0.1 - 0.5$ degrees/yr in the first 50 years of the earthquake cycle and become smaller in later years.

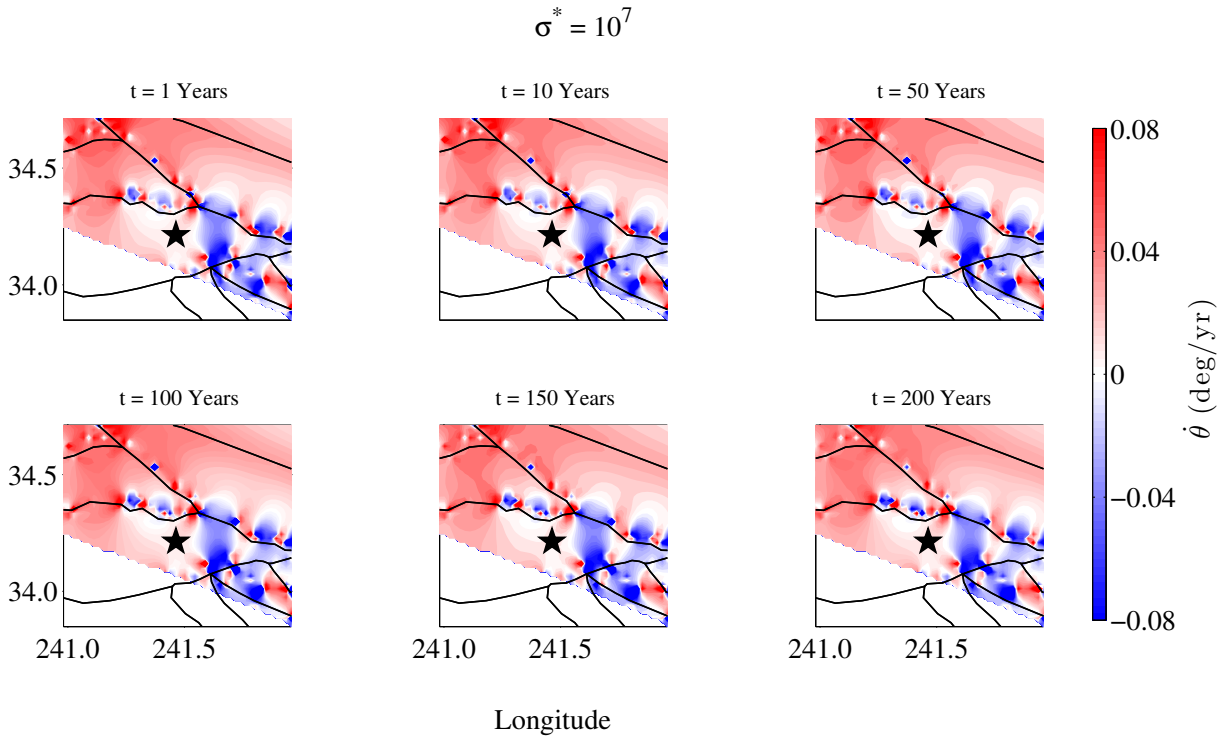

Figure 5.32: Principal stress axes rotation rates at 5 km depth within 0.5° longitude and latitude of the epicenter of the January 17, 1994 $M_W = 6.7$ Northridge earthquake. The background stress is $\sigma^b_{xx} = -\sigma^b_{yy} = \sigma^* = 10^7$ Pa. Here red colors indicate positive rotation rates, blue colors indicate negative rotation rates, and colors saturate at ±0.08 degrees/yr. The black star indicates the location of the Northridge mainshock. Rotation rates are relatively constant over the entire earthquake cycle and are typically $|\dot{\theta}| < 0.1$ degrees/yr.

and 24 degrees/yr in the respective time periods (and < 2 years into the earthquake cycle). By the end of 1995, p-axis orientations are close to those prior to the earthquake. We compare these rotation rates to our $\dot{\theta}$ calculations for the first year of the earthquake cycle and consider the region within 0.5° longitude and latitude of the epicenter of the Northridge earthquake (a region spanning ∼90 km in the east-west direction and ∼97 km in the north-south direction, 1717 points). A closer look at rotation rates in this region for background stresses ranging from $\sigma^* = \pm 10^4 - \pm 10^9$ Pa are shown in Figures 5.29 - 5.40.

During the first year of the earthquake cycle in the Northridge region, $|\dot{\theta}|$ is > 5 degrees/yr only when $\sigma^* = \pm 10^4$ Pa (Figures 5.29 and 5.35). When $\sigma^* = 10^4$ Pa (Figure 5.29), only ∼7% of the Northridge region rotation rates satisfy $|\dot{\theta}| > 20$ degrees/yr, and an equal number of rotation rates are positive and negative. ∼92% of rotation rates satisfy $|\dot{\theta}|$ is > 5 degrees/yr, and are dominantly positive, consistent with the Zhao et al. (1997) observations. Rotation rates within $\sim 5 - 100$ km of the mainshock are positive and > 5 degrees/yr, and the largest negative rotation rates occur $\sim 5 - 30$ km east of the mainshock. When $\sigma^* = -10^4$ Pa (Figure 5.35), this pattern is reversed: $< 3\%$ of points have rotation rates where $|\dot{\theta}| > 20$ degrees/yr, and 88% of points satisfy $|\dot{\theta}| > 5$ degrees/yr. Here rotation rates are predominantly negative, with the exception of the region $\sim 5 - 30$ km east of the mainshock epicenter, where rotation rates are positive. The bulk of these results are inconsistent with positive rotation rates observed by p-axis rotation (Zhao et al., 1997), but the region to the east, where $\dot{\theta} > 5$ degrees/yr, is broadly consistent with p-axis results.

In contrast, Hardebeck and Hauksson (2001) find rotation rates that range from $-2.0 - 2.0$ degrees/yr in the vicinity of the Northridge mainshock. Data from this focal mechanism in-

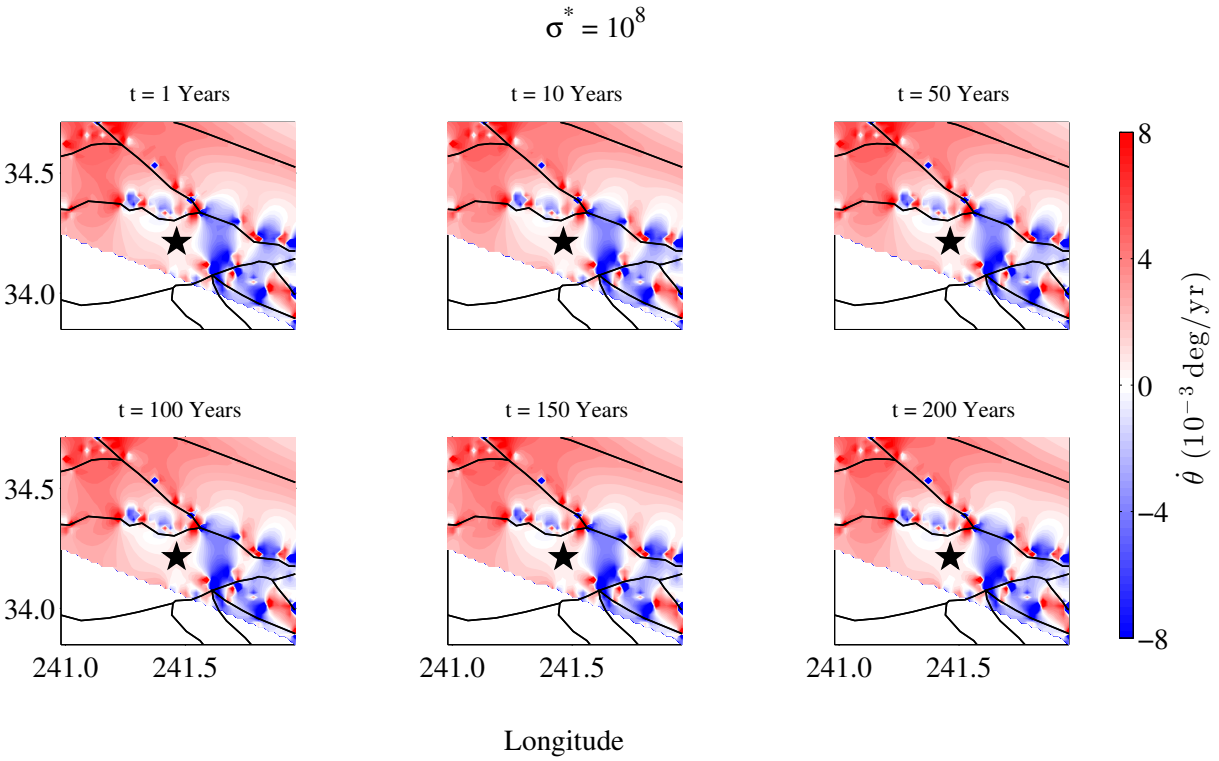

Figure 5.33: Principal stress axes rotation rates at 5 km depth within 0.5° longitude and latitude of the epicenter of the January 17, 1994 $M_W = 6.7$ Northridge earthquake. The background stress is $\sigma^b_{xx} = -\sigma^b_{yy} = \sigma^* = 10^8$ Pa. Here red colors indicate positive rotation rates, blue colors indicate negative rotation rates, and colors saturate at ±0.008 degrees/yr. The black star indicates the location of the Northridge mainshock. Rotation rates are relatively constant over the entire earthquake cycle and are typically $|\dot{\theta}| < 0.01$ degrees/yr.

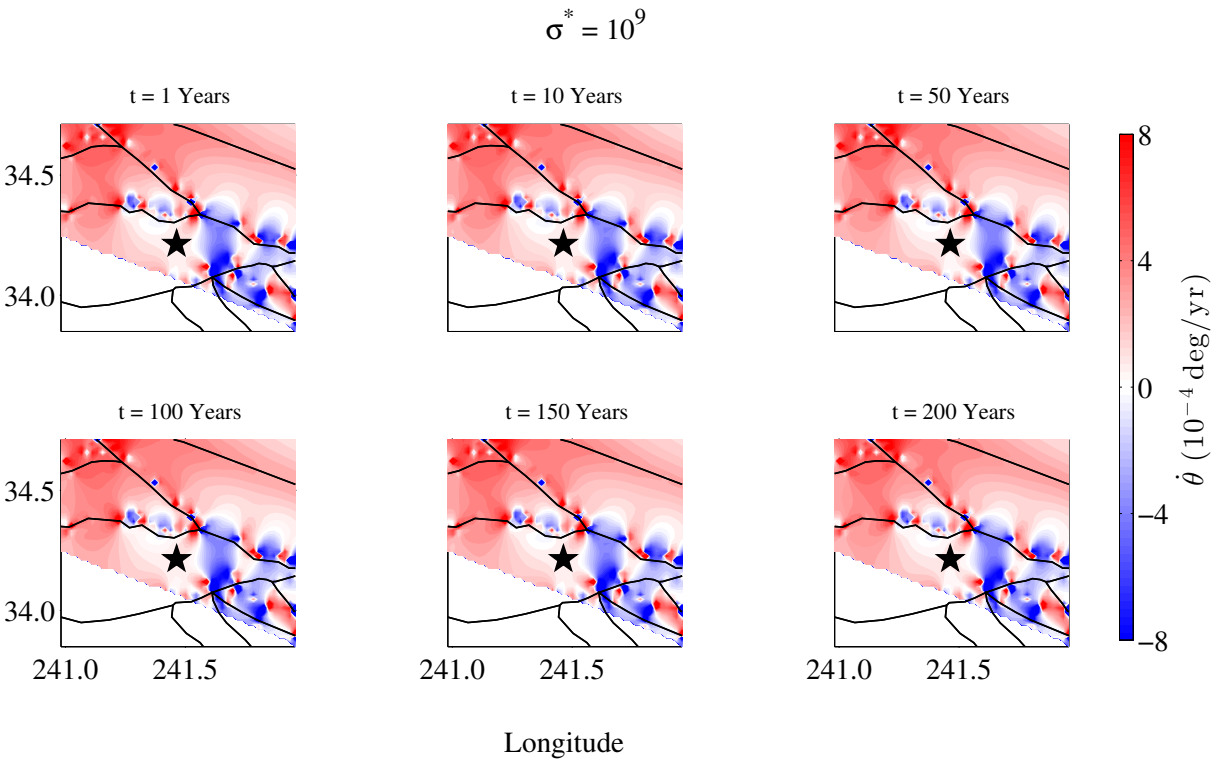

Figure 5.34: Principal stress axes rotation rates at 5 km depth within 0.5° longitude and latitude of the epicenter of the January 17, 1994 $M_W = 6.7$ Northridge earthquake. The background stress is $\sigma^b_{xx} = -\sigma^b_{yy} = \sigma^* = 10^9$ Pa. Here red colors indicate positive rotation rates, blue colors indicate negative rotation rates, and colors saturate at $\pm 8 \times 10^{-4}$ degrees/yr. The black star indicates the location of the Northridge mainshock. Rotation rates are relatively constant over the entire earthquake cycle and are typically $|\dot{\theta}| < 0.001$ degrees/yr.

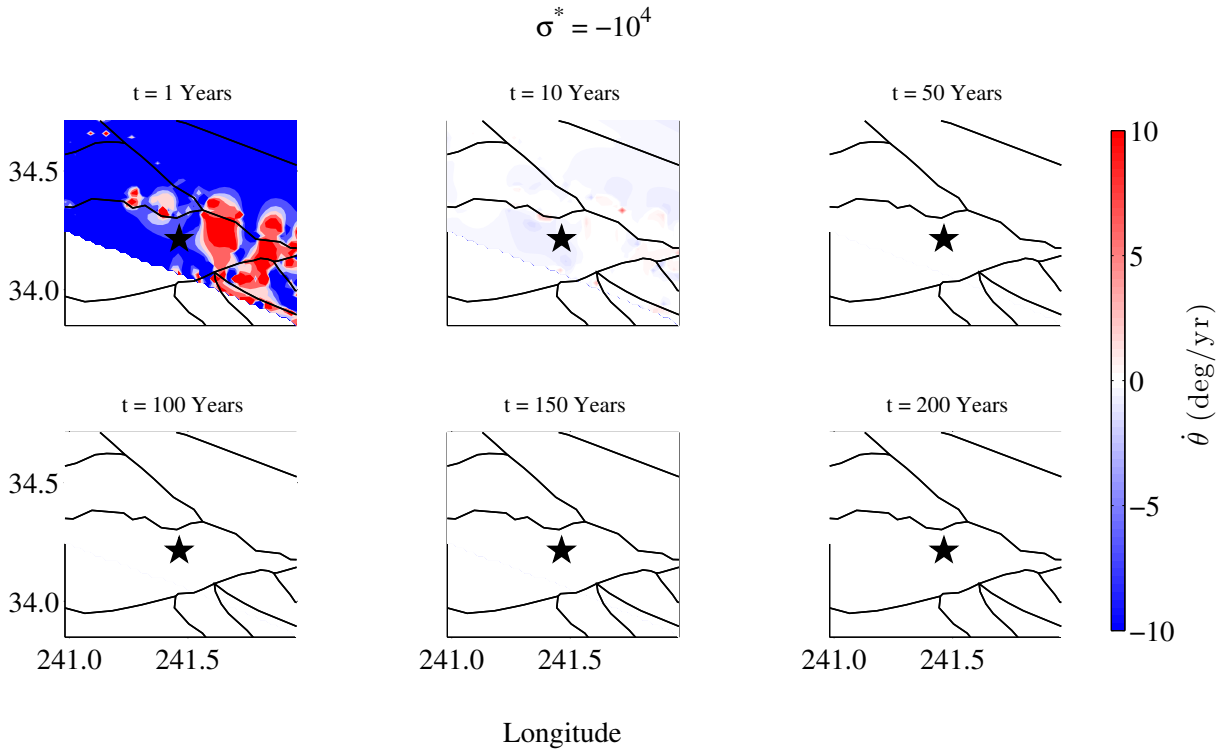

Figure 5.35: Principal stress axes rotation rates at 5 km depth within 0.5° longitude and latitude of the epicenter of the January 17, 1994 $M_W = 6.7$ Northridge earthquake. The background stress is $\sigma^b_{xx} = -\sigma^b_{yy} = \sigma^* = -10^4$ Pa. Here red colors indicate positive rotation rates, blue colors indicate negative rotation rates, and colors saturate at ±10 degrees/yr. The black star indicates the location of the Northridge mainshock. At this background stress rotation rates are very fast (< -5 degrees/yr) in the first year of the earthquake cycle but decay quickly and are ∼0 degrees/yr by year 50.

version spans the time both before and after the Northridge earthquake, and it is impossible to ascertain whether rotation rates are constant over the earthquake cycle or faster following the Northridge event. While background stresses where $\sigma^* = \pm 10^4$ are consistent with rotation rates from Zhao et al. (1997), the predicted rotation rates (typically $|\dot{\theta}| > 5$ degrees/yr) from these background stresses are more than two times higher than those found by Hardebeck and Hauksson (2001).

In the Northridge region when $\sigma^* = 10^5$ Pa (Figure 5.30) and $t = 1$ year, most rotation rates range from $|\dot{\theta}| = 1 - 5$ degrees/yr, where $|\dot{\theta}| > 5$ degrees/yr accounts for ∼11% of the region and $|\dot{\theta}| > 1$ degrees/yr ∼93% of the region. Rotation rates are predominantly positive (though they are negative to the east of the mainshock), and while rotation rates right at the mainshock are > 1 degree/yr, just to the south, east, and north they range form $|\dot{\theta}| = 0.5 - 1$ degrees/yr. Rotation rates for this region and at this background stress are slightly slower in year 10 of the earthquake cycle, with $< 1\%$ of points satisfying typically $|\dot{\theta}| > 5$ and ∼79% of points satisfying typically $|\dot{\theta}| > 1$ degrees/yr. Here all points within ∼5 km of the mainshock have a rotation rate > 1 degree/yr. By year 50 in the earthquake cycle, $< 1\%$ of points have a rotation rate $|\dot{\theta}| > 1$ degrees/yr. When $\sigma = -10^5$ Pa (Figure 5.36), rotation rates are dominantly negative but follow a similar pattern: in year 1 of the earthquake cycle 10% of points satisfy $|\dot{\theta}| > 5$ degrees/yr and 93% of points satisfy $|\dot{\theta}| > 1$ degrees/yr. Within $\sim 2 - 10$ km of the epicenter, rotation rates range from -0.5 degrees/yr to -1 degree/yr. In year 10 of the earthquake cycle $< 1\%$ of points have rotation rates $|\dot{\theta}| > 5$ and only 64% have rotation rates $|\dot{\theta}| > 1$ degrees/yr. In the region of the epicenter (within $\sim 10 - 20$ km), rotation rates range between -0.5 degrees/yr to -1 degrees/yr. $|\dot{\theta}| < 0.5$ degrees/yr by year

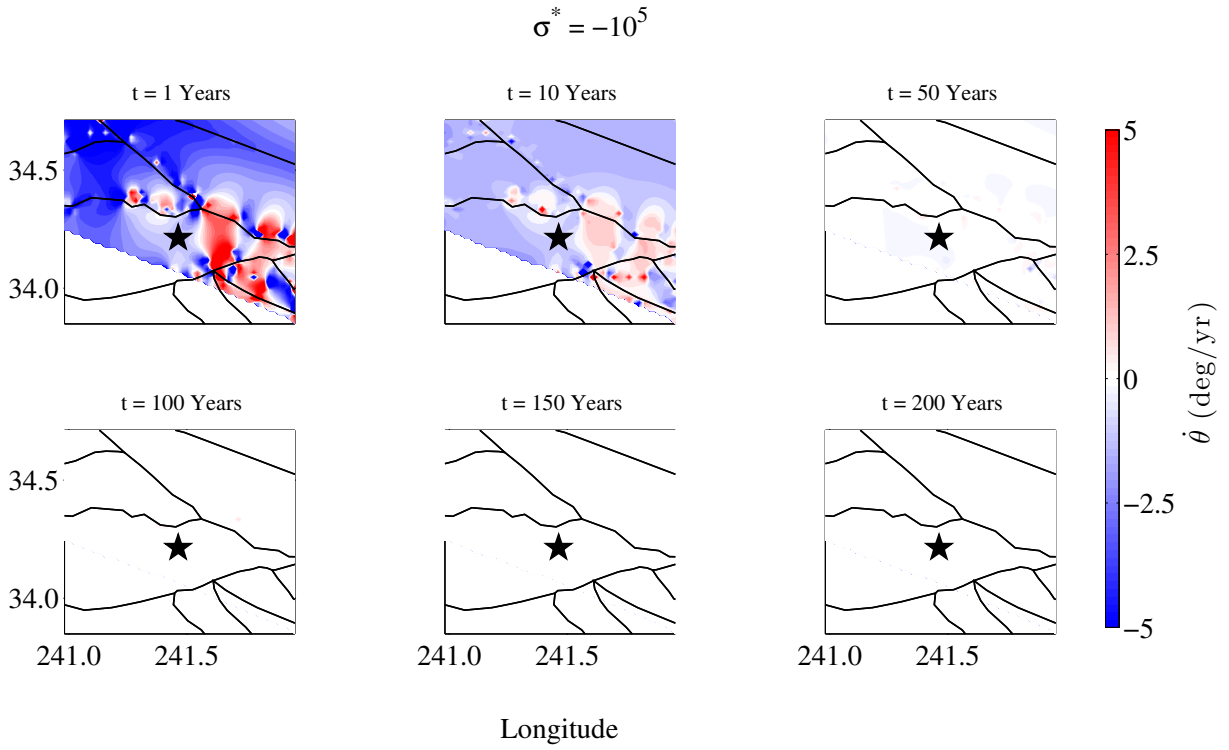

Figure 5.36: Principal stress axes rotation rates at 5 km depth within 0.5° longitude and latitude of the epicenter of the January 17, 1994 $M_W = 6.7$ Northridge earthquake. The background stress is $\sigma^b_{xx} = -\sigma^b_{yy} = \sigma^* = -10^5$ Pa. Here red colors indicate positive rotation rates, blue colors indicate negative rotation rates, and colors saturate at ±5 degrees/yr. The black star indicates the location of the Northridge mainshock. At this background stress rotation rates are nearly all > 1 degree/yr in the first 10 years of the earthquake cycle but are typically < 0.5 degrees/yr by year 50.

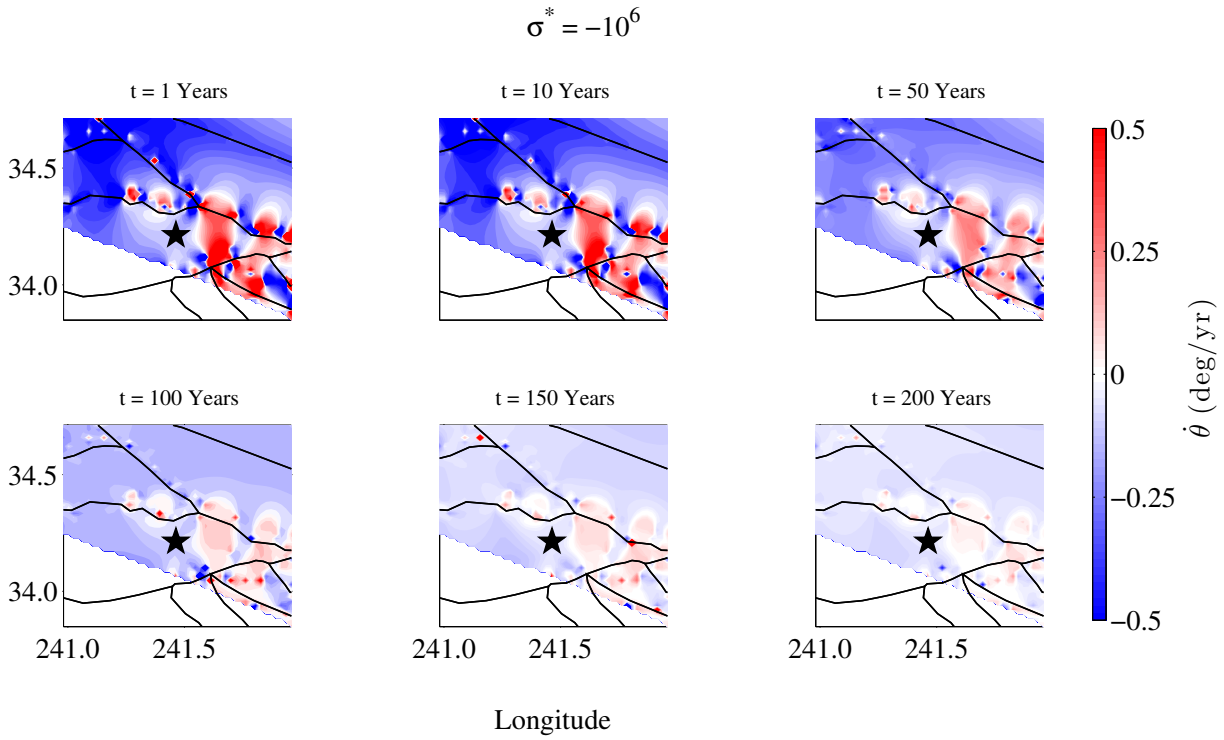

Figure 5.37: Principal stress axes rotation rates at 5 km depth within 0.5° longitude and latitude of the epicenter of the January 17, 1994 $M_W = 6.7$ Northridge earthquake. The background stress is $\sigma^b_{xx} = -\sigma^b_{yy} = \sigma^* = -10^6$ Pa. Here red colors indicate positive rotation rates, blue colors indicate negative rotation rates, and colors saturate at ±0.5 degrees/yr. The black star indicates the location of the Northridge mainshock. Rotation rates are $|\dot{\theta}| = 0.1 - 0.5$ degrees/yr in the first 50 years of the earthquake cycle and become smaller later in later years.

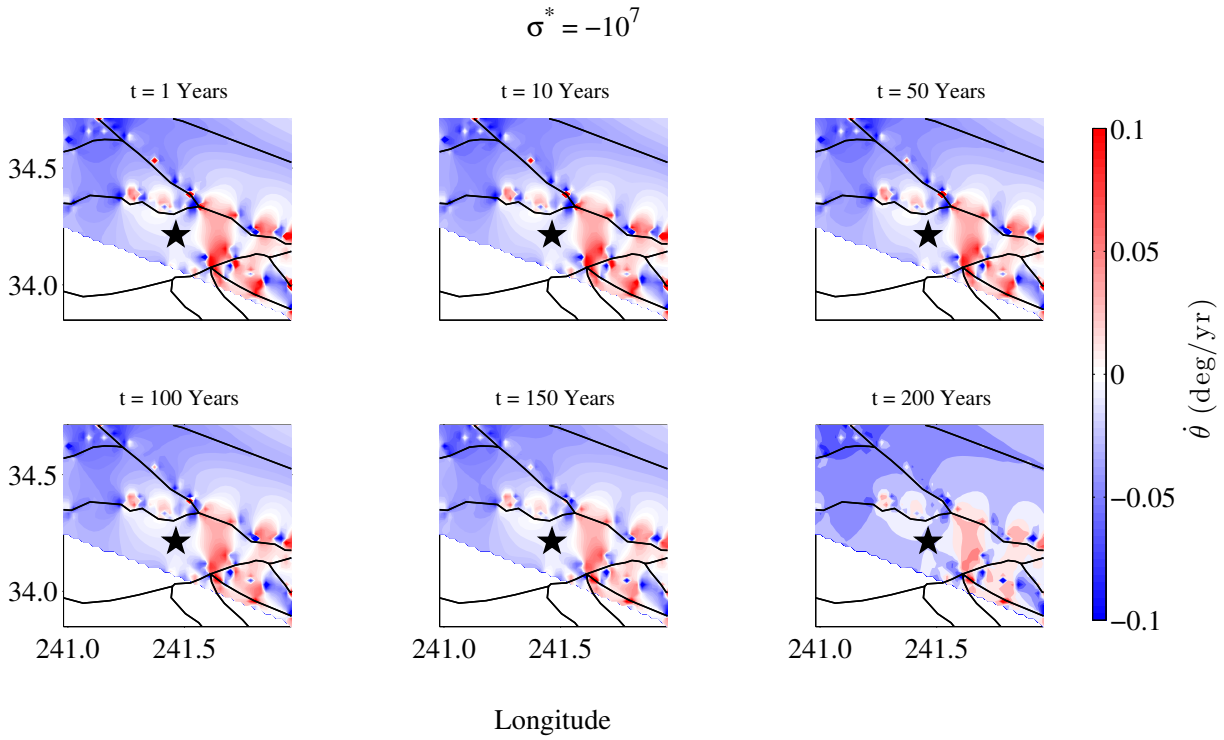

Figure 5.38: Principal stress axes rotation rates at 5 km depth within 0.5° longitude and latitude of the epicenter of the January 17, 1994 $M_W = 6.7$ Northridge earthquake. The background stress is $\sigma^b_{xx} = -\sigma^b_{yy} = \sigma^* = -10^7$ Pa. Here red colors indicate positive rotation rates, blue colors indicate negative rotation rates, and colors saturate at ± 0.1 degrees/yr. The black star indicates the location of the Northridge mainshock. Rotation rates are relatively constant over the entire earthquake cycle and are typically $|\dot{\theta}| < 0.1$ degrees/yr.

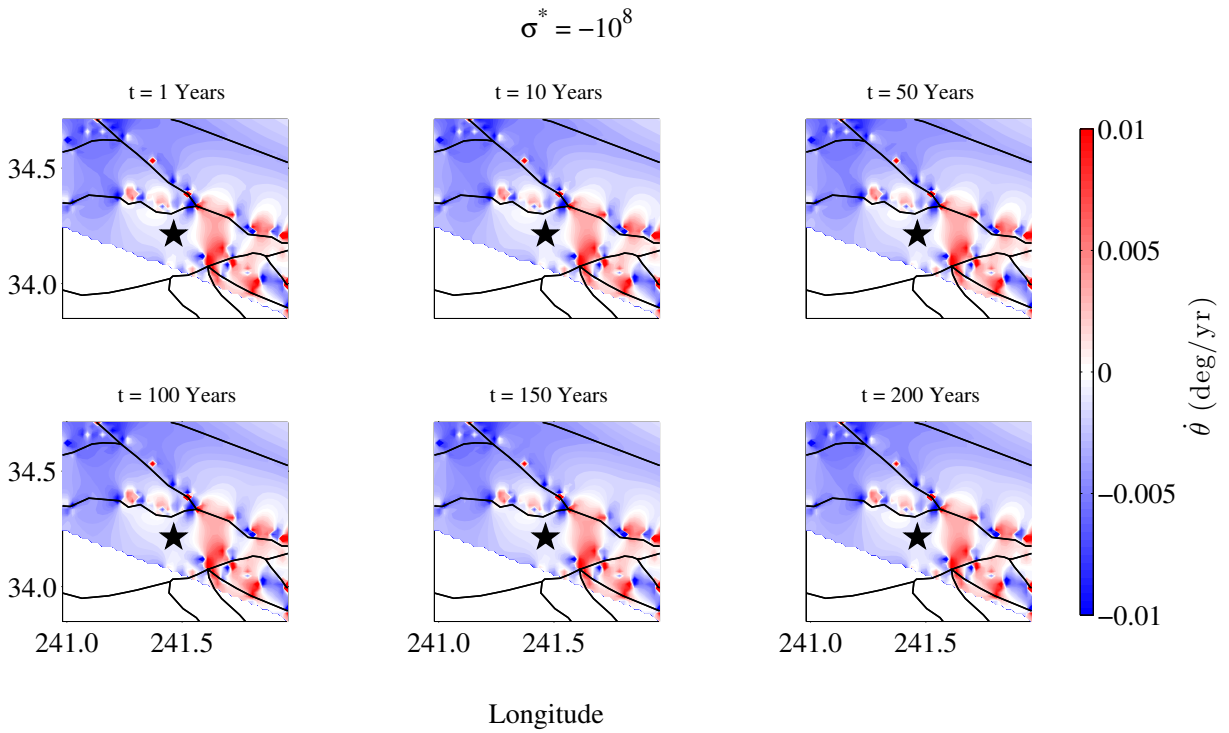

Figure 5.39: Principal stress axes rotation rates at 5 km depth within 0.5° longitude and latitude of the epicenter of the January 17, 1994 $M_W = 6.7$ Northridge earthquake. The background stress is $\sigma^b_{xx} = -\sigma^b_{yy} = \sigma^* = -10^8$ Pa. Here red colors indicate positive rotation rates, blue colors indicate negative rotation rates, and colors saturate at ± 0.01 degrees/yr. The black star indicates the location of the Northridge mainshock. Rotation rates are relatively constant over the entire earthquake cycle and are typically $|\dot{\theta}| < 0.01$ degrees/yr.

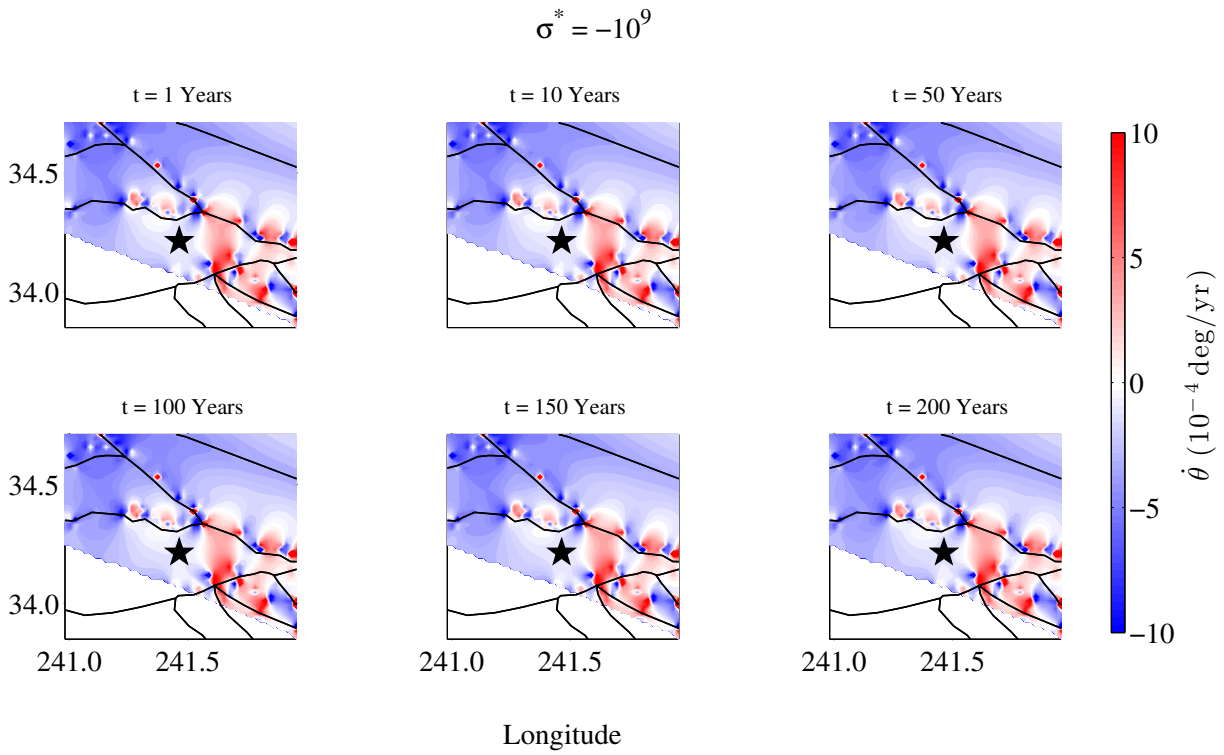

Figure 5.40: Principal stress axes rotation rates at 5 km depth within 0.5° longitude and latitude of the epicenter of the January 17, 1994 $M_W = 6.7$ Northridge earthquake. The background stress is $\sigma^b_{xx} = -\sigma^b_{yy} = \sigma^* = -10^9$ Pa. Here red colors indicate positive rotation rates, blue colors indicate negative rotation rates, and colors saturate at $\pm 1 \times 10^{-4}$ degrees/yr. The black star indicates the location of the Northridge mainshock. Rotation rates are relatively constant over the entire earthquake cycle and are typically $|\dot{\theta}| < 0.001$ degrees/yr.

50 in the earthquake cycle.

Rotation rates in the Northridge region are typically $|\dot{\theta}| = 0.1 - 0.5$ degrees/yr when $\sigma^* = \pm 10^6$ Pa (Figures 5.31 and 5.37) in the first 50 years of the earthquake cycle (and smaller in later years) and are smaller than those determined by Hardebeck and Hauksson (2001). Thus while it is possible to say that our model with $\sigma^* = \pm 10^5$ Pa is largely consistent with rotation rates from Hardebeck and Hauksson (2001), it is not possible to determine which of these two background stresses is most consistent with the focal mechanism inversions. In both our models and the rates determined by Hardebeck and Hauksson (2001), there is some heterogeneity in the sign of the rotation rate. Further, it is notable that our models do not predict large (e.g., $|\dot{\theta}| = 1 - 2$ degrees/yr) rotation rates after year 50 in the earthquake cycle while Hardebeck and Hauksson (2001) use data from both before and after the Northridge mainshock to calculate their rotation rates.

5.8.3 Comparison to estimates of stress rotations in the vicinity of the Landers earthquake

Very little can be said about the temporal evolution of the regional stress field after the June 28, 1992 Landers earthquake. Some focal mechanism studies have inferred a $7^\circ - 20^\circ$ change in the orientation of the principal stresses following the earthquake (Hardebeck and Hauksson, 2001; Hauksson, 1994), but unlike Northridge, a temporal analysis of the stress field following the earthquake is not available. Using focal mechanism data from $1981 - 1999$, Hardebeck and Hauksson (2001) infer a rotation rate of $\sim$1.5 degrees/yr. The rotation rate from Hardebeck and Hauksson (2001) is largely positive, although some spatial heterogeneity in the rotation rate sign may be inferred. To explore our calculated rotation rates in the

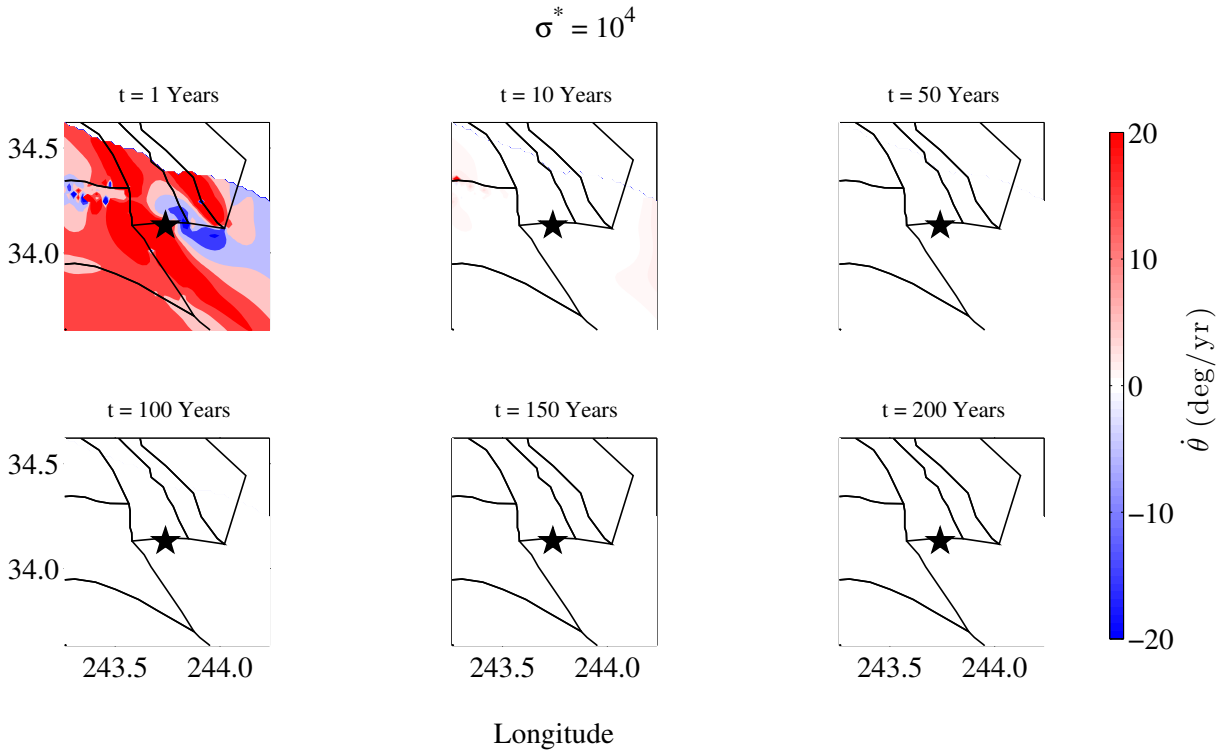

Figure 5.41: Principal stress axes rotation rates at 5 km depth within 0.5° longitude and latitude of the epicenter of the June 28, 1992 $M_W = 7.3$ Landers earthquake. The background stress is $\sigma^b_{xx} = -\sigma^b_{yy} = \sigma^* = 10^4$ Pa. Here red colors indicate positive rotation rates, blue colors indicate negative rotation rates, and colors saturate at ±20 degrees/yr. The black star indicates the location of the Landers mainshock. At this background stress rotation rates are ~ 20 degrees/yr in the first year of the earthquake cycle but decay quickly and are ~ 0 degrees/yr by year 50.

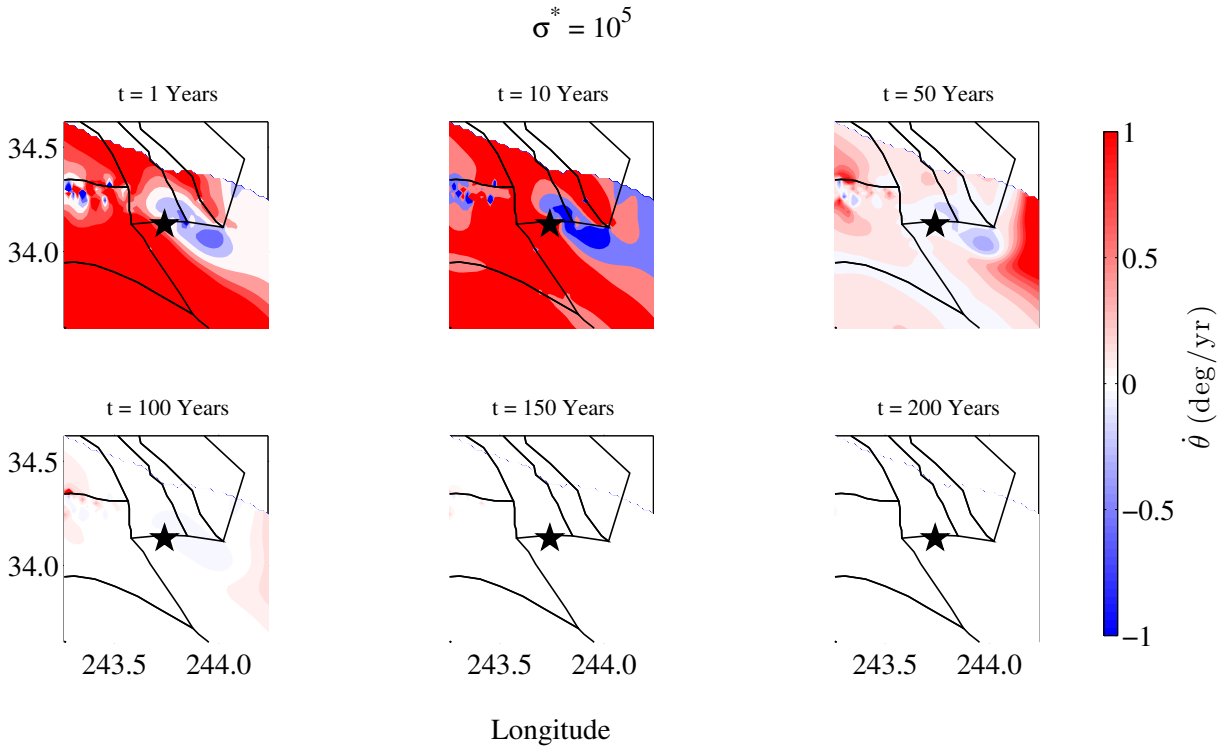

Figure 5.42: Principal stress axes rotation rates at 5 km depth within 0.5° longitude and latitude of the epicenter of the June 28, 1992 $M_W = 7.3$ Landers earthquake. The background stress is $\sigma^b_{xx} = -\sigma^b_{yy} = \sigma^* = 10^5$ Pa. Here red colors indicate positive rotation rates, blue colors indicate negative rotation rates, and colors saturate at ± 1 degrees/yr. The black star indicates the location of the Landers mainshock. At this background stress rotation rates are largely > 1 degree/yr in the first 10 years of the earthquake cycle but are typically < 0.5 degrees/yr by year 50.

Landers region in more detail, we consider a region within 0.5° longitude and latitude of the earthquake epicenter (∼92 km by 110 km, 2078 points). We consider background stresses with $\sigma^* = \pm 10^4 - \pm 10^9$ Pa, shown in Figures 5.41 - 5.52.

When $\sigma^* = 10^4$ Pa (Figure 5.41), rotation rates are > 20 degrees/yr during the first year of the earthquake cycle at the earthquake epicenter and are inconsistent with the rotation rates from Hardebeck and Hauksson (2001). When $\sigma^* = -10^4$ Pa (Figure 5.47), rotation rates are approximately the right order of magnitude in the first year of the earthquake cycle: $|\dot{\theta}| = 1 - 2$ degrees/yr at the earthquake epicenter, > 2 degrees/yr north and east of the mainshock, and $5 - 10$ degrees/yr south and west of the Landers event (in the vicinity of the Joshua Tree earthquake). However, with the exception of a ∼40 km by ∼10 km region just east of the epicenter with $|\dot{\theta}| = 0.1 - 2$ degrees/yr, all rotation rates are negative and appear to be inconsistent with focal mechanism inversions (Hardebeck and Hauksson, 2001). By year 10 in the earthquake cycle all rotation rates are $|\dot{\theta}| < 0.5$ degrees/yr.

When $\sigma^* = 10^5$ Pa (Figure 5.42), model-predicted rotation rates are more consistent with those from focal mechanism inversions. In the first year of the earthquake cycle, rotation rates are > 1 degree/yr over ∼58% of the model domain (40% of the model domain has rotation rates $\dot{\theta} = 1 - 3$ degrees/yr). At the location of the Landers mainshock, rotation rates range between $\dot{\theta} = 0.1 - 1$ degrees/yr. East of the epicenter, rotation rates are slightly negative ($\dot{\theta} < -0.5$ degrees/yr). In year 10 of the earthquake cycle, rotation rates are largely the same: $\dot{\theta}$ is > 1 degree/yr for 75% of the Landers region and $\dot{\theta} = 1 - 3$ degrees/yr for 59% of the same area. $|\dot{\theta}| = 2 - 4$ degrees/yr in the vicinity of the mainshock and for > 30 km south, west, and northwest. By year 50 in the earthquake cycle, rotation rates at

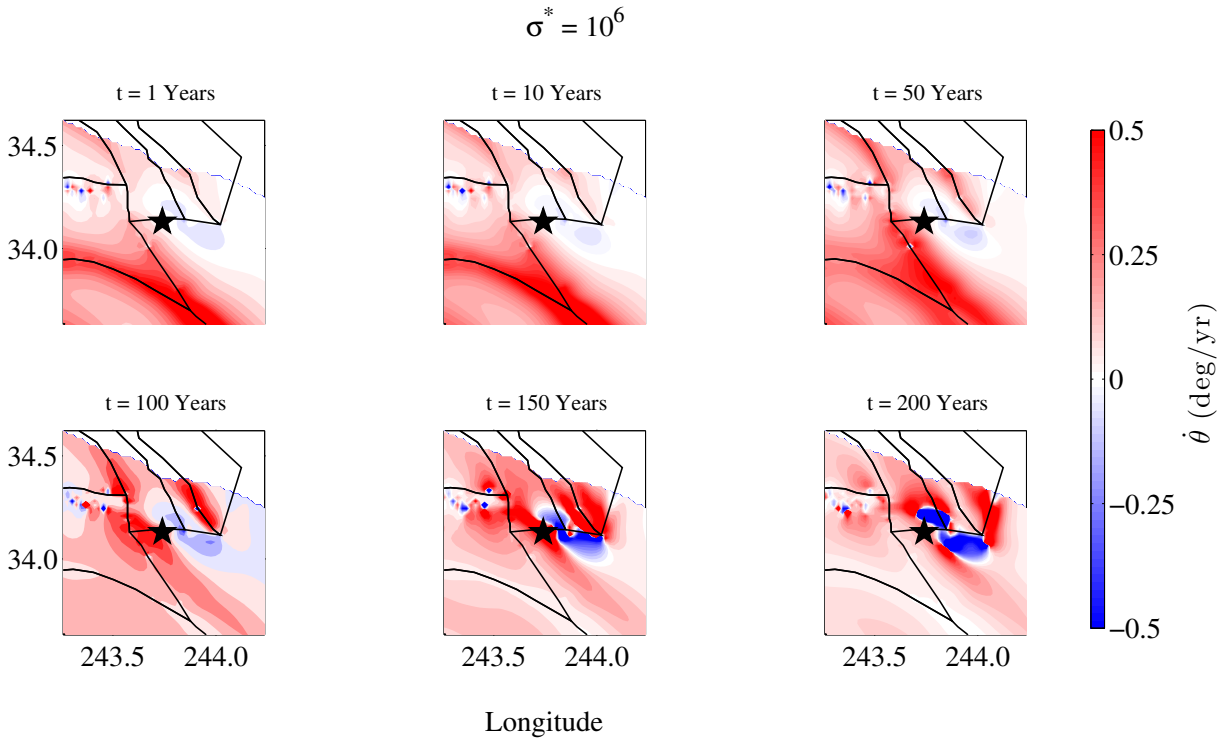

Figure 5.43: Principal stress axes rotation rates at 5 km depth within 0.5° longitude and latitude of the epicenter of the June 28, 1992 $M_W = 7.3$ Landers earthquake. The background stress is $\sigma^b_{xx} = -\sigma^b_{yy} = \sigma^* = 10^6$ Pa. Here red colors indicate positive rotation rates, blue colors indicate negative rotation rates, and colors saturate at ± 0.5 degrees/yr. The black star indicates the location of the Landers mainshock. At this background stress rotation rates are largely $|\dot{\theta}| = 0.1 - 0.5$ degrees/yr over much of the earthquake cycle.

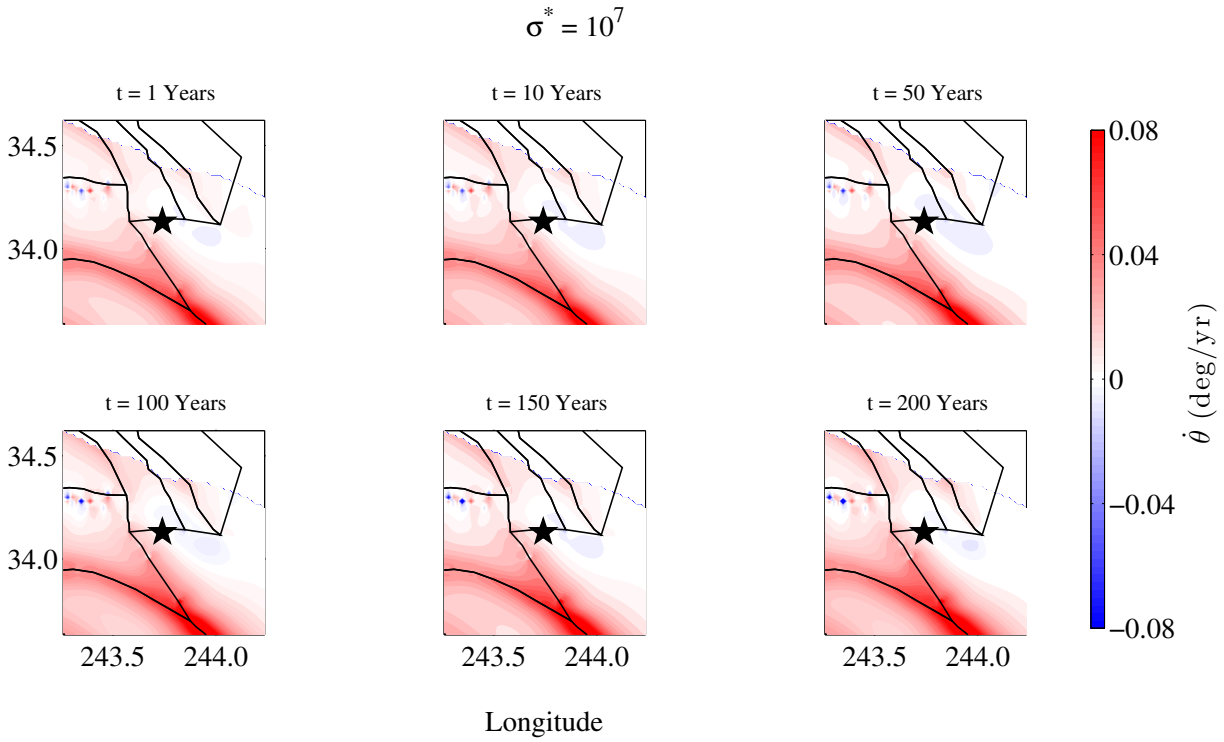

Figure 5.44: Principal stress axes rotation rates at 5 km depth within 0.5° longitude and latitude of the epicenter of the June 28, 1992 $M_W = 7.3$ Landers earthquake. The background stress is $\sigma^b_{xx} = -\sigma^b_{yy} = \sigma^* = 10^7$ Pa. Here red colors indicate positive rotation rates, blue colors indicate negative rotation rates, and colors saturate at ±0.08 degrees/yr. The black star indicates the location of the Landers mainshock. Rotation rates are relatively constant over the entire earthquake cycle and are typically $|\dot{\theta}| < 0.1$ degrees/yr.

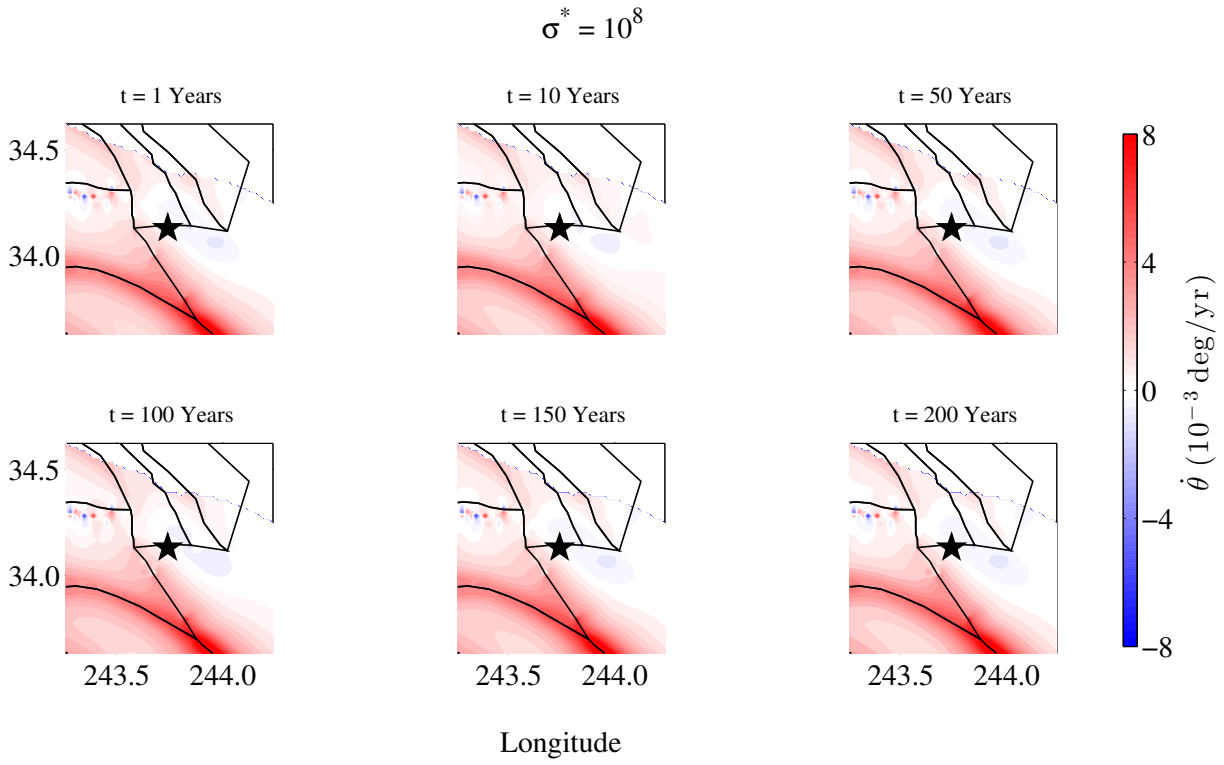

Figure 5.45: Principal stress axes rotation rates at 5 km depth within 0.5° longitude and latitude of the epicenter of the June 28, 1992 $M_W = 7.3$ Landers earthquake. The background stress is $\sigma^b_{xx} = -\sigma^b_{yy} = \sigma^* = 10^8$ Pa. Here red colors indicate positive rotation rates, blue colors indicate negative rotation rates, and colors saturate at ± 0.008 degrees/yr. The black star indicates the location of the Landers mainshock. Rotation rates are relatively constant over the entire earthquake cycle and are typically $|\dot{\theta}| < 0.01$ degrees/yr.

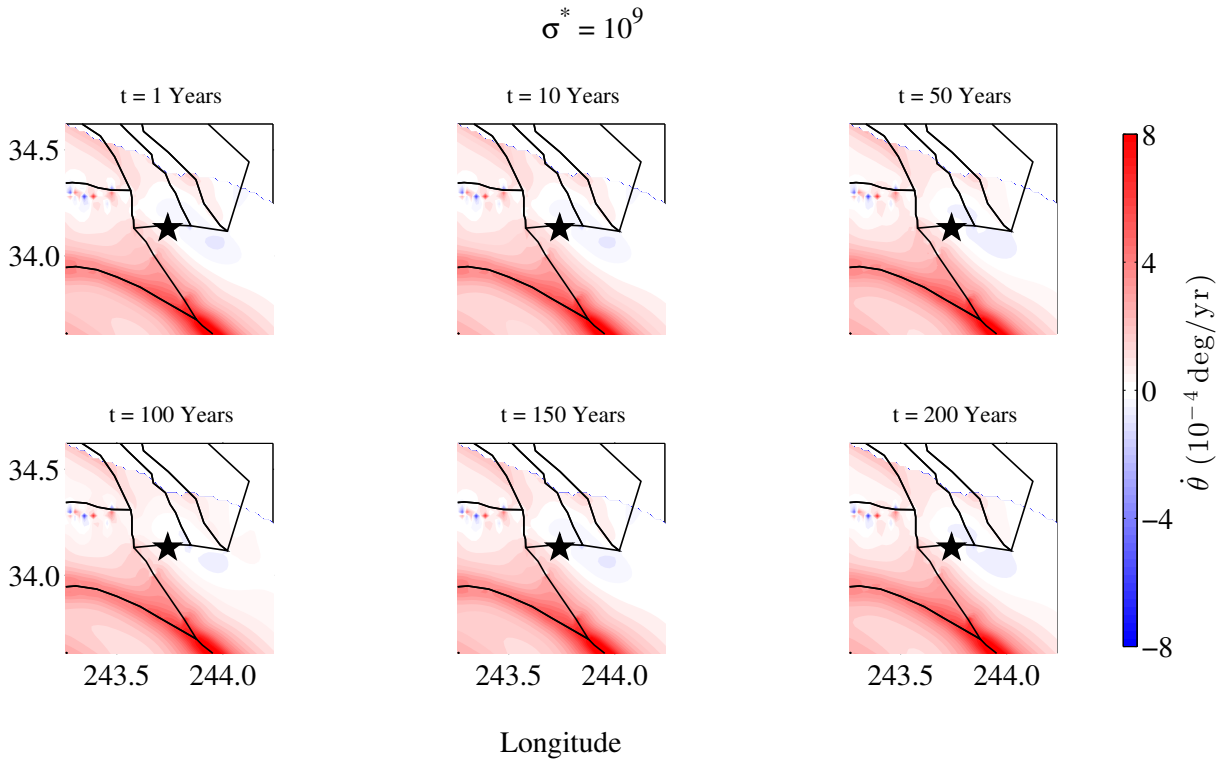

Figure 5.46: Principal stress axes rotation rates at 5 km depth within 0.5° longitude and latitude of the epicenter of the June 28, 1992 $M_W = 7.3$ Landers earthquake. The background stress is $\sigma^b_{xx} = -\sigma^b_{yy} = \sigma^* = 10^9$ Pa. Here red colors indicate positive rotation rates, blue colors indicate negative rotation rates, and colors saturate at $\pm 8 \times 10^{-4}$ degrees/yr. The black star indicates the location of the Landers mainshock. Rotation rates are relatively constant over the entire earthquake cycle and are typically $|\dot{\theta}| < 0.001$ degrees/yr.

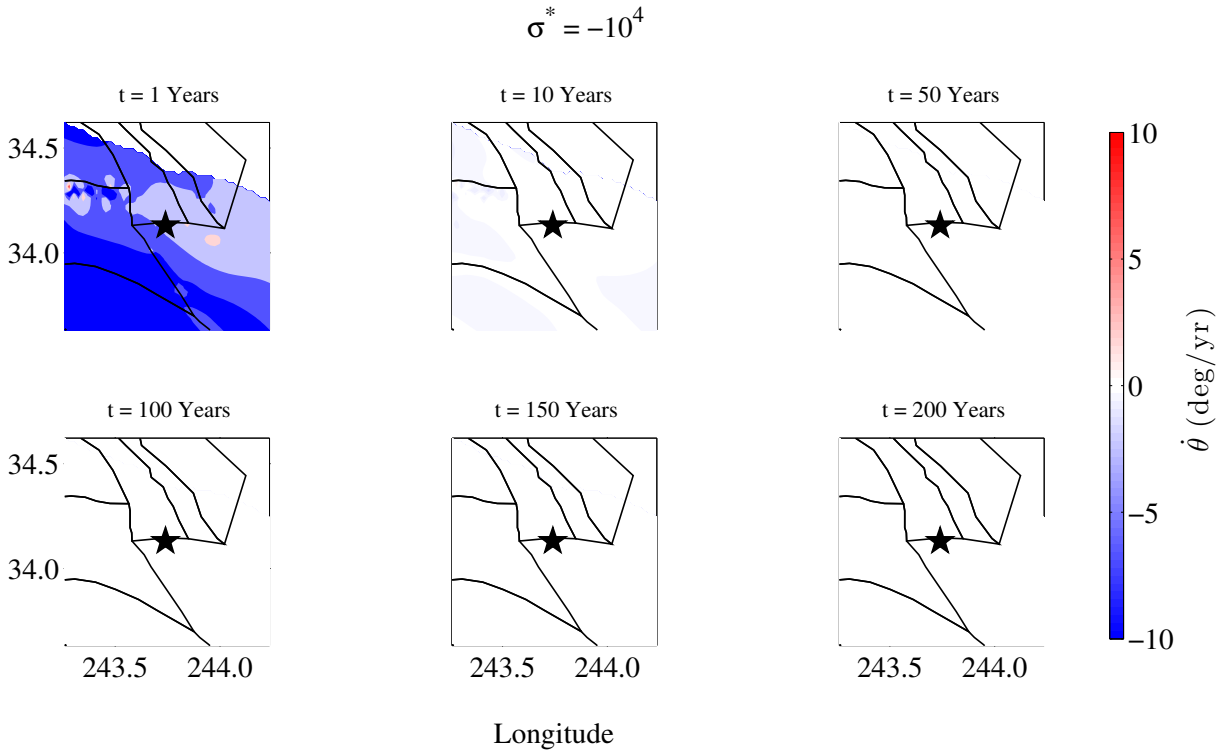

Figure 5.47: Principal stress axes rotation rates at 5 km depth within 0.5° longitude and latitude of the epicenter of the June 28, 1992 $M_W = 7.3$ Landers earthquake. The background stress is $\sigma^b_{xx} = -\sigma^b_{yy} = \sigma^* = -10^4$ Pa. Here red colors indicate positive rotation rates, blue colors indicate negative rotation rates, and colors saturate at ± 10 degrees/yr. The black star indicates the location of the Landers mainshock. At this background stress rotation rates are -1 to -10 in the first year of the earthquake cycle but decay quickly and are ~ 0 degrees/yr by year 50.

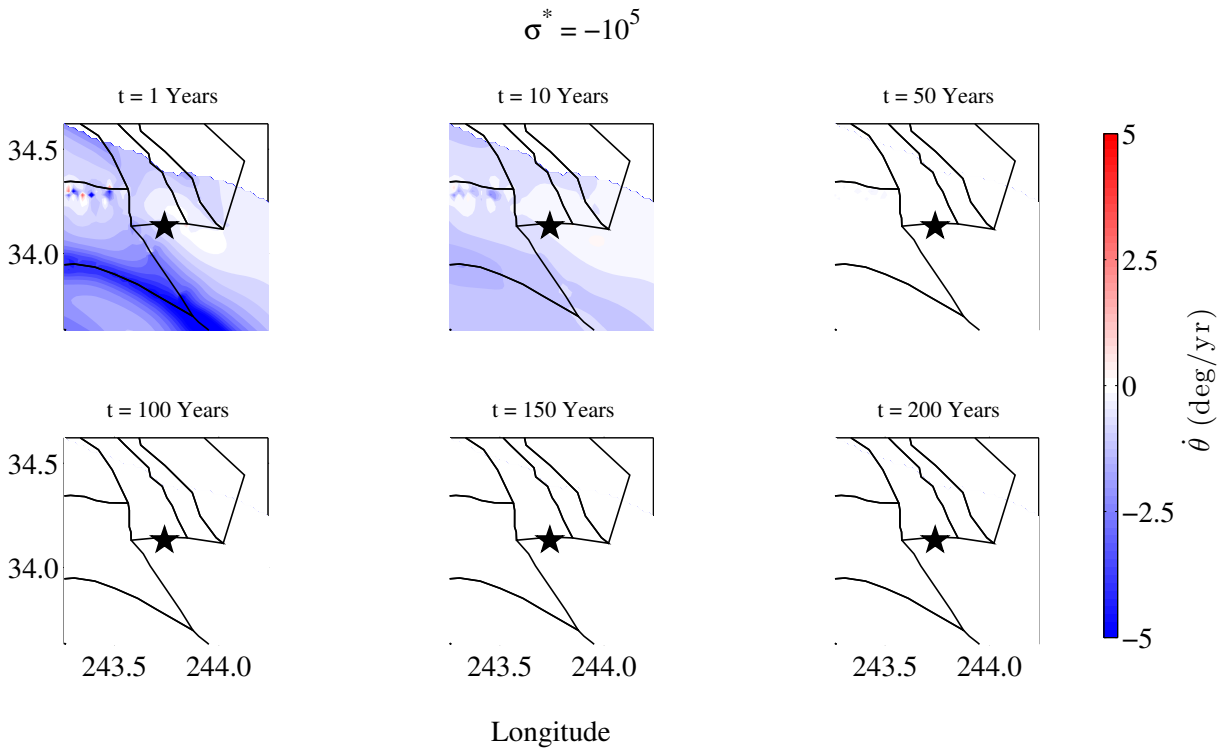

Figure 5.48: Principal stress axes rotation rates at 5 km depth within 0.5° longitude and latitude of the epicenter of the June 28, 1992 $M_W = 7.3$ Landers earthquake. The background stress is $\sigma^b_{xx} = -\sigma^b_{yy} = \sigma^* = -10^5$ Pa. Here red colors indicate positive rotation rates, blue colors indicate negative rotation rates, and colors saturate at ± 5 degrees/yr. The black star indicates the location of the Landers mainshock. At this background stress rotation rates are typically $|\dot{\theta}| < 2$ degrees/yr in the first year of the earthquake cycle but are typically $|\dot{\theta}| < 1$ degree/yr by year 10.

this background stress are < 0.5 degrees/yr in the Landers region. When $\sigma^* = -10^5$ Pa (Figure 5.48), $\dot{\theta}$ is typically $|\dot{\theta}| < 2$ degrees/yr and is $|\dot{\theta}| < 0.5$ degrees/yr in the vicinity of the earthquake epicenter. Rotation rates are predominantly negative. By year 10 in the earthquake cycle, only 9% of the Landers area has $|\dot{\theta}| > 1$ degree/yr. These results are inconsistent with Hardebeck and Hauksson (2001) rotation rate directions and magnitudes.

When $\sigma^* = \pm 10^6$ Pa (Figures 5.43 and 5.49), rotation rates in the Landers area are $|\dot{\theta}| < 0.5$ degrees/yr over the entire earthquake cycle and often $|\dot{\theta}| < 0.1$ degrees/yr. These rotation rates are an order of magnitude smaller than the > 1.5 degrees/yr rate inferred from Hardebeck and Hauksson (2001).

5.9 Discussion

5.9.1 Estimates of accumulated tectonic stress in the context of other known stresses

The total tectonic stress accumulated over the course of the earthquake cycle is the tectonic stressing rate multiplied by the duration of the earthquake cycle. In the models presented here we have considered a 200-year earthquake cycle. Stressing rate magnitudes (Figure 5.9), as previously discussed, range from 313.16 Pa/yr to 3.98×10^5 Pa/yr at 5 km depth, but on the SAF the majority of stressing rate magnitudes fall between $1 - 6 \times 10^4$ Pa/yr. Over a 200-year earthquake cycle, then, the total accumulated stress magnitude in southern California ranges from 6.26×10^4 Pa to 7.96×10^7 Pa. The median accumulated tectonic stress is 1.68×10^6 Pa/yr, and on the SAF the accumulated tectonic stress values typically range between 2×10^6 Pa/yr and 1.2×10^7 Pa/yr.

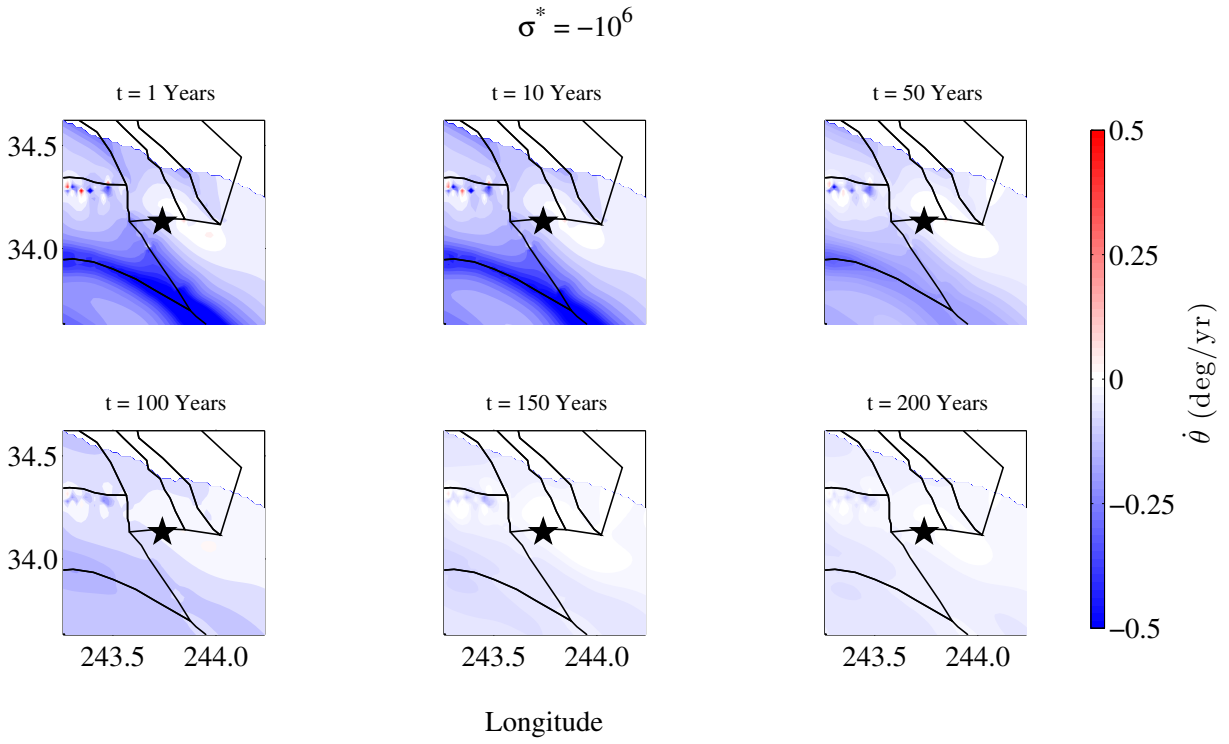

Figure 5.49: Principal stress axes rotation rates at 5 km depth within 0.5° longitude and latitude of the epicenter of the June 28, 1992 $M_W = 7.3$ Landers earthquake. The background stress is $\sigma^b_{xx} = -\sigma^b_{yy} = \sigma^* = -10^6$ Pa. Here red colors indicate positive rotation rates, blue colors indicate negative rotation rates, and colors saturate at ± 0.5 degrees/yr. The black star indicates the location of the Landers mainshock. At this background stress rotation rates are typically $|\dot{\theta}| < 0.1 - 0.5$ degrees/yr over the entire earthquake cycle

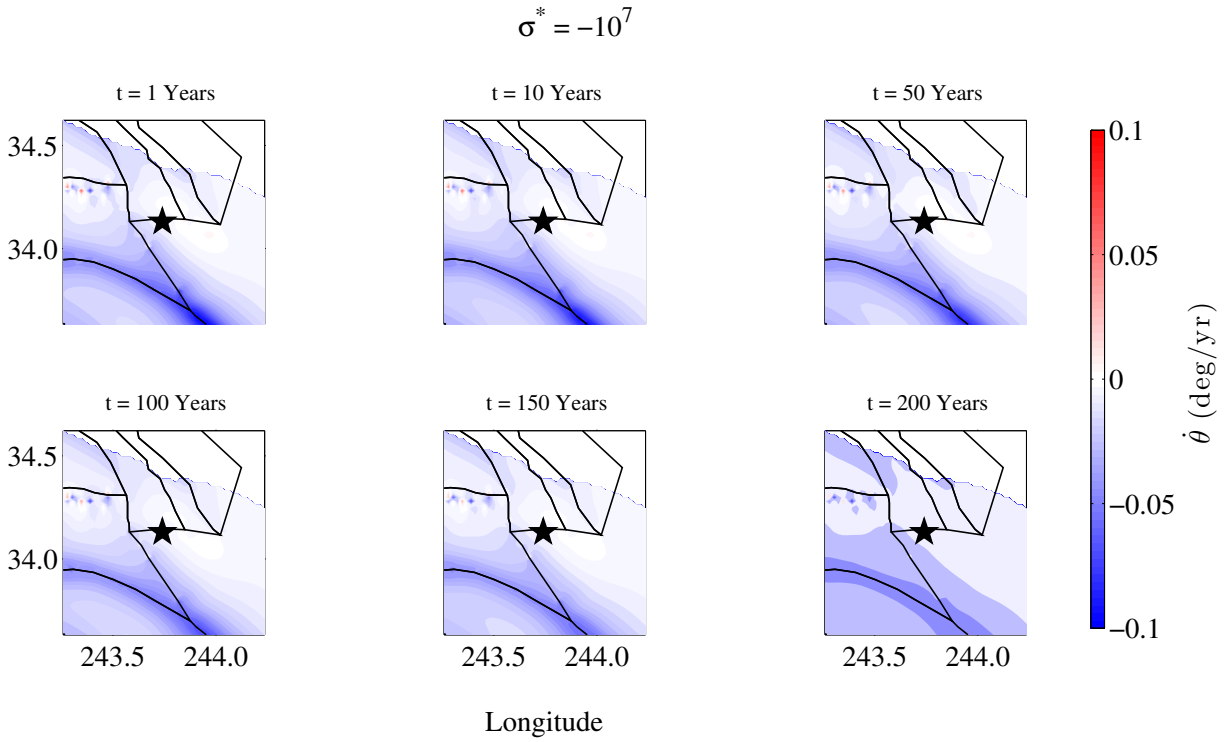

Figure 5.50: Principal stress axes rotation rates at 5 km depth within 0.5° longitude and latitude of the epicenter of the June 28, 1992 $M_W = 7.3$ Landers earthquake. The background stress is $\sigma^b_{xx} = -\sigma^b_{yy} = \sigma^* = -10^7$ Pa. Here red colors indicate positive rotation rates, blue colors indicate negative rotation rates, and colors saturate at ± 0.1 degrees/yr. The black star indicates the location of the Landers mainshock. Rotation rates are relatively constant over the entire earthquake cycle and are typically $|\dot{\theta}| < 0.1$ degrees/yr.

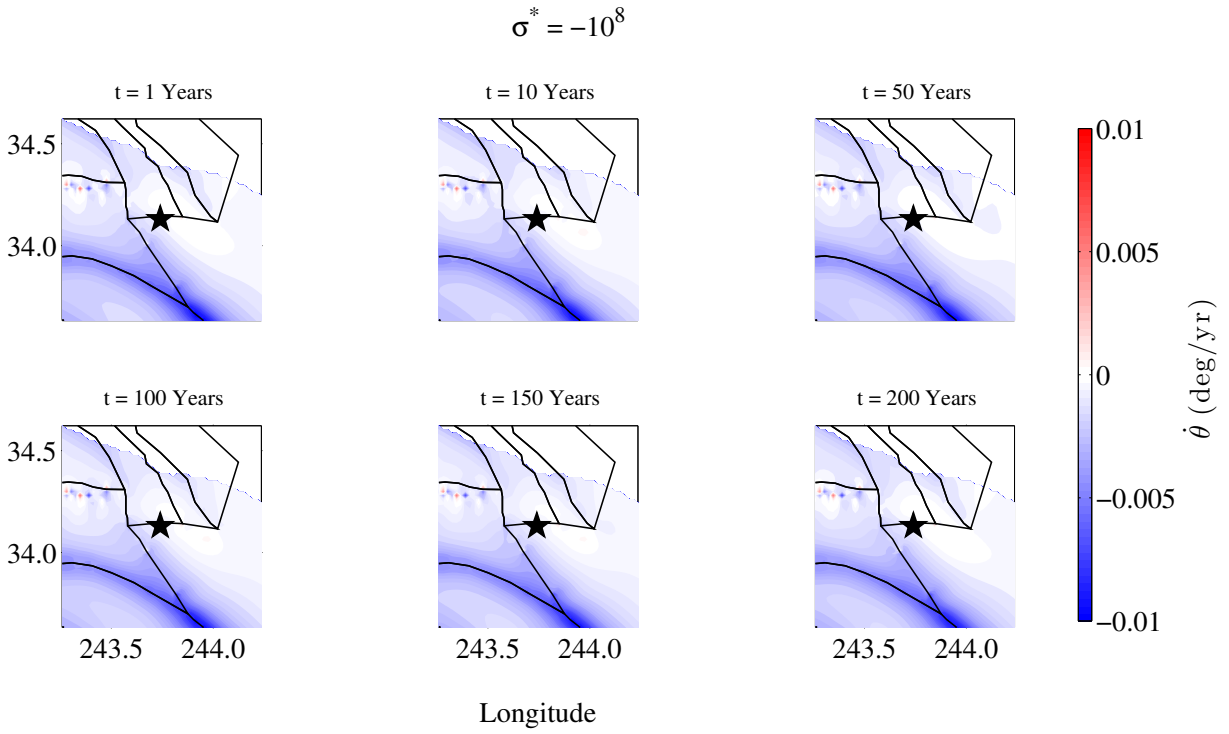

Figure 5.51: Principal stress axes rotation rates at 5 km depth within 0.5° longitude and latitude of the epicenter of the June 28, 1992 $M_W = 7.3$ Landers earthquake. The background stress is $\sigma^b_{xx} = -\sigma^b_{yy} = \sigma^* = -10^8$ Pa. Here red colors indicate positive rotation rates, blue colors indicate negative rotation rates, and colors saturate at ± 0.01 degrees/yr. The black star indicates the location of the Landers mainshock. Rotation rates are relatively constant over the entire earthquake cycle and are typically $|\dot{\theta}| < 0.01$ degrees/yr.

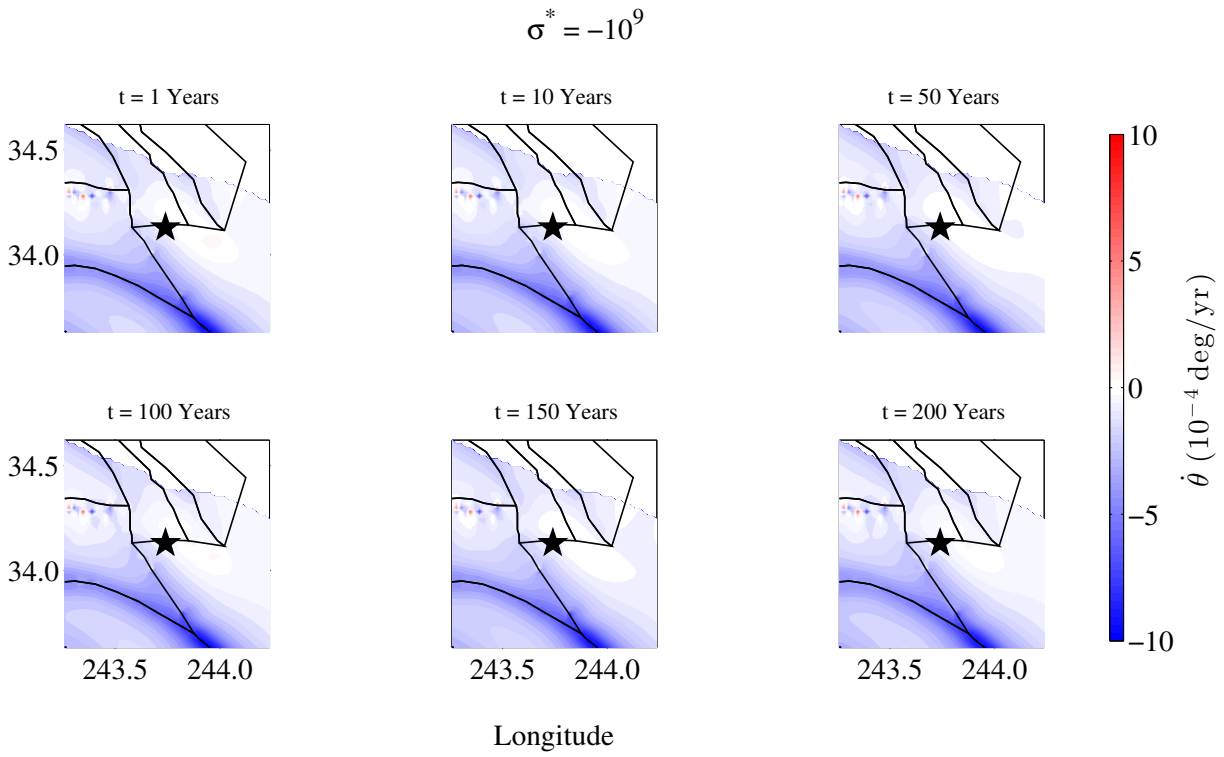

Figure 5.52: Principal stress axes rotation rates at 5 km depth within 0.5° longitude and latitude of the epicenter of the June 28, 1992 $M_W = 7.3$ Landers earthquake. The background stress is $\sigma^b_{xx} = -\sigma^b_{yy} = \sigma^* = -10^9$ Pa. Here red colors indicate positive rotation rates, blue colors indicate negative rotation rates, and colors saturate at $\pm 1 \times 10^{-4}$ degrees/yr. The black star indicates the location of the Landers mainshock. Rotation rates are relatively constant over the entire earthquake cycle and are typically $|\dot{\theta}| < 0.001$ degrees/yr.

We consider these values in the context of other estimates of stress at 5 km depth. At this depth the lithostatic stress, defined as $\sigma_L = \rho g h$, where ρ is the crustal density (2600 kg/m^3, Dziewonski and Anderson, 1981), g is gravity (9.8 m/s^2), and h is the depth (5 km), is 1.27×10^8 Pa. This value is nearly an order of magnitude higher than the highest accumulated tectonic stresses and is two orders of magnitude higher than the median accumulated tectonic stress.

Similarly, we consider the accumulated tectonic stresses as compared to the strength of crustal rocks. Rock strength, typically determined by the stress at which rocks fracture, is reported as the difference between maximum and minimum principal stresses in three dimensions, or $\sigma_1 - \sigma_3$. As a result, direct comparisons to the magnitude of the accumulated tectonic stress may not be appropriate, but rock strengths provide a useful context for considering the accumulated tectonic stress. At depths of $\sim$5 km, the differential stress at which rocks fracture is on the order of several MPa, or $\sim 1 - 10 \times 10^8$ Pa (Brace et al., 1966; Byerlee, 1967; Hadley, 1975; Scholz, 2002). As with the lithostatic stress, these values are nearly a factor of 10 higher than the maximum accumulated tectonic stress and a factor of 100 higher than the median accumulated tectonic stress.

Finally, we compare the accumulated tectonic stress to theoretical models of rupture dynamics and propagation. Many models are nondimensional (e.g., Fliss et al., 2005; Kame et al., 2003) and cannot be compared to our accumulated tectonic stress magnitudes. However, model simulations of the Landers earthquake have used stresses comparable to the lithostatic and rock strength values. In one estimation for the Landers earthquake, the initial stress in the y-direction, σ^0_{yy}, is taken to be 5×10^7 Pa at 3.3 km and 1×10^8 Pa at 6.6

km. All other values are normalized to the σ^0_{yy} value (Fliss et al., 2005). In a finite element approach to dynamic rupture modeling the regional background stress is $\sigma_1 = 3 \times 10^8$ Pa and $\sigma_2 = 1 \times 10^8$ Pa, but at site of the Landers rupture nucleation $\sigma_2 = 7 \times 10^7$ Pa. Again, these stresses are typically higher than the calculated accumulated tectonic stress. Lower values ($5 - 7 \times 10^7$ Pa) are consistent with upper estimates of the accumulated tectonic stress, but higher values ($1 - 3 \times 10^8$ Pa) are close to a factor of 10 higher.

5.9.2 Comparing stressing rate models

The Loveless and Meade (2011b) block-model derived stressing rates may be directly compared to other stressing rate contributions to the Community Stress Model that satisfy the conservation of momentum constraints (Aagaard and Hardebeck, 2013). Of these contributions, quantitative comparisons are only currently possible between the block model stressing rates and an approach that combines a four-dimensional model composed of connected vertical faults in an elastic plate overlying a Maxwell viscoelastic halfspace with a Coulomb stress model (Smith-Konter and Sandwell, 2009). To enable a direct comparison between these two models we calculate the Coulomb failure stressing rates (Figure 5.53) for the Loveless and Meade (2011b) results. The Coulomb failure stress, σ_f, is a measure of the normal and shear stress resolved on a fault plane (King et al., 1994), and we define the Coulomb failure stressing rate as:

$$\dot{\sigma_f} = \dot{\sigma}_{xy} - \mu \dot{\sigma}_n \tag{5.29}$$

where $\dot{\sigma}_{xy}$ is the shear stressing rate, μ is the coefficient of friction, and $\dot{\sigma}_n$ is the normal stressing rate acting on the fault (King et al., 1994; Okada, 1992). Positive Coulomb failure

values suggest the fault is getting closer to failure (King et al., 1994). Here we have followed King et al. (1994) and taken $\mu = 0.4$. The Coulomb failure stressing rates are resolved on the SAF and are calculated from the strike of the closest SAF fault segment. In all, 101 different fault segments with individual strikes are considered in the calculation.

The calculated Coulomb failure stressing rates are shown in Figure 5.53. Rates are highest on the northern Parkfield, Carrizo, and northern Indio segments of the SAF (corresponding to the Parkfield, Carrizo, Coachella, and Palm Springs segments from Smith-Konter and Sandwell, 2009). On these segments the Coulomb failure stressing rates range from $2.0 - 3.5 \times 10^4$ Pa/yr. These values are at least two times lower than Parkfield estimates of 7.0×10^4 Pa/yr (Smith-Konter and Sandwell, 2009) but are higher than previous Coulomb failure stressing rate estimates of 1.1×10^4 Pa/yr and 1.8×10^4 Pa/yr on the Palm Springs and Coachella segments, respectively (here collectively referred to as the northern Indio segment, Smith-Konter and Sandwell, 2009). The $2.0 - 3.5 \times 10^4$ Pa/yr Coulomb failure stressing rate is in good agreement with the Smith-Konter and Sandwell (2009) estimates of 2.3×10^4 Pa/yr on the Carrizo segment. Block model-derived Coulomb stressing rates on the San Bernardino segment of the SAF are between $1.5 - 2.5 \times 10^4$ Pa/yr and are slightly higher than the 0.5×10^4 Pa/yr estimated by Smith-Konter and Sandwell (2009). Loveless and Meade (2011b) Coulomb stressing rates are lowest on the Mojave segment of the SAF and range from $1.0 - 1.5 \times 10^4$ Pa/yr, consistent with the Smith-Konter and Sandwell (2009) Coulomb stressing rate calculations of 1.4×10^4 Pa/yr for this segment. On the San Jacinto fault, Loveless and Meade (2011b) Coulomb failure stressing rates range from $1.0 - 1.8 \times 10^4$ Pa/yr in the north to $0.4 - 1.0 \times 10^4$ Pa/yr in the south. Northern San Jacinto fault values are

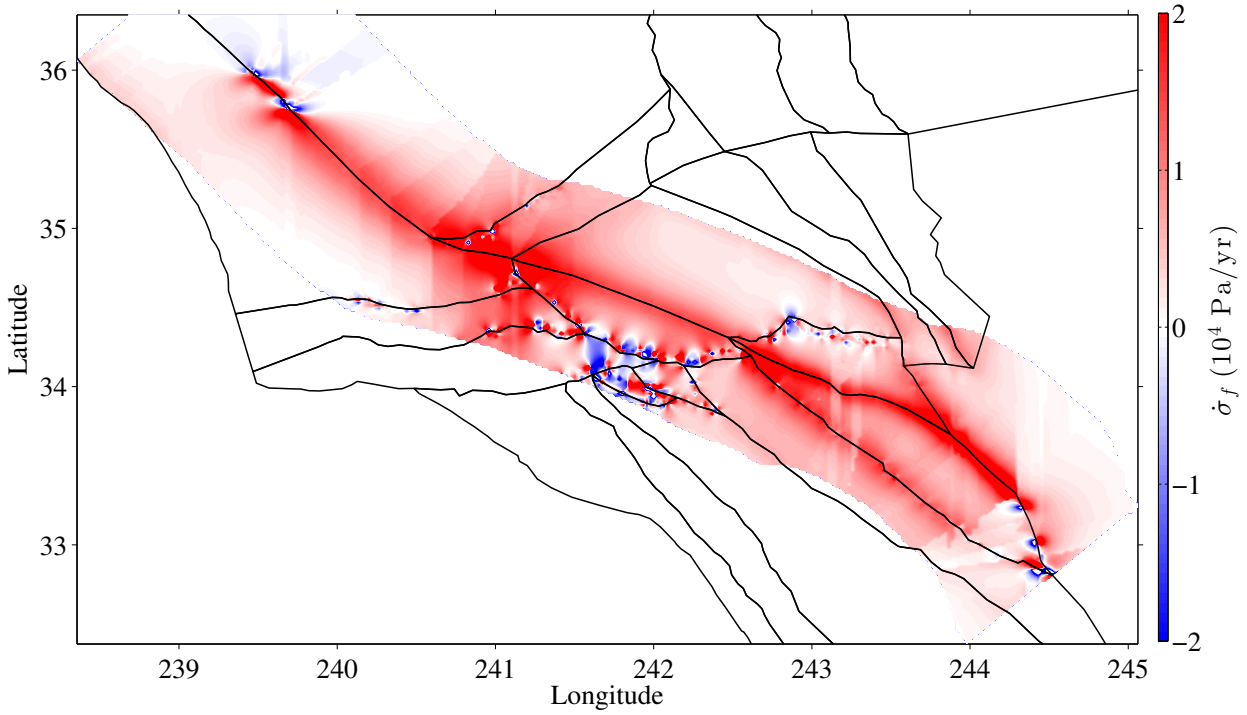

Figure 5.53: Coulomb failure stressing rates resolved on the SAF from the Loveless and Meade (2011b) block model-derived stressing rates at 5 km depth. Here red colors indicate positive values and blue colors indicate negative values. Colors are saturated at $\pm 2 \times 10^4$ Pa/yr. Coulomb failure stressing rates are highest on the northern Parkfield, Carrizo, and northern Indio segments of the SAF. Here Coulomb failure stressing rates range from $2.0 - 3.5 \times 10^4$ Pa/yr. The Coulomb failure stressing rate is $1.0 - 2.5 \times 10^4$ Pa/yr on the San Bernardino segment and $1.0 - 1.5 \times 10^4$ Pa/yr on the Mojave segment.

consistent with Smith-Konter and Sandwell (2009) estimates of a 1.7×10^4 Pa/yr Coulomb failure stressing rate.

While the Coulomb stressing rate calculations for the two models do not always agree, they are consistent for the Carrizo and Mojave segments of the SAF and within a factor of 2-3 on all segments of the southern SAF. These results suggest that while some differences in calculated principal stress rotation rate might be expected from the Smith-Konter and Sandwell (2009) stressing rate model, the magnitude of principal stress rotation rates at

different background stresses may be relatively robust to changes in the stressing rate model. We may expect the largest discrepancies in the vicinity of the Parkfield and San Bernardino segments of the SAF where the largest disagreements between the two stressing rate models occur. It should be noted, however, that the Coulomb failure stressing rates discussed here are relevant only in the vicinity of the SAF. A quantitative analysis of the differences between the stressing rate models at points at a distance from the SAF is not possible, as quantitative information on the Smith-Konter and Sandwell (2009) stressing rates is not available.

5.9.3 Median total principal stress axes rotations and implications for measuring stress fields in southern California

Rotation rate results, described above, provide some understanding of the total principal stress rotations that may be expected over the course of a ∼200 year earthquake cycle. To find the total principal stress axes rotation over the entire earthquake cycle we calculate the median rotation rate for each of the twelve background stresses described above at each year in the 200-year earthquake cycle. We then sum the rotation rates to find the total principal stress axes rotation. Results for the median total rotation at each background stress are summarized in Table 5.2.

The median total principal stress rotations occur when $\sigma^* = 10^5$ Pa (36.83 degrees when σ^* is positive and -24.64 degrees when σ^* is negative). Median rotation rates are fastest in the first 10 years of the earthquake cycle, but this period only accounts for ∼36% (σ^* positive) and ∼38% (σ^* negative) of the total stress rotation. By year 50, 84% (σ^* positive) and 83% (σ^* negative) of the total stress rotation has already occurred, suggesting that for background stresses of this magnitude, stress measurements in the first 50 years of the

earthquake cycle will best capture principal stress rotations.

For background stresses with $\sigma^* = \pm 10^6$ Pa, median total principal stress rotations are 21.42 degrees (σ^* positive) and -14.60 degrees (σ^* negative). Here rotation rates are relatively constant over the entire 200-year earthquake cycle, with only $\sim$59% (σ^* positive) and $\sim$ 64% (σ^* negative) of the median total principal stress rotations complete by year 100. While these results suggest that stress measurements from any point in the earthquake cycle may reveal principal stress axes rotations, in any 10-year period, median total stress rotations will be < 1.3 degrees. For background stresses of this magnitude it is likely that stress measurements from many different times in the earthquake cycle will best be able to capture the stress axes rotations.

For $\sigma^* = \pm 10^7$ Pa, the total median principal stress axes rotation is $|\theta| < 3$ degrees over the entire earthquake cycle, and for $\sigma^* = \pm 10^8$ Pa and $\sigma^* = \pm 10^9$ Pa, $|\theta|$ is < 1 degree over the entire earthquake cycle. Detection of these small-scale stress rotations would likely require dense sampling across the entire earthquake cycle and stress azimuth precision to a hundredth or thousandth of a degree.

As described previously, several authors have worked to characterize the state of stress in southern California through direct measurements of borehole breakouts and focal mechanism inversions (Abers and Gephart, 2001; Hardebeck and Hauksson, 2001; Hardebeck and Michael, 2006; Hauksson, 1994; Hickman and Zoback, 2004; Shamir and Zoback, 1992; Townend and Zoback, 2004; Wilde and Stock, 1997; Zhao et al., 1997; Zoback and Healy, 1992). Reported uncertainties for borehole breakouts in southern California range from $4^\circ - 23^\circ$ (Hickman and Zoback, 2004; Shamir and Zoback, 1992; Townend and Zoback, 2004; Wilde

and Stock, 1997; Zoback and Healy, 1992) and focal mechanism and p-axis inversions report $5^\circ - 30^\circ$ error bars (Abers and Gephart, 2001; Hardebeck and Hauksson, 2001; Hardebeck and Michael, 2006; Hauksson, 1994; Zhao et al., 1997). These uncertainties suggest that we may not be able to capture even the highest (>35 degrees) total stress field rotation calculated above and that with the data available thus far it may not be possible to distinguish between the background stress magnitudes. Future stress studies, with dense temporal sampling, binning by earthquake cycle time, and smaller uncertainties may have more success in determining if principal stress rotations are occurring and in distinguishing between prospective background stress magnitudes.

5.9.4 Additional mechanisms for stress loading

In the approach above we have combined a constant regional background stress of different magnitudes with a tectonic stressing rate derived from block model calculations. However, several processes may alter stress fields on a local level and may play a significant role in altering the expected principal stresses and principal stress rotation rates.

Several authors have documented local static stress changes following large earthquake events. Focal mechanism studies have found $\sim 10^\circ - 15^\circ$ of rotation in the maximum horizontal stress following the $M_W = 6.7$ Coalinga earthquake. In the vicinity of the $M_W = 6.1$ Joshua Tree earthquake one focal mechanism study reports a change in principal stress axis orientation from N14°E to N28°E following the Joshua Tree event and then a rotation back to N16°E following the nearby $M_W = 7.3$ Landers earthquake (Hauksson, 1994). The Landers earthquake itself is estimated (from focal mechanism studies) to have rotated the principal stress axes by $\sim 7^\circ - 20^\circ$ (Hardebeck and Hauksson, 2001; Hauksson, 1994).

Other studies have explored the changes in the static Coulomb failure stress, static stress drop, and rate and state friction following major earthquakes and have suggested that these events locally alter the stress field to promote or inhibit future earthquake ruptures (Freed et al., 2007; Harris and Simpson, 2002; King et al., 1994; Price and Bürgmann, 2002; Steacy et al., 2005; Stein, 1999; Toda et al., 2005). Indeed, estimates of the Landers-induced static Coulomb failure stress change in the region of the $M_W = 7.1$ Hector Mine earthquake range from $-3 - 3$ MPa, or $-3 - 3 \times 10^7$ Pa (Harris and Simpson, 2002; Parsons and Dreger, 2000; Scientists of the US Geological Survey et al., 2000). The static stress drops associated with large earthquakes may also locally alter the stress field, and stress drops for the Landers, Northridge, and Hector Mine earthquakes have been estimated as $3.5 - 20$ MPa, 11.8 MPa, and 10 MPa, respectively (Hardebeck and Hauksson, 2001; King et al., 1994; Mayeda and Walter, 1996; Price and Bürgmann, 2002; Sieh et al., 1993). If these local Coulomb failure stress changes and static stress drops are combined with the background stresses and stressing rates we have considered here, they may significantly alter the local stress fields and change the principal stress rotation rates.

An additional mechanism for local stress variations may be viscoelastic stress relaxation and transfer (Freed et al., 2007; Steacy et al., 2005; Zeng, 2001). Several authors have proposed that viscoelastic stress transfer may explain the temporal proximity of the Landers and Hector Mine earthquakes. Here the viscoelastic relaxation of the lower crust and upper mantle allows for a time dependent stress transfer to adjacent regions. Viscoelastic Coulomb failure stress changes from the Landers earthquake in the vicinity of the Hector Mine earthquake, which occurred 7 years after the Landers mainshock, have been estimated at $0.02 - 0.2$

MPa (Masterlark and Wang, 2002; Pollitz and Sacks, 2002; Zeng, 2001). Viscoelastic stress loading has also been proposed as a mechanism to explain ∼2 year decay in aftershocks following the Northridge earthquake (Deng et al., 1999).

Other mechanisms for modifying the local stress field include local and temporal variations in the pore fluid pressure (Cocco and Rice, 2002; Masterlark and Wang, 2002; Nur and Booker, 1972; Steacy et al., 2005). Additionally, some evidence exists for local stress loading as a result of geothermal energy and hydrocarbon production and from mining activities (Richardson and Jordan, 2002; Trifu and Felher, 1998).

The processes described above may significantly alter the local stress fields and result in considerable heterogeneity in the regional southern California total stress tensor. Such spatial heterogeneity in the total stress tensor may, in turn, result in more spatially heterogeneous rotation rates than those we have shown here. Local variations in the total stress tensor may also account for the discrepancy between the previously reported extremely heterogeneous rotation rates (Hardebeck and Hauksson, 2001) and the more regionally uniform rotation rates described above.

Finally, the rotation rates described above are valid for the simple, purely north-south and east-west background stress tensor we have described. Some regional and magnitude differences may be expected with alternative constructions of the background stress tensor. In addition, the models described above have assumed a regionally constant background stress tensor. Spatially heterogeneous rotation rates (e.g., Hardebeck and Hauksson, 2001) may be explained by a regionally heterogeneous background stress. Current data, however, does not constrain the nature of the background stress.

5.10 Conclusion

We have presented an analytical solution for the rotation rate of the principal stress axes as a function of the background stress, the stressing rate, and the time in the earthquake cycle. To constrain the range of background stresses over which principal stress axes rotations may be observed, we have performed a sensitivity analysis of the different input parameters. The interseismic rotation rates of the principal stress axes across an idealized fault are calculated by combining the classic homogeneous elastic halfspace cut by an infinitely long strike-slip fault with a constant north-south east-west background stress of magnitude $10^4 - 10^9$ Pa.

To constrain the range of rotation rates in southern California, we have combined a block model-derived interseismic stressing rate model with a regionally uniform north-south east-west background stress at 12 different magnitudes ranging from $\pm 10^4 - \pm 10^9$ Pa. We have also calculated the median total rotation in the axes of principal stress expected from these background stresses and found that maximum rotation occurs when $\pm\sigma^* = 10^5$ Pa. The fastest rotation rates occur in the first year of the earthquake cycle with $\pm\sigma^* = 10^4$ Pa. Rotation rates are relatively constant over the entire earthquake cycle when $\sigma^* = \pm 10^6$ Pa.

Our results show that for a purely north-south and east-west oriented background stress, the maximum median total principal stress rotation over the entire earthquake cycle is 36.83 degrees and occurs when $\sigma^* = 10^5$ Pa. Previously estimated stress rotation rates are consistent with background stresses of $\sigma^* = \pm 10^4$ Pa (for the Northridge earthquake, Zhao et al., 1997) and $\sigma^* = \pm 10^5$ Pa (for regions in the vicinity of major southern California earthquakes of the past 30 years, Hardebeck and Hauksson, 2001). However, at these background

stresses, these rotation rates persist for only the first $0 - 20$ years of the earthquake cycle before the total stress axes align with the tectonic stressing rate and rotation rates approach zero. We have shown that at background stresses of $\sigma^* = \pm 10^6$ Pa, median values of $|\dot{\theta}|$ are < 0.15 degrees/yr over the entire earthquake cycle and it will take ~ 100 years to accumulate median total stress rotations of 10 degrees. When $\sigma^* = \pm 10^7$ Pa, median total stress axes rotations are < 3 degrees over the entire 200-year earthquake cycle, and when $|\sigma^*| \geq 10^8$ Pa, median total stress axes rotations are < 0.5 degrees over the 200-year earthquake cycle.

The results described above suggest that a dense spatial and temporal sampling of the crust may be required to fully capture the nature of proposed interseismic principal stress rotations. Previous studies of the state of stress in southern California from borehole breakouts and focal mechanism inversions suggest that uncertainties in stress measurements range from $4 - 30$ degrees (Abers and Gephart, 2001; Hardebeck and Hauksson, 2001; Hardebeck and Michael, 2006; Hauksson, 1994; Hickman and Zoback, 2004; Shamir and Zoback, 1992; Townend and Zoback, 2004; Wilde and Stock, 1997; Zhao et al., 1997; Zoback and Healy, 1992). With the exception of the case of a low background stress ($\sigma^* = \pm 10^4 - \pm 10^5$ Pa) immediately ($0 - 20$ years) following a large earthquake, median total stress rotations over 10 years may be $< 1 - 2$ degrees and $<\sim 0.15$ degrees in a single year. Results from this study suggest that measurement techniques with precisions of < 1 degree may be required to determine if rotations in the principal stress axes are occurring.

Chapter 6

Conclusions and future work

This thesis has developed tools to make testable predictions of fault slip rates, and it has principal stress axes rotation rates and applied these methods to continental boundary regions in Tibet and southern California. Chapter 2 presented a new deformable microplate modeling technique that combines discrete slip on frictionless faults (microplate boundaries) with continuous deformation in microplate interiors. These two-dimensional, two-stage, linear elastic models are driven by Dirichlet and force boundary conditions and make fault slip rate predictions. In Chapter 2, we presented the methodology for these DM models and solved two idealized problems simulating continental collisions.

In Chapter 3, we applied the DM modeling approach to a simple ten-microplate representation of the India-Asia boundary zone and the Tibetan plateau. We tested a suite of displacement and force boundary conditions to determine the parameters that best predict slip rates on major Tibetan faults and the observed southeastern extrusion of Tibetan crustal material (Meade, 2007). We found that a model with a Dirichlet boundary condition on the eastern three-quarters of the Himalayan Range Front and a force boundary condition along the southeastern margin was the only model that could accurately predict slip rates on the

Altyn Tagh and Karakorum faults, left-lateral slip along the entire Kunlun fault, and the southeastern extrusion of Tibet.

Chapter 4 presented a DM model for the southern California fault system and the San Andreas fault. We tested a range of models from fully continuous (all Pacific-North America plate motion on the western boundary) to fully localized (all Pacific-North America plate motion isolated on the San Andreas fault). By minimizing the weighted sum of squared residuals between geologic and geodetic measurements of the slip rate on the San Andreas and the model-predicted slip rates, we found that a model with $\sim$36 mm/yr of localized slip beneath the San Andreas and $\sim$14 mm/yr of displacement on the western boundary could best explain San Andreas fault slip rates.

In Chapter 5, we explored the evolution of the southern California stress field. We developed an analytical equation, derived from Mohr's Circle, for the axes of principal stress rotation rate as a function of the background stress, stressing rate, and time in the earthquake cycle. We then performed a parameter sensitivity test to determine under what range of values of background stress and stressing rate there are observable rotations in the principal stress axes. Using the equations for an infinitely long strike-slip fault in an elastic halfspace underlain by a viscoelastic layer (Savage and Burford, 1973; Savage and Prescott, 1978), we calculated the principal stress rotation rates for an idealized strike-slip fault at different background stresses. Finally, we combined a block model-derived southern California stressing rate model (Loveless and Meade, 2011b) with a regional background stress to constrain the range of hypothetical background stresses for which rotations in the southern California stress field might be observed. These results were then compared to previous

estimates of rotation rates.

The tools developed here make testable predictions of fault slip rates and principal stress rotation rates, thus allowing us to explore the range of initial and boundary conditions that are required to reproduce tectonic observations. Future work may extend the DM models presented here to other regions or to three dimensions. The principal stress axes rotation calculations presented here neglect viscoelastic relaxation and other stress loading effects, and the incorporation of these elements may result in more accurate and more heterogeneous rotation rates. In addition, a denser temporal and spatial sampling of faults and stress fields, with increased precision, will provide additional information against which the predictions presented here may be compared.

Bibliography

Aagaard, B., Hardebeck, J., March 15 2013. Overview of the SCEC community stress model.

Abdrakhmatov, K. Y., Aldazhanov, S. A., Hamburger, M. W., Herring, T. A., Kalabev, K. B., Makarov, V. I., Molnar, P., Panasyuk, S. V., Prilepin, M. T., Reiliner, R. E., Sadybakasov, I. S., Souter, B. J., Trapeznikov, Y. A., Tsurkov, V. Y., Zubovich, A. V., 1996. Relatively recent construction of the Tien Shan inferred from GPS measurements of present-day crustal deformation rates. Nature 384, 450–453, doi: 10.1038/384450a0.

Abers, G. A., Gephart, G. W., 2001. Direct inversion of earthquake first motions for both the stress tensor and focal mechanisms and application to southern California. Journal of Geophysical Research 106 (B11), 26,523–26,540.

Allen, C. R., Zhuoli, L., Hong, Q., Xuize, W., Huawei, Z., Weishe, H., 1991. Field study of a highly active fault zone: the Xianshuihe fault of southwestern China. Geological Society of America Bulletin 103 (9), 1178–1199, doi: 10.1130/0016–7606(1991).

Allmann, B. P., Shearer, P. M., 2009. Global variations of stress drop for moderate to large earthquakes. Journal of Geophysical Research 114 (B01310), doi: 10.1029/2008JB005821.

Ambraseys, N., Bilham, R., 2003. Reevaluated intensities for the great Assam earthquake of 12 June 1897, Shillong, India. Bulletin of the Seismological Society of America 92 (2), 655–673, doi: 10.1785/0120020093.

Armijo, R., Tapponnier, P., Han, T., 1989. Late Cenozoic right-lateral strike-slip faulting in southern Tibet. Journal of Geophysical Research 94 (B3), 2787–2838, doi: 10.1029/JB094iB03p02787.

Atwater, T., 1970. Implications of plate tectonics for the Cenozoic tectonic evolution of western North America. GSA Bulletin 81 (12), 3513–3536, doi: 10.1130/0016–16–7606(1970).

Avouac, J.-P., Tapponnier, P., 1993. Kinematic model of active deformation in central Asia. Geophysical Research Letters 20 (10), 895–898, doi: 10.1029/93GL00128.

Baldock, G., Stern, T., 2005. Width of mantle deformation across a continental transform: Evidence from upper mantle (Pn) seismic anisotropy measurements. Geology 33 (9), 741–744, doi: 10.1130/G21605.1.

Bell, M. A., Elliott, J. R., Parsons, B. E., 2011. Interseismic strain accumulation across the Manyi fault (Tibet) prior to the 1997 M_W 7.6 earthquake. Geophysical Research Letters 38 (24), doi: 10.1029/2011GL049762.

Bendick, R., Bilham, R., Freymueller, J., Larson, K., Yin, G., 2000. Geodetic evidence for a low slip rate in the Altyn Tagh fault system. Nature 404, 67–72.

Bennett, R. A., Rodi, W., Reilinger, R. E., 1996. Global Positioning System constraints on fault slip rates in southern California and northern Baja, Mexico. Journal of Geophysical Research 101 (B10), 21,943–21,960.

Bilham, R., England, P., 2001. Plateau pop-up during the 1897 Assam earthquake. Nature 410 (6830), 806–809.

Bilham, R., Karson, K., Freymueller, J., Jouanne, F., LeFort, P., Leturmy, P., Mugnier, J. L., Gamond, J. F., Glot, J. P., Matrinod, J., Chaudury, N. L., Chitrakar, G. R., Gautam, U. P., Koirala, B. P., Pandey, M. R., Ranabhat, R., Sapkota, S. N., Shrestha, P. L., Thakuri, M. C., Timilsina, U. R., Tiwari, D. R., Vidal, G., Vigny, C., Galy, A., deVoogd, B., 1997. GPS measurements of the present-day convergence across the Nepal Himalaya. Nature 386 (6620), 61–64.

Bird, P., Rosenstock, R. W., 1984. Kinematics of present crust and mantle flow in southern California. Geological Society of America Bulletin 95 (8), 946–957.

Blisniuk, P. M., Hacker, B. R., Glodny, J., Ratschbacher, L., Bi, S., Wu, Z., McWilliams, M. O., Calvert, A., 2001. Normal faulting in central Tibet since at least 13.5 Myr ago. Nature 412, 628–632, doi: 10.1038/35088045.

Boness, N. L., Zoback, M. D., 2004. Stress-induced seismic velocity anisotropy and physical properties in the SAFOD pilot hole in Parkfield, CA. Geophysical Research Letters 31 (15), doi: 10.1029/2003GL019020.

Bott, M. H. P., 1959. The mechanics of oblique slip faulting. Geological Magazine 96, 109–117.

Bourne, S. J., England, P. C., Parsons, B., 1998. The motion of crustal blocks driven by flow of the lower lithosphere and implications for slip rates of continental strike-slip faults. Nature 391 (6668), 655–659.

Brace, W., Paulding Jr, B. W., Scholz, C., 1966. Dilatancy in the fracture of crystalline rocks. Journal of Geophysical Research 71 (16), 10.1029/JZ071i016p03939.

Brown, E. T., Bendick, R., Bourles, D. L., Gaur, V., Molnar, P., Raisbeck, G. M., Yiou, F., 2002. Slip rates of the Karakorum fault, Ladakh, India, determined using cosmic ray exposure dating of debris flows and moraines. Journal of Geophysical Research 107 (B9), doi: 10.1029/2000JB000100.

Byerlee, J. D., 1967. Frictional characteristics of granite under high confining pressure. Journal of Geophysical Research 72 (14), 3639–3648.

Calais, E., Vergnolle, M., Sankov, V., Lukhnev, A., Miroshnitchenko, A., Amarjargal, S., Déverchere, J., 2003. GPS measurements of crustal deformation in the Baikal-Mongolia

area (1994-2002): Implications for current kinematics of Asia. Journal of Geophysical Research 108 (B10), doi:10.1029/2002/JB002373.

Carpenter, B. M., Marone, C., Saffer, D. M., 2011. Weakness of the San Andreas fault revealed by samples from the active fault zone. Nature 4, doi: 10.1038/NGEO1089.

Cavalié, O., Lasserre, C., Koin, M.-P., Peltzer, G., Sun, J., Xu, X., Shen, Z.-K., 2008. Measurement of interseismic strain across the Haiyuan fault (Gansu, China) by InSAR. Earth and Planetary Science Letters 275, 246–257, doi: 10.1016/j.epsl.2008.07.057.

Chen, Q., Freymeuller, J. T., Wang, Q., Zhiqiang, Y., Xu, C., Liu, J., 2004. A deforming block model for the present-day tectonics of Tibet. Journal of Geophysical Research 109 (B1), doi: 10.1029/2002JB002151.

Chen, W. P., Molnar, P., 1981. Constraints on the seismic wave velocity structure beneath the Tibetan plateau and their tectonic implications. Journal of Geophysical Research 86 (B7), 5937–5962, doi:10.1029/JB086iB07p05937.

Chen, Z., Burchfiel, B. C., Liu, Y., King, R. W., Royden, L. H., Tang, W., Wang, W., Zhao, J., Zhang, X., 2012. Global Positioning System measurements from eastern Tibet and their implications for India/Eurasia intercontinental deformation. Journal of Geophysical Research 105 (B7), 16,215–16,227, doi:10.1029/2000JB900092.

Cheng, A., Jackson, D. D., Matsuura, M., 1987. Aseismic Crustal Deformation in the Transverse Ranges of Southern-California. Tectonophysics 144 (1-3), 159–180.

Chéry, J., 2008. Geodetic strain across the San Andreas fault reflects elastic plate thickness variations (rather than fault slip rate). Earth and Planetary Science Letters 269, 352–365, doi:10.1016/j.epsl.2008.01.046.

Chevalier, M. L., Ryerson, F. J., Tapponnier, P., Finkel, R. C., Van der Woerd, J., Li, H. B., Liu, Q., 2005. Slip-rate measurements on the Karakorum fault may imply secular variations in fault motion. Science 307 (5708), 411–414.

Chuang, R. Y., Johnson, K. M., 2011. Reconciling geologic and geodetic model fault slip-rate discrepancies in southern California: Consideration of non steady mantel flow and lower crustal fault creep. Geology 39 (7), 627–630, doi: 10.1130/G32120.1.

Cocco, M., Rice, J. R., 2002. Pore pressure and poroelastic effects in Coulomb stress analysis of earthquake interactions. Journal of Geophysical Research 107 (B2), doi: 10.1029/2000JB000138.

Coleman, M., Hodges, K., 1995. Evidence for Tibetan plateau uplift before 14 Myr ago from a new minimum age for east-west extension. Nature 374, 49–52.

Cooke, M. L., Dair, L. C., 2011. Simulating the recent evolution of the southern big bend of the San Andreas fault, southern California. Journal of Geophysical Research 116 (B04405), doi:10.1029/2010JB007835.

Corsini, M., Vauchez, A., Archanjo, C., de Sá, E. F. J., 1991. Strain transfer at continental scale from a transcurrent shear zone to a transpressional fold belt: The Patos-Seridó system, northeastern Brazil. Geology 19 (6), 586–589, doi: 10.1130/0091–7613(1991).

Cowgill, E., Gold, R. D., Xuanhua, C., Xiah-Feng, W., Arrowsmith, J. R., Southon, J., 2009. Low Quaternary slip rate reconciles geodetic and geologic rates along the Altyn Tagh fault, northwestern Tibet. Geology 37 (7), 647–650.

DeMets, C., Dixon, T. H., 1999. New kinematic models for Pacific-North America motion from 3 Ma to present, I: Evidence for steady motion and biases in the NUVEL-1A model. Geophysical Research Letters 26 (13), 1921–1924.

DeMets, C., Gordon, R. G., Argus, D. F., Stein, S., 1994. Effect of recent revisions to the geomagnetic reversal time scale on estimates of current plate motions. Geophysical Research Letters 21 (20), 2191–2194.

DeMets, C., Stein, S., 1990. Present-day kinematics of the Rivera Plate and implications for the tectonics in southwestern Mexico. Journal of Geophysical Research 95 (B13), 21,931–21,948.

Deng, J., Hudnut, K., Gurnis, M., Hauksson, E., 1999. Stress loading from viscous flow in the lower crust and triggering of aftershocks following the 1994 Northridge, California, earthquake. Geophysical Research Letters 26 (21), 3209–3212.

Dunbar, J. A., Cook, R. W., 2003. Palinspastic reconstruction of structure maps: an automated finite element approach with heterogeneous strain. Journal of Structural Geology 25 (7), 1021–1036.

Durand-Riard, P., Caumon, G., Muron, P., 2010. Balanced restoration of geological volumes with relaxed meshing constraints. Computers and Geosciences 36 (4), 441–452.

Dziewonski, A. M., Anderson, D. L., 1981. Preliminary reference Earth model. Physics of the Earth and Planetary Interiors 25 (4), 297–356.

Ekström, G., England, P., 1989. Seismic Strain Rates in Regions of Distributed Continental Deformation. Journal of Geophysical Research-Solid Earth and Planets 94 (B8), 10231–10257.

England, P., McKenzie, D., 1982. A thin viscous sheet model for continental deformation. Geophysical Journal of the Royal Astronomical Society 70 (2), 295–321.

England, P., Molnar, P., 1997. Active deformation of Asia: From kinematics to dynamics. Science 278, 647–650.

England, P., Molnar, P., 2005. Late quaternary to decadal velocity fields in Asia. Journal of Geophysical Research 106 (B12), doi: 10.1029/2004JB003541.

Feldl, N., Bilham, R., 2006. Great Himalayan earthquakes and the Tibetan plateau. Nature 444, 165–170, doi: 10.1038/nature05199.

Fialko, Y., 2006. Interseismic strain accumulation and the earthquake potential on the southern San Andreas fault system. Nature 441, 968–971.

Flesch, L. M., Haines, J., Holt, W. E., 2001. Dynamics of the India-Eurasia collision zone. Journal of Geophysical Research 106 (B8), 16,435–16,460.

Flesch, L. M., Holt, W. E., Haines, J. A., Shen-Tu, B., 2010. Dynamics of the Pacific-North American plate boundary in the Western United States. Science 287 (5454), 834–836.

Fliss, S., Bhat, H. S., Dmowska, R., Rice, J. R., 2005. Fault branching and rupture directivity. Journal of Geophysical Research 110 (B06312), doi: 10.1029/2004JB003368.

Freed, A. M., Ali, S. T., Bürgmann, 2007. Evolution of stress in southern California for the past 200 years from coseismic, postseismic, and interseismic stress changes. Geophysical Journal International 169, 1164–1179, doi: 10.1111/j.1365–264X.2007.03391.x.

Fu, B., Awata, Y., 2007. Displacement and timing of left-lateral faulting in the Kunlun fault zone, northern Tibet, inferred from geologic and geomorphic features. Journal of Asian Earth Sciences 29, 253–265, doi:10.1016/j/jseaes.2006.03.004.

Gan, W., Zhang, P., Shen, Z.-K., Niu, Z., Wang, M., Wan, Y., Zhou, D., Cheng, J., 2007. Present-day crustal motion within the Tibetan plateau inferred from GPS measurements. Journal of Geophysical Research 112 (B8), doi: 10.1029/2005JB004120.

Gephart, J. W., Forsyth, D. W., 1984. An improved method for deterring the regional stress tensor using earthquake focal mechanism data: Application to the San Fernando earthquake sequence. Journal of Geophysical Research 89 (B11), 9305–9320.

Hadley, K., 1975. Azimuthal variation of dilatancy. Journal of Geophysical Research 80 (35), 4845–4850.

Hardebeck, J., 2010. Aftershocks are well aligned with the background stress field, contradicting the hypothesis of highly heterogeneous crustal stress. Journal of Geophysical Research 115 (B12308), doi: 10.1029/2010JB007586.

Hardebeck, J. L., Hauksson, E., 1997. Static stress drop in the 1994 Northridge, California, aftershock sequence. Bulletin of the Seismological Society of America 87 (6), 1495–1501.

Hardebeck, J. L., Hauksson, E., 1999. Role of fluids in faulting inferred from stress field signatures. Science 285, 233–236.

Hardebeck, J. L., Hauksson, E., 2001. Crustal stress field in southern California and its implications for fault mechanics. Journal of Geophysical Research 106 (B10), 21,859–21,882.

Hardebeck, J. L., Michael, A. J., 2004. Stress orientation at intermediate angles to the San Andreas Fault, California. Journal of Geophysical Research 109, B11303, doi:10.1029/2004JB003239.

Hardebeck, J. L., Michael, A. J., 2006. Damped regional-scale stress inversions: Methodology and examples for southern California and the Coalinga aftershock sequence. Journal of Geophysical Research 111, B11310, doi:10.1029/2005JB004144.

Harris, R. A., Simpson, R. W., 2002. The 1999 Mw 7.1 Hector Mine, California, earthquake: A test of the stress shadow hypothesis. Bulletin of the Seismological Society of America 92 (4), 1497–1512.

Harrrison, M. T., Copeland, P., Kidd, W. S. F., Lovera, O. M., 1995. Activation of the Nyainqentanghla shear zone: Implications for uplift of the southern Tibetan plateau. Tectonics 14 (3), 658–676.

Hauksson, E., 1990. Earthquakes, faulting, and stress in the Los Angeles basin. Journal of Geophysical Research 95, 15,365–15,394.

Hauksson, E., 1994. State of stress from focal mechanisms before and after the 1992 Landers earthquake sequence. Bulletin of the Seismological Society of America 84 (3), 917–934.

He, H., Ran, H., Ikeda, Y., 2006. Uniform strike-slip rate along the Xianshuihe-Xiaojiang fault system and its implications for active tectonics in southeastern Tibet. Acta Geologica Sinica 80 (3), 376–386, doi: 10.1111/j.1755–6724.2006.tb00255.x.

Herquel, G., Tapponnier, P., Wittlinger, G., Mei, J., Danian, S., 1999. Teleseismic shear wave splitting and lithospheric anisotropy beneath and across the Altyn Tagh fault. Geophysical Research Letters 26 (21), 3225–3228, doi: 10.1029/1999GL005387.

Hetland, E. A., Hager, B. H., 2005. Postseismic and interseismic displacements near a strike-slip fault; a two-dimensional theory for general linear viscoelastic rheologies. Journal of Geophysical Research 110.

Hetzel, R., Tao, M., Stokes, M., Niedermann, S., Ivy-Ochs, S., Gao, B., Strecker, M. R., Kubik, P. W., 2004. Late Pleistocene/Holocene slip rate of the Zhangye thrust (Qilian Shan, China) and implications for the active growth of the northeastern Tibetan platreau. Tectonics 23 (6), doi: 10.1029/2004TC001653.

Hickman, S., Zoback, M., 2004. Stress orientations and magnitudes in the SAFOD pilot hole. Geophysical Research Letters 31 (L15S12), doi: 10.1029/2004GL020043.

Hilley, G., Bürgmann, R., Zhang, P. Z., Molnar, P., 2005. Bayesian inference of plastosphere viscosities near the Kunlun fault, northern Tibet. Geophysical Research Letters 32 (1), L01302, doi: 10.1029/2004GL021658.

Hilley, G. E., Johnson, K. M., Wang, M., Shen, Z.-K., Bürgmann, R., 2009. Earthquake-cycle deformation and fault slip rates in northern Tibet. Geology 37 (1), 31–34, doi: 10.1130/G25157A.1.

Holt, W. E., Chamont-Rooke, N., Le Pichon, X., Haines, A. J., Shen-Tu, B., Ren, J., 2000. Velocity field in Asia inferred from Quaternary fault slip rates and Global Positioning System observations. Journal Geophysical Research 105 (B8), 19,185–19,209.

Jolivet, M., Brunel, M., Seward, D., Xu, Z., Yang, J., Malavielle, J., Roger, F., Leyreloup, A., 2003. Neogene extension and volcanism in the Kunlun fault zone, northern Tibet: new constraints on the age of the Kunlun fault. Tectonics 22 (5), 10.1029/2002TC001428.

Jones, L. M., 1988. Focal mechanisms and the state of stress on the San Andreas fault in southern California. Journal of Geophysical Research 93 (B8), 8869–8891.

Jouanne, F., Mugnier, J. L., Gamond, J. F., Le Fort, P., Pandley, M. R., Bollinger, L., Flouzat, M., Avouac, J.-P., 2004. Current shortening across the Himalayas of Nepal. Geophysics Journal International 157, 1–14, doi:10.1111/j.1365–246X.2004.02180.x.

Jungels, P. H., Frazier, G. A., 1973. Finite element analysis of the residual displacements for an earthquake rupture: source parameters for the San Fernando earthquake. Journal of Geophysical Research 78 (23), 5062–5083.

Jungles, P. H., 1973. Models of tectonic processes associated with earthquakes. Ph.D. thesis, California Institute of Technology.

Kame, N., Rice, J. R., Dmowska, R., 2003. Effects of prestress state and rupture velocity on dynamic fault branching. Journal of Geophysical Research 108 (B5), 2265, doi: 10.1029/2002JB002189.

Kind, R., Yuan, X., Saul, J., Nelson, D., Sobolev, S. V., Mechie, J., Zhao, W., Kosarev, G., Ni, J., Achauer, U., Jiang, M., 2002. Seismic images of crust and upper mantle beneath Tibet: evidence for Eurasian plate subduction. Science 298 (1219), 10.1126/science.1078115.

King, G. C., Stein, R. S., Lin, J., 1994. Static stress changes and the triggering of earthquakes. Bulletin of the Seismological Society of America 84 (3), 935–953.

Kirby, E., Harkins, N., Wang, E., Shi, X., Fan, C., Burbank, D., 2007. Slip rate gradients along the eastern Kunlun fault. Tectonics 26 (2), doi: 10.1029/2006TC002033.

Kwon, Y. W., Bang, H., 2000. The Finite Element Method Using Matlab, 2nd Edition. CRC Press, Boca Raton, Florida.

Lamb, S., 1994a. A simple method for estimating the horizontal velocity field in wide zones of active deformation - I. description, with an example from California. Geophysical Journal International 119 (1), 297–312.

Lamb, S. H., 1994b. Behavior of the brittle crust in wide plate boundaries. Journal of Geophysical Research 99 (B3), 4457–4483.

Langstaff, M. A., Meade, B. J., 2013. Edge-driven mechanical models of strike-slip faulting in the Tibetan plateau. Journal of Geophysical Research 118 (7), 10.1002/jgrb.50272.

Laursen, T. A., 2002. Computation Contact and Impact Mechanics: Fundamentals of Modeling Interfacial Phenomena in Nonlinear Finite Element Analysis. Springer-Verlag, Berlin, Heidelberg, and New York.

Lavé, J., Avouac, J. P., 2000. Active folding of fluvial terraces across the Siwaliks Hills, Himalayas of central Nepal. Journal of Geophysical Research 105 (B3), 5735–5770.

Leloup, P. H., Arnaud, N., Lacassin, R., Kienast, J. R., Harrison, T. M., Phan Trong, T. T., Replumaz, A., Tapponnier, P., 2001. New constraints on the structure, thermochronology, and timing of the Ailao Shan-Red River shear zone, SE Asia. Journal of Geophysical Research 106 (B4), 6683–6732, doi: 10.1029/2000JB900322.

Leloup, P. H., Lacassin, R., Tapponnier, P., Schärer, U., Dalai, Z., Xiaohan, L., Liangshang, Z., Shaocheng, J., Trinh, P. T., 1995. The Ailao Shan-Red River shear zone (Yunnan, China), Tertiary transform boundary of Indochina. Tectonophysics 251, 3–84.

Li, C., Zhang, P., Yin, J., Min, W., 2009. Late Quaternary left-lateral slip rate of the Haiyuan fault, northeastern margin of the Tibetan plateau. Tectonics 28 (5), doi: 10.1029/2008TC002302.

Li, S., Mooney, W. D., Fan, J., 2006. Crustal structure of mainland China from deep seismic sounding data. Tectonophysics 420, 239–252, doi:10.1016/j/tecto/2006.01.026.

Lockner, D. A., Morrow, C., Moore, D., Hickman, S., 2011. Low strength of deep San Andreas fault gauge from SAFOD core. Nature 472, doi:10.1038/nature09927.

Lohman, R. B., Simons, M., 2005. Locations of selected small earthquakes in the Zagros mountains. Geochemistry Geophysics Geosystems 6 (1), Q03001, doi:10.1029/2004GC000849.

Loveless, J. P., Meade, B. J., 2011a. Partitioning of localized and diffuse deformation in the Tibetan plateau from joint geologic and geodetic observations. Earth and Planetary Science Letters 303, 11–24.

Loveless, J. P., Meade, B. J., 2011b. Stress modulation on the San Andreas fault by interseismic fault system interactions. Geology 39 (11), 1035–1038.

Maerten, L., Maerten, F., 2002. Chronologic modeling of faulted and fractured reservoirs using geomechanically based restoration: Technique and industry applications. AAPG Bulletin 90 (8), 1201–1226.

Marshall, S. T., Cooke, M. L., Owen, S. E., 2009. Interseismic deformation associated with three-dimensional faults in the greater Los Angeles region, California. Journal of Geophysical Research 114 (B12403), doi: 10.1029/JB006439.

Masterlark, T., Wang, H. F., 2002. Transient stress-coupling between the 1992 Landers and 1999 Hector Mine, California, earthquakes. Bulletin of the Seismological Society of America 92 (4), 1470–1486.

Matmon, A., Schwartz, D. P., Finkel, R., Clemmens, S., Hanks, T., 2005. Dating offset fans along the Mojave section of the San Andreas fault using cosmogenic ^{26}Al and ^{10}Be. GSA Bulletin 117 (5-6), 795–807, doi: 10.1130/B25590.1.

Mayeda, K., Walter, W. R., 1996. Moment, energy, stress drop, and source spectra of western United States earthquakes from regional code envelopes. Journal of Geophysical Research 101 (B5), 11,195–11,208.

McCaffrey, R., 2005. Block kinematics of the Pacific-North America plate boundary in the southwestern United States from inversion of GPS, seismological, and geologic data. Journal of Geophysical Research 110 (B7), B07401, doi:10.1029/2004JB003307.

McGill, S. F., Owen, L. A., Weldon II, R. J., Kendrick, K. J., 2013. Latest Pleistocene and Holocene slip rate for the San Bernardino strand of the San Andreas fault, Plunge Creek, southern California: Implications for strain partitioning within the southern San Andreas fault system for the last $\sim$ 35 k.y. GSA Bulletin, doi: 10.1130/B30647.1.

McKenzie, D. P., 1969. The relation between fault plane solutions for earthquakes and the directions of the principal stresses. Bulletin of the Seismological Society of America 59, 591–601.

Meade, B. J., 2007. Present-day kinematics at the India-Asia collision zone. Geology 35 (1), 81–84.

Meade, B. J., Hager, B. H., 2005. Block models of crustal motion in southern California constrained by gps measurements. Journal of Geophysical Research 110 (B03403), doi: 10.1029/2004JB003209.

Melosh, H. J., Raefsky, A., 1981. A simple and efficient method for introducing faults into finite element computations. Bulletin of the Seismological Society of America 71 (5), 1391–1400.

Mériaux, A. S., Tapponnier, P., Ryerson, F. J., Xiwei, X., King, G., Van der Woerd, J., Finkel, R. C., Haibing, L., Caffee, M. W., Zhiqin, X., Wenbin, C., 2005. The Aksay segment of the northern Altyn Tagh fault: Tectonic geomorphology, landscape evolution, and Holocene slip rate. Journal of Geophysical Research 110 (B04404), doi: 10.1029/2004JB003210.

Michael, A. J., 1984. Determination of stress from slip data: Faults and folds. Journal of Geophysical Research 89 (B13), 11,517–11,526.

Michael, A. J., 1987. Use of focal mechanisms to determine stress: A control study. Journal of Geophysical Research 92 (B1), 357–368.

Molnar, P., Tapponnier, P., 1975. Cenozoic tectonics of Asia, effects of a continental collision. Science 189, 419–426.

Moore, M., England, P., Parsons, B., 2002. Relation between surface velocity field and shear wave splitting in the South Island of New Zeland. Journal of Geophysical Research 107 (B9), 10.1029/2000JB000093.

Mori, J., Abercrombie, R. E., Kanamori, H., 2003. Stress drops and radiated energies of aftershocks of the 1994 Northridge, California, earthquake. Journal of Geophysical Research 108 (B11), doi: 10.1029/2001JB000474.

Munjiza, A., 2004. The Combined Finite-Discrete Element Method. John Wiley & Sons, Ltd., West Sussex, England.

Muron, P., 2005. Méthodes numériques 3-d de restauration des structures géologiques faillées. Ph.D. thesis, Institut National Polytechnique de Lorriane.

Murphy, M. A., Yin, A., Kapp, P., Harrison, T. M., Lin, D., Jinghui, G., 2000. Southward propagation of the Karakorum fault system, southwest Tibet: timing and magnitude of slip. Geology 28 (5), 451–454, doi: 10.1130/00917613.

Murray, J. R., Segall, P., Cervelli, P., Prescott, W., Svarc, J., 2001. Inversion of GPS data for spatially variable slip-rate on the San Andreas Fault near Parkfield, CA. Geophysical Research Letters 28 (2), 359–362.

Nur, A., Booker, J. R., 1972. Aftershocks caused by pore fluid flow? Nature 175, 885–887.

Nur, A., Ron, H., Beroza, G. C., 1993. The nature of the Landers-Mojave earthquake line. Science 261 (5118), 201–203.

Oakley, D., Knight, N., 1995. Adaptive dynamic relaxation for non-linear hyper elastic structures, Part I. Formulation. Computer Methods in Applied Mechanics and Engineering 126, 67–89.

Okada, Y., 1992. Internal deformation due to shear and tensile faults in a half-space. Bulletin of the Seismological Society of America 82 (2), 1018–1040.

Owens, T. J., Zandt, G., 1997. Implications of crustal property variations for models of Tibetan plateau evolution. Nature 387, 37–43, doi: 10.1038/387037a0.

Parsons, T., Dreger, D. S., 2000. Static-stress impact of the 1992 Landers earthquake sequence on nucleation and slip at the site of the 1999 M = 7.1 Hector Mine earthquake, southern California. Geophysical Research Letters 27 (13), 1949 – 1952.

Paul, J., Bürgmann, Gaur, V. K., Larson, K. M., Ananda, M. B., Jade, S., Mukal, M., Anupama, T. S., Satyal, G., Kumar, D., 2001. The motion and active deformation of India. Geophysical Research Letters 28 (4), doi: 10.1029/2000GL011832.

Pelties, C., de la Puente, J., Ampuero, J.-P., Brietzke, G. B., Käser, M., 2012. Three-dimensional dynamic rupture simulation with a high-order discontinuous Galerkin method on unstructured tetrahedral meshes. Journal of Geophysical Research 117 (B02309), doi: 10.1029/2011JB008857.

Pelzer, G., Saucier, F., 1996. Present-day kinematics of Asia derived from geologic fault slip rates. Journal of Geophysical Research 101, 27,943–27,956.

Pili, E., Ricard, Y., Lardeaux, J.-M., Sheppard, S. M. F., 1997. Lithospheric shear zones and mantle-crust connections. Tectonophysics 280, 15–29.

Platt, J. P., Becker, T. W., 2010. Where is the real transform boundary in California? Geochemistry, Geophysics, Geosystems 11 (6), doi: 10.1029/2010GC003060.

Platt, J. P., Kaus, B., Becker, T. W., 2008. The mechanics of continental transforms: An alternative approach with applications to the San Andreas fault system and the tectonics of California. Earth and Planetary Science Letters 274, 380–391, doi: 10.1016/j.epsl.2008.07.052.

Plesch, A., Shaw, J. H., Benson, C., Bryant, W. A., Carena, S., Cooke, M., Dolan, J., Fuis, G., Gath, E., Grant, L., Hauksson, E., Jordan, T., Kamerling, M., Legg, M., Lindvall, S., Magistrale, H., Nicholson, C., Niemi, N., Oskin, M., Perry, S., Planansky, G., Rockwell, T., Shearer, P., Sorlien, C., Süss, P. M., Suppe, J., Treiman, J., Yeats, R., 2007. Community fault model (CFM) for southern California. Bulletin of the Seismological Society of America 97 (6), 1793–1802, doi: 10.1785/0120050211.

Pollitz, F. F., Sacks, S., 2002. Stress triggering of the 1999 Hector Mine earthquake by transient deformation following the 1992 Landers earthquake. Bulletin of Seismological Society of America 92 (4), 1487–1496.

Price, E. J., Bürgmann, R., 2002. Interactions between the Landers and Hector Mine, California, earthquakes from space geodesy, boundary element modeling, and time-dependent friction. Bulletin of the Seismological Society of America 92 (4), 1450–1469.

Richardson, E., Jordan, T., 2002. Seismicity in deep gold mines of South Africa: Implications for tectonic earthquakes. Bulletin of the Seismological Society of America 92 (5), 1766–1782.

Rivera, L., Kanamori, H., 2002. Spatial heterogeneity of tectonic stress and friction in the crust. Geophysical Research Letters 29 (6), doi: 10.1029/2001GL013803.

Royden, L. H., Burchfiel, B. C., Van der Hilst, R. D., 2008. The geologic evolution of the Tibetan plateau. Science 321, 1054–1058.

Rümpker, G., Ryberg, T., Bock, G., Group, D. S., 2003. Boundary layer mantle flow under the Dead Sea transform fault inferred from seismic anisotropy. Nature 425, 497–501.

Savage, J., Prescott, W. H., 1978. Asthenosphere readjustment and the earthquake cycle. Journal of Geophysical Research 83 (B7), 3369–3376.

Savage, J. C., 1983. A dislocation model of strain accumulation and release at a subduction zone. Journal of Geophysical Research 88 (B6), 4984–4996.

Savage, J. C., Burford, R. O., 1973. Geodetic Determination of Relative Plate Motion in Central California. Journal of Geophysical Research 78 (5), 832–845.

Savage, J. C., Lisowski, M., 1998. Viscoelastic coupling model of the San Andreas Fault along the big bend, southern California. Journal of Geophysical Research-Solid Earth 103 (B4), 7281–7292.

Schmalzle, G., Dixon, T., Malservisi, R., Govers, R., 2006. Strain accumulation across the Carrizo segment of the San Andreas fault, California: Impact of laterally varying crustal properties. Journal of Geophysical Research 111 (B05403), doi: 10.1029/2005JB003843.

Scholz, C. H., 2000. A fault in the "weak San Andreas" theory. Nature 406, 234.

Scholz, C. H., 2002. The Mechanics of Earthquakes and Faulting, 2nd Edition. Cambridge University Press, Cambridge.

Scientists of the US Geological Survey, ., Southern California Earthquake Center, ., California Division of Mines & Geology, ., 2000. Preliminary report on the 16 Ooctober 16 1999 M 7.1 Hector Mine, California, earthquake. Seismological Research Letters 71 (1), 11–23.

Segall, P., 2002. Integrating geologic and geodetic estimates of slip rate on the San Andreas fault system. International Geology Review 44 (1), 62–82.

Shamir, G., Zoback, M. D., 1992. Stress orientation profile to 3.5 km depth near the San Andreas fault at Cajon Pass, California. Journal of Geophysical Research 97 (B4), 5059–5080.

Sieh, K., Jones, L., Haukisson, E., Hudnut, K., Eberhart-Phillips, D., Heaton, T., Hough, S., Hutton, K., Kanamori, H., Lilje, A., Lindvall, S., McGill, S. F., Mori, J., Rubin, C., Spotila, J. A., Stock, J., Thio, H. K., Treiman, J., Wernicke, B., Zachariasen, J., 1993. Near-field investigations of the Landers earthquake sequence, April to July 1992. Science 260, 171–175.

Sieh, K. E., Jahns, R. H., 1984. Holocene Activity of the San-Andreas Fault at Wallace-Creek, California. Geological Society of America Bulletin 95 (8), 883–896.

Smith, D. E., Heaton, T. H., 2011. Models of stochastic, spatially varying stress in the crust compatible with focal-mechanism data, and how stress inversions can be biased toward the stress state. Bulletin of the Seismological Society of America 101 (3), 1396–1421, doi: 10.1785/01201000058.

Smith-Konter, B., Sandwell, D., 2009. Stress evolution of the San Andreas fault system: Recurrence interval versus locking depth. Geophysical Research Letters 36, doi: 10.1029/2009GL037235.

Steacy, S., Gomberg, J., Cocco, M., 2005. Introduction to special section: Stress transfer, earthquake triggering, and time-dependent seismic hazard. Journal of Geophysical Research 110 (B05501), doi: 10.1029/2005JB003692.

Stein, R. S., 1999. The role of stress transfer in earthquake occurrence. Nature 402, 605–609.

Stock, J. M., Hodges, K. V., 1989. Pre-Pliocene extension around the Gulf of California and the transfer of Baja California to the Pacific plate. Tectonics 8 (1), doi: 10/1029/TC008i001p00099.

Tapponnier, P., Meyer, B., Avouac, J. P., Peltzer, G., Gaudemer, Y., Shunmin, G., Hongfa, X., Kelun, Y., Zhitai, C., Shuahua, C., Huangang, D., 1990. Active thrusting and folding in the Qilan Shan, and decoupling between upper crust and mantle in northeastern Tibet. Earth and Planetary Science Letters 97, 382–403.

Tapponnier, P., Peltzer, G., Le Dain, A. Y., Armijo, R., Cobbard, P., 1982. Propagating extrusion tectonics in Asia: New insights from simple experiments with plasticine. Geology 10 (12), 611–616, doi: 10.1130/0091–7613(1982).

Taylor, M., Yin, A., 2009. Acitve structures of the Himalayan-Tibetan orogen and their relationships to earthquake distribution, contemporary strain field, and Cenozoic volconism. Geosphere 5 (3), 199–214, doi:10.1130/GES00217.1.

Taylor, R. L., 2013. FEAP - A finite element analysis program, Version 8.4 user manual.

Thatcher, W., 2007. Microplate model for the present-day deformation in Tibet. Journal of Geophysical Research 112 (B01401), dot: 10.1029/2005JB004244.

Thatcher, W., England, P. C., 1998. Ductile shear zones beneath strike-slip faults: Implications for the thermomechanics of the San Andreas fault zone. Journal of Geophysical Research 103 (B1), 891–905.

Thompson, S. C., Weldon, R. J., Rubin, C. M., 2002. Late Quaternary slip rates across the central Tien Shan, Kyrgyzstan, central Asia. Journal of Geophysical Research 107 (B9), doi: 10.1029/2001JB000596.

Toda, S., Stein, R. S., Richards-Dinger, K., Bozkurt, S. B., 2005. Forecasting the evolution of seismicity in southern California: Animations built on earthquake stress transfer. Journal of Geophysical Research 110 (B5), doi: 10.1029/2004JB003415.

Townend, J., Zoback, M. D., 2004. Regional tectonic stress near the San Andreas fault in central and southern California. Geophysical Research Letters 31, L15S11, doi:10.1029/2003GL018918.

Trifu, C., Felher, M., 1998. Preface to the special issue on "new trends in seismological research: Studies of seismicity induced by mining, petroleum, and geothermal activities". Tectonophysics 289, vii – ix.

Turcotte, D. L., Spence, D. A., 1974. An analysis of strain accumulation on a strike slip fault. Journal of Geophysical Research 79 (29), 4407–4412.

Van der Woerd, J., Klinger, Y., Sieh, K., Tapponnier, P., Ryerson, F. J., Mériaux, A.-S., 2006. Long-term slip rate of the southern San Andreas Fault from ^{10}Be-^{26}Al surface exposure dating of an offset alluvial fan. Journal of Geophysical Research 111 (B4), doi: 10.1029/2004JB0035559.

Van der Woerd, J., Mériaux, A., Klinger, Y., Ryerson, F. J., Daudemer, Y., Tapponnier, P., 2002a. The 14 November 2001 Mw = 7.8 Kokoxili earthquake in northern Kunlun (Qinghai Province, China. Seismological Research Letters 73 (2), 125–135.

Van der Woerd, J., Tapponnier, P., Ryerson, F., Mériaux, A., Meyer, B., Gaudemer, Y., Finkel, R., Caffee, M., Guoguang, Z., Zhiqin, X., 2002b. Uniform postglacial slip-rate along the central 600 km of the Xianshuihe fault (Tibet), from 26Al, 10Be, and 14C dating of riser offsets, and climatic origin of the regional morphology. Geophysical Journal International 148 (3), 356–388, doi: 10.1046/j.1365–246x.2002.01556.x.

Wallace, K., Yin, G. H., Bilham, R., 2004. Inescapable slow slip on the Altyn Tagh fault. Geophysical Research Letters 31 (L06613), 10.1029/2004GL021014.

Wang, C.-Y., Chan, W. W., Mooney, W. D., 2003. Three dimensional velocity structure of crust and upper mantle in southwestern China and its tectonic implications. Journal of Geophysical Research 108 (B9), doi:10.1029/2002JB001973.

Wang, H., Wright, T. J., Biggs, J., 2009. Interseismic slip rate of the northwestern Xianshuihe fault from InSAR data. Geophysical Research Letters 36 (L03302), doi:10.1029/2008GL036560.

Wang, Q., Zhang, P. Z., Freymueller, J. T., Bilham, R., Larson, K. M., Lai, X., You, X. Z., Niu, Z. J., Wu, J. C., Li, Y. X., Liu, J. N., Yang, Z. Q., Chen, Q. Z., 2001. Present-day crustal deformation in China constrained by global positioning system measurements. Science 294 (5542), 574–577.

Weldon, R., Humphreys, E., 1986. A Kinematic Model of Southern-California. Tectonics 5 (1), 33–48.

Weldon, R. J., Fumal, T. E., Biasi, G. P., Scharer, K. M., 2005. Past and future earthquakes on the San Andreas fault. Science 308 (5724), 966–967, doi: 10.1126/science.1111707.

Weldon, R. J., Sieh, K. E., 1985. Holocene Rate of Slip and Tentative Recurrence Interval for Large Earthquakes on the San-Andreas Fault, Cajon-Pass, Southern-California. Geological Society of America Bulletin 96 (6), 793–812.

West, D. P., Hubbard, M. S., 1997. Progressive localization of deformation during exhumation of a major strike-slip shear zone: Norumbega fault zone, south-central maine, USA. Tectonophysics 273, 185–201.

Wilde, M., Stock, J., 1997. Comparison directions in southern California (from Santa Barbara to Los Angeles Basin) obtained from borehole breakouts. Journal of Geophysical Research 102 (B3), 4969–4983, doi: 10.1029/96JB03734.

Working Group on California Earthquake Probabilities, ., 1995. Seismic hazards in southern California: Probable earthquakes, 1994-2024. Bulletin of the Seismological Society of America 85 (2), 379–439.

Wriggers, P., 2006. Computation Contact Mechanics, 2nd Edition. Springer-Verlag, Berlin, Heidelberg, and New York.

Wright, T. J., Parsons, B., England, P. C., Fielding, E. J., 2004. InSAR observations of low slip rates on the major faults of western Tibet. Science 305, 236–239.

Yang, W., Hauksson, E., 2013. The tectonic crustal stress field and style of faulting along the Pacific North America Plate boundary in southern California. Geophysical Journal International 194, 100 – 117, doi: 10.1093/gji/ggt113.

Yue, Y., Ritts, B. D., Graham, S. A., 2001. Initiation and long-term slip history of the Altyn Tagh fault. International Geologic Review 43, 1087–1093.

Zang, A., Stephansson, O., 2010. Stress Field of the Earth's Crust. Springer Science and Business Media, Heidelberg, London, and New York.

Zeng, Y., 2001. Viscoelastic stress-triggering of the 1999 Hector Mine earthquake by the 1992 Landers earthquake. Geophysical Research Letters 28 (15), doi: 10.1029/2000GL012806.

Zhang, Z., Klemperer, S. L., 2005. West-east variation in crustal thickness in northern Lhasa block, central Tibet, from deep seismic sounding data. Journal of Geophysical Research 110 (B09403), 10.1029/2004JB003139.

Zhao, D., Kanamori, H., Wiens, D., 1997. State of stress before and after the 1994 Northridge earthquake. Geophysical Research Letters 24 (5), 519–522.

Zhen-Kang, S., Lu, J., Wang, M., Bürgmann, R., 2005. Contemporary crustal deformation around the southeast borderland of the Tibetan plateau. Journal of Geophysical Research 110 (B11), 1978–2012, doi: 10.1029/2004JB003421.

Zienkiewicz, O. C., Taylor, R. L., 2005. The Finite Element Method for Solid and Structural Mechanics, 6th Edition. Butterworth-Heinemann, Oxford, United Kingdom and Burlington, United States.

Zoback, M., Hickman, S., Ellsworth, W., the SAFOD Science Team, 2011. Scientific drilling into the San Andreas fault zone - An overview of SAFOD's first five years. Scientific Drilling 11, doi: 10.2204/lodp.sd.11.02.2011.

Zoback, M. D., Healy, J. H., 1992. In situ stress measurements to 3.5 km depth in the Cajon Pass scientific research borehole: Implications for the mechanics of crustal faulting. Journal of Geophysical Research 97 (B4), 5039–5057.

Zoback, M. D., Zoback, M. L., Mount, V. S., Suppe, J., Eaton, J. P., Healy, J. H., Oppenheimer, D., Reasenberg, P., Jones, L., Raleigh, C. B., Wong, I. G., Scotti, O., Wentworth, C., 1987. New evidence on the state of stress of the San Andreas fault system. Science 238, 1105–1111.